Politecnico di Milano

Department of Aerospace Science and Technology

Doctoral Programme In Aerospace Engineering

Multireceiver radar technologies for space surveillance and tracking

Doctoral Dissertation of:

Marco Felice Montaruli

Supervisors: **Prof. Pierluigi Di Lizia**, **Prof. Stefano Tebaldini**

Tutor: **Prof. Antonio Grande**

The Chair of the Doctoral Program: **Prof. Pierangelo Masarati**

2022 – XXXV Cycle

Multireceiver radar technologies for space surveillance and tracking

by

Marco Felice Montaruli

Abstract

The increasing population of resident space objects is currently fostering many Space Surveillance and Tracking initiatives, which rely on the use of ground sensors. In this framework, besides slant range and Doppler shift measurements, surveillance radars can provide the angular track as well, but the related accuracy may be quite poor.
This thesis shows the advantage which may derive from an adaptive beamfoming technique in multi-receiver surveillance radars devoted to SST-related activities. Combining such an approach with a proper clustering strategy and criteria to solve the possible estimations ambiguity, the resulting MATER algorithm is capable of providing angular track either in presence of a single or multiple targets, in a robust way. In both cases, the accuracy is in the order of 1e-03 deg, but may deteriorate depending on the impinging signal power, the number of samples integrated to generate each estimation and the related integration time length. Nevertheless, MATER represents a remarkable step forward in favour of the surveillance radars contribution to SST-related activities, such as Collision Avoidance, Re-entry and Fragmentations Analysis services.
Particular attention is devoted to fragments cloud monitoring. Specifically, the fragmentation epoch identification problem from a single fragment observation is dealt with. Given the initial orbit determination accuracy, the uncertainty associated to the fragment orbital state cannot be neglected, and a stochastic approach is introduced. The resulting FRED algorithm ranks a set of fragmentation epoch candidates according to the statistical matching between the minimum orbital intersection distance and the relative distance distributions, and the optimal candidate is returned. The convergence to the correct solution strongly depends on the mutual geometry between fragment and parent orbits, the fragment orbital state accuracy and the time elapsed between the event and the observation, but FRED always performs better than an alternative deterministic metrics. MATER allows to exploit such an approach, but the associated non-zero mean and non-Gaussian error of measurements would prevent from stable and reliable results. Nevertheless, in operational applications, the detected fragment may be later tracked with additional sensors to derive a more accurate orbital state to be used in FRED algorithm.

Sommario

L'aumento della popolazione di oggetti in orbita terrestre sta attualmente incoraggiando molte iniziative di sorveglianza e tracciamento spaziale (SST), che si basano sull'utilizzo di sensori a terra. In questo contesto, oltre alle misure di distanza obliqua e di effetto Doppler, i radar di sorveglianza sono in grado di fornire anche la traccia angolare, ma con un'accuratezza che rischia di essere piuttosto scarsa.
Questa tesi illustra i vantaggi che potrebbero derivare da una tecnica di beamforming adattativo nei radar di sorveglianza multi-ricevitori che vengono impiegati in attività SST. Combinando tale approccio con un'appropriata strategia di clustering e con criteri per risolvere eventuali ambiguità, l'algoritmo MATER che ne deriva è in grado di fornire in modo robusto la traccia angolare in presenza sia di una sola che di molteplici sorgenti. In entrambi i casi l'accuratezza ottenuta è nell'ordine di 1e-03 gradi, ma può deteriorarsi a seconda della potenza del segnale rilevato, del numero di campioni integrati per generare ciascuna stima e della connessa lunghezza del tempo di integrazione. Ad ogni modo, MATER rappresenta un passo importante per il contributo dei sensori radar di sorveglianza alle attività SST quali i servizi di anticollisione, di analisi di rientro e di analisi di frammentazioni.
Particolare attenzione viene dedicata al monitoraggio della nube di frammenti. Specificatamente, si affronta il problema dell'identificazione dell'epoca di frammentazione dall'osservazione di un solo frammento. Data l'accuratezza della determinazione orbitale iniziale, l'incertezza associata allo stato orbitale del frammento non può essere trascurata e si introduce quindi un approccio stocastico. L'algoritmo FRED che ne deriva ordina una serie di epoche di frammentazione candidate a seconda della corrispondenza statistica tra le distribuzioni di distanza di intersezione orbitale minima e di distanza relativa e viene così restituito il candidato ottimale. La convergenza alla soluzione corretta dipende fortemente dalla geometria relativa tra le orbite del frammento e dell'oggetto genitore, dall'accuratezza dello stato orbitale del frammento e dal tempo intercorso tra l'evento e l'osservazione, ma FRED dà risultati sempre migliori di una metrica deterministica alternativa. MATER permette di sfruttare tale approccio, ma l'errore di misura, non Gaussiano e a media diversa da zero, impedirebbe di ottenere risultati stabili e affidabili. Comunque sia, in applicazioni operative, il frammento rilevato può poi essere tracciato con altri sensori per ottenere uno stato orbitale più accurato che possa essere usato nell'algoritmo FRED.

To my family

Ringraziamenti

Possiamo soltanto decidere cosa fare con il tempo che ci viene concesso.

Non è semplice riassumere la serie di eventi che mi hanno infine condotto a fare il dottorato: l'ernia al disco che mi ha impedito di accettare opportunità lavorative all'estero subito dopo il conseguimento della Laurea Magistrale, la casuale scoperta di questa opportunità, il rifiuto del candidato prima di me in classifica, ... Fatto sta che questo percorso provvidenziale è stato possibile solo e soltanto grazie al prof. Pierluigi Di Lizia, il mio saggio Gandalf, che mi ha guidato attraverso questi anni, con consigli fondamentali e infinita pazienza, con un cuore appassionato capace di motivare le altre persone. Ma Pierluigi non è stata l'unica guida che ho avuto: fin dall'inizio del viaggio verso il mio Monte Fato, prof. Mauro Massari è sempre stato presente, come Aragorn, con la sua infallibile capacità di giudizio.

Coraggio, padron Frodo! Non posso portare l'Anello per voi, ma posso portare voi!

Mi è sempre stato chiaro che non ero capace di condurre da solo il Dottorato e sono stato così fortunato da incontrare ben due Samvise Gamgee: Michele Maestrini e Giovanni Purpura. Non solo: come Frodo ha potuto contare pure sul supporto dei suoi due cugini, in questi anni ho potuto contare sui miei Meriadoc Brandibuck e Peregrino Tuc, mascherati da Riccardo Cipollone e Luca Facchini. Senza Sam, Merry e Pipino, Frodo non avrebbe nemmeno mai iniziato il proprio viaggio: allo stesso modo, senza Miki, Giovanni, Luca e Rick, la mia tesi avrebbe difficilmente visto la luce.

Nove saranno i membri della Compagnia dell'Anello, e i Nove Viandanti si opporranno ai Nove Cavalieri che sono malvagi.

Non sono affatto sicuro che la nostra "Compagnia" sia esattamente composta di nove persone, come non sono nemmeno sicuro del nome della nostra "Compagnia" (se SpireLab, Spire o S4U), ma sono sicuro e orgoglioso dei viandanti che si sono opposti ai cavalieri oscuri. Oltre ai membri già menzionati sopra, ho avuto l'onore, oltre al piacere, di combattere sotto le stesse insegne di Andrea De Vittori, Niccolò Faraco, Chuncheng Zhao e Sergio Bonaccorsi e, più recentemente, Gaetano Calabrò e Alessia De Riz. Voglio ricordare anche il nostro Boromir, Lorenzo Ticozzi, che ci ha accompagnato per alcuni mesi prima di partire per gli Stati Uniti.

Gli Hobbit sono veramente esseri stupefacenti, come ho sempre sostenuto.

Oltre agli stupefacenti compagni con cui ho lavorato costantemente in questi anni, alcuni volti del PoliMi sono stati di importanza fondamentale: Federico Ghioldi, Gianmario Merisio, Mattia Pugliatti e Ruggiero Signoriello con cui ho trascorso tanti pranzi meravigliosi, Emanuele Gallorini per la compagnia costante in ufficio, Andrea Muciaccia e Francesca Scala per i lavori svolti insieme, Andrea Pasquale per il tempo passato insieme in Germania e Margherita Piccinin per le attività di rappresentanza. Vorrei anche ringraziare il prof. Tebaldini del Dipartimento di Elettronica, Informazione e Bioingegneria (DEIB) per l'aiuto nella parte di processamento del segnale, la prof.ssa Colombo per gli utili consigli su come tenere una presentazione e il prof. Dozio per tutti i momenti di confronto avuti in questi anni.

È come nelle grandi storie, padron Frodo. Quelle che contano davvero.

Mi commuovo se penso a quel tema, scritto in terza media, in cui dicevo che mi sarebbe piaciuto lavorare all'Agenzia Spaziale Europea (ESA): dopo circa quindici anni ho avuto l'opportunità (sempre grazie a Pierluigi) di svolgere un periodo come ricercatore in visita presso lo Space Debris Office dell'ESA. Vorrei perciò dedicare un ringraziamento speciale a Emiliano Cordelli (GMV), Hélène Ma (RHEA Group) e Jan Siminski (ESA), per il proficuo aiuto e il tempo speso a coltivare le mie capacità di ricerca, e ad Alejandro Pastor-Rodriguez, il saggio collega che ognuno vorrebbe incontrare all'estero.

Ci sono altre forze che agiscono in questo mondo, Frodo, a parte la volontà del Male.

Sono consapevole che le forze che hanno reso questo mio viaggio possibile non riguardano solamente il PoliMi. Senza l'Istituto Nazionale di Astrofisica (INAF) e senza l'Aeronautica Militare (AM) il nostro gruppo di ricerca sarebbe stato piuttosto diverso (e più piccolo) di quello che è in realtà. Voglio ringraziare soprattutto due persone: Germano Bianchi di INAF e Capitano Moreno Peroni di AM. Credo fortemente che l'Italia abbia bisogno di più persone come loro, capaci di scommettere sulle abilità nazionali, permettendole di crescere e di provare il loro talento. Vorrei ringraziare anche Giuseppe Pupillo e Giovanni Naldi di INAF e, soprattutto, il Maggiore Giuseppe Pariti di AM, per tutte le opportunità che mi ha dato in questi anni.

Casa è alle spalle, il mondo avanti, le strade da seguire tante.

Per prendere le decisioni più importanti della vita, bisogna essere certi che ci è promesso un bene, qualunque strada prenderemo. Nel cammino verso questa certezza, di cui rimane ancora una bella strada da fare, la Germania è stato un momento decisivo. E decisivi i volti incontrati: Miriam, Enrico, Elisabetta, Irene, Caterina, Teresa, Bernardo, Sara, Fabian, Lucia, Virginia, Aldo e Sara.

Sento che finché saprò che la mia Contea è sempre qui, comoda e sicura, girovagare ed errare sarà per me più facile, conscio che in una parte del mondo c'è un appoggio stabile e saldo che mi attende, anche se non vi dovessi più metter piede.

Ho lasciato in fondo chi nel mio cuore ringrazio ogni giorno per primo: mia madre, mio padre, mio fratello Matteo e mia sorella Anna, mia nipote Maddalena, mio cognato Giovanni, mia nonna Rita, mia zia Valeria, mio zio Andrea, i miei cugini Francesco e Sofia, e, anche se c'è stata davvero poca occasione di vedersi in questi anni, Silvia, Flavia, Paolo, mio zio Luca, Emi e mia cugina Chiara. Infine, un ricordo va ai miei cari che non ci sono più: mia nonna Iride, mio nonno Andrea, mio zio Agostino, mio nonno Carlo e mia zia Annita. Tra i miei parenti io ci metto anche Giovanni e Noemi, perché non ci credo che non abbiamo nemmeno una goccia di sangue in comune, così come Elio e zia Giulia, che ci hanno lasciato in questi anni.

Ci sono poi tanti volti di amici che mi hanno sostenuto e accompagnato e sarebbe impossibile nominarli tutti. I miei cari Paccari al Sugo: Francesco, Daniela, Camilla, Emanuele, Gabriele, Andrea, Marco, Alessandro, Luca, Ludovico, Matteo e Simone. I miei compagni di liceo e di vacanze estive: Alessandra, Alice, Giulia, Francesco, Marco, Filippo, Jacopo, Aldri, Ilaria, Nicolò e Camilla. Volti singoli che non mi abbandonano mai: Filippo, Gabriele, Emanuele, Samuele, Arianna, Marco, Maria Concetta, Marilù, Francesca, Pasquale, Sara e Giacomo, che mi ha concesso l'onore di essere suo testimone di nozze. E poi ancora don Alessandro Suma, un incontro inaspettato e speciale, e don Alessandro Morini, che ha avuto così grande responsabilità nelle scelte che ho intrapreso. E ancora tutti i volti della Scuola di Comunità: Giulio, Simona, Mattia, Matteo, Giovanni, Marco, Lorenzo, Samuele, Caterina e, soprattutto, Davide e Claudio: "Partire o restare? No, seguire. Cioè appartenere".

Ci sono infine molte persone che ho tralasciato. Alcune hanno costituito un incontro importante, seppure a volte estremamente rapido. Altre sono state molto presenti nella mia

mente e nel mio cuore, sebbene assenti fisicamente, o perché così ha voluto il nostro destino (penso, per esempio, a Marco, Stefano, Fabio e Giacomo, i miei mitici compagni di Laurea Triennale), o perché così abbiamo scelto noi. Quello che oggi sono lo devo anche a loro.

Molto ragionamento e poca osservazione, conducono all'errore. Molta osservazione e poco ragionamento conducono alla verità.

Vorrei infine dedicare un pensiero alle vittime del Covid-19, in particolare a don Luigi Giussani. Non riuscirò mai a comprendere appieno la grandezza del regalo che mi ha fatto.

Quando tramonta lontano la luna, resta l'attesa del ciel; quando scompare lontano la riva, resta l'attesa del mar.

Acknowledgments

All we have to decide is what to do with the time that is given us.

It is not easy to sum up the series of events which eventually pushed me to the Ph.D: the herniated back which prevented me to accept jobs abroad right after my Master's Degree, the accidental discovery of this opportunity, the refusal of the candidate before me in the ranking, ... Nevertheless, this providential path was possible only thanks to prof. Pierluigi Di Lizia, my wise Gandalf who led me across these years, with fundamental advice and infinite patience, with a passionate heart able to thrill other people. But Pierluigi was not the only lead I had: from the very beginning of the journey to my Mount Doom, prof. Mauro Massari has always been present, like Aragorn, with his unerring ability to judge.

Come on, Mr. Frodo. I can't carry it for you... but I can carry you!

It has always been clear to me that I was not able to carry out my Ph.D alone, and I was so lucky that I met two Samvise Gamgee: Michele Maestrini and Giovanni Purpura. But not only that: as Frodo could count on the support of his cousins as well, in these years I could count on my Meriadoc Brandibuck and Peregrin Took, masked as Riccardo Cipollone and Luca Facchini. Without Sam, Merry and Pipin, Frodo would have neither started his journey: analogously, without Miki, Giovanni, Luca and Rick, my thesis would have hardly seen the light.

The Company of the Ring shall be Nine; and the Nine Walkers shall be set against the Nine Riders that are evil.

I am not at all sure that our "Company" is exactly made of nine people, as I am neither sure of our "Company" name (either SpireLab, or Spire or S4U), but I am sure and proud of the walkers who opposed to the evil riders. In addition to the ones already mentioned, I had the honour, besides the pleasure, to fight under the same banners as Andrea De Vittori, Niccolò Faraco, Chuncheng Zhao and Sergio Bonaccorsi and, more recently, Gaetano Calabrò and Alessia De Riz. I want also to mention our Boromir, Lorenzo Ticozzi, who accompanied us for a while before moving to the USA.

Hobbits really are amazing creatures, as I have said before.

Besides the amazing mates I constantly worked with in these years, some faces from PoliMi have been of utmost importance: Federico Ghioldi, Gianmario Merisio, Mattia Pugliatti and Ruggiero Signoriello I spent so many awesome lunches with, Emanuele Gallorini for the constant companionship in the office, Francesca Scala and Andrea Muciaccia for the works carried out together, Andrea Pasquale for the time spent together in Germany and Margherita Piccinin for the representative activities. I would also thank prof. Tabldini from the Electronic, Information and Bio-Engineering Department (DEIB) for the advise in the signal processing, prof. Colombo for the useful suggestions in holding presentations and prof. Dozio for all the moments of confrontation in these years.

It's like in the great stories, Mr. Frodo. The ones that really mattered.

I am moved thinking about that essay, written when I was thirteen, in which I said that I would have liked to work in the European Space Agency (ESA): after about fifteen years I had the chance (always thanks to Pierluigi) to carry out a visiting research period in the Space Debris Office of the ESA. So I would dedicate a special thanks to Emiliano Cordelli (GMV), Hélène Ma (RHEA Group) and Jan Siminski (ESA), for the proficient advise and the time spent to grow my research skills, and to Alejandro Pastor-Rodriguez, the wise colleague everybody would like to encounter abroad.

There are other forces at work in this world, Frodo, besides that of evil.

I am aware that the forces which made this journey possible and safe do not relate to PoliMi only. Without the National Institute of Astrophyics (INAF) and without the Italian Airforce (Aeronautica Militare, AM) our research group would have become pretty different (and much smaller) from what it actually is. Two people I moreover want to thank: Germano Bianchi from INAF and Capitano Moreno Peroni from AM. I strongly believe that Italy needs more people like them, capable of betting on national abilities, allowing them to grow and to prove their worth. I would like to thank also Giuseppe Pupillo e Giovanni Naldi from INAF and, moreover, Maggiore Giuseppe Pariti from AM, for all the opportunities he gave me in these years.

Home is behind, the world ahead, and there are many paths to tread.

To take the most important decisions in the life, it is needed to be sure that we are promised a good whichever route we will take. In the path to this certainty, there is still a long way to go throughout, the time I spent in Germany was a defining moment. And indeed the faces I met were decisive: Miriam, Enrico, Elisabetta, Irene, Caterina, Teresa, Bernardo, Sara, Fabian, Lucia, Virginia, Aldo and Sara.

I feel that as long as the Shire lies behind, safe and comfortable, I shall find wandering more bearable: I shall know that somewhere there is a firm foothold, even if my feet cannot stand there again.

I left at the end those who in my heart I thank everyday first: my mother, my father, my brother Matteo and my sister Anna, my niece Maddalena, my brother-in-law Giovanni, my grandmother Rita, my aunt Valeria, my uncle Andrea, my cousins Francesco and Sofia, and, even if we have not had the chance to meet each other a lot in these years, Silvia, Flavia, Paolo, my uncle Luca, Emi and my cousin Chiara. To conclude, I dedicate a thought to all my loved ones who have passed: my grandmother Iride, my grandfather Andrea, my uncle Agostino, my grandfather Carlo and my aunt Annita. Among my relatives, I also consider Giovanni and Noemi, because I do not believe that we do not have a single drop of blood in common, as like as Elio and my aunt Giulia, who died in these years.
Then, there are lot of faces of friends who supported and accompanied me, and it would be impossible to mention all of them. My dear Paccari al Sugo: Francesco, Daniela, Camilla, Emanuele, Gabriele, Andrea, Marco, Alessandro, Luca, Ludovico, Matteo and Simone. All my high school mates and holidays groups: Alessandra, Alice, Giulia, Francesco, Marco, Filippo, Jacopo, Aldri, Ilaria, Nicolò and Camilla. Single faces who never leave me: Filippo, Gabriele, Emanuele, Samuele, Arianna, Marco, Maria Concetta, Marilù, Francesca, Pasquale, Sara and Giacomo, who gave me the honour to be his best man. And then don Alessandro Suma, an unexpected and special encounter, and don Alessandro Morini, who played a so important role in my choices. And then again all the faces of Scuola di Comunità: Giulio, Simona, Mattia, Matteo, Giovanni, Marco, Lorenzo, Samuele, Caterina and, moreover, Davide and Claudio: "Leave or stay? No, follow. That is belong".
Finally, there are lots of people I forgot. Some of them constituted an important encounter, although sometimes extremely quick. Some others have been present in my mind and in my heart, although physically absent, either because our destiny wanted so (for instance, I

think about Marco, Stefano, Fabio and Giacomo, my Bachelor's Degree legendary mates), or because we decided so. Who I am today I owe to them as well.

A few observation and much reasoning lead to error; many observations and a little reasoning to truth.

To conclude, I would also devote a thought to all the Covid-19 victims, in particular to my professor and friend don Luigi Giussani. I will never be able to fully understand the size of the present he gave me.

When the moon sets away, there is the waiting of the sky; when the shore disappears away, there is the waiting of the sea.

Contents

List of Figures

List of Tables

FRED algorithm nomenclature

$\boldsymbol{x}^p$	Parent last available ephemeris.
t_{eph}	Epoch of the parent object last available ephemeris.
t_0	Fragmentation epoch.
t_a	Fragmentation event alert epoch.
t_{obs}	Fragment observation epoch.
$\boldsymbol{x}^{fg}$	Orbital state mean of the observed fragment.
$\boldsymbol{P}^{fg}$	Orbital state covariance of the observed fragment.
N_s	Number of samples used to represent the fragment Initial Orbit Determination result.
$\boldsymbol{x}^s$	Single sample orbital state.
T^p	Parent orbital period.
t_i	i-th epoch of the analysis time window sampling.
n^{orb}	Number of intervals the analysis time window is divided in, based on parent orbital period.
t_j^p	Epoch at which the parent transits through the MOID. The MOID is computed between the parent and the fragment j-th sample orbits.
t_j^s	Epoch at which the fragment j-th sample transits through the MOID. The MOID is computed between the parent and the fragment j-th sample orbits.

$\boldsymbol{x}^p(t_j^p)$ Orbital state of the parent at the epoch of transit through the MOID. The MOID is computed between the parent and the fragment j-th sample orbits.

$\boldsymbol{x}^s(t_j^s)$ Orbital state of the fragment sample at the epoch of transit through the MOID. The MOID is computed between the parent and the fragment j-th sample orbits.

$\boldsymbol{m}_j$ 3-dimensional MOID computed between the parent and the fragment j-th sample orbits.

$\boldsymbol{x}^s(t_j^p)$ Orbital state of the fragment sample at the epoch of parent transit through the MOID. The MOID is computed between the parent and the fragment j-th sample orbits.

$\boldsymbol{\rho}_j$ 3-dimensional relative distance between parent and the fragment j-th sample at the epoch of parent transit through the MOID. The MOID is computed between the parent and the fragment j-th sample orbits.

n_{filter} Number of samples passing the filtering phase.

n_{cl} Number of clusters identified after the filtering phase.

t_n^{fg} Candidate fragmentation epoch for the n-th cluster.

F Distribution of the epochs at which the parent transits through the MOID. Each MOID is computed between the parent and each fragment sample orbits.

$\boldsymbol{M}$ Distribution of the 3-dimensional MOID. Each MOID is computed between the parent and each fragment sample orbits.

$\boldsymbol{P}$ Distribution of the 3-dimensional relative distance between the parent and all the fragment samples at the epochs of the parent transit through the MOID. Each MOID is computed between the parent and each fragment sample orbits.

μ_t Fragmentation epoch mean returned by FRED algorithm.

σ_t Fragmentation epoch standard deviation returned by FRED algorithm.

Chapter 1

Introduction

In the last decades, the number of man-made objects orbiting the Earth has dramatically increased. In around 65 years of space activities, more than 6180 successful launches have taken place, which turned out in about 12720 objects placed in Earth orbit [1]. Among these, 7810 are still orbiting, but only 5400 are active. Furthermore, about 630 break-ups, explosions, collisions, or anomalous events resulting in fragmentation have been recorded, which have further contributed to the increase in the orbiting population of man-made objects, such that 29860 debris objects are regularly tracked by space surveillance networks and maintained in their catalogue. In addition to them, statistical models estimate that there are 36500 objects greater than 10 cm, one million objects between 1 cm and 10 cm, and 130 million objects between 1 mm and 1 cm. The numerical evolution of the geocentric orbiting objects from the start of space activities is represented in Fig. 1-1.

Due to this overpopulation, in 1978 Donald Kessler postulated that the generation of space debris via collisions and explosions could lead to an exponential increase in the amount of artificial objects in space, in a chain reaction which would render spaceflight too hazardous to conduct [3].

Given the global concern about the issue, multi-lateral meetings started under the initiative of the National Aeronautics and Space Administration (NASA), eventually resulting in 1993 in the creation of the Inter-Agency Space Debris Coordination Committee (IADC), founded by ESA (Europe), NASA (USA), NASDA (now JAXA, Japan), and RSA (now Roscosmos, Russian Federation). Nine more agencies have then joined the IADC: ASI (Italy), CNES (France), CNSA (China), CSA (Canada), DLR (Germany), KARI (South Korea), ISRO

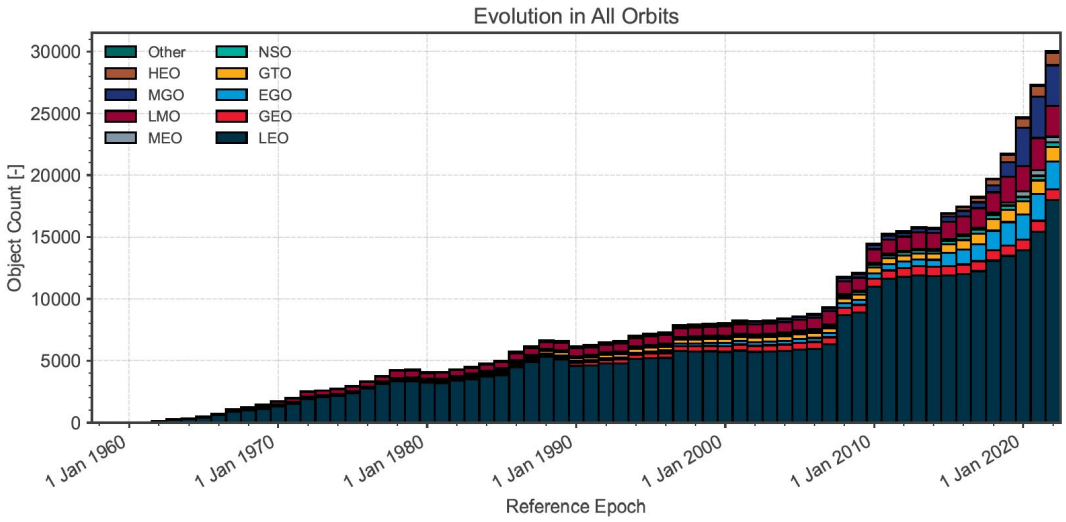

Figure 1-1: Evolution of number of objects in geocentric orbit, subdivided by orbit class. Credits [2].

(India), NSAU (Ukraine), and UKSA (United Kingdom) [2]. The IADC was founded as a forum for technical exchange and coordination on space debris matters, and can today be regarded as the leading international technical body in the field of space debris. Space debris has also been a recurring agenda item for the Scientific & Technical Subcommittee of the United Nations' Committee on the Peaceful Uses of Outer Space (UNCOPUOS) since 1994.

In 2002 the IADC published the IADC Space Debris Mitigation Guidelines [4] (then presented to UNCOPUOS Scientific & Technical Subcommittee), which also gave the definition of space debris as *all artificial objects including fragments and elements thereof, in Earth orbit or re-entering the atmosphere, that are non functional.* From 2002, IADC Space Debris Mitigation Guidelines has represented a baseline for non-binding policy documents, national legislation, and as starting point for the derivation of technical standards. Based on this document, nations around the world have developed safety standards and specific guidelines. In order to keep the standardisation of mitigation measures among all the players, normative international standardisation bodies, such as the International Standards Organisation (ISO) [5], are in charge of maintaining transparent and comparable processes also for space applications. Furthermore, to address the issues posed by space debris on spaceflight activities, UNCOPUOS created the guidelines for the long-term sustainability of outer space activities [6]. These guidelines regard several aspects, from the policy for space activities to

the scientific and technical research and development.

1.1 The Near-Earth environment

Orbiting objects can be classified as identified (which can be traced back to a launch event) and unidentified (that cannot). Following the division in [2], the former can be further categorised in:

- *Payloads*: space object designed to perform a specific function in space excluding launch functionality. This includes operational satellites as well as calibration objects.
- *Payload mission related objects*: space objects released as space debris which served a purpose for the functioning of a payload. Common examples include covers for optical instruments or astronaut tools.
- *Payload fragmentation debris*: space objects fragmented or unintentionally released from a payload as space debris for which their genesis can be traced back to a unique event. This class includes objects created when a payload explodes or when it collides with another object.
- *Payload debris*: space objects fragmented or unintentionally released from a payload as space debris for which the genesis is unclear but orbital or physical properties enable a correlation with a source.
- *Rocket body*: space object designed to perform launch related functionality. This includes the various orbital stages of launch vehicles, but not payloads which release smaller payloads themselves.
- *Rocket mission related objects*: space objects intentionally released as space debris which served a purpose for the function of a rocket body. Common examples include shrouds and engines.
- *Rocket fragmentation debris*: space objects fragmented or unintentionally released from a rocket body as space debris for which their genesis can be traced back to a unique event. This class includes objects created when a launch vehicle explodes.

- *Rocket debris*: space objects fragmented or unintentionally released from a rocket body as space debris for which the genesis is unclear but orbital or physical properties enable a correlation with a source.

It is possible that several payloads are deployed in-orbit with the aim at operating in a coordinate manner, like as the Global Positioning System (GPS), forming a constellation, that is *a set of at least 20 individual Payloads objects, released into orbits over more than 2 events and spreading more than 1 year in time, sharing the same objective as a combined system, and with the orbits in which they are deployed directly related to the systems objective* [2].

An object (either identified or unidentified) can be considered catalogued, uncatalogued or asserted (without mutual exclusion). In the first case, its orbital elements are maintained for prolonged periods of time in a catalogue created by a space surveillance system. Then, if an object is not included in a catalogue, it is referred to as uncatalogued. Finally an object is asserted when it has not been reported by a space surveillance system but is known to exist in the space environment by design. Asserted objects are, for instance, rocket bodies that perform a re-entry burn after inserting a payload into orbit prior to repeated detections by a space surveillance system. Catalogued and asserted objects can be categorised in terms of their orbital elements for a given epoch, as reported in Tab. 1.1, which lists the orbital classes based on semi-major axis a, eccentricity e, inclination i, perigee height h_p and apogee height h_a [2]. In particular, the IADC identified two protected regions: the Low Earth Orbit (LEO) and the Geostationary Orbit (GEO), which are specifically defined in Tab 1.2.

1.2 Space Surveillance & Tracking

The monitoring of the Near-Earth environment described above is one of the crucial points Space Situational Awareness (SSA) is in charge of. SSA is *the requisite foundational, current, and predictive knowledge and characterisation of space objects and the operational environment upon which space operations depend, including physical, virtual, information, and human dimensions—as well as all factors, activities, and events of all entities conducting, or preparing to conduct, space operations* [7].

Starting from the above-mentioned high-level definition, different fields of application can be identified in SSA framework [8]:

Orbit	**Description**	**Definition**		
GEO	Geostationary Orbit	$i \epsilon [0, 25]$	$h_p \epsilon [35586, 35986]$	$h_a \epsilon [35586, 35986]$
IGO	Inclined Geosynchronous Orbit	$a \epsilon [37948, 46380]$	$e \epsilon [0.00, 0.25]$	$i \epsilon [25, 180]$
EGO	Extended Geostationary Orbit	$a \epsilon [37948, 46380]$	$e \epsilon [0.00, 0.25]$	$i \epsilon [0, 25]$
NSO	Navigation Satellites Orbit	$i \epsilon [50, 70]$	$h_p \epsilon [18100, 24300]$	$h_a \epsilon [18100, 24300]$
GTO	GEO Transfer Orbit	$i \epsilon [0, 90]$	$h_p \epsilon [0, 2000]$	$h_a \epsilon [31570, 40002]$
MEO	Medium Earth Orbit	$h_p \epsilon [2000, 31570]$	$h_a \epsilon [2000, 31570]$	
GHO	GEO-superGEO Crossing Orbits	$h_p \epsilon [31570, 40002]$	$h_a > 40002$	
LEO	Low Earth Orbit	$h_p \epsilon [0, 2000]$	$h_a \epsilon [0, 2000]$	
HAO	High Altitude Earth Orbit	$h_p > 40002$	$h_a > 40002$	
MGO	MEO-GEO Crossing Orbits	$h_p \epsilon [2000, 31570]$	$h_a \epsilon [31570, 40002]$	
HEO	Highly Eccentric Earth Orbit	$h_p \epsilon [0, 31570]$	$h_a > 40002$	
LMO	LEO-MEO Crossing Orbits	h_p $[0, 2000]$	h_p $[2000, 31570]$	
UFO	Undefined Orbit			
ESO	Escape Orbits			

Table 1.1: Ranges defining each orbital class, with semi-major axis a, eccentricity e, inclination i, perigee height h_p and apogee height h_a. The units are km and degrees. Taken from [2].

Orbit	Description	Definition
LEO_{IADC}	IADC LEO Protected Region	$h\ \epsilon\,[0, 2000]$
GEO_{IADC}	IADC GEO Protected Region	$h_p\ \epsilon\,[35586, 35986] \quad \delta\ \epsilon\,[-15, 15]$

Table 1.2: Ranges defining each protected region, with altitude h and declination δ. The units are km and degrees. Credits [2].

- Space weather (SWE): monitoring and predicting the state of the Sun and the interplanetary and planetary environments, including Earth's magnetosphere, ionosphere and thermosphere, which can affect spaceborne and ground-based infrastructure thereby endangering human health and safety.

- Near-Earth objects (NEO): detecting natural objects such as asteroids that can potentially impact Earth and cause damage.

- Space Surveillance and Tracking (SST): watching for active and inactive satellites, discarded launch stages and fragmentation debris orbiting Earth.

Specific SST programs were started to build the expertise required to manage the challenges posed by the space traffic control problem. In particular, the presence of space debris may jeopardise the operative mission of active satellites, as the consequences of a possible collision with a space debris ranges from cumulative erosion of satellite surface to possible catastrophic aftermaths for the satellite. Most internationally accepted space debris mitigation measures can be traced back to the following objectives [2]:

- The limitation of space debris released during normal operations: payloads and rocket bodies should be designed to minimise the release space debris during normal operations.

- The minimisation of the potential for on-orbit break-ups: minimise the potential for break-ups during operational phases, through failure trees analysis and (sub)system reliability improvement, for instance, and the one for post-mission break-ups resulting from stored energy. In addition, intentional destruction and other harmful activities should be either avoided, or -if needed- conducted at sufficiently low altitudes, in order to reduce the expected fragments lifetime.

- Post mission disposal: LEO_{IADC} and GEO_{IADC}, the IADC protected regions, should

be cleared from permanent or (quasi-) periodic presence of non-functional man-made objects. In other orbital regions, payloads or rocket bodies, after their operational phases, should either be manoeuvred to reduce their orbital lifetime, or to be relocated.

- Prevention of on-orbit collisions: limit the probability of accidental collision with known objects during the payload or rocket body orbital lifetime, by possibly conducting avoidance manoeuvres.

These high-level objectives are generally declined in several actions, whose core is represented by the managing of data catalogued, which is regularly updated according to measurements data, derived from observations performed by optical, radar and laser sensors and gathered in Tracking Data Messages (TDM) [9]. Based on the catalogue, collision risk assessment is performed daily by satellite operators who are provided with Conjunction Data Messages (CDM) [10] to support decisions on the execution of collision avoidance manoeuvres. In addition, in-orbit fragmentations are detected and characterised, and uncontrolled re-entry predictions of objects are regularly produced to estimate on ground risks. Active debris removal initiatives are under development.
In the last decades both national and international partnerships were established to deal with SST-related applications. Hereafter, Sec. 1.3 describes the United States Space Surveillance Network (US-SSN). Then, Sec. 1.4 illustrates both the European Space Surveillance and Tracking (EUSST) consortium and the SST segment of the ESA SSA program.

1.3 United States Space Surveillance Network

US-SSN is a combination of optical and radar sensors used to detect, track, identify, and catalogue all man-made objects orbiting the Earth [11]. All sensors in the US-SSN are responsible for providing space surveillance and space object identification to the Combined Space Operations Center (CSpOC), former Joint Space Operations Center's (JSpOC), located at Vandenberg AFB, California, and to the Alternate Space Control Center (ASCC) at Dahlgren, Virginia. In particular, CSpOC is responsible for setting prioritisation for monitoring more than 23,000 space objects and re-tasking sensors in real time during contingencies [12]. By this way, data are processed to update the space objects catalogue and, in addition to it, some orbital information are published on Spacetrack website [13] in the

Two-Line Element set (TLE) format [14].
The sensors in the network are categorised primarily by their availability to support the CSpOC. This availability is based on the primary mission of each sensor. The SSN sensor missions are divided into three categories [11]:

- Dedicated sensors: US Strategic Command (USSTRATCOM) operationally controlled sensors with a primary mission of space surveillance support.
- Collateral sensors: USSTRATCOM operationally controlled sensors with a primary mission other than space surveillance (usually, the site's secondary mission is to provide surveillance support).
- Contributing sensors: those owned and operated by other agencies that provide space surveillance support upon request from the CSpOC.

From 2005, the U.S. Air Force started developing the Space Fence System as part of the US-SSN, that is a system of geographically dispersed S-Band phased array radars which provide 24/7 un-cued capability to find, fix, and track small objects in LEO, through unprecedented detection sensitivity, coverage and tracking accuracy [15]. In June 2014, the Lockheed Martin industry team was awarded the contract for the Engineering, Manufacturing, Development, Production and Deployment (EMDPD) of the Space Fence System. The U. S. Space Force declared the system operational on March 28, 2020, after a cost of 1.5 G$ [16].
The Space Fence design was shaped by the need of flexible sensor coverage and affordability through use of digital array technology that employs element-level Digital Beam Forming (DBF) and is capable of many independent beams to support simultaneous functions [17]. In particular, the un-cued LEO surveillance fence is a fan-shaped search volume aligned in an east-west direction that detects objects as they pass through. When a detection occurs, SF tracks the object long enough to determine its observed locations. The observations are then combined to estimate its orbital elements set. This is compared to the space catalogue to determine if the object elements set correlates with one already catalogued or if it is an uncorrelated target. Use of element-level DBF allows Space Fence to maintain persistent surveillance while tracking hundreds of simultaneous objects detected in the fence.
The system automatically manages resources by performing long-arc tracks on uncorrelated targets to support accurate Initial Orbit Determination (IOD). The SF system is designed

to run the un-cued surveillance mission with the majority of the radar transmit power. A portion of the radar remaining resources are available for precision tracking of high-interest objects. For such objects, a "mini-fence" can be electronically constructed to gather more tracking data, focusing radar resources specifically on that object, providing more timely and accurate information. Scheduling of the mini-fences is automated and based on orbital algorithms and system parameters [17] [18]. The Space Fence is expected to observe about 200,000 objects and make 1.5 million observations per day, about 10 times what made by existing assets [19].

1.4 SST in Europe

At European level, two major SST programs have been started: the EUSST consortium and the SST segment of the ESA SSA program. They are described hereafter.

1.4.1 European SST consortium

Given the space domain strategic importance for Europe, as space applications are essential for its economies, societies and citizens, the European Parliament and Council established the EUSST support framework [20], following the decision No. 541/2014/EU. This framework is implemented by the EUSST Consortium, subscribed in 2015, in cooperation with the European Union Satellite Centre (SatCen). Since 2016, EUSST Consortium and SatCen have worked together to develop a European SST capability, and formed the SST Cooperation, with the support of the European Union under different funding lines (H2020, Galileo & Copernicus programs). Today, the SST Consortium EU Member States are represented through their national designated entities: CNES for France, German Space Agency at DLR for Germany, ASI and INAF for Italy, POLSA for Poland, PT MoD for Portugal, ROSA for Romania and CDTI for Spain. These agencies cooperate with international organisations, space agencies, and other SSA initiatives, including US-SSN and ESA (which is not directly involved in EUSST) [21].

The EUSST capability consists of three main functions: sensor network, data processing and service provision [22]. Data are acquired by member states sensors and later analysed in the processing function and inserted in a database, which is then exploited for the services

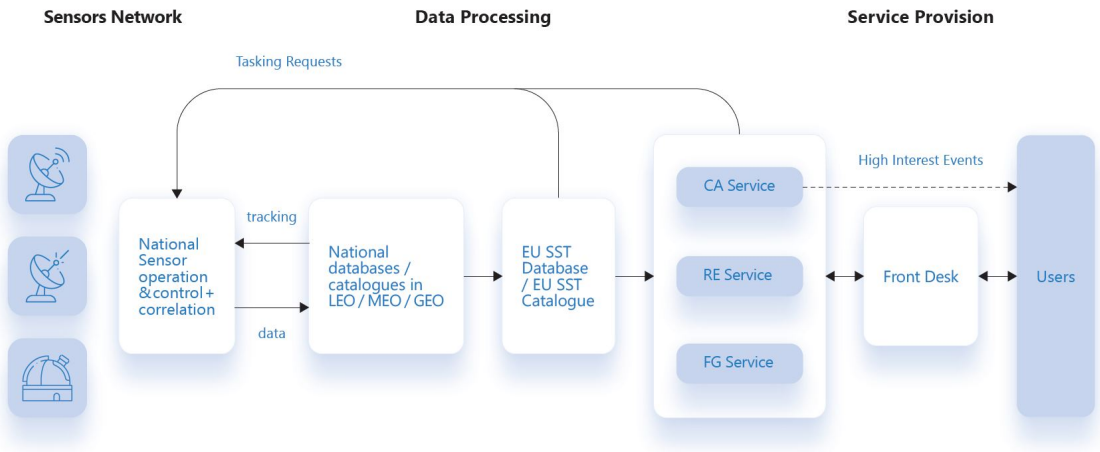

Figure 1-2: EUSST processing chain, subdivided in the three functions: sensor, processing and service provision. Credits [22].

provided by the Operations Centres (OCs) and delivered to users. The EUSST functions scheme is represented in Fig. 1-2.

The sensor network function consists of optical, radar and laser ranging stations of the member states of the EUSST Consortium, which monitor space objects in LEO, MEO, HEO and GEO. EUSST seeks to increase its autonomy and, so, its sensors network is under continuous upgrade and expansion, which improves the EUSST coverage and orbital information accuracy and timeliness. The current network configuration is represented in Fig. 1-3.

The data processing function coordinates the data-sharing among the OCs and processes thousands of daily measurements from the sensors contributing to EUSST. The German SSA Centre (GSSAC) is responsible for this function, in particular for the development, maintenance and operation of the current database, which is the basis for a future EUSST catalogue. In order to upgrade the data processing function, the research aims at developing methods to improve correlation and orbit determination quality, manoeuvre and conjunction detection, short-term and long-term collision risk assessment, radar and optical data fusion and uncertainty propagation.

The service provision function analyses both EUSST and external information, in order to provide [23]:

- Collision Avoidance (CA) service: provides risk assessment of collision between spacecraft and between spacecraft and space debris, and generates collision avoidance alerts.

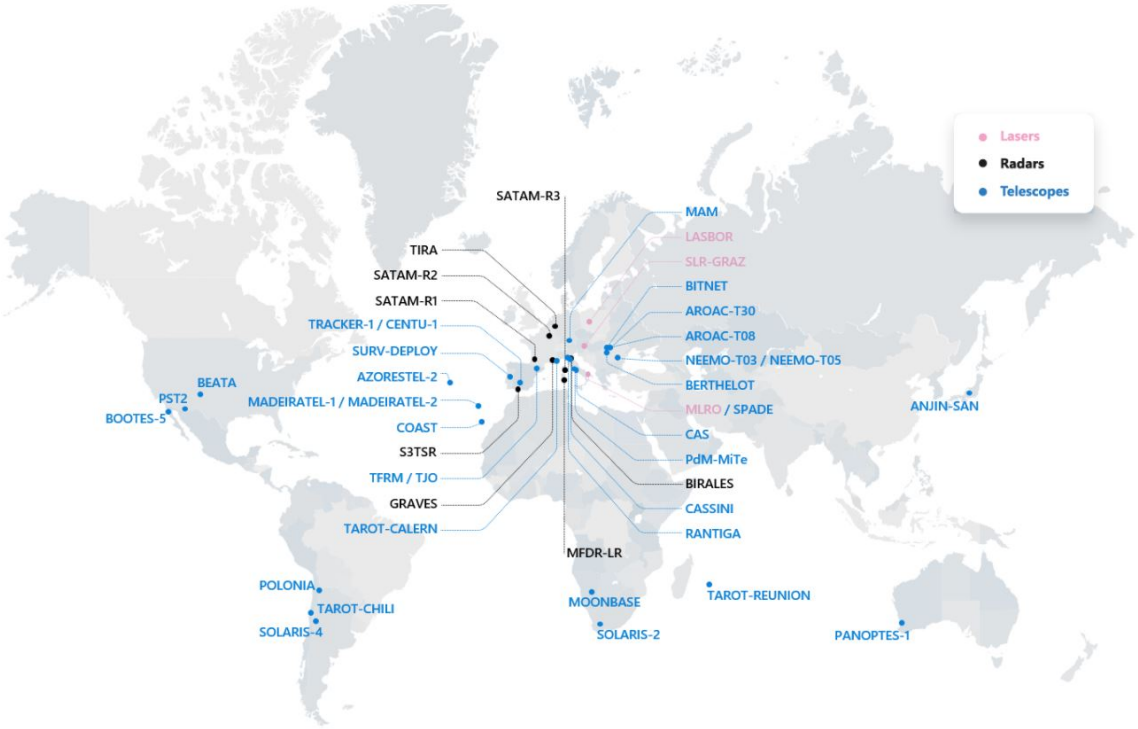

Figure 1-3: EUSST sensor network, subdivided in optical, radar and laser stations. Credits [21].

Information are processed to distinguish between the close approaches with a low level of risk (INFOs), those that require further analysis due to the level of risk (Interest Events, IEs) and those with a high level of risk (High Interest Events, HIEs), possibly requiring Collision Avoidance Manoeuvres (CAMs). Currently, the French and Spanish OCs are responsible for the CA service.

- Re-entry Analysis (RE) service: provides risk assessment of the uncontrolled re-entry of man-made space objects into the Earth's atmosphere that may constitute a potential risk to the safety of EU citizens and to terrestrial infrastructure. It carries out re-entry predictions, both long-term (within 30 days) and short-term (few days), by possibly providing overflight predictions over areas of interest. Currently, the Italian OC is responsible for the RE service.

- Fragmentation Analysis (FG) service: provides detection and characterisation of in-orbit fragmentations, break-ups or collisions, and analyses all the available information regarding the object(s) involved in the event. Short, middle and long-term analysis are conducted. Currently, the Italian OC is responsible for the FG service.

For critical operations and events of media interest, the service provision function produces in a timely and coordinated manner dedicated outputs to inform key stakeholders and for dissemination purposes. The SST Service Provision Portal is managed by the SatCen, which acts as Front Desk by also providing a Helpdesk to support users, and more than 135 organisations are receiving these services, with more than 240 European satellites safeguarded from the risk of collision [23]. The EUSST services are provided upon request to all EU Member States, the European Council, the European Commission, the European Union's External Action Service, public and private spacecraft owners and operators, and public authorities concerned with civil protection [22].

The three aforementioned functions, in particular the SST services, are continuously developed with the support of the European Union. The SST Cooperation created a Research and Development (R&D) plan, including both hardware-based and software-based activities. The effort related to the R&D plan involves both the Consortium partners and the industry, both the academia and the start-ups, with about 80% of the investments allocated through subcontracts [21]. The EUSST Consortium established the R&D plan to be achieved between 2021 and 2028, is subdivided in:

- Medium term (2021-2023): achieve high autonomy in observing and cataloguing objects flying in LEO, MEO and GEO, through a proper sensors improvement. Then, develop new technologies and operations concepts (e.g. in-orbit servicing and active debris removal) and enhance data-processing capabilities, which would provide top-quality services.

- Long term (2024-2028): keep pursuing the medium-term objectives, by also developing and demonstrating innovative SST sensors (e.g. for space-based space surveillance), and by evolving data-processing capabilities, both on-ground and on-board. Then, develop new EUSST services, by supporting launch, early orbit phase and end-of-life operations, and enable a higher coordination among space operators.

At the moment, the EUSST Catalogue is not planned to be made publicly available, similarly to Spacetrack database [13]. In any case, discussions are ongoing and a subset could be made publicly available at a later stage [21].

1.4.2 ESA SST

In 2009 ESA started the SSA program with a total financial participation between 2009 and 2020 of approximately 200 M€ (95 M€ from 2017), by 19 Member States. It is providing strong benefits to European industry. For example, between 2009 and 2016, over 100 contracts were issued to industry for SSA-related work with a total value in excess of 70 M€ [8]. The following Member States have participated in the period 2017-2020: Austria, Belgium, Czech Republic, Denmark, Finland, France, Germany, Greece, Italy, Luxembourg, Netherlands, Norway, Poland, Portugal, Romania, Spain, Sweden, Switzerland, and the United Kingdom. The SSA Programme is managed through a Programme Office that is based at the European Space Operations Centre (ESOC), in Darmstadt (Germany), while technology research and development, project planning and industrial contracting are being conducted by teams located across the Agency, and at European industrial partners [24].

The core of the SST segment of the SSA program is an updated catalogue, which contains information about the detected objects, such as their orbits and physical properties [25]. The Database and Information System Characterising Objects in Space (DISCOS) provides orbital information on catalogued and asserted objects. From the physical parameters there contained, both the characterisation and the propagation of the object trajectories can be derived, also for the orbital lifetime assessments [2]. Based on these information, the services of conjunction prediction, fragmentation detection and reentry prediction are accomplished. ESA SST team is based at the ESOC, and it works closely both with an extensive network of industry experts, sensor operators, scientists and engineers across Europe, and international partners. For instance, a data-sharing agreement between USSTRATCOM and ESA was signed in 2014, allowing ESA's operations to be alerted in case of an identified risk of collision [24]. Furthermore, it is very active in the technical standardisation field, in particular in cooperation with the Consultative Committee for Space Data Systems (CCSDS) [26], the European Committee for Standardization (CEN) [27] and the European Electrotechnical Committee for Standardization (CENELEC) [28].

Between 2013 and 2016, prototype SST systems were developed and deployed. Then, in the period 2017-2020, a core software has been established, consisting of back-end data processing from observations to orbits (both sensor planning and object database) and front-end services (the above-mentioned services, together with the catalogue query) [25]. In particu-

lar, the interoperability have been further improved and national assets (including radars, optical telescopes and laser-ranging systems) further qualified, by also seeking to develop both on-ground and space-based sensors.

1.4.3 European SST radars

EUSST consortium and the SST segment of ESA SSA program grant an autonomous European capability able to safeguard the European economies, societies and citizens that rely on space-based applications such as communication, navigation and observation. In order to provide the services illustrated in Sec. 1.4.1 and Sec. 1.4.2, the process chain exploits observations data derived from optical, radar and laser sensors. These sensors can measure angles (all of them), slant range (radar and laser sensors) and Doppler shift information (only radars). They can be subdivided in tracking and survey sensors: the former observe the object by tracking it, whereas the latter detect objects while they cross the sensor Field of View (FoV). Optical telescopes can be used to monitor objects orbiting at any altitude, as they do not need a transmitted power, but they are limited by weather and illumination conditions. On the contrary, radars are more versatile, as the target is illuminated by the transmitting station, but this makes a constrain on the altitude they can monitor. Thus, radars are predominantly used to monitor LEO orbits. Another remark is that the optical telescopes can provide just the angular track, and this usually forces to carry out an association task to link measurements acquired through different sensors, in order to pursue high-level orbit determination quality. On the contrary, the radars are capable to provide all the measurements, but their angular track generally results less accurate, and, so, it is of paramount importance to develop high-resolution techniques to improve the angular measurements quality.

Concerning the radars, the surveillance ones are mainly useful for the regular observation of the space object population, whereas the tracking ones are necessary to achieve high-fidelity orbits. In particular, the surveillance radars regularly scan a region of interest, called Field of Regard (FoR), using electric beamforming by phased-array radar, or create an additional beam to track a newly detected object [29]. The most remarkable European ground-based radars are described below.

The German Tracking and Imaging RAdar (TIRA), developed and operated at Fraunhofer FHR, combines two radars: a tracking radar operated in L-band with a central frequency of 1.3 GHz and an imaging radar operated in Ku-band with a central frequency of 16.7 GHz [30]. Both radars are coherent pulse radars. The L-band radar is equipped with a monopulse system for real-time tracking and controls the Ku-band radar. The core component of TIRA system is the 34 m reflector antenna, whose resulting high gain enables the imaging of LEO satellites with a high radiometric resolution. In addition, small space objects can be reliably detected and their parameters accurately estimated.

The French GRAVES system (Grand Réseau Adapté à la Veille Spatiale) is a bistatic radar working with a VHF continuous wave pure carrier transmission at 143.05 MHz [31]. The transmitting station (located near Dijon, France) is composed of four linearly polarised transmitting arrays, each covering 30 deg in elevation and 45 deg in Azimuth, granting a total coverage of 180 deg in Azimuth. Each FoV is individually scanned by electronic deflection forming a fence in the sky. The receiver station is represented by a 60 m diameter sparse array of circularly-polarised antenna elements, located 400 km south of the transmission site. Digital static beamforming is performed in more than one thousand different directions to detect the objects and an associated signal processing is performed real time at the receiver antenna site [32]. This process enables the localisation of the objects along azimuth and elevation, while the frequency shift caused by the Doppler effect enables the radial velocity, and hence the orbit altitude, to be determined. Thanks to its configuration, GRAVES is able to detect each satellite at least once every 24 hours.

The Spanish S3TSR is a ground-based radar, exploiting a close monostatic configuration, which operates in L band [33]. Both, transmitting and receiving antennas are separated electronically scanning arrays. The receiver static beamforming architecture is fully digital and each antenna input is digitised to maximise functional flexibility. Specifically, the resulting beamforming process can arrange bundles of up to 7 receiver beams for covering each transmitter beam (which are 6), with a total of 42 simultaneous receiver beams. The radar provides automatic surveillance and tracking of space objects in LEO by continuously scanning the instrumented Field of Regard (FoR) and generating track reports for all the detected objects.

In recent years the German Experimental Space Surveillance and Tracking Radar (GESTRA) has been developed [34] [35]. It is a close monostatic pulsed phased array radar,

operated in L-band (at about 1.3 GHz), able to accomplish space surveillance observations in LEO and beyond, up to altitudes of 3000 km. Both antenna frontends use planar phased arrays with a diameter of 3 m, integrated into 3-axis positioners in order to point the FoV in all space directions. In the reception, the optical digital outputs are combined using static beamforming units, which can be modified to arbitrarily shape multibeam pattern of the receiving antenna [36]. Surveillance flexibility is further improved by the combination of mechanical and electronical beam steering.

The under-development EISCAT 3D system is a multistatic High-Power Large-Aperture (HPLA) radar located in Northern Scandinavia using phased array antennas for both transmission and reception. It is designed to investigate how the Earth's atmosphere is coupled to space but it will also be suitable for a wide range of other scientific targets, like as space weather forecasts and detecting space debris [37]. The radar is multi-static, and is therefore capable of observing instantaneous three-dimensional vector velocity and position by observing round-trip delay and Doppler shift between the transmitter and three receiver sites [38].

The Italian BIstatic RAdar for LEo Survey (BIRALES) is a bistatic radar sensor, whose transmitter is the TRF (Trasmettitore a Radio Frequenza) located at the Italian Joint Test Range of Salto di Quirra in Sardinia (capable to supply a maximum power of 10 kW in the bandwidth 410-415 MHz), while the receiver is part of the Northern Cross radio telescope of the Radio Astronomical Station of Medicina (Bologna, Italy) [39] [40] [41] [42] [43]. The latter is a multi-receiver array, whose cylinders can be mechanically pointed only in elevation along the local meridian. In addition to Doppler shift and slant range measurements, the system is able to provide angular track, thanks to a static multibeam. Due to its characteristics, BIRALES is used as baseline in this work, and a more detailed description is provided in Sec. 1.5

The BIstatic RAdar for LEo Tracking (BIRALET) is an Italian bistatic radar sensor devoted to tracking operations [44]. It shares the same transmitter as BIRALES, while the receiver is represented by the Sardinia Radio Telescope, which is located close to Cagliari, with a baseline of about 20 km. It provides both Doppler shift and slant range measurements. It does not compare in Fig. 1-3, because it is currently under maintenance.

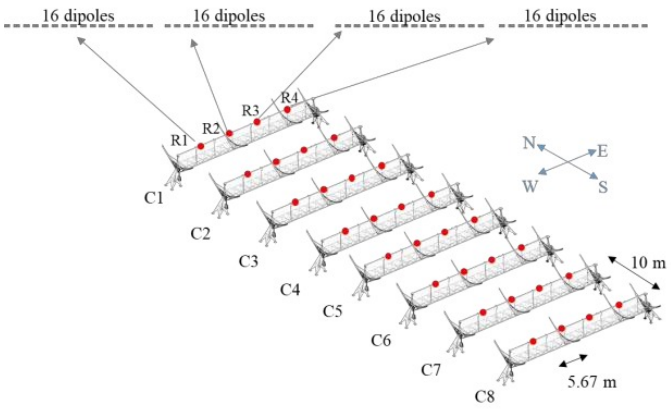

Figure 1-4: BIRALES receivers (red dots) installed along the antenna focal line. Each receiver contains 16 dipoles.

1.5 Bistatic Radar for LEO survey

As mentioned above, BIRALES is used as baseline in this work, and a detailed description of its receiver station system and data processing chain is provided hereafter.

BIRALES receiver is part of the Northern Cross radio telescope of the Radio Astronomical Station of Medicina (Bologna, Italy), which consists of two perpendicular branches: the East-West (E-W) arm is 564 m long and is made of a single 35 m wide cylindrical antenna, whereas the North-South (N-S) branch is made of 64 parallel antennas each 23.5 m long and 7.5 m wide. The portion currently dedicated to the BIRALES receiving antenna is called *1N-section*, which is an array composed of 8 cylindrical parabolic concentrators belonging to the N-S arm. Each cylinder contains four receivers installed on the focal line (aligned with the E-W direction). Therefore, the receiving system is composed of a matrix of 8x4 receivers spaced 5.67 m in E-W (d_{E-W}) and 10 m in N-S (d_{N-S}), as represented in Fig. 1-4. The 8 cylinders of the 1N-section can be mechanically pointed only in elevation (El_{RX}) along the local meridian. The mechanical elevation limits are 42 deg $< El_{RX} <$ 90 deg both in North and South pointing configuration. This mechanical pointing involves all the array elements. With a total collecting area of about 1400 square meters, the system allows to detect small objects with a size of 10 cm at 2000 km slant range. The FoV is 5.7 deg $\times$ 6.6 deg (at half power beam width).

BIRALES exploits two different systems, working at the same time: a multibeam Continuous Wave (CW) unmodulated radar system, operating at 410 MHz, and a single beam pulse compressed radar system, based on a pulsed chirp at 412.5 MHz with a bandwidth of

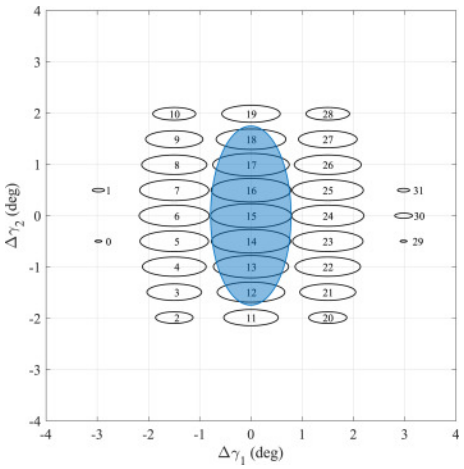

Figure 1-5: Multibeam configuration of BIRALES receiver. Contours define the -3 dB beamwidth of each beam main lobe with respect to the RX main lobe maximum gain. The blue ellipse represents the single analogue beam used for slant range measurements.

4 MHz, which is used to measure the slant range [39]. Since the receiver single beam for the compressed pulse covers partially the receiving antenna FoV, slant range measurements are available only for a portion of the pass over BIRALES FoV. Thanks to dedicated calibration campaigns, the slant range and Doppler shift measurements errors were assessed to be 30 m and 10 Hz respectively.

Based on its receiver array configuration, BIRALES currently exploits 32 digitally formed beams, whose direction is kept fixed in the FoV. The multibeam configuration in the receiver FoV is represented in Fig. 1-5, where the blue circle is the beam currently used for slant range measurement, which is obtained electronically by combining only 3 cylinders out of 8. The angles $\Delta\gamma_1$ and $\Delta\gamma_2$ represent the angular deviation from the Line of Sight (LOS). Theoretically, as soon as the observed object crosses a beam, the latter is expected to generate data. Thus, collecting all measurements along the entire pass should eventually provide the time history of the angular coordinates in the receiver FoV. However, the receiver array geometry introduces a spatial ambiguity. Indeed, even if, in the receiver reference frame, the mutual distances among array elements vary with the receiver elevation, they are always larger than half-wavelength (being the CW wavelength $\lambda = 0.73$ m) in both directions. Consequently, multiple grating lobes simultaneously appear in the sensor FoV for any beam, and their shape and mutual spacing depends on the receiver elevation. Thus, it is not straightforward to link the beam illumination to a specific direction in the receiver FoV. By collecting the contribution of the 32 beams, the overall gain pattern turns out to

be relatively complex and the angular track reconstruction difficult to be achieved.
In previous works, the Multibeam Orbit Determination Algorithm (MODA) was developed to address the angular track reconstruction problem in this multibeam configuration, through a chain of optimisation processes which exploit both the Doppler shift and the slant range measurements at the same time [41]. Despite the interesting performances on numerical simulation, when dealing with real observations, the method tends to be affected by the lobe ambiguity problem due to several factors, such as a high sensitivity to the SNR quality in the optimisation process. This may generate coarse angular coordinates estimation, with a maximum error of about 2.5 deg for passes with peculiar geometries. Furthermore, it is worth remarking that the angular track can only be estimated if both Doppler shift and slant range measurements are available and reliable.

1.6 Research activity and outline

As mentioned in Sec. 1.4.3, in surveillance radars the angular track measurement generally results less accurate. Thus, it is of paramount importance to develop high-resolution techniques to improve its quality. The aim of this thesis is to illustrate the potential of adaptive beamforming techniques to derive the angular track in array radars devoted to space surveillance, and assess the benefits for the SST activities. On the one hand, a high-quality angular track reconstruction would allow a more accurate IOD from a single measurements track (that is, from a single observation), with the related improvement in Re-entry Analysis and Collision Avoidance services. On the other hand, a proper development of the adaptive beamforming based technique would allow to derive the tracks of multiple targets simultaneously observed, and this would enhance both survey applications, proximity operations recognition and Fragmentation Analysis service.
To fulfil the above-stated objective, the thesis is structured as follows. Chapter 2 is dedicated to the fundamentals of the thesis: it gives a definition of the reference frames, and it presents the propagation models, the uncertainty propagation tools and the radar basics. Moreover, it introduces the orbit determination techniques for the correlation process, the Refined Orbit Determination (ROD) and the IOD.
Next, Ch. 3 describes the MATER algorithm, which embeds the adaptive beamforming

technique to derive the angular track in array radars, both for the catalogued and the uncatalogued case. In this latter situation, ambiguous solutions may appear because of the mutual distance among array radar antennas (like the ones in Sec. 1.5), and different solving criteria (exploiting either the statistics, or the signal processing, or the observation geometry) are proposed. MATER algorithm is tested through an extensive numerical analysis in Ch. 4 by considering BIRALES as baseline on single source process. Besides the array receiver characteristics, this choice is motivated by the fact that BIRALES back-end allows to record raw data and, so, to work in post-processing, partially attenuating the operational drawback of the large computational demand required by the adaptive approach. A sensitivity analysis is also conducted to assess the performance in non nominal situations. In addition, numerical simulations on Re-entry Analysis and Collision Avoidance services are carried out, and a real case scenario is reported as well.

Analogously, Ch. 5 is dedicated to the numerical analysis of the multiple sources scenario, and simulations of a close proximity operation and of a fragments cloud observation are provided and discussed. In this latter simulation, the capability of reconstructing the fragment track allows to run an IOD, which can be further exploited in fragmentation event monitoring to detect the epoch of the event. Therefore, Ch. 6 presents the FRED algorithm, which deals with the problem of identifying the fragmentation epoch in a stochastic way, starting from the last available ephemeris of the parent object (that is the satellite which broke up) and a single fragment observation through a surveillance radar. Finally, Ch. 7 discusses FRED performance on numerical simulations and it presents an application to an operational scenario in which radar measurements include the angular track reconstructed through MATER algorithm.

Chapter 2

Fundamentals

This chapter offers a general description of the basic mathematical concepts used throughout the thesis. First, reference frames are introduced in Sec. 2.1, which are widely exploited across the entire work. Next, the propagation models are discussed in Sec. 2.2, and they are fundamental in Ch. 4, Ch. 5 and Ch. 7, both to derive the analysis data set and in the numerical simulations.

Afterwards, the most common methodologies for the uncertainty propagation are presented in Sec. 2.3. In particular, the Montecarlo approach is applied to describe the uncertainty associated to the fragment orbital state in FRED algorithm, which is presented in Sec. 6.2 and whose performance are assessed by the numerical simulations in Ch. 7. Instead the Unscented Transformation is used in Sec. 4.4.2 during the simulation regarding the Collision Avoidance service introduced in Sec. 1.4, that is a conjunction scenario. The radar basics later introduced in Sec. 2.4 are fundamental for MATER algorithm definition in Ch. 3 and in the simulations in Ch. 4, Ch. 5 and in Ch. 7.

The orbit determination techniques are then discussed in Sec. 2.5. Both the correlation procedure, the refined orbit determination and the initial orbit determination are strongly linked to the MATER algorithm definition in Ch. 3 and to the related simulations in Ch. 4. Concerning particular applications of the refined orbit determination, the Non-linear Least Squares and the Unscented Kalman Filter are used in the simulations of the Re-entry Analysis and of the Collision Avoidance services (introduced in Sec. 1.4) respectively, in Sec. 4.4.1 and in Sec. 4.4.2. The presented initial orbit determination technique is also exploited in Ch. 7 simulations which assess the FRED algorithm performance.

2.1 Reference Frames

The reference frames represent a key point in the celestial mechanics, the most remarkable being the Earth-Centered Inertial (ECI), the Earth-Centered Earth-Fixed (ECEF) and the Radial-Tranverse-Normal (RTN) ones. Then, for on-ground observations, also the Topocentric and the Sensor reference frames are fundamental. A recap of all of them is here proposed, based on [45].

Earth-Centered Inertial reference frame

The Earth-Centered Inertial (ECI) reference frame, often addressed as EME2000 or J2000 (as explained in this paragraph), is centered in the Earth center of mass and is fixed with respect to the stars. In more detail:

- $\hat{x}_{ECI}$: points towards the vernal equinox, that is the ascending node of the Sun on the 21^{st} of March.
- $\hat{z}_{ECI}$: points towards the North pole.
- $\hat{y}_{ECI}$: belongs to the the mean equator and is normal to the other two axes according to the right hand rule.

Besides the cartesian coordinates, in ECI reference frame two angles uniquely identify the direction of a generic point: the right ascension (α, defined between 00 h 00 min 00 s and 23 h 59 min 59 s) and the declination (δ, between -90 deg and +90 deg). The former is the angle (measured counterclockwise) between $\hat{x}_{ECI}$ and the projection of $\vec{r}$ on the equatorial plane, while the latter between such a projection and $\vec{r}$.
Figure 2-1 represents ECI reference frame according to the definitions provided above. ECI reference frame is fixed (that is inertial) as long as the vernal equinox is defined for a specific epoch. A common choice is to refer to the vernal equinox on January 1, 2000, 12 hrs and the system defined for this date is known as the J2000 system. An alternative is represented by the M50 system, which is defined by the mean equator and equinox of 1950. The present thesis considers J2000 system only which, for this reason, is simply referred to as ECI reference frame.

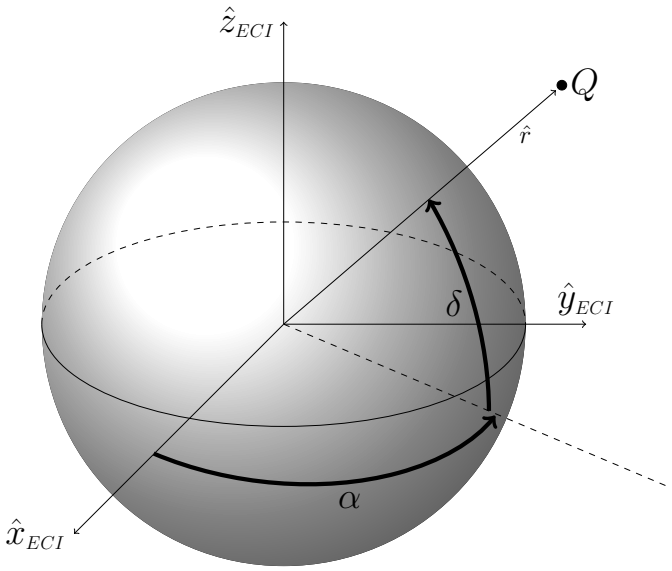

Figure 2-1: Earth-Centered Inertial reference frame. The $\hat{x}_{ECI}$ unitary vector is directed towards the vernal equinox on January 1, 2000, 12 hrs, $\hat{z}_{ECI}$ towards the North pole and $\hat{y}_{ECI}$ is normal to the other two axes according to the right hand rule. Both $\hat{x}_{ECI}$ and $\hat{y}_{ECI}$ belong to the mean equator. The direction $\hat{r}$ of a generic point Q can be defined according to α and δ, which are right ascension and declination respectively.

Earth-Centered Earth-Fixed reference frame

The Earth-Centered Earth-Fixed (ECEF, or ECF) reference frame is centered in the Earth centre of mass and rotates solidly to the planet. In more detail:

- x_{ECEF}: belongs to the equator and points towards the prime meridian.
- z_{ECEF}: points towards the North pole.
- y_{ECEF}: belongs to the equator and is normal to the other two axes according to the right hand rule.

Similarly to ECI reference frame, also for ECEF two angles uniquely identify the direction of a generic point: the longitude (λ, defined between -180 deg and +180 deg) and the latitude (ϕ, between -90 deg and +90 deg). The former is the angle (measured counterclockwise) between $\hat{x}_{ECEF}$ and the projection of $\vec{r}$ on the equatorial plane, while the latter between such a projection and $\vec{r}$. It is worth to remark that, for the Earth oblateness, a distinction exists between geodetic and astronomic latitude.

Fig. 2-2 represents ECEF reference frame according to the definitions provided above.

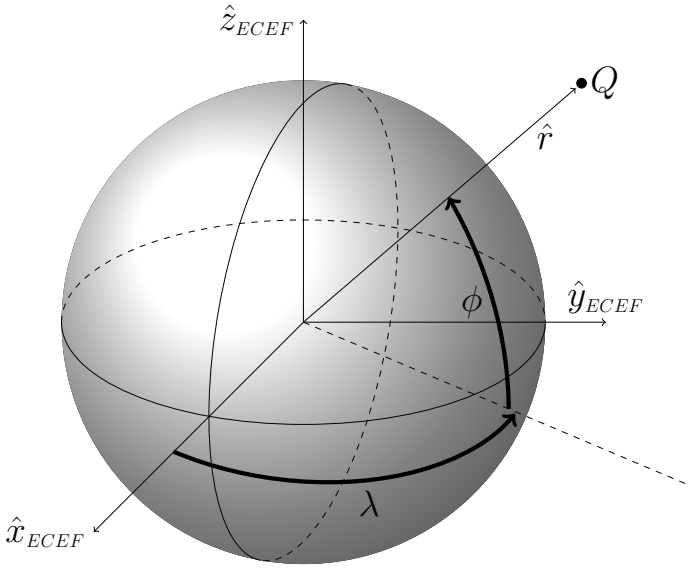

Figure 2-2: Earth-Centered Earth Fixed reference frame. The $\hat{x}_{ECEF}$ unitary vector is directed towards the prime meridian (drawn as well), $\hat{z}_{ECEF}$ towards the North pole and $\hat{y}_{ECEF}$ is normal to the other two axes according to the right hand rule. Both $\hat{x}_{ECEF}$ and $\hat{y}_{ECEF}$ belong to the mean equator. The direction $\hat{r}$ of a generic point Q can be defined according to λ and ϕ, which are longitude and latitude respectively.

Radial-Transversal-Normal reference frame

The Radial-Transversal-Normal (RTN) reference frame is centered in the center of mass of the orbiting object under consideration and moves solidly to its motion. In more detail:

- $\hat{x}_{RTN}$: points towards the orbiting radius, that is the unitary vector instantaneously joining the center of mass of the Earth to the one of the object.
- $\hat{z}_{RTN}$: points towards the orbit angular momentum and is normal to the other two axes according to the right hand rule.
- $\hat{y}_{RTN}$: belongs to the orbital plane and is normal to the other two axes according to the right hand rule. It is equivalent to orbital velocity direction only in circular orbits.

Fig. 2-3 represents RTN reference frame according to the definitions provided above.

Topocentric reference frame

For some applications, a coordinate system attached to a point on the surface of the Earth is useful in the description of satellite motion from a ground-based observer's viewpoint. Such topocentric coordinate system is centered in the observer's position and rotates solidly to

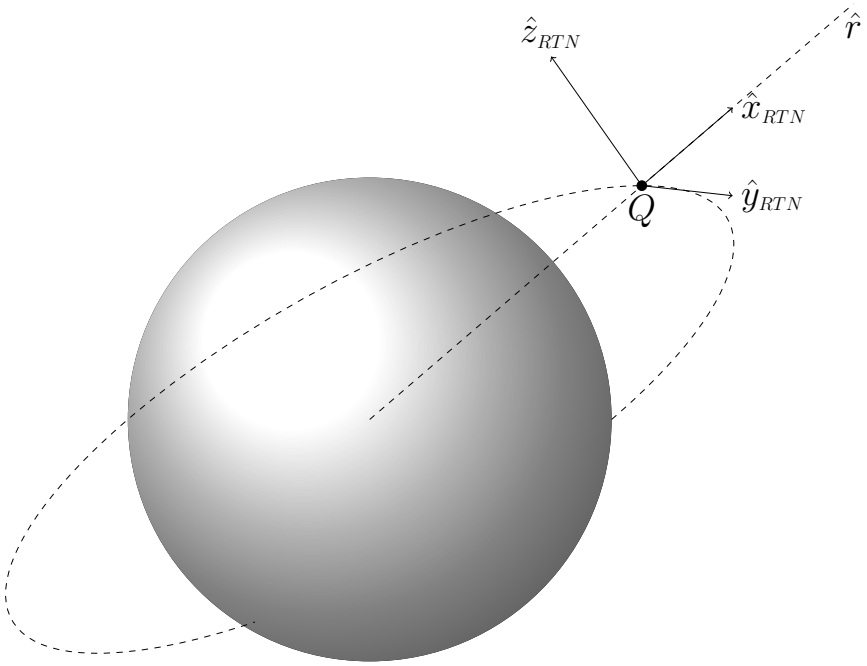

Figure 2-3: Radial-Transversal-Normal reference frame, which is centered in the center of mass of the orbiting object under consideration (point Q) and rotates solidly to its motion. The $\hat{x}_{RTN}$ unitary vector points towards the orbiting radius ($\hat{r}$ direction), $\hat{z}_{RTN}$ towards the orbit angular momentum and $\hat{y}_{RTN}$ is normal to the other two axes according to the right hand rule. Both $\hat{x}_{RTN}$ and $\hat{y}_{RTN}$ belong to the orbital plane.

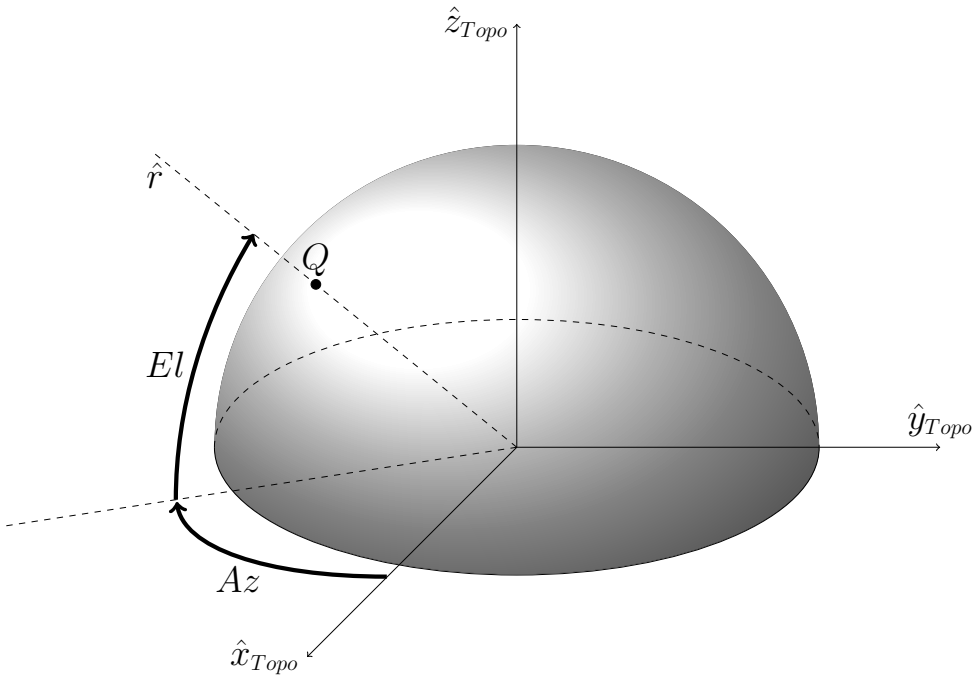

Figure 2-4: Topocentric reference frame, which is centered in the observer's position. The $\hat{x}_{Topo}$ unitary vector is directed towards the local North, $\hat{y}_{Topo}$ towards the local West and $\hat{z}_{Topo}$ towards the local zenith. The observer plane is identified by $\hat{x}_{Topo}$ and $\hat{y}_{Topo}$. The direction $\hat{r}$ of a generic point Q can be defined according to Az and El, which are azimuth and elevation respectively.

the Earth. There is no unique way to define it and this thesis uses the definition proposed by [46]:

- $\hat{x}_{Topo}$: points towards the local North direction.
- $\hat{y}_{Topo}$: points towards the local West direction.
- $\hat{z}_{Topo}$: points towards the local zenith direction.

The direction $\hat{x}_{Topo}$ and $\hat{y}_{Topo}$ identify the observation plane. Two angles uniquely identify the direction $\vec{r}$ of a generic point in topocentric reference frame: the azimuth (Az, defined between 0 deg and 360 deg) and the elevation (El, between 0 deg and +90 deg). The former is the angle (measured clockwise) between the local North direction ($\hat{x}_{Topo}$) and the projection of $\hat{r}$ on the observation plane, while the latter between such a projection and $\hat{r}$. Fig. 2-4 represents the topocentric reference frame according to the definitions provided above.

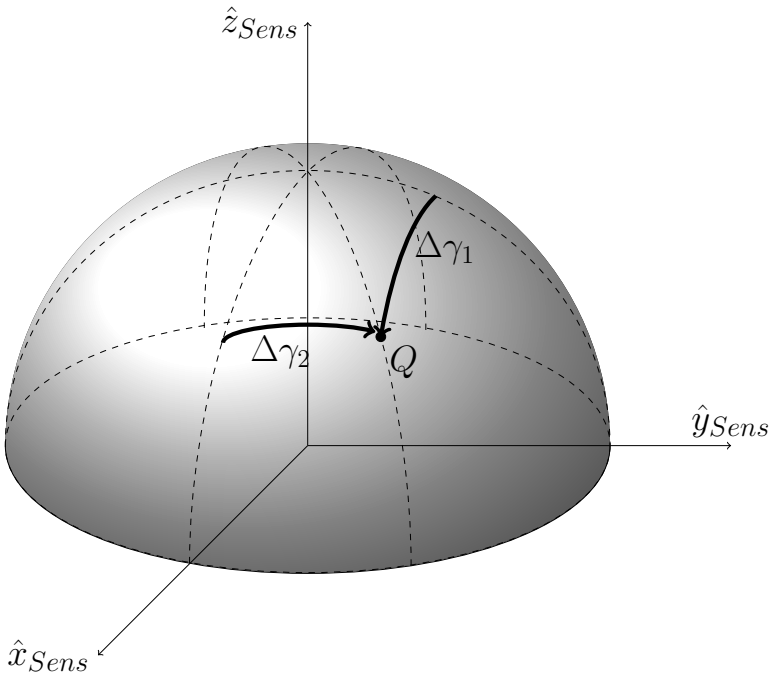

Figure 2-5: Sensor reference frame, which is centered in the sensor position. The $\hat{z}_{Sens}$ axis points towards the LoS, while $\hat{x}_{Sens}$ and $\hat{y}_{Sens}$ are orthogonal to it and arbitrary selected, according to the right hand rule. The position of a generic observed target Q can be expressed through the angular coordinates $\Delta\gamma_1$ and $\Delta\gamma_2$, which express its angular deviation from the LoS along $\hat{x}_{Sens}$ and $\hat{y}_{Sens}$, respectively.

Sensor reference frame

During an on-ground observation, measurements depend on the Line of Sight (LoS) direction of the sensor, which defines one of the sensor reference frame axes. Figure 2-5 reports a representation of such a reference frame inspired from [47], where:

- $\hat{z}_{Sens}$: points towards the LoS.
- $\hat{x}_{Sens}$ and $\hat{y}_{Sens}$: are orthogonal to $\hat{z}_{Sens}$ and arbitrary selected, according to the right hand rule.

The position of a generic observed target can be indicated through the angular coordinates $\Delta\gamma_1$ and $\Delta\gamma_2$, which express its angular deviation from the LoS ($\hat{z}_{Sens}$ direction) along $\hat{x}_{Sens}$ and $\hat{y}_{Sens}$, respectively.

In many applications it is useful to represent the angular deviation of the observed target with respect to the LoS on a two-dimensional angular graph $\hat{\Delta}\gamma_1$-$\hat{\Delta}\gamma_2$, that is the sensor Field of View (FoV), as represented in Fig. 2-6.

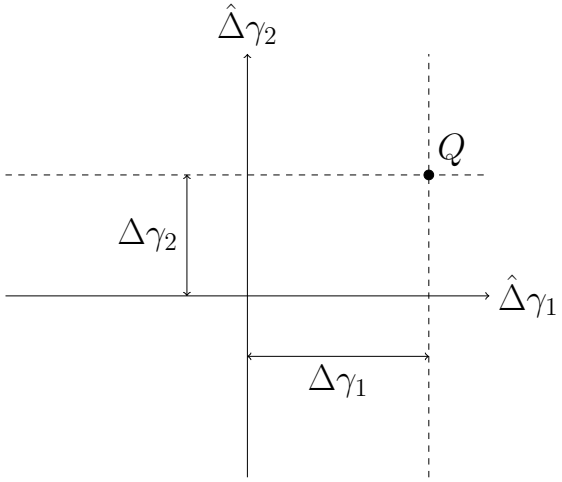

Figure 2-6: Field of View, that is the two-dimensional sensor reference frame centered in the sensor position. The $\hat{\Delta}\gamma_1$ and $\hat{\Delta}\gamma_2$ axes express the angular deviation from the sensor LoS along $\hat{x}_{Sens}$ and $\hat{y}_{Sens}$, respectively.

2.2 Astrodynamics and Propagation Models

Among the simplest approach to model the dynamics of an orbiting object is through the Keplerian equation, which describes the two-body problem motion in unperturbed environment:

$$\ddot{\boldsymbol{r}} = -\mu \frac{\boldsymbol{r}}{|\boldsymbol{r}|^3} \tag{2.1}$$

Where $\mu = 398600.4418$ km^3/s^2 is the Earth gravitational constant and:

$$\boldsymbol{r} = \begin{bmatrix} r_x \\ r_y \\ r_z \end{bmatrix} \tag{2.2}$$

is the satellite position in ECI reference frame. This motion can be derived analytically, as described in [48].

However, in addition to Keplerian gravitational acceleration, orbital perturbations affect satellites flying in the Near-Earth environment [49]:

$$\ddot{\boldsymbol{r}} = -\mu \frac{\boldsymbol{r}}{|\boldsymbol{r}|^3} + \boldsymbol{a_p} \tag{2.3}$$

Where $\boldsymbol{a_p}$ includes different kinds of perturbations:

$$\boldsymbol{a_p} = \boldsymbol{a_D} + \boldsymbol{a_{GH}} + \boldsymbol{a_{3^{rd}}} + \boldsymbol{a_{SRP}} + \boldsymbol{a_{ERP}} \tag{2.4}$$

which are listed below:

- Acceleration due to the aerodynamic drag:

$$\boldsymbol{a_D} = \frac{1}{2}\,\rho\,|\boldsymbol{v}|^2\,C_d\,\frac{A_{aer}}{M}\,\frac{\boldsymbol{v}}{|\boldsymbol{v}|} \tag{2.5}$$

  It is effective at those heights at which the atmospheric density ρ is not negligible (generally below 1000 km altitude). It is proportional to the square of the air relative velocity modulus $|\boldsymbol{v}|^2$, to the drag coefficient C_d and to the ratio between the aerodynamic area A_{aer} and the satellite mass M. The term $Cd\,A_{aer}/M$ is generally known as ballistic coefficient. The aerodynamic drag perturbation can possibly account for atmospheric winds effects, usually below 500 km altitude.

- Acceleration due to the gravitational harmonics: $\boldsymbol{a_{GH}}$. It accounts for the not perfectly spherical shape of the Earth. It is important to remark that the second order term of the harmonics, usually indicated as J2, represents the most effective perturbation in LEO environment. The gravitational harmonic perturbation can also account for solid and ocean tides effects (both permanent and time-varying).

- Acceleration due to the third-body perturbation, that is the gravitational attraction exerted on the satellite by a body (typically Sun and Moon, in Near-Earth environment) which is not the main attractor (the Earth) and can be modeled like:

$$\boldsymbol{a_{3^{rd}}} = \mu_{3^{rd}}\left(\frac{\boldsymbol{r_{3^{rd}}} - \boldsymbol{r}}{|\boldsymbol{r_{3^{rd}}} - \boldsymbol{r}|^3} - \frac{\boldsymbol{r_{3^{rd}}}}{|\boldsymbol{r_{3^{rd}}}|^3}\right) \tag{2.6}$$

  where $\mu_{3^{rd}}$ and $\boldsymbol{r_{3^{rd}}}$ are the third-body gravitational constant and inertial position with respect to the main attractor, respectively.

- Acceleration due to solar radiation pressure:

$$\boldsymbol{a_{SRP}} = \frac{P_{Sun}}{c}\,C_r\,\frac{A_{rad}}{M}\,\nu\,\frac{\boldsymbol{r} - \boldsymbol{r_S}}{|\boldsymbol{r} - \boldsymbol{r_S}|} \tag{2.7}$$

Where P_{Sun} is the Solar Energy reaching the satellite, c is the light velocity, $\boldsymbol{r_S}$ is the Sun inertial position with respect to the main attractor and C_r and A_{rad} are the satellite radiation pressure coefficient and radiative area, respectively. Finally ν is the shadow function, which considers the Earth as the occulting body and can be determined according to either a biconical or a cylindrical model.

- Acceleration due to the Earth radiation pressure: $\boldsymbol{a_{ERP}}$. It accounts for radiating effects involving the Earth either as reflecting or radiating body, such as the albedo and the infrared radiation. A detailed description of this perturbation can be found in [50].

Without any approximation and differently from Eq. 2.1, there is no analytical way to integrate Eq. 2.3. Thus, to compute the satellite position and velocity in time considering the orbital perturbations, numerical integration must be used and several schemes can be considered, such as the Runge-Kutta 8-7^{th} order Dorman and Prince formulas [51]. The numerical integration allows a high-fidelity orbital propagation, but also provokes a remarkable increase of the computational demand. On the one hand, it is fundamental to include in the propagation only those perturbations actually effective, on the other hand particular analytical and semi-analytical approaches were developed in the past to boost the computational time, despite an accuracy reduction.

As mentioned above, Eq. 2.1 can be analytically integrated only if particular approximations are exploited, e.g. when only J2 perturbation is considered. In this framework, one of the most popular analytical model which accounts also for perturbations is the Simplified General Perturbations model #4 (SGP4) propagator. The version used throughout the thesis is the one from [52], which, depending on the orbital regime, considers secular and periodic variations due to the Earth oblateness, the solar and lunar gravitational effects, the gravitational resonance effects, and the orbital decay using a drag model.

To conclude, although no semi-analytical propagator is used throughout the thesis, it is worth to mention the Draper Semi-analytical Satellite Theory (DSST) [53], which couples analytical integration (for the J2 perturbation, for instance) with numerical schemes for non-conservative perturbations (such as the atmospheric drag and the solar radiation pressure).

2.3 Uncertainty propagation

Section 2.2 describes how an orbital state, assumed as deterministic, can be propagated in time. However, in practical applications, it is always associated to a degree of uncertainty and it is important to account for its effects in the propagation. This aspect is also true for any kind of random variable transformation. If the Gaussian assumption holds, such as for short-term propagations or small initial uncertainties, the State Transition Matrix (STM) [54] is often used.

In SST-related applications, Gaussian assumption is widely exploited for many kinds of operations, but it turns out not to be adequate when the non-linearity of a transformation cannot be neglected. In the past, several works were conducted to establish an optimal way to deal with this issue. In this context, a widely used methodology is the Gaussian Mixtures model [55], which splits the Gaussianly-distributed orbital state in multiple sub-distributions and propagate each one singularly. This methodology is often joint with other actions aimed at remedying to non-linearity effects. In [56], for instance, equinoctial elements [57] are used to propagate uncertainty, instead of cartesian coordinates.

This thesis does not discuss the non-Gaussian methodologies for the uncertainty propagation of the orbital state in detail. If the Gaussian assumption holds, random variables can be expressed according to a distribution $\boldsymbol{Q} \sim \mathcal{N}(\boldsymbol{\mu},\ \boldsymbol{P})$, where $\boldsymbol{\mu}$ stands for the mean and $\boldsymbol{P}$ for the covariance. The most basic way to transform $\boldsymbol{Q}$ is through a Montecarlo approach, which can turn out to be computationally demanding. Therefore, several methods were developed in the past to transform random variables in an efficient way. The present thesis exploits the Unscented Transformation, given its efficiency and accuracy and the fact that it nonlinearly approximates the first two statistical moments of the propagated distribution [58].

Both the Montecarlo approach and the Unscented Transformation are described below.

Montecarlo

According to the Montecarlo approach, an initial N_d-dimensional distribution $\boldsymbol{Q} \sim \mathcal{N}(\boldsymbol{\mu},\ \boldsymbol{P})$ is populated with N_s samples, such that N_s N_d-dimensional vectors are obtained, which are representative of $\boldsymbol{Q}$. Under Gaussianity assumption, if $\mathrm{N}_d = 1$, the operation is called *univariate normal distribution*, otherwise it is called *multivariate normal distribution* [59].

Starting from it, samples can be propagated both linearly and non-linearly, according to the applied transformation, up to the final condition. At the end mean and covariance can be retrieved back from the propagated samples.

Montecarlo approaches are the most general way to deal with the uncertainty transformation and, for this reason, they are used as reference in many applications. However, the result accuracy is proportional to the number of initial samples N_s used and, so, to the computational demand which, for some applications, becomes prohibitive. Therefore, alternative approaches have been developed to reduce time consumption.

Unscented Transformation [58]

An alternative way to propagate $\boldsymbol{Q}$ is through the linearisation of the involved transformation function, that is the prediction part of the *Extended Kalman Filter* (EKF) [60]. This is based on a Taylor Series expansion about the estimate, which is truncated at the first order. This approximation is valid if the contributions of the truncated higher order terms are negligible. However, in many practical situations, linearisation introduces significant biases or errors. This approach can also be prohibitively difficult to implement because deriving Jacobians can be cumbersome and time consuming (especially when the system is complicated and of high order), and they must be reevaluated at every prediction step of the filter.

The Unscented Transformation (UT) solves these issues, based on the assumption that it is easier to approximate a probability distribution than to approximate an arbitrary nonlinear function or transformation. Hence, a set of points is generated from the distribution $\boldsymbol{Q}$ and the nonlinear function is applied to each of them in turn to yield a transformed sample, and the predicted mean and covariance are calculated from the transformed sample. Although this superficially resembles a Monte Carlo method, the samples are not drawn at random. Rather, the samples are deterministically chosen so that they capture specific information about the distribution. In general, this intuition can be applied to capture many kinds of information about many types of distributions. The procedure is described in more detail as follows.

The N_d-dimensional random variable $\boldsymbol{Q}$ is approximated by $2N_d+1$ weighted samples $\tilde{\boldsymbol{\mu}}$, the

so-called sigma points, selected by the algorithm which, at a generic step k, are defined as:

$$\begin{aligned}
\tilde{\boldsymbol{\mu}}\left(k|k\right) &= \boldsymbol{\mu}\left(k|k\right) \\
\bar{\boldsymbol{\mu}}^{\boldsymbol{i}}\left(k|k\right) &= \boldsymbol{\mu} + \left(\sqrt{\left(\mathrm{N}_d + \lambda\right)\boldsymbol{P}\left(k|k\right)}\right)^i \\
\bar{\boldsymbol{\mu}}^{\boldsymbol{i+\mathrm{N}_d}}\left(k|k\right) &= \boldsymbol{\mu} - \left(\sqrt{\left(\mathrm{N}_d + \lambda\right)\boldsymbol{P}\left(k|k\right)}\right)^i
\end{aligned} \tag{2.8}$$

Where $\lambda \in \Re$ such that $\left(\mathrm{N}_d + \lambda\right) \neq 0$, and $\left(\sqrt{\left(\mathrm{N}_d + \lambda\right)\boldsymbol{P}\left(k|k\right)}\right)^i$ is the i-th row or column of the matrix square root of $\left(\mathrm{N}_d + \lambda\right)\boldsymbol{P}\left(k|k\right)$. The set of samples chosen by Eq. 2.8 have the same sample mean, covariance, and all higher odd-ordered central moments as the distribution $\boldsymbol{Q}\left(k\right)$. The matrix square root and k affect the fourth and higher order sample moments of the sigma points.

The sigma points are then transformed up to a generic step z according to the transformation g (either linear or non-linear):

$$\bar{\boldsymbol{\mu}}\left(z|k\right) = g\left(\bar{\boldsymbol{\mu}}\left(k|k\right),\ \boldsymbol{u}\left(k\right),\ k\right) \tag{2.9}$$

Where $\boldsymbol{u}\left(k\right)$ is a generic input vector. The predicted mean and covariance at step z are computed as:

$$\begin{aligned}
\boldsymbol{\mu}\left(z|k\right) &= \sum_{i=0}^{2\mathrm{N}_d} w_i\, \bar{\boldsymbol{\mu}}_i\left(z|k\right) \\
\boldsymbol{P}\left(z|k\right) &= \sum_{i=0}^{2\mathrm{N}_d} w_i\ \left(\bar{\boldsymbol{\mu}}_i\left(z|k\right) - \boldsymbol{\mu}\left(z|k\right)\right)\ \left(\bar{\boldsymbol{\mu}}_i\left(z|k\right) - \boldsymbol{\mu}\left(z|k\right)\right)^T
\end{aligned} \tag{2.10}$$

Where:

$$\begin{aligned}
w^0 &= k/\left(\mathrm{N}_d + k\right) \\
w^i &= 1/\left(2\mathrm{N}_d + k\right) \\
w^{i+\mathrm{N}_d} &= 1/\left(2\mathrm{N}_d + k\right)
\end{aligned} \tag{2.11}$$

The mean and covariance are calculated using standard vector and matrix operations, which means that the algorithm is suitable for any choice of process model, and implementation is extremely convenient because it is not necessary to evaluate the Jacobians, which are needed in an EKF. The method has a further advantage: it yields more accurate predictions than those determined through linearisation.

It is worth observing that the parameter λ provides an extra degree of freedom to "fine tune" the higher order moments of the approximation, and can be used to reduce the overall prediction errors. When $\boldsymbol{x}(k)$ is assumed Gaussian, a useful heuristic is to select $\mathrm{N}_d + \lambda = 3$, otherwise a different choice of k might be more appropriate.
The UT operation represents the prediction part of the Unscented Kalman Filter (UKF) described in Sec. 2.5.2.

2.4 Radar basics

This section is based on [61] and [62]. Considering the general case of a bistatic configuration, let us consider the signal transmitted by the radar. By naming P_{TX} the power radiated by the transmitter, $G_{TX} = G_{TX}\left(\Delta\gamma_1^{TX}, \Delta\gamma_2^{TX}\right)$ the transmitting antenna gain expressed as a function of the angular deviations with respect to the LoS pointing direction (Sec. 2.1), the power density S_{TX} at a distance ρ_{TX} from the transmitter is:

$$S_{TX} = \frac{G_{TX}\, P_{TX}}{4\pi\rho_{TX}^2} \tag{2.12}$$

When this signal is intercepted by a transiting object, the amount of power that it reflects depends on its physical and electrical properties, which can be summarised in a single parameter: the Radar Cross Section (RCS). It defines the effective area of the object, and it is not a constant property, as it depends on both the wavelength of the incoming signal, the area of the object and its attitude. By introducing this parameter, the intercepted power can be expressed as:

$$P_i = S_{TX}\, RCS \tag{2.13}$$

Assuming that all the intercepted power is reflected in an isotropic way, the power that is collected at the receiver is equal to:

$$P_{rx} = \frac{P_{TX}\, G_{TX}\, G_{RX}\, RCS\, c^2}{(4\pi)^3\, f_c^2\, \rho_{TX}^2\, \rho_{RX}^2} \tag{2.14}$$

Where $G_{RX}\left(\Delta\gamma_1^{RX}, \Delta\gamma_2^{RX}\right)$ is the gain of the receiver as a function of the angular deviations with respect to its LoS, c is the light speed, f_c is the carrier frequency considered, ρ_{RX} is the distance of the object from the receiver. Eq. 2.14 is the simplified version of the so-called

bistatic radar equation, in which no system and propagation losses are considered. The receiver also measures a noise power, which can be expressed as:

$$N = k_B \, Bw \, T_{eq} \tag{2.15}$$

Where $k_B = 1.380658e - 23 \, JK^{-1}$ is the Boltzmann's constant, T_{eq} is the equivalent temperature of the system and Bw is the channel bandwidth, corresponding to the frequency f_s used to sample the received signal.

The Signal to Noise Ratio (SNR) is defined as the ratio between the received and the noise powers:

$$SNR = 10 \, \log_{10} \left(\frac{P_{rx}}{N} \right) \tag{2.16}$$

When the value is larger than an imposed threshold, the object is detected, and other quantities can be derived. Typical radar systems provide two different measurements per time instant: slant range (SR) and Doppler shift (DS) measurements.

The slant range is the sum of the distances of the the detected object from transmitter and receiver:

$$\mathrm{SR} = \rho_{TX} + \rho_{RX} \tag{2.17}$$

The Doppler shift is instead the variation in frequency of the signal generated by the motion of the target, and can be expressed as:

$$\mathrm{DS} = f_c^{RX} - f_c^{TX} = \frac{c}{f_c^{TX}} \frac{d}{dt} \left(\rho_{TX} + \rho_{RX} \right) = \frac{c}{f_c} \left(v_{rel}^{TX} + v_{rel}^{RX} \right) = \frac{c}{f_c^{TX}} \frac{d \, \mathrm{SR}}{dt} \tag{2.18}$$

where v_{rel}^{TX} and v_{rel}^{RX} are the magnitudes of the satellite relative velocities with respect to transmitter and receiver, respectively. The definition of Eq. 2.18 allows to appreciate the close relationship between Doppler shift and slant range rate, which are linked through the signal features.

When operating a radar system, both slant range and Doppler shift measurements are derived by analysing the received signal. The Doppler shift is directly obtained by comparing the received signal frequency with the transmitted one, while the derivation of slant range measurements depends on the nature of the transmitted signal. For continuous wave systems, range measurements can be obtained by analysing the spectrum of the reflected signal. For pulse compression radars, the computation of the time delay between the transmission and

reception of the signal provides an estimate for the slant range.
Besides slant range and Doppler shift measurements, also angular coordinates of the source in the receiver FoV can be derived, according to the implemented signal processing chain. As stated in Sec. 1.6, this thesis investigates a new approach to compute the angular track, as widely discussed in Chapters 3 to 5 and in Ch. 7.

2.5 Orbit determination techniques

In SST related applications, sensor measurements are processed in order to reconstruct orbital states of the observed object. This process is known as Orbit Determination (OD). In order to determine the orbital state of an observed object, sensor measurements can be processed in two ways, depending on whether the data refer to a catalogued object or not.
In the catalogued case, orbital state predictions of the object are available, which, besides position and velocity, can include additional parameters (such as the ballistic coefficient). These are refined using the measurements and this process is known as Refined Orbit Determination (ROD). It is typically based on larger amounts of available data and can be distinguished between batch methods, in which the complete data set acquired over a certain time horizon is used to find a solution, and sequential methods, in which measurement information is processed as soon as it is available. Both batch and sequential methods are iterative and require sufficiently good initial guesses.
For uncatalogued objects, instead, no prediction is available and only measurements can be exploited. In this case, an Initial Orbit Determination (IOD) is performed, through dedicated algorithms. In this context, the most reliable methodologies usually estimate orbital position and velocity only.
In an operational scenario, the measurements are first recorded without any possible contribution from the a-priori knowledge of the observed object, but for what concerns the observation time schedule and the station pointing when a specific target is observed. A correlation procedure is then performed to link the measurements to a catalogued object, which is propagated towards the observation epochs according to one of the propagation model described in Sec. 2.2 and, if the predicted state uncertainty is considered as well, to one of the uncertainty transformation techniques discussed in Sec. 2.3. If the correlation is successful, a ROD is run, otherwise an IOD procedure is performed. A similar correlation

process can be later performed to check the compatibility of the OD result with respect to the input measurements, as deepened below.

2.5.1 Correlation

In this work, a statistical correlation index is computed using the concept of Mahalanobis distance [63]. Assuming a normal distribution, the acquired measurements, at each observation epoch t_k, can be expressed as $\boldsymbol{Y}(t_k) \sim \mathcal{N}(\boldsymbol{\mu_y}(t_k), \boldsymbol{P_y})$, where $\boldsymbol{P_y}$ is constant and is defined based on the sensor accuracy. The dimension N_y of $\boldsymbol{Y}$ depends on the acquired measurements. In order to verify the correlation status of a generic catalogued orbital state $\boldsymbol{X} \sim \mathcal{N}(\boldsymbol{\mu_x},\ \boldsymbol{P_x})$, this can be propagated (according to one of the propagation models discussed in Sec. 2.2) up to the observation epochs and then projected in the measurement space, according to an UT transformation (Sec. 2.3). This operation results in the synthetic measurement set $\tilde{\boldsymbol{Y}}(t_k) \sim \mathcal{N}\left(\tilde{\boldsymbol{\mu}}_{\boldsymbol{y}}(t_k), \tilde{\boldsymbol{P}}_{\boldsymbol{y}}(t_k)\right)$, where, differently from $\boldsymbol{P_y}$, $\tilde{\boldsymbol{P}}_{\boldsymbol{y}}$ depends on the observation epoch t_k considered.

For each observation epoch t_k, the Mahalanobis distance is computed as:

$$\xi(t_k) = \{\tilde{\boldsymbol{\mu}}_{\boldsymbol{y}}(t_k) - \boldsymbol{\mu_y}(t_k)\}^T \left\{\boldsymbol{P_y} + \tilde{\boldsymbol{P}}_{\boldsymbol{y}}(t_k)\right\}^{-1} \{\tilde{\boldsymbol{\mu}}_{\boldsymbol{y}}(t_k) - \boldsymbol{\mu_y}(t_k)\} \tag{2.19}$$

And it is divided by the inverse of the χ^2 cumulative distribution function, which depends on the uncertainty level (usually addressed to as σ level), and to the N_y number of degrees of freedom:

$$\zeta(t_k) = \frac{\xi(t_k)}{\bar{\chi}^2} \tag{2.20}$$

In this work, the 3-σ level is generally used, which corresponds to a probability of 99.8 %. Finally, the correlation index $\overline{\zeta}$ is selected as the mean value of all the $\zeta(t_k)$ computed along the observation window. If this quantity satisfies a given threshold τ, the measurements can be considered correlated to the catalogued orbital state $\boldsymbol{X}$. To pass the χ^2 test described above, the threshold τ shall be theoretically set equal to 1. However, for noisy and not accurate measurements (such as in real case scenario), it may occur that such a threshold is not respected even for correct correlations, and τ shall be relaxed accordingly. This takes place, for instance, when the measurement noise exceeds the declared accuracy (information included in the covariance matrix $\boldsymbol{P_y}$), or when the Gaussian assumption does not hold.

As mentioned above, this procedure is here used also to define an index which assesses the compatibility of the OD results with the measurements adopted in the estimation process. From the resulting mean $\boldsymbol{\mu_x}$ and covariance $\boldsymbol{P_x}$ at the OD reference epoch, the related synthetic measurements $\tilde{\boldsymbol{Y}}(t_k)$ are computed at each t_k. Then, the Mahalanobis distance is computed according to Eq. 2.19 on each measurement and the mean correlation index $\overline{\zeta}$ is computed. Then, Eq. 2.19 and Eq. 2.20 are evaluated, and the mean correlation index $\overline{\zeta}$ is computed. Finally an OD result is considered to be satisfactory if $\overline{\zeta} < \tau$, where the same considerations as above apply to τ.

It is worth pointing out that the larger the residuals of the OD process are, the larger the orbital state covariance $\tilde{\boldsymbol{P}}_{\boldsymbol{x}}$ and the smaller the correlation index computed according to Eq. 2.19 is. Hence, an object affected by noisy measurements may turn out to feature good correlation index values despite the presence of large residuals. In order to avoid this problem, Eq. 2.19 can be modified as:

$$\zeta(t_k) = \{\tilde{\boldsymbol{\mu}}_{\boldsymbol{y}}(t_k) - \boldsymbol{\mu_y}(t_k)\}^T \ \boldsymbol{P}_{\boldsymbol{y}}^{-1} \{\tilde{\boldsymbol{\mu}}_{\boldsymbol{y}}(t_k) - \boldsymbol{\mu_y}(t_k)\} \tag{2.21}$$

such that only the sensor accuracy is considered in the correlation index. Since the index increases as a consequence of this modification, the threshold τ shall be relaxed accordingly. In this work, the compatibility of the OD result with the measurements is checked according to Eq. 2.21.

2.5.2 Refined Orbit Determination

In ROD processes, an orbital state prediction $\boldsymbol{X_0} \sim \mathcal{N}(\boldsymbol{\mu_{x0}},\ \boldsymbol{P_{x0}})$ is refined based on the acquired measurements $\boldsymbol{Y} \sim \mathcal{N}(\boldsymbol{\mu_y}, \boldsymbol{P_y})$. Generally, either batch filters like the Non-linear Least Squares, or sequential filters like the Kalman Filters are used [60]. The former can refine the orbital state prediction also when the covariance $\boldsymbol{P_{x0}}$ is not known, while the latter cannot. Furthermore, the batch filters allow greater flexibility in the choice of the epoch at which the orbital state has to be refined, as it can either belong to the observation window or not. On the contrary, even if also sequential filters can theoretically refine orbital states which are outside of the observation time window, by properly setting the transformation function, this choice is usually not taken, because of the increasing transformation non-linearity (leading to performance deterioration) and longer computational time. Thus,

sequential filters provide the estimate only at the final-step observation epoch, which can be the first in time (for backward ROD), or the last one (for forward ROD), but they are generally more stable and, consequently, more reliable.

In the past, multiple works were carried out to establish optimal formulations for batch and sequential filters applied to ROD problems. In [64] the OD problem is formulated as a batch parameter estimation problem which refines multiple intermediate orbital states in the observation window, such that a faster and more robust convergence is granted. In [65] the Extended Kalman Filter (EKF) [60] is used as sequential filter, by propagating the orbital state uncertainty, expressed through equinoctial elements [57], through Gaussian Mixtures [55].

A detailed discussion about ROD filters is beyond the objective of this thesis. For this reason, the widely used Non-linear Least Squares (as batch filter) and Unscented Kalman Filters (as sequential filter) are considered and they are presented in this section.

Non-linear Least Squares [60]

Generally speaking, the Non-linear Least Squares method seeks to refine an orbital state $\boldsymbol{\mu_{x0}}$ (of dimension N_x), defined at time $\hat{t}$ and considered as process first guess, by searching for the mean orbital state $\boldsymbol{\mu_x}$ as that value that minimises the sum of the squares of the calculated observation residuals.

Let the residual vector be:

$$\boldsymbol{\varepsilon}\left(\boldsymbol{\mu_x}\right) = \left(\boldsymbol{\mu_y} - \tilde{\boldsymbol{\mu}}_{\boldsymbol{y}}\left(\boldsymbol{\mu_x}\right)\right) \tag{2.22}$$

Whose dimension is N_ε=N_{obs}+N_y, where N_{obs} is the observation epochs number and N_y is the dimension of the measurement state. Then, $\boldsymbol{\mu_y}$ is the set of the observation data (mapped in the measurements space) and $\tilde{\boldsymbol{\mu}}_{\boldsymbol{y}}$ is the synthetic measurements set, retrieved from $\boldsymbol{\mu_{x0}}$ according to the procedure described in Sec. 2.5.1. The process searches for the value of $\boldsymbol{\mu_x}$ which minimises the following performance index:

$$h\left(\boldsymbol{\mu_x}\right) = \frac{1}{2}\boldsymbol{\varepsilon}\left(\boldsymbol{\mu_x}\right)^T \boldsymbol{\varepsilon}\left(\boldsymbol{\mu_x}\right) \tag{2.23}$$

Note that Eq. 2.23 is a quadratic function of $\boldsymbol{\mu_x}$, and, as a consequence, the expression has a unique minimum when:

$$\frac{\partial h}{\partial \boldsymbol{\mu_x}} = 0 \quad \text{and} \quad \delta\boldsymbol{\mu_x}^T \frac{\partial^2 h}{\partial \boldsymbol{\mu_x}^2} \delta\boldsymbol{\mu_x} > 0 \tag{2.24}$$

for $\delta\boldsymbol{\mu_x} \neq 0$. The second condition of Eq. 2.24 means that $\partial^2 h / \partial \boldsymbol{\mu_x}^2$ is positive defined.
The non-linear transformation from $\boldsymbol{\mu_{x0}}$ to $\tilde{\boldsymbol{\mu}}_{\boldsymbol{y}}$ can have several shapes, depending on the epoch $\hat{t}$ (either related to observation window or not) and on the propagation model adopted, but all propagate the orbital state $\boldsymbol{\mu_{x0}}$ along the observation epochs and then project the computed states on the measurements space, according to the available data contained in $\boldsymbol{\mu_y}$. If the process converges, the orbital state $\boldsymbol{X}$ is found, both in terms of the estimated $\boldsymbol{\mu_x}$ and covariance, which is computed as:

$$\boldsymbol{P_x} = \frac{\boldsymbol{\varepsilon}\left(\boldsymbol{\mu_x}\right)^T \boldsymbol{\varepsilon}\left(\boldsymbol{\mu_x}\right)}{\mathrm{N}_\epsilon - \mathrm{N}_x} \left(\boldsymbol{J}\left(\boldsymbol{\mu_x}\right)^T \boldsymbol{J}\left(\boldsymbol{\mu_x}\right) \right)^{-1} \tag{2.25}$$

Where $\boldsymbol{J}\left(\boldsymbol{\mu_x}\right)$ is the Jacobian of $\boldsymbol{\varepsilon}\left(\boldsymbol{\mu_x}\right)$ at the solution $\boldsymbol{\mu_x}$.
There are different variations to this scheme, the most remarkable being the weighted Non-linear Least Squares and the a-priori Non-linear Least Squares.
In the weighted Non-linear Least Squares, Eq. 2.23 is modified as:

$$h\left(\boldsymbol{\mu_x}\right) = \frac{1}{2} \boldsymbol{\varepsilon}\left(\boldsymbol{\mu_x}\right)^T \boldsymbol{W_y}\, \boldsymbol{\varepsilon}\left(\boldsymbol{\mu_x}\right) \tag{2.26}$$

where $\boldsymbol{W_y}$ is the matrix weighting the observation errors and usually results from an initial judgement on the accuracy of the observations (the sensor accuracy, for instance), followed by a normalisation procedure to scale the weights to values between zero and one.
The a-priori Non-linear Least Squares also considers the predicted orbital state $\bar{\boldsymbol{\mu}}_{\boldsymbol{x0}}$ as a further data to fit, together with an associated weighting matrix $\boldsymbol{W_{x0}}$, and Eq. 2.23 is modified as:

$$h\left(\boldsymbol{\mu_x}\right) = \frac{1}{2} \boldsymbol{\varepsilon}\left(\boldsymbol{\mu_x}\right)^T \boldsymbol{W_y}\, \boldsymbol{\varepsilon}\left(\boldsymbol{\mu_x}\right) + \frac{1}{2} \left(\boldsymbol{\mu_x} - \boldsymbol{\mu_{x0}}\right)^T \boldsymbol{W_{x0}} \left(\boldsymbol{\mu_x} - \boldsymbol{\mu_{x0}}\right) \tag{2.27}$$

Usually, $\boldsymbol{W_{x0}}$ is derived from the covariance $\boldsymbol{P_{x0}}$ associated to $\boldsymbol{\mu_{x0}}$.
Even if the Non-linear Least Squares approaches are theoretically exploitable for IOD (start-

ing from a circular first guess, for instance), they are operationally considered just for ROD operations, as an accurate $\boldsymbol{\mu_{x0}}$ is fundamental to get convergence, except for particular procedures in which they are combined with other algorithms to provide an IOD result, such as described in Sec. 2.5.3 if angles and Doppler shift measurements are provided.

Unscented Kalman Filter

An efficient way to perform ROD with a sequential filter is represented by the Unscented Kalman Filter, which is a technique based on the Unscented Transformation (Sec. 2.3), which does not contain any linearisation, and thus provides superior performance with respect to the EKF in nonlinear problems [58] [66].

In a ROD operation, let's consider a prediction state $\boldsymbol{X_0} \sim \mathcal{N}(\boldsymbol{\mu_{x0}},\ \boldsymbol{P_{x0}})$ defined at reference time t_0. Its dimension N_x depends on the parameters to be refined: N_x=6 to refine just the orbital state, N_x=7 if an additional physical parameter (such as the ballistic coefficient) is considered, and so on. Let the ROD measurements set be $\boldsymbol{Y}(t_k) \sim \mathcal{N}(\boldsymbol{\mu_y}(t_k),\ \boldsymbol{P_y})$, where $\boldsymbol{\mu_y}(t_k)$ represents the acquired measurements at each observation epoch t_k and $\boldsymbol{P_y}$ the constant covariance defined up to the sensor accuracy.

From $\boldsymbol{X}$, sigma points are created according to Eq. 2.8: $\bar{\boldsymbol{\mu}}_{\boldsymbol{x}}(t_0)$. These are propagated up to the first-step observation epoch t_1 through one of the approaches described in Sec. 2.2, resulting in the propagated N_x-dimensional sigma points: $\bar{\boldsymbol{\mu}}_{\boldsymbol{x}}^{\boldsymbol{i}}(t_1|t_0)$ (for the i-th sigma point). Given the non-linear function g which projects an orbital state in the measurement space, the predicted measurements sigma points can be computed at the first-step observation epoch t_1, whose dimension N_y corresponds to the number of considered measurements: $\bar{\boldsymbol{\mu}}_{\boldsymbol{y}}^{\boldsymbol{i}}(t_1|t_0) = g\left(\bar{\boldsymbol{\mu}}_{\boldsymbol{x}}^{\boldsymbol{i}}(t_1|t_0)\right)$. Then, the augmented sigma point $\bar{\boldsymbol{\mu}}_{\boldsymbol{\xi}}^{\boldsymbol{i}}(t_1|t_0)$ is created, chaining $\bar{\boldsymbol{\mu}}_{\boldsymbol{x}}^{\boldsymbol{i}}$ and $\bar{\boldsymbol{\mu}}_{\boldsymbol{y}}^{\boldsymbol{i}}$:

$$\bar{\boldsymbol{\mu}}_{\boldsymbol{\xi}}^{\boldsymbol{i}}(t_1|t_0) = \begin{bmatrix} \bar{\boldsymbol{\mu}}_{\boldsymbol{x}}^{\boldsymbol{i}}(t_1|t_0) \\ \bar{\boldsymbol{\mu}}_{\boldsymbol{y}}^{\boldsymbol{i}}(t_1|t_0) \end{bmatrix} \tag{2.28}$$

And its dimension N_ξ turns out to be equal to N_x+N_y.

At this point, Eq. 2.8 is applied on the entire set of sigma points $\bar{\boldsymbol{\mu}}_{\boldsymbol{\xi}}^{\boldsymbol{i}}(t_1|t_0)$ and N_ξ-dimensional state is returned, both in terms of mean $\hat{\boldsymbol{\mu}}_{\boldsymbol{\xi}}(t_1|t_0)$ (dimension N_ξx1) and co-

variance $\hat{\boldsymbol{P}}_{\boldsymbol{\xi}}(t_1|t_0)$ (dimension N_ξxN_ξ). It is now possible to split $\hat{\boldsymbol{\mu}}_{\boldsymbol{\xi}}(t_1|t_0)$ in:

$$\hat{\boldsymbol{\mu}}_{\boldsymbol{\xi}}(t_1|t_0) = \begin{bmatrix} \hat{\boldsymbol{\mu}}_{\boldsymbol{x}}(t_1|t_0) \\ \hat{\boldsymbol{\mu}}_{\boldsymbol{y}}(t_1|t_0) \end{bmatrix} \tag{2.29}$$

And $\hat{\boldsymbol{P}}_{\boldsymbol{\xi}}(t_1|t_0)$ in:

$$\hat{\boldsymbol{P}}_{\boldsymbol{\xi}}(t_1|t_0) = \begin{bmatrix} \hat{\boldsymbol{P}}_{\boldsymbol{x}}(t_1|t_0) & \hat{\boldsymbol{P}}_{\boldsymbol{xy}}(t_1|t_0) \\ \hat{\boldsymbol{P}}^T_{\boldsymbol{xy}}(t_1|t_0) & \hat{\boldsymbol{P}}_{\boldsymbol{y}}(t_1|t_0) \end{bmatrix} \tag{2.30}$$

Such that the dimensions are N_xx1 for $\hat{\boldsymbol{\mu}}_{\boldsymbol{x}}(t_1|t_0)$, N_yx1 for $\hat{\boldsymbol{\mu}}_{\boldsymbol{y}}(t_1|t_0)$, N_xxN_x for $\hat{\boldsymbol{P}}_{\boldsymbol{x}}(t_1|t_0)$, N_yxN_y for $\hat{\boldsymbol{P}}_{\boldsymbol{y}}(t_1|t_0)$, N_xxN_y for $\hat{\boldsymbol{P}}_{\boldsymbol{xy}}(t_1|t_0)$.
By defining:

$$\hat{\boldsymbol{P}}_{\boldsymbol{e}}(t_1|t_0) = \hat{\boldsymbol{P}}_{\boldsymbol{y}}(t_1|t_0) + \boldsymbol{P}_{\boldsymbol{y}} \tag{2.31}$$

and the covariance gain as:

$$\boldsymbol{K}(t_1|t_0) = \hat{\boldsymbol{P}}_{\boldsymbol{xy}}(t_1|t_0)\,\hat{\boldsymbol{P}}_{\boldsymbol{e}}(t_1|t_0)^{-1} \tag{2.32}$$

The orbital state is updated as:

$$\begin{aligned} \boldsymbol{\mu}_{\boldsymbol{x}}(t_1|t_0) =& \hat{\boldsymbol{\mu}}_{\boldsymbol{x}}(t_1|t_0) + \boldsymbol{K}(t_1|t_0)\left\{\boldsymbol{\mu}_{\boldsymbol{y}}(t_1) - \hat{\boldsymbol{\mu}}_{\boldsymbol{y}}(t_1|t_0)\right\} \\ \boldsymbol{P}_{\boldsymbol{x}}(t_1|t_0) =& \hat{\boldsymbol{P}}_{\boldsymbol{\mu}}(t_1|t_0) - \boldsymbol{K}(t_1|t_0)\,\hat{\boldsymbol{P}}_{\boldsymbol{e}}(t_1|t_0)\,\boldsymbol{K}^T(t_1|t_0) \end{aligned} \tag{2.33}$$

By repeating this procedure for all the conditional estimations $(t_{k+1}|t_k)$ sequentially, up to the final-step observation epoch t_f, the orbital state is refined through the measurements. It is important to stress that the sequential filter procedure is possible only if a covariance can be associated to the orbital prediction. Then, as remarked above, the procedure can be performed either forward or backward with respect to the observation timeline (being sequential), but the result is always associated to the final-step observation epoch considered.

2.5.3 Initial Orbit Determination

As illustrated above, no orbital predictions are available for the observed object in the IOD context. In this case the Non-linear Least Squares approaches, theoretically, could still be applied (and would allow to estimate other parameters in addition to position and velocity),

but they turn out to be quite unstable, mainly due to the lack of a sufficiently accurate first guess. Thus, alternative methodologies have been developed by the scientific community that are applied depending on the available radar measurements.

Let's consider a set of radar sensor observations $\boldsymbol{Y}(t_k) \sim \mathcal{N}(\boldsymbol{\mu_y}(t_k), \boldsymbol{P_y})$, where t_k are the N_{obs} observation epochs, $\boldsymbol{\mu_y}(t_k)$ the measurements acquired at t_k and $\boldsymbol{P_y}$ the covariance associated to the measurements and which is derived from the sensor accuracy. The acquired measurements are assumed to be angular coordinates (azimuth and elevation, or right ascension and declination) and SR, such that $\boldsymbol{\mu_y}$ and $\boldsymbol{P_y}$ result to have dimension $3\mathrm{xN}_{obs}$ and 3x3, respectively. These information, together with the time-dependent inertial sensor position $\boldsymbol{s}(t_k)$, can be processed to estimate the object orbital position $\boldsymbol{r}(t_k)$, whose uncertainty is described in terms of a multivariate normal distribution. In particular, the covariance $\boldsymbol{P_r}(t_k)$ can be derived from $\boldsymbol{Y}(t_k)$ with an UT (Sec. 2.3), by projecting the sigma points from the measurements to the inertial space.

Several methods exist to obtain a preliminary orbit from two or three geocentric positions, such as Lambert's problem solver or the Herrick-Gibbs approach as provided in [67]. Then, the GTDS range and angles method from [68] provides a stable fixed-point iteration scheme using the full acquired measurements, that is all the N_{obs} available observations. These methods are adapted in [69], which gives the definition of the IOD process applied in the present thesis and which is described as follows.

The $\boldsymbol{r}(t_k)$ vectors can be grouped in a unique matrix: $\boldsymbol{Z} = \left(\boldsymbol{r}^T(t_1), \boldsymbol{r}^T(t_2), ..., \boldsymbol{r}^T(t_{\mathrm{N}_{obs}})\right)$. From $\boldsymbol{Z}$, the algorithm proceeds iteratively by modifying the orbital mean state with a fixed-point update process, starting from a first guess $\boldsymbol{\mu_0}$ (e.g. obtained with a Keplerian circular orbit assumption):

$$\boldsymbol{\mu}_{\boldsymbol{x}}^{j} = \boldsymbol{H}(\boldsymbol{\mu}_{\boldsymbol{x}}^{j-1})\boldsymbol{Z} \tag{2.34}$$

By defining the j-th residual as $R^j = \max(|\boldsymbol{x}^j - \boldsymbol{x}^{j-1}|)$, the iterations proceed as long as $\left(R^j - R^{j-1}\right)/R^j$ is larger than a tolerance τ and a maximum number of iterations λ is reached. In this work, $\tau = 1e-9$ and $\lambda = 100$.

At any iteration j, the matrix $\boldsymbol{H}(\boldsymbol{\mu}_{\boldsymbol{x}}^{j-1})$ is defined according to $\boldsymbol{f}(\boldsymbol{\mu}_{\boldsymbol{x}}^{j-1})$ and $\boldsymbol{g}(\boldsymbol{\mu}_{\boldsymbol{x}}^{j-1})$, which are vectors grouping the Lagrangian coefficients, whose derivations are provided in e.g. [70]:

$$\boldsymbol{H}\left(\boldsymbol{\mu}_{\boldsymbol{x}}^{j-1}\right) = \frac{1}{\delta}\begin{pmatrix} \boldsymbol{g^T g F} - \boldsymbol{f^T g G} \\ \boldsymbol{f^T f G} - \boldsymbol{f^T g F} \end{pmatrix} \tag{2.35}$$

where the denominator is:

$$\delta = \left(\boldsymbol{f}^{\boldsymbol{T}}\boldsymbol{f}\right)\,\left(\boldsymbol{g}^{\boldsymbol{T}}\boldsymbol{g}\right) - \left(\boldsymbol{f}^{\boldsymbol{T}}\boldsymbol{g}\right)^2 \tag{2.36}$$

while the auxiliary matrix $\boldsymbol{F}$ (and equivalently $\boldsymbol{G}$) is defined as:

$$\boldsymbol{F} = \begin{pmatrix} f_1 & 0 & 0 & ... & f_{\mathrm{N}_{obs}} & 0 & 0 \\ 0 & f_1 & 0 & ... & 0 & f_{\mathrm{N}_{obs}} & 0 \\ 0 & 0 & f_1 & ... & 0 & 0 & f_{\mathrm{N}_{obs}} \end{pmatrix} \tag{2.37}$$

where f_k is the Lagrangian coefficient f relative to k-th epoch.
The method converges towards the solution $\boldsymbol{\mu_x}$. The orbital state covariance is finally determined through the linear approximation:

$$\boldsymbol{P_x} = \boldsymbol{H}\left(\boldsymbol{\mu_x}\right)\boldsymbol{P_r}\,\boldsymbol{H}^{\boldsymbol{T}}\left(\boldsymbol{\mu_x}\right) \tag{2.38}$$

where $\boldsymbol{P_r} = \mathrm{diag}\left(\boldsymbol{P_r}(t_1), ..., \boldsymbol{P_r}(\boldsymbol{t}_{\mathrm{N}_{\boldsymbol{obs}}})\right)$, and the orbital state $\boldsymbol{X}(\hat{t}) \sim \mathcal{N}\left(\boldsymbol{\mu_x}(\hat{t}), \boldsymbol{P_x}(\hat{t})\right)$ is determined. The epoch $\hat{t}$ is selected by the user (the first observation epoch in this work). The resulting $\boldsymbol{X}(\hat{t})$ can be further refined through the filters described above, as later done for SST services simulations in Sec. 4.4.
It is worth observing that, if an orbital prediction with no uncertainty associated (retrieved, for example, from Two-Line Elements TLE [14]) is exploited as the first guess $\boldsymbol{x_0}$, this procedure can work as a ROD process as well.

Slant Range as derived measurement

The method described above determines the orbital mean state and covariance from radar measurements including angles and SR, regardless the availability of DS. However, SR is not always included in the set of available measurements and this may represent a major limitation. To alleviate this issue and enhance the versatility of the method proposed, when the SR is not measured, its values are derived from DS measurements. To this aim, the approach proposed in [71] is applied and summarised below.
As mentioned in Sec. 2.4 and appreciable in Eq. 2.18, from DS measurements it is possible to derive the SR time derivative $d\mathrm{SR}/dt$ by knowing the transmitted frequency. Therefore,

if the SR initial value SR_0 is known, the SR can be computed at any epoch as:

$$\mathrm{SR}\,(t) = \mathrm{SR}_0 + \int_{t_0}^{t} \frac{d\,\mathrm{SR}}{dt}\, dt \tag{2.39}$$

Assuming that $d\,\mathrm{SR}/dt$ is known from DS measurements (Sec. 2.4), together with t, t_0 and dt (from the observation epochs), the problem reduces to the estimation of the SR initial value SR_0 associated to the first observation epoch t_0. The procedure for its determination, described hereafter, is based on the conservation of the total orbital energy.

Let $\boldsymbol{r_i} = \boldsymbol{r}(t_i, \mathrm{SR}_i)\,\hat{r_i}$ and $\boldsymbol{r_j} = \boldsymbol{r}(t_i, \mathrm{SR}_j)\,\hat{r_j}$ be the inertial position vectors at the i-th and j-th observation epochs, and $\Delta t = t_j - t_i > 0$ the corresponding flight time. SR_i and SR_j are related to SR_0 through Eq. 2.39. It is possible to solve the Lambert's problem for $\boldsymbol{r_i}$ and $\boldsymbol{r_j}$ to get the specific orbital energy of the connecting arc:

$$\varepsilon_{i,j}\,(\mathrm{SR}_0) = -\mu/2a \tag{2.40}$$

Being μ the Earth gravitational parameter and a the orbit semi-major axis. An ideal two-body system is conservative, that is the total energy of the problem is conserved. Therefore, after $\varepsilon_{i,j}\,(\mathrm{SR}_0)$ has been computed for any combination of two observations (i, j), it is possible to identify the value of SR_0 that yields the minimum standard deviation σ_ε in the distribution of energies. This SR_0 represents the optimal solution, and the standard deviation of the energy distribution is a univariate function that only depends on the scalar integration constant SR_0.

In this work, the approach is included in a process, schematised in Fig. 2-7, which first searches for the optimal solution on a coarse grid, by using a golden section search and parabolic interpolation. The resulting SR_0 is the first guess entering a Non-linear Least Squares process (Sec. 2.5.2), that refines the estimate by iteratively performing IOD (according to the procedure described above) and minimising the difference (weighted with the sensor accuracy $\boldsymbol{P_y}$) between the real measurements $\boldsymbol{\mu_y}$ and the predicted ones $\tilde{\boldsymbol{\mu}}_{\boldsymbol{y}}$ (computed from IOD result).

The final estimate SR_0 is used to derive the SR profile at all the observation epochs, according to Eq. 2.39 and the IOD process can be finally run based on angles and on the derived SR.

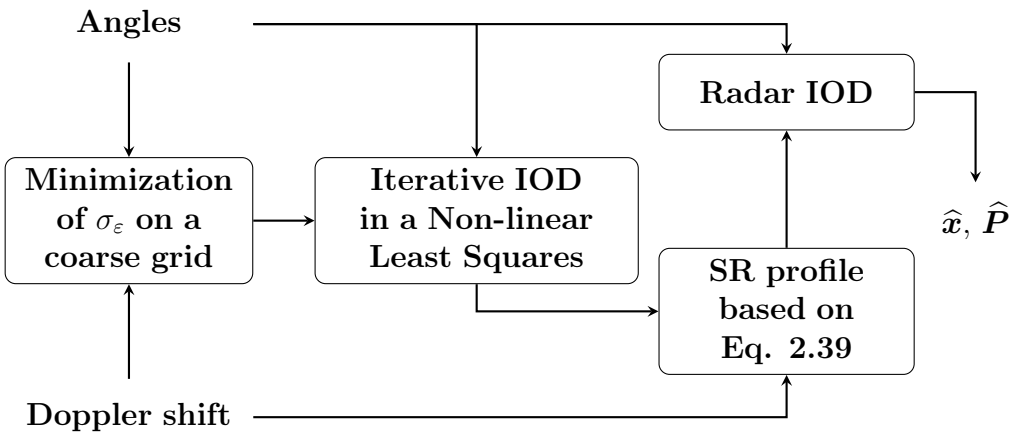

Figure 2-7: Flow diagram of the radar IOD procedure with SR as derived measurement.

Chapter 3

MUSIC Approach for Track Estimation and Refinement

As stated in Sec. 1.6, the main research objective of this thesis is represented by an adaptive beamforming approach to derive the angular track in array radars devoted to space surveillance. To accomplish such a purpose, MATER algorithm has been developed and is presented in this chapter.

First, the adaptive techniques that estimate the signal direction of arrival are described in Sec. 3.1. Among them, MUSIC is selected both because of its high-level resolution and for the possible application to a multiple sources scenario, which may occur during a survey application, a proximity operation monitoring or a fragments cloud observation. Then, the data model is defined in Sec. 3.2 and MUSIC is presented in Sec. 3.3. Afterwards, Sec. 3.4 discusses the ambiguous solutions problem, which may arise because of the mutual geometry among array receivers, and introduces MATER algorithm, which embeds both MUSIC and a clustering strategy, and deals with the ambiguous solutions problem. In particular, if the target transit prediction is available, the ambiguity can be solved a-priori, as described in Sec. 3.5. Otherwise, criteria are presented in Sec. 3.6, which are based either on statistical considerations (maximum occurrence criterion), or on the signal processing (*delta-k* technique), or even on the merging with additional measurements (OD-based, SNR and SR criteria).

3.1 Direction of Arrival estimation algorithms

As stated in Sec. 1.6, the basic objective of the research is to improve the angular track estimation in ground-based array radars, for space surveillance related applications. This can be accomplished by exploiting a digital signal processing approach implementing an adaptive beamforming logic.

The problem of the adaptive beamforming consists in the signal Direction of Arrival (DOA) estimation in presence of interference and noise. Two philosophies to deal with this subject exist: the optimum beamformers and the parameters estimation, the latter being further subdivided in statistics and subspace techniques.

The optimum beamformers purpose is to estimate the signal waveform [72], and the most remarkable ones are listed in the following. The Minimum Variance Distortionless Response (MVDR) algorithm is a filter which tries to keep only the signals propagating along specified directions by minimising the output noise power. If the noise is a sample function from a Gaussian random process then the output of the optimum distortionless filter is the maximum likelihood estimate of the signal. The Minimum Mean-Square Error (MMSE) algorithm is an optimum linear processor which tries to minimise the mean square error of the estimated signal. The Maximum Signal-to-Noise Ratio (Maximum SNR) beamformer maximises the output SNR. The Minimum Power Distortionless Response (MPDR) filter tries to steer the beamformer direction by finding the optimum distortionless filter for that direction. If the steering direction corresponds to the actual signal one, then the MPDR beamformer reduces to the MVDR beamformer.

In actual applications, to estimate the signal DOA, the above-mentioned beamformers have to adapt to the incoming data (from which the *adaptive beamformers* definition), and several techniques are available to perform such an operation [73]. The Sample Matrix Inversion (SMI) technique, also known as the Direct Matrix Inversion (DMI), performs this adaptation by estimating the spatial spectral matrix, through the inversion of the sample covariance matrix (CM). The Recursive Least Squares (RLS) performs this inversion recursively through a Least Squares algorithm. The Least Mean Square (LMS) algorithm adapts the beamforming through classical steepest descent algorithms.

The statistical parameter estimation approach for the DOA estimation problem basically consists in the Maximum Likelihood Estimation (MLE), always based on the sample CM, de-

clined in multiple versions [74]. The Conditional Maximum Likelihood Estimation (CMLE), or Deterministic Maximum Likelihood Estimation (DMLE), estimator assumes the source signals are unknown, but non-random, signals. Instead, the Stochastic Maximum Likelihood Estimation (SMLE), also known as Unconditional Maximum Likelihood Estimation (UMLE), estimator assumes the source signals are sample functions from Gaussian random processes and its performance approaches the Cramer-Rao bound asymptotically (that is, the lower bound on the variance), but it requires a significant amount of computation to find the estimate. Other multidimensional estimators exist that have similar asymptotic performance, but, in general, still require a significant amount of computation.

In practice, the above-mentioned MLE versions can be solved through the gradient techniques, such as quasi-Newton methods, or the so-called *relaxation methods*, or the *expectation methods* [74].

The subspace parameter estimation approach for the DOA estimation problem exploits the signal subspace of the received data, and the most remarkable are the Estimation of Signal Parameter via Rotational Invariance Techniques (ESPRIT) and the Multiple Signal Classification (MUSIC) [75]. The ESPRIT first performs an eigendecomposition of the samples CM, retaining the same number of orthonormal eigenvectors as the number of observed sources. Then, it splits these eigenvectors in different subsets (representing the array subdivision in multiple subarrays), and exploits the CM rotation. Instead, the MUSIC splits the CM space in signal and noise subspaces, and exploits their mutual orthogonality to identify the DOA which maximises the array response to the impinging signal. Generally, the subspace methods are considered hyper-resolution techniques, for their high-level accuracy, and they are more computationally efficient than the statistics one.

The subspace parameter estimation algorithms are considered in this work, as they are more accurate than the optimum beamformers and more computationally efficient than the statistical parameter estimation techniques. In addition, they allow to detect multiple uncorrelated sources simultaneously, and this is a key aspect in surveillance radars, whenever multiple objects can cross the receiver FoV simultaneously, as during a survey application, a fragment cloud observation, or a proximity operation monitoring . In more detail, the thesis deals with the DOA estimation problem by using MUSIC algorithm [76] [77], as it does not need regularly shaped receiver arrays (differently from ESPRIT) and, so, it can have a more general application. Furthermore, the study presented in [78] assesses MUSIC as the most

promising hyper-resolution algorithm.

3.2 Data Model

Consider the case of a source detected by a planar rectangular array of $M = N_x \times N_y$ uniformly distributed elements and with physical spacing d_x and d_y.
Let $\Delta\gamma_1$ and $\Delta\gamma_2$ denote the two angular deviations relative to the LOS (in azimuth and elevation respectively), according to their definition in Sec. 2.1. From [79], the direction cosines corresponding to the DOA are:

$$\begin{aligned} u &= \sin\Delta\gamma_1 \cos\Delta\gamma_2 \\ v &= \sin\Delta\gamma_2 \end{aligned} \tag{3.1}$$

The planar wave on a generic position $\boldsymbol{r}$ can be written as $E(t) = Ae^{j(\omega t - k\boldsymbol{r}\cdot\boldsymbol{u})}$ where $k = 2\pi/\lambda$ is the wave number and $\boldsymbol{u}$ is the unit vector of the impinging DOA.
From [80], the distances measured in wavelength are:

$$\begin{aligned} d_{x_\lambda} &= \frac{d_x}{\lambda} \\ d_{y_\lambda} &= \frac{d_y}{\lambda} \end{aligned} \tag{3.2}$$

After having defined the electric angles as:

$$\begin{aligned} \phi_x &= 2\pi d_{x_\lambda} u \\ \phi_y &= 2\pi d_{y_\lambda} v \end{aligned} \tag{3.3}$$

it is possible to write the steering vector corresponding to the m-th line of sensors (where $m = 0 : N_y - 1$) as

$$\boldsymbol{a}_m(\Delta\boldsymbol{\gamma}) = \begin{bmatrix} e^{-jm\phi_y} \\ e^{-j(\phi_x + m\phi_y)} \\ \vdots \\ e^{-j((N_x-1)\phi_x + m\phi_y)} \end{bmatrix} \tag{3.4}$$

where the bold notation $\boldsymbol{a}_m(\Delta\boldsymbol{\gamma})$ indicates that the steering vector indirectly depends on the vectorial parameter $\Delta\boldsymbol{\gamma} = [\Delta\gamma_1\,,\,\Delta\gamma_2]^T$. By stacking the steering vectors corresponding to the lines of the array, it is possible to define the $M \times 1$ steering vector ($M = N_x \times N_y$) as

$$\boldsymbol{a}(\Delta\boldsymbol{\gamma}) = \begin{bmatrix} \boldsymbol{a}_0(\Delta\boldsymbol{\gamma}) \\ \vdots \\ \boldsymbol{a}_{N_y-1}(\Delta\boldsymbol{\gamma}) \end{bmatrix} \tag{3.5}$$

Then, the signal received by the array at any time instant can be expressed as:

$$\boldsymbol{x}(t) = \boldsymbol{a}(\Delta\boldsymbol{\gamma})\, s(t) + \boldsymbol{n} \tag{3.6}$$

where $s(t)$ is the envelope of the signal emitted by the source and impinging on the array, and $\boldsymbol{n}$ is the process noise.

If N_s sources are detected simultaneously, Eq. 3.6 can be generalised as:

$$\boldsymbol{x}(t) = \sum_{z=1}^{N_s} \boldsymbol{a}(\Delta\boldsymbol{\gamma}_z)\, s_z(t) + \boldsymbol{n} \tag{3.7}$$

Based on $\boldsymbol{x}(t)$, the signal Covariance Matrix (CM) can be computed as:

$$\boldsymbol{R}_{\boldsymbol{xx}} = E\left[\boldsymbol{x}(t)\boldsymbol{x}(t)^H\right] \tag{3.8}$$

where $E[\cdot]$ is the expected value operator and $\boldsymbol{x}(t)^H$ is the hermitian of $\boldsymbol{x}(t)$.

In the discrete time domain, N_k is considered as the number of samples integrated to generate one single CM. For the k-th sample, $\boldsymbol{a}(\Delta\boldsymbol{\gamma})$, $s(t)$ and $\boldsymbol{n}$ can be expressed as $\boldsymbol{a}(\Delta\boldsymbol{\gamma})_k$, s_k and $\boldsymbol{n}_k$ respectively, and Eq. 3.6 becomes:

$$\boldsymbol{x}_k = \boldsymbol{a}(\Delta\boldsymbol{\gamma})_k\, s_k + \boldsymbol{n}_k \tag{3.9}$$

In this way, the discrete CM derived from integrating the N_k samples can be expressed as:

$$\widehat{\boldsymbol{R}}_{\boldsymbol{xx}} = \frac{1}{N_k} \sum_{k=1}^{N_k} \boldsymbol{x}_k \boldsymbol{x}_k^H \tag{3.10}$$

3.3 Multiple Signal Classification algorithm

Ideally, without any noise contribution, the $\boldsymbol{R_{xx}}$ rank is equal to the signal sources number N_s. In real scenarios instead, which are affected by noise, $\boldsymbol{R_{xx}}$ shows N_s eigenvalues much larger than the other $M - N_s$. Therefore, it is possible to split $\boldsymbol{R_{xx}}$ space in signal and noise subspaces, which are assumed to be orthogonal (based on the assumption that signal and noise are uncorrelated). Denoting the largest eigenvalues matrix as $\boldsymbol{\Lambda_s}$ and the corresponding eigenvectors subspace as $\boldsymbol{U_s}$ and, similarly, indicating noise subspace matrices as $\boldsymbol{\Lambda_n}$ and $\boldsymbol{U_n}$, the CM can be decomposed as:

$$\boldsymbol{R_{xx}} = \boldsymbol{U_s}\boldsymbol{\Lambda_s}\boldsymbol{U_s}^H + \boldsymbol{U_n}\boldsymbol{\Lambda_n}\boldsymbol{U_n}^H \tag{3.11}$$

MUSIC method [76] [77] assumes that $\boldsymbol{U_s}$ and $\boldsymbol{U_n}$ span orthogonal complements and it can be proved that $\boldsymbol{U_s}\boldsymbol{\Lambda_s}\boldsymbol{U_s}^H$ has $M - N_s$ eigenvalues equal to zero.
The estimate $\boldsymbol{\Delta\gamma}$ can thus be computed through the maximisation of the following spectrum, which represents the array response to the impinging wave:

$$P(\boldsymbol{\Delta\gamma}) = \boldsymbol{a}(\boldsymbol{\Delta\gamma})^H \boldsymbol{U_s}\boldsymbol{U_s}^H \boldsymbol{a}(\boldsymbol{\Delta\gamma}) \tag{3.12}$$

An alternative formulation is obtained by considering that $\boldsymbol{U_n}^H \boldsymbol{a}(\boldsymbol{\Delta\gamma}) = 0$. Due to the orthogonality between signal and noise subspaces, the estimate $\boldsymbol{\Delta\gamma}$ can be computed through the maximisation of the following spectrum:

$$P(\boldsymbol{\Delta\gamma}) = \frac{1}{\boldsymbol{a}(\boldsymbol{\Delta\gamma})^H \boldsymbol{U_n}\boldsymbol{U_n}^H \boldsymbol{a}(\boldsymbol{\Delta\gamma})} \tag{3.13}$$

or by considering that $\boldsymbol{U_n}\boldsymbol{U_n}^H = \boldsymbol{I} - \boldsymbol{U_s}\boldsymbol{U_s}^H$ (where $\boldsymbol{I}$ is a $M \times M$ identity matrix), through:

$$P(\boldsymbol{\Delta\gamma}) = \frac{1}{\boldsymbol{a}(\boldsymbol{\Delta\gamma})^H \left[\boldsymbol{I} - \boldsymbol{U_s}\boldsymbol{U_s}^H\right] \boldsymbol{a}(\boldsymbol{\Delta\gamma})} \tag{3.14}$$

Finally, the sensor directional properties can be taken into account by introducing a tapering action $\Upsilon_s(\boldsymbol{\Delta\gamma})$ on the total array response:

$$\Gamma(\boldsymbol{\Delta\gamma}) = P(\boldsymbol{\Delta\gamma})\, \Upsilon_s(\boldsymbol{\Delta\gamma}) \tag{3.15}$$

In this work no tapering action is considered, and MUSIC algorithm is applied based on Eq. 3.14.

3.4 Ambiguous solutions

A fundamental condition must be met to have a unique solution of Eq. 3.14, that is:

$$\begin{aligned} \frac{d_x}{\lambda} &\leq \frac{1}{2} \\ \frac{d_y}{\lambda} &\leq \frac{1}{2} \end{aligned} \tag{3.16}$$

Eq. 3.16 is analogous in space-domain to the Shannon theorem: the spacing between samples of the signal, which is provided by the array elements position, must be lower than the half-distance between the sinusoidal peaks, that is the half-wavelength [80]. As a consequence, if the spacing is longer than half-wavelength, spatial ambiguity (aliasing) occurs and so grating lobes appear. The shift of the i-th (in direction E-W) and j-th (in direction N-S) grating lobe with respect to the boresight, expressed in direction cosines space (Eq. 3.17) is:

$$\begin{aligned} u &= \frac{i}{d_{x_\lambda}} \\ v &= \frac{j}{d_{y_\lambda}} \end{aligned} \tag{3.17}$$

where d_{x_λ} and d_{y_λ} are defined in Eq. 3.2.
According to Eq. 3.1, it is possible to express such a shift in angular coordinates as:

$$\begin{aligned} \Delta\theta_x &\approx \arcsin \frac{i}{d_{x_\lambda}} \\ \Delta\theta_y &= \arcsin \frac{j}{d_{y_\lambda}} \end{aligned} \tag{3.18}$$

which holds as long as $\Delta\theta_y$ (that is the angular shift, in direction N-S, of the j-th grating lobe with respect to the boresight) is small, which allows the approximation $\cos \Delta\theta_y \approx 1$.
Given this problem, ad-hoc solutions shall be identified for the DOA estimation ambiguities, by possibly exploiting problem geometry and pass predictions. In this framework, the MUSIC Approach for Track Estimate and Refinement (MATER) algorithm has been developed. As the name suggests, the algorithm core is composed of two steps: track estimate,

performed with MUSIC, and track refinement, where clustering, regression and ambiguity solving criteria are adopted. The way MATER algorithm processes data depends whether an a-priori information of the target pass is available or not, that is in the catalogued and the uncatalogued case, respectively

3.5 MATER - Catalogued case

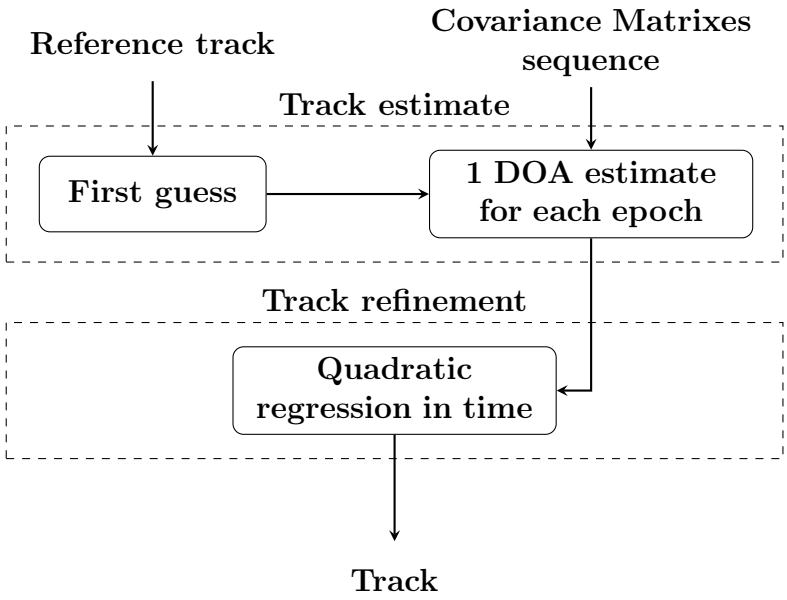

Figure 3-1: MATER: catalogued case flowchart.

In the case the observed object is catalogued, MATER processes observation data as illustrated in Fig. 3-1. In the track estimate phase, the DOA is estimated, time by time, from the CM eigendecomposition, thanks to an optimisation process aimed at maximising Eq. 3.14. The reference track (derived from pass prediction) can directly be used as first guess in the optimisation, such that the DOA corresponding to the closest peak is selected. In this way, if the first guess is sufficiently close to the actual DOA (i.e. if the a-priori orbital estimate is sufficiently accurate), the DOA ambiguity is solved, as reported in the sensor FoV in Fig. 3-2a for a generic LEO pass. Then, after a quadratic regression in time for the two angular coordinates separately, a single track is eventually obtained, as represented in Fig. 3-2b.

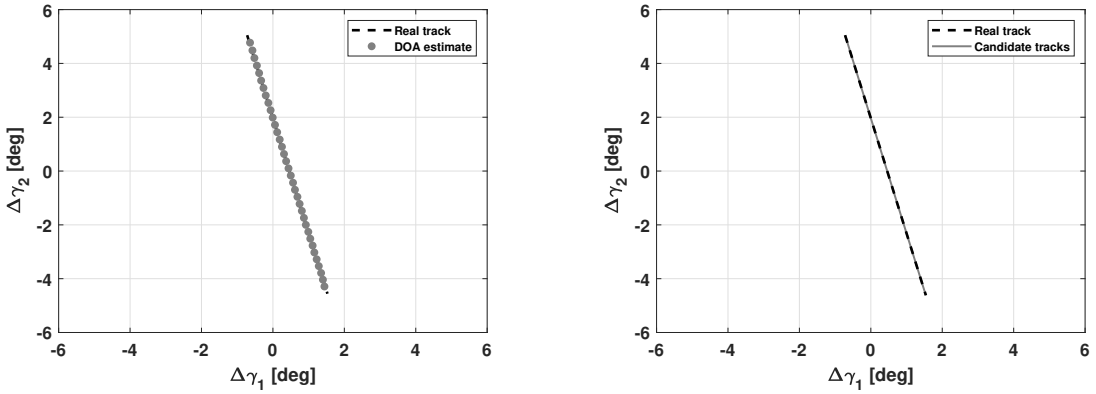

(a) Track estimate phase result.

(b) Track refinement phase result.

Figure 3-2: MATER: catalogued case results.

At this point, the track can be used to refine the orbital state of the observed object according to the ROD procedures described in Sec. 2.5.2. Usually, this is done after having transformed the angular profile $\Delta\gamma_1(t)$ and $\Delta\gamma_2(t)$ in topocentric azimuth and elevation, according to the relationship discussed in Sec. 2.1.

3.6 MATER - Uncatalogued case

For the uncatalogued case (i.e. when the detected measurements do not correlate to any catalogued object) no pass prediction is available. In this case, track shall be reconstructed based on acquired measurements only. In this framework, Sec. 3.6.1 and Sec. 3.6.2 present two ways to reconstruct track if the CMs are the only input, at a post-processing and at a signal-processing level respectively. Then, Sec. 3.6.3 presents the MATER version for the uncatalogued case if additional measurements can be exploited, that is either SR, or DS, or both of them.

3.6.1 Maximum Occurrence Criterion

If, in the uncatalogued case, no additional measurement is available and just the angular path can be used to solve the ambiguity, the maximum occurrence criterion can be applied, according to the assumption that the correct track is the one spending the longest time in the sensor FoV and, so, it is expected to spend significant time in a central region of it. This procedure is represented in Fig. 3-3.

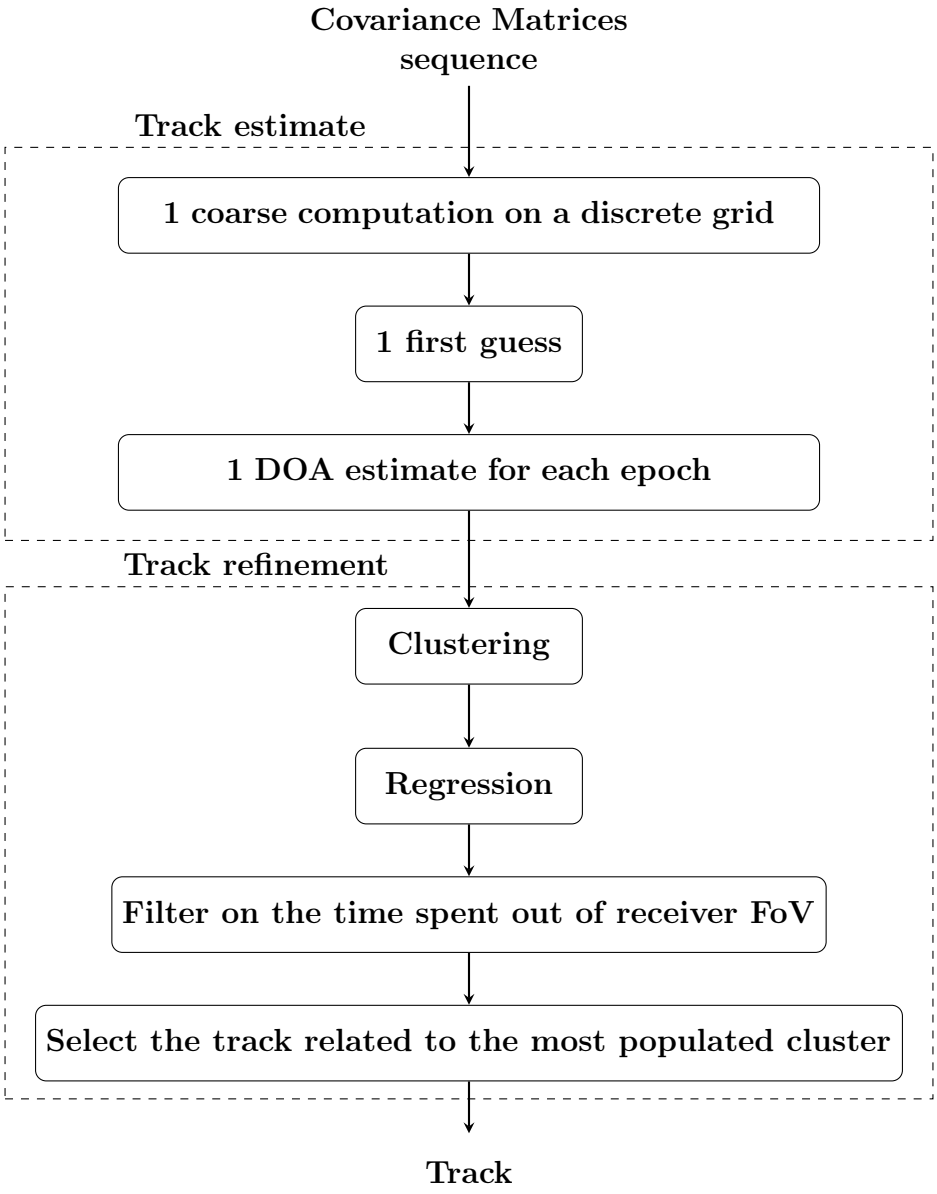

Figure 3-3: MATER: uncatalogued case flowchart with no additional measurement and maximum occurrence criterion application.

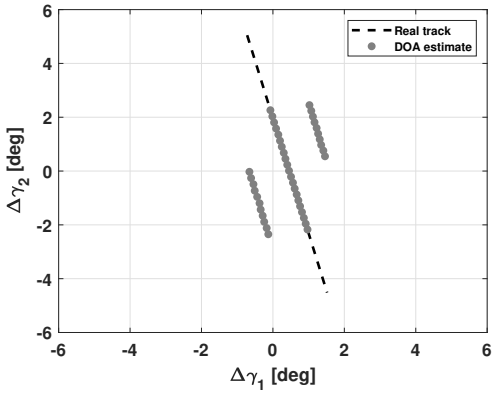

(a) Track estimate phase result.

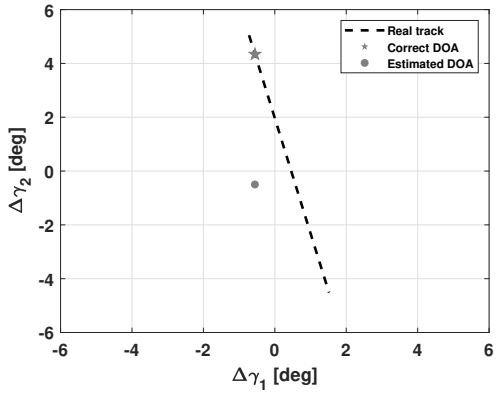

(b) Possible wrong DOA estimation.

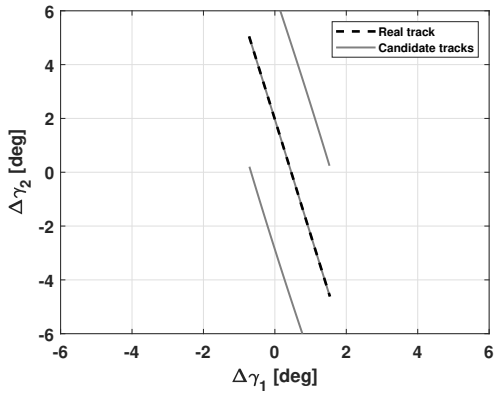

(c) Track refinement phase candidates.

Figure 3-4: MATER: uncatalogued case results obtained with no additional measurement solved with the maximum occurrence criterion.

Based on the above assumption, in the track estimate phase a weighting action is applied to favour the central peaks of the array response. So, in a first coarse grid computation, only the angular coordinates corresponding to the maximum peak are selected and are used as first guesses for the maximisation process of Eq. 3.14. In this way, multiple track candidates are expected to appear at the end of the track estimation phase, as represented in Fig. 3-4a. It is possible to observe that, when the source is in a border region of the receiver FoV, the algorithm converges to a more central ambiguous solution, like in Fig. 3-4b.

In order to identify the multiple candidates, the track refinement phase starts by clustering the DOAs according to a RANdom SAmple Consensus (RANSAC) process, which iteratively performs a regression among a data subset, distinguishing inliers from outliers. In this phase, clusters that do not satisfy a population threshold are discarded. At the end, a quadratic regression in time is performed on the two angular coordinates for each cluster,

such that time-dependent profiles $\Delta\gamma_1(t)$ and $\Delta\gamma_2(t)$ are obtained for all candidates, as represented in Fig. 3-4c.

At this point, multiple track candidates are present and the unfeasible solutions can be rejected first. Considering the $[-6, +6]$ deg FoV represented in Fig. 3-4c, the correct track is not expected to spend significant time out of that region, as it is unlikely that the receiver array detects signal while the source is out of the FoV. Therefore, a threshold on the maximum percentage of time spent out of this FoV shall be respected (5% in this work).

Finally, among the survived tracks, the one related to the most populated cluster is selected. This represents the result of the process and corresponds to the one represented in Fig. 3-2b, which can be later used for OD purposes.

As stated above, this approach assumes that the source spends most of the pass in the central part of the sensor FoV. Consequently, it is worth remarking that it can hardly solve ambiguities for objects crossing the FoV close to the border, as it favours central solutions.

3.6.2 Delta-k technique

From Eq. 3.18 it is evident that signals at different frequencies (and, so, experiencing different sampling) exhibit different angular shifts of the ambiguous DOA estimation with respect to the correct one. Hence, it is possible to distinguish between the correct DOA estimation by comparing data processed at two different frequencies. This leads to an extension of the so called *delta-k* technique (also known as *split-spectrum* or *split-bandwidth* method), which was developed for synthetic aperture radar (SAR) applications to determine the absolute value of the unwrapped phase directly from the data, without any a-priori information [81] [82].

Delta-k technique for signal DOA estimation in multireceiver radars

The *delta-k* technique consists in splitting the range bandwidth $[f_- \; f_+]$ centred in f_0 into two subbands in the processor and processing each individually, like as represented in Fig. 3-5. Further *delta-k* technique applications in SAR problems are present in [83] and in [84]. The same method is applied in [85] and in [86] to compensate the ionospheric delay. Such a technique is here adapted to the DOA ambiguity problem for multi-receivers radars, as

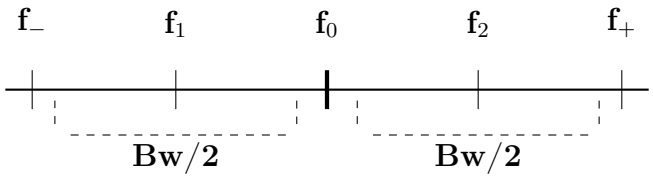

Figure 3-5: Signal bandwidth subdivision for the *delta-k* technique. From the original bandwidth [f_- f_+] centered in f_c, two subbands are created (dashed lines) centered in f_1 and f_2.

follows.

Let's generalise Eq. 3.18 for any coordinate as:

$$\Delta\theta = \arcsin \frac{m\,\lambda}{d} \tag{3.19}$$

where d is the generic physical distance among array elements and m the generalisation of i and j indexes. Let's now consider f_1 and f_2 as the frequencies of two unmodulated continuous waves reflected from the same source. For each frequency, Eq. 3.19 describes the angular shift $\Delta\theta_1$ and $\Delta\theta_2$ of the m-th ambiguity with respect to the correct DOA and their mutual difference is:

$$|\Delta\theta_2 - \Delta\theta_1| = \left|\arcsin \frac{m\,\lambda_2}{d} - \arcsin \frac{m\,\lambda_1}{d}\right| \tag{3.20}$$

Therefore, by using any two frequencies (no matter their characteristics) and comparing the two DOA estimations, it is theoretically possible to identify the correct solution, as it shall show the same angular location, unlike the ambiguous ones, which are expected to be differently located in the angular FoV.

However, in real applications, the validity of this conclusion is affected by the presence of noise, which causes an angular shift $\Delta\theta_n > 0$, no matter the estimation is correct or ambiguous. Thus, in order to distinguish the correct DOA from the ambiguous ones, it is necessary that $|\Delta\theta_2 - \Delta\theta_1| > \Delta\theta_n$, that is:

$$\left|\arcsin \frac{m\,\lambda_2}{d} - \arcsin \frac{m\,\lambda_1}{d}\right| > \Delta\theta_n \tag{3.21}$$

Equation 3.21 can be expressed in terms of frequencies as:

$$\left|\arcsin\left(\frac{m\,c}{d\,f_2}\right) - \arcsin\left(\frac{m\,c}{d\,f_1}\right)\right| > \Delta\theta_n \tag{3.22}$$

where c is the speed of light. Equation 3.22 relates analytically the two frequencies f_1 and f_2 needed to obtain an angular shift of the ambiguous solutions larger than $\Delta\theta_n$, i.e. larger than the angular shift induced by the noise. Thanks to this relationship, the correct DOA can be identified even in real applications, by first identifying an angular shift $\Delta\theta_\tau$ which is expected to be larger than $\Delta\theta_n$, and then selecting f_1 and f_2 accordingly.

MATER - Delta-k technique

The MATER algorithm workflow which embeds the *delta-k* technique is reported in Fig. 3-6. It starts performing the track estimate phase on the two CM sequences (related to the two frequencies at which they are constructed). First a coarse computation is performed on a grid of angular coordinates, aimed at identifying the highest N_p peaks of the pattern obtained from Eq. 3.14. The peaks searching is performed by identifying the global maximum first. Then, the other $N_p - 1$ peaks coordinates are determined analytically, according to the angular shift of Eq. 3.18. These N_p angular coordinates pairs represent the first guess for the maximisation process of Eq. 3.14. Thus, N_p angular positions in the receiver FoV are identified at each epoch. As a consequence, multiple DOA sequences appear in the sensor FoV for both frequencies, among which only one is correct and can be identified as the one related to the best matching between the two frequencies trends (see Fig. 3-7a). Then, in the track refinement phase, the correct signal DOA is identified at each epoch by selecting the estimation exhibiting the minimum angular deviation and the other solutions are discarded. This results in a FoV less populated of DOAs estimations, as represented in Fig. 3-7b (where just the estimations along the correct track are present).

The next steps are similar to the ones of Sec. 3.6.1. The estimations are clustered according to a RANSAC algorithm and the quadratic regression in time, for the two angular coordinates separately, is performed. If multiple clusters are still present, the algorithm discards those related to tracks which spend too much time out of the receiver FoV. Among the survived tracks, the one related to the most populated cluster is selected. This represents

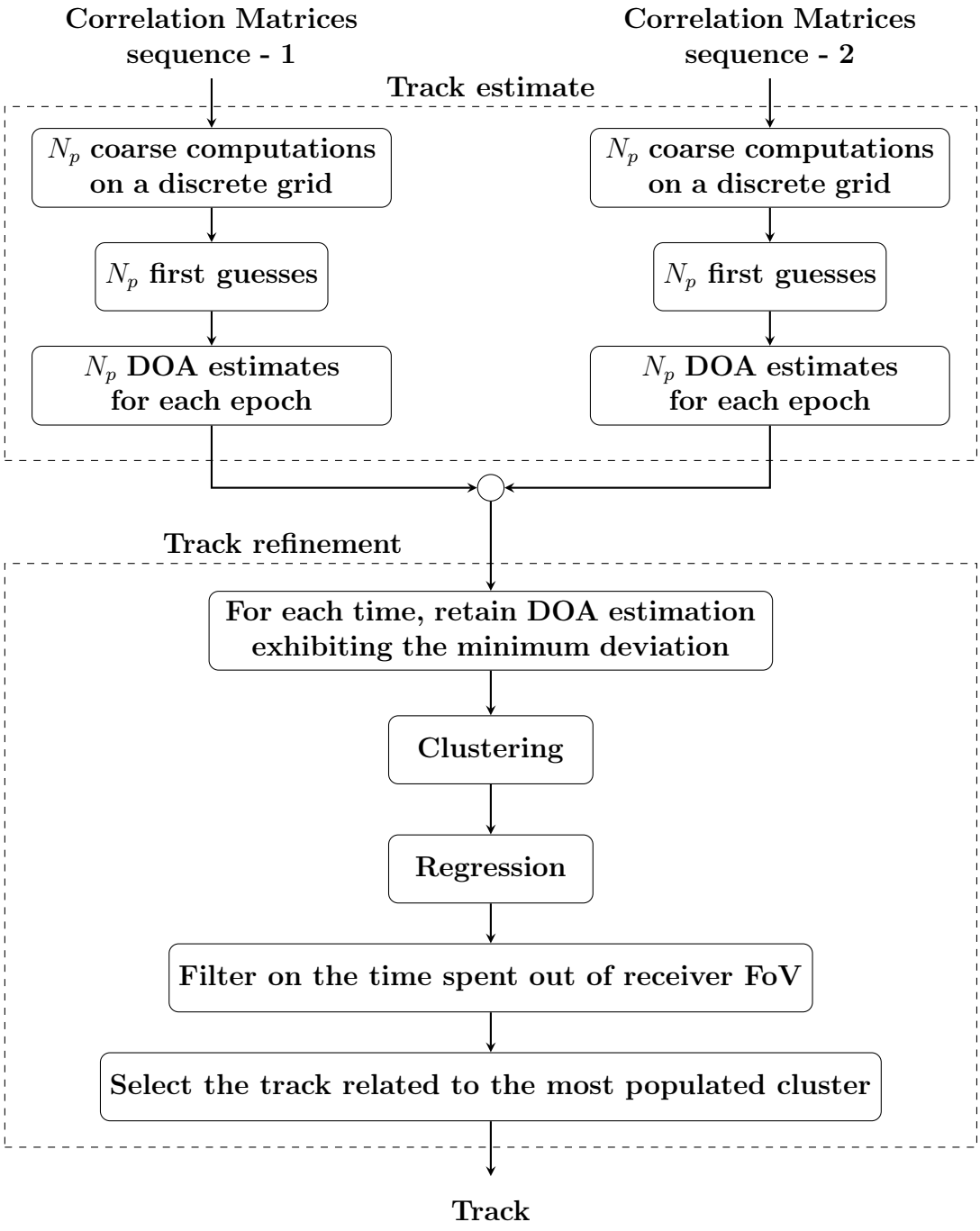

Figure 3-6: MATER: uncatalogued case flowchart with no additional measurement and *delta-k* technique application.

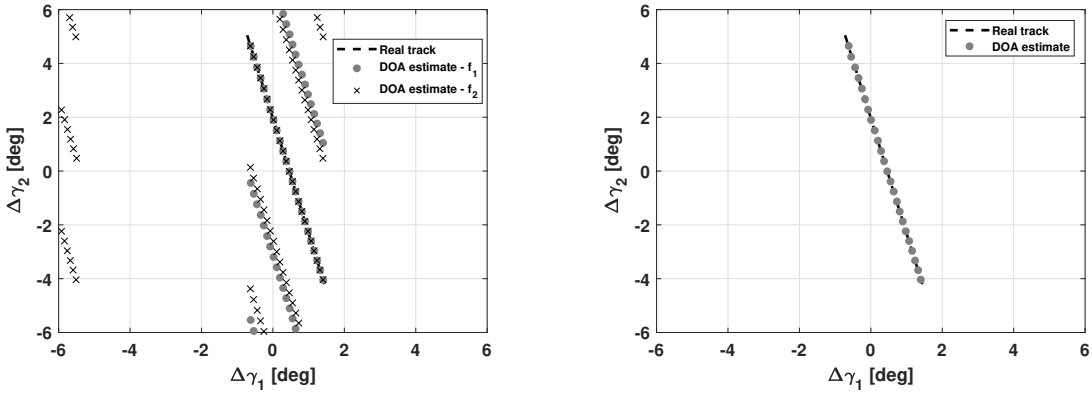

(a) Track estimate phase result.

(b) DOA ambiguity solved.

Figure 3-7: MATER: uncatalogued case results obtained with no additional measurements solved with the *delta-k* technique.

the result of the process and corresponds to the one represented in Fig. 3-2b, and can be later used for OD purposes.

It is important to highlight that, differently from the maximum occurrence criterion and from those criteria which exploit additional measurements, the *delta-k* technique acts at a signal processing level, and this, in the practical applications, would set design constraints in the signal processing chain.

3.6.3 Methods based on additional measurements

MATER can possibly exploit additional measurements (either SR, or DS, or both of them) to solve the angular track ambiguity as follows. First, a coarse computation on a discrete grid is performed, analogously to the one in Sec. 3.6.2, returning N_p angular positions in the receiver FoV, later refined through the maximisation of Eq. 3.14. Consequently, N_p angular positions in the receiver FoV are identified at each epoch, as represented in Fig. 3-9a.

Similarly to Sec. 3.6.1, in the track refinement phase both the RANSAC clustering and the quadratic regression in time, for the two angular coordinates separately, are performed. At the end, time-dependent profiles $\Delta\gamma_1(t)$ and $\Delta\gamma_2(t)$ are obtained for all the candidates, as represented in Fig. 3-9b. It can be noticed that some side points present in Fig. 3-9a do not have any related track, since they form clusters which do not satisfy the population threshold and they have been rejected.

Then, the algorithm discards the clusters related to tracks which spend too much time out

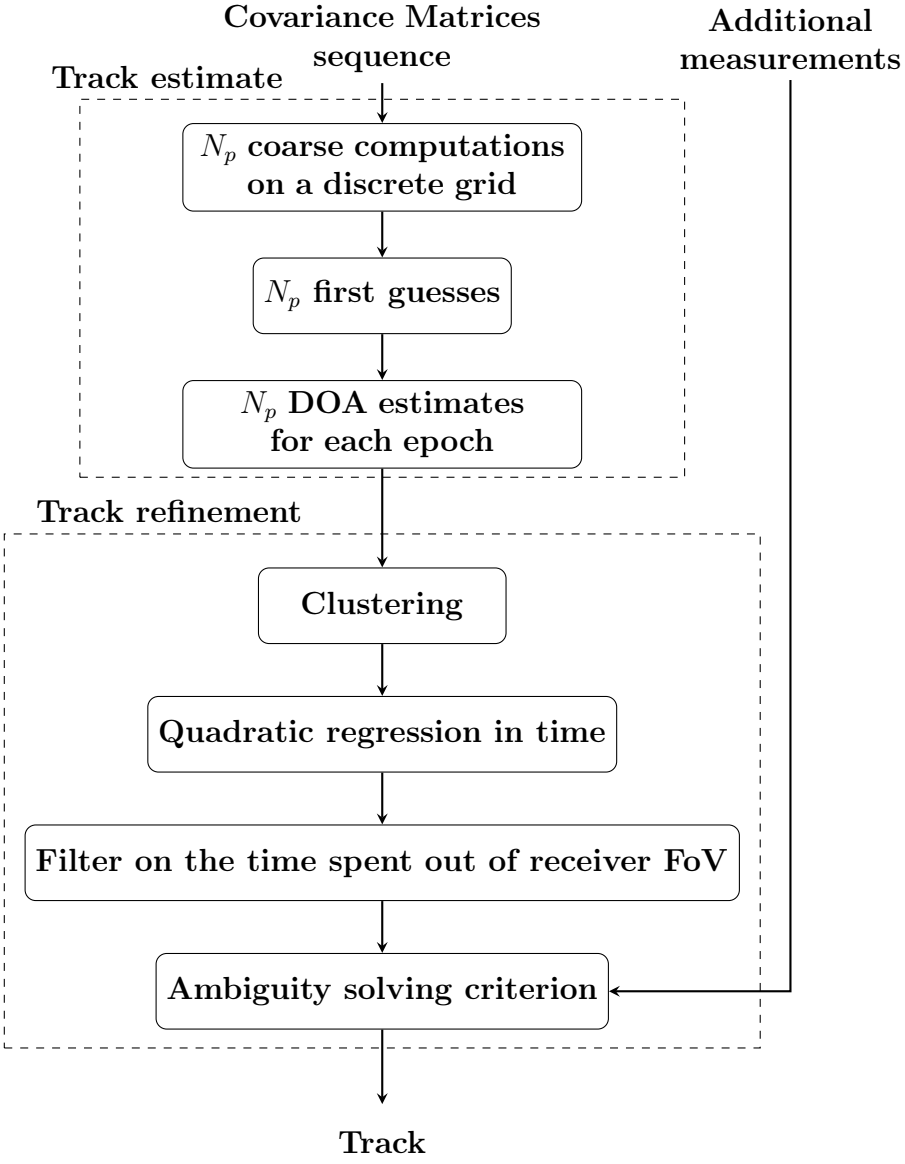

Figure 3-8: MATER: uncatalogued case flowchart with additional measurements.

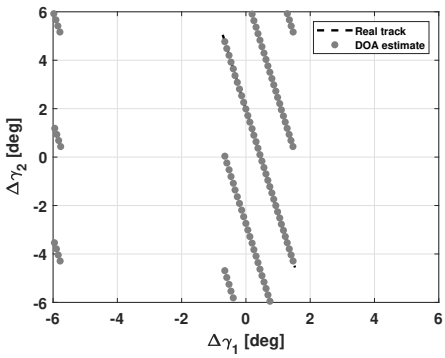

(a) Track estimate phase result.

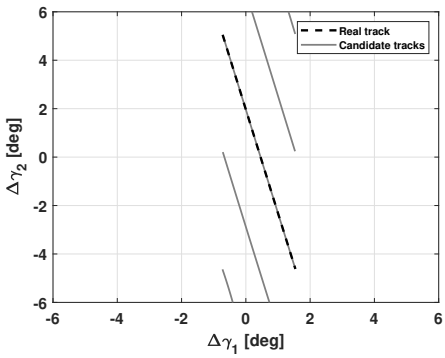

(b) Track refinement phase candidates.

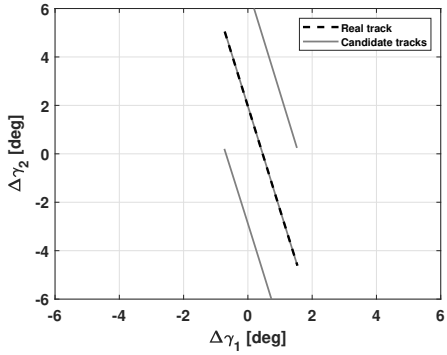

(c) Track refinement phase feasible candidates.

Figure 3-9: MATER: uncatalogued case results obtained with additional measurements.

of the receiver FoV. The result is shown in Fig. 3-9c, where it can be observed that some track candidates have been rejected. At this point, multiple candidates may still appear (like in Fig. 3-9c) and proper criteria must be applied to solve the ambiguity and select the correct solution. Four procedures have been investigated to this purpose, which are applied depending on the available additional measurements.

The first one is the OD-based criterion, according to which the correct track is the one generating the orbit featuring the best correlation to the measurements. Each track candidate enters an IOD process (according to the procedure described in Sec. 2.5.3): an orbital state estimate is obtained and the associated correlation index is computed through the Eq. 2.21 and, in general, as illustrated in Sec. 2.5.1. Finally the best candidate is selected.

The second procedure is the SNR criterion, according to which the correct track is the one whose predicted SNR profile best matches the measured one. The predicted SNR is derived in Eq. 2.16, where P_{rx} and N are defined in Eq. 2.14 and Eq. 2.15 respectively, and all the involved parameters are described in Sec. 2.4. Since, in Eq. 2.14, the values of G_{rx}, G_{tx}, ρ_{TX} and ρ_{RX} depend on the relative position between the observed object and the ground stations, the predicted SNR profiles computed from the candidate tracks are expected to significantly differ one from another and this makes the SNR criterion theoretically robust. In order to apply this criterion, a RCS value must be assumed and it possibly introduces a bias term in the difference between the measured SNR and the predicted one. However, this term affects all the candidates equally and it does not have an impact on the validity of the criterion. To determine G_{rx}, G_{tx}, ρ_{TX} and ρ_{RX}, the orbital state for each candidate shall be determined, and, for this purpose, the radar IOD procedure described in Sec. 2.5.3 is used, which can be applied even if only either SR or DS measurements are available. Indeed, in the latter case, SR is computed from DS, observation epochs and track angles, and this also allows to derive the terms ρ_{TX} and ρ_{RX}.

The third procedure is the SR criterion: the correct track is the one which, combined with DS and according to the procedure described in Sec. 2.5.3, returns the predicted SR profile that best matches the measured one. This criterion provides a straightforward process to solve the ambiguity, although it needs both SR and DS measurements.

Regardless the approach adopted, the track obtained at the end of the process is the same as the one reported in Fig. 3-2b and can enter an IOD process. It is important to point out that, for the SNR and OD solving criteria, the IOD is already performed during the

ambiguity solving phase.

Chapter 4

MATER applied to single source observations

A numerical analysis is here conducted to test MATER algorithm performance. All the simulations were implemented in MATLAB [87] and run with an Intel(R) Core(TM) i7-8700 CPU @ 3.20 GHz - 3.19 GHz processor. BIRALES sensor, introduced in Sec. 1.4.3 and described in Sec. 1.5, is taken as reference, as its back-end allows to record raw data and, so, to work in post-processing, partially attenuating the operational drawback of the computational demand of the adaptive beamforming approach. In addition, it is a ground-based multi-receiver radar, used for SST-related applications, which does not fulfil the requirement expressed in Eq. 3.16 and so the MATER ambiguity solving criteria can be tested. BIRALES characteristics are further detailed in Sec. 4.1.

A first analysis in Sec. 4.2 assesses MATER performance in a nominal scenario, both for the catalogued and the uncatalogued case. In the latter situation, all the ambiguity solving criteria introduced in Sec. 3.6 are evaluated. Then, a sensitivity analysis is conducted in Sec. 4.3 to test MATER robustness to different transmitter and receiver pointing, detected signal interruption, lower transmitted power, RCS fluctuations, different sampling frequency, mismatching between the actual RCS and the one used to predict the SNR, as well as to a real signal scenario. In such a sensitivity analysis, both SNR criterion and *delta-k* technique are used to solve the ambiguity.

Afterwards, Sec. 4.4 applies MATER algorithm to the Re-entry Analysis and the Collision Avoidance services, introduced in Sec. 1.4. Finally, a real application of MATER algorithm

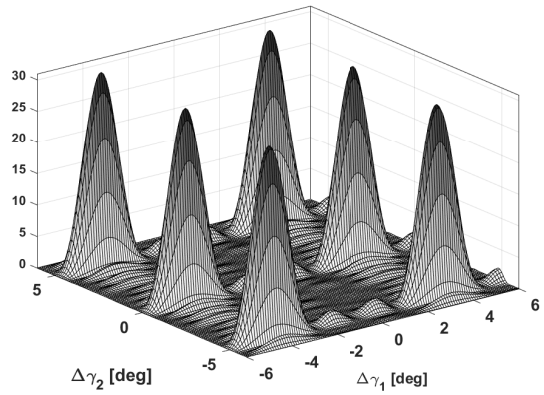

Figure 4-1: BIRALES array response based on MUSIC for a single source observation.

is presented in Sec. 4.5.

4.1 BIRALES data

Based on the BIRALES characteristics presented in Sec. 1.5 and referring to the data model described in Sec. 3.2, the number of array elements results in: $M = N_x \times N_y = 32$, being $N_x = 4$ and $N_y = 8$. Thus, $\boldsymbol{a}(\boldsymbol{\Delta\gamma})$ dimension is 32×1 and $\widehat{\boldsymbol{R}}_{\boldsymbol{xx}}$ size is 32×32, regardless the snapshot number N_k.

As mentioned above, BIRALES does not fulfil the requirement expressed in Eq. 3.16, being $\lambda = 0.73$ m, $d_x = 5.67$ m and $d_y = 10$ m. This generates an ambiguity in the array response to the impinging signal and multiple peaks (that is multiple DOA solutions) are simultaneously present at any epoch, as represented in Fig. 4-1, which shows MUSIC output for a $N_s = 1$ source observation. $\Delta\gamma_1$ and $\Delta\gamma_2$ represent the angular deviation with respect to the receiver LOS, as discussed in Sec. 2.1. Since the receiver pointing can be moved along the local meridian (that is in elevation only), $\Delta\gamma_1$ and $\Delta\gamma_2$ turn out to represent the East-West and the North-South directions respectively. The peaks lobes are larger along $\Delta\gamma_1$, as the East-West direction has less receivers than the North-South one (4 against 8), and this theoretically makes DOA estimation more accurate along the $\Delta\gamma_2$ direction. The mutual angular distance among these peaks is defined according to Eq. 3.18.

Concerning the signal processing criterion for the ambiguity resolution, Eq. 3.22 can be evaluated by considering the euclidean distance $d = \sqrt{(d_{E-W}^2 + d_{N-S}^2)} = 11.5$ m and two given frequencies. Figure 4-2 reports the angular shift of the ambiguous solution (in degree)

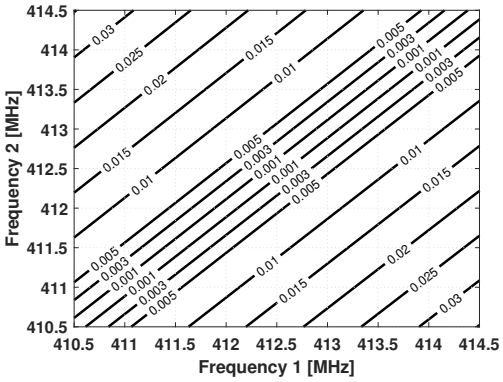

Figure 4-2: Angular shift of the ambiguous solution (in degree) for a given frequencies couple.

provoked by a given frequency couple between 410.5 MHz and 414.5 MHz. The two central frequencies involved in the *delta-k* technique for the multireceiver radars are set to 411.5 MHz and 413.5 MHz. From Fig. 4-2 (also appreciable in Eq. 3.22), this frequency choice provokes an angular shift of the ambiguous estimations of 0.017 deg.

BIRALES FoV, presented in Sec. 1.5, is extended to $[-6, +6]$ deg, in order to keep all the significant signal contributions. An equivalent temperature T_{eq} of 86 K is then considered.

Concerning Eq. 2.14, the carrier frequency f_c is set equal to 410 MHz, which is the CW signal currently used for the multibeam, but when the *delta-k* technique is applied. In this latter case, Eq. 2.14 is evaluated for both of the central frequencies involved in the computations (that is 411.5 MHz and 413.5 MHz).

4.2 Numerical Nominal Analysis

A synthetic data set (taken from [41]) composed of 899 passes related to 537 LEO objects from the NORAD catalogue [52] is analysed. The analysis considers an observation window of one week, from December 15^{th} to December 21^{th}, 2018. The passes projections in the measurements space provide their nominal angular tracks, SR and DS measurements. The transmitter and receiver pointing angles, provided in terms of azimuth and elevation are set to [7.69, 40.45] deg and [0, 60] deg respectively. According to [41], this configuration allows the observations to cover most objects and the angular tracks to spread over the entire receiver FoV.

Then, the data for the testing procedure are generated as follows:

- The measured SNR is simulated according to Eq. 2.14, Eq. 2.15 and Eq. 2.16, with a 1e+05 W transmitted power, a RCS of 1 m^2 and the addition of Gaussian noise (standard deviation of 0.5 dB) to include the effect of the RCS fluctuation. Focusing on Eq. 2.15, besides the 86 K equivalent temperature mentioned above, a 1 kHz sampling frequency f_s is selected, which is equal to the receiver channel bandwidth Bw.

- The measured SR and DS, derived from the synthetic data set, are artificially corrupted with a Gaussian noise coherent with the sensor accuracy, that is 30 m and 10 Hz respectively.

According to the 1 KHz f_s selected, one CM is created along the pass each 0.1 s (the integration time) with $N_k = 100$ snapshots, through the implementation of the formulas reported in Sec. 3.2, and the mean snapshot epoch is taken as the DOA estimation epoch. Thus, the half of the integration time theoretically bounds the angular error in the DOA estimation (without considering the noise effect), depending on the relative velocity and on the relative distance between the station and the observed target. The angular error generated by the integration time resolution is then mediated by the clustering and the regression phases, where the outliers are rejected.

Starting from these data, MATER is run and the performance is assessed in terms of convergence rate and of median value (that is the 50-th percentile) η between all the root mean square errors (RMSEs) of the data set, each of them computed as:

$$\mathrm{RMSE} = \sqrt{\frac{1}{N}\sum\left(\Delta\gamma - \overline{\Delta\gamma}\right)^2} \tag{4.1}$$

for the two angular coordinates separately. $\overline{\Delta\gamma}$ stands for the correct angular position and N is the number of the observation epochs. The quantity η is computed only on the cases where MATER successfully converged to the solution. Then, the mean value of the correlation index, indicated as $\overline{\zeta}$, is usually computed as an additional metrics, according to Eq. 2.21.

First of all, MATER is run by assuming that all the objects are catalogued, i.e. an a-priori estimate of their orbit is available. The results are summarised in Tab. 4.1, which reports the success rate (in percentage), $\eta_{\Delta\gamma_1}$ and $\eta_{\Delta\gamma_2}$ (in degree) and $\overline{\zeta}$. The algorithm was able to converge in all the cases. In addition, the low values of angular error and correlation

Success [%]	$\eta_{\Delta\gamma_1}$ [deg]	$\eta_{\Delta\gamma_2}$ [deg]	$\overline{\zeta}$
100	7.5e-03	1.0e-02	9.0e-02

Table 4.1: Catalogued case: statistical analysis on synthetic data.

index confirm the accurate performance of MATER in the catalogued objects observation. Although the solution along $\Delta\gamma_2$ might be expected to be finer (as discussed in Sec. 4.1), it presents a slightly larger RMSE. This is due to the length of the angular path travelled during the integration time, as the estimated DOA can correspond to any actual value assumed in the meanwhile. Since most of the data set passes correspond to high-inclination orbits, the angular path travelled in the North-South direction is usually larger than the one travelled in the East-West one and this makes the angular RMSE larger along $\Delta\gamma_2$ than along $\Delta\gamma_1$. A detailed computational demand analysis is beyond the purpose of this work, given the current prototype implementation in MATLAB [87], but it can be quantified in less than 10 s per track by using a single core with an Intel(R) Core(TM) i7-8700 CPU @ 3.20 GHz - 3.19 GHz processor.

Then, MATER is applied on the same passes in uncatalogued mode, i.e. by assuming that no a-priori orbital estimates of the objects are available. The results are reported in Tab. 4.2. Each row in the table provides the performance obtained by one of the different solving criteria introduced in Sec. 3.6. For both the SNR and the OD criteria, the brackets in the first column specify which measurement is available to solve the ambiguity. The correlation index $\overline{\zeta}$ is not reported for the criteria which solve the ambiguity without performing orbit determination (as no additional measurement is available), that is the maximum occurrence and the *delta-k* method criteria.

Focusing on the success rate, it is possible to note that the *delta-k* method and the SNR criteria present a 100% success rate. On the contrary, the uncertainty introduced by the integration time, coupled with the random noise associated to SR and DS profiles, makes the OD-based criteria less robust. Multiple solutions featuring similar correlation indexes may occur, and the wrong solution may feature a better correlation index. Furthermore, this problem affects more the procedure when only DS is available, as the noisy DS profile affects the SR reconstruction process (see Sec. 2.5.3): multiple SR profiles tend to match the measured one and a wrong solution may happen to provide the best matching, and the same problem affects the SR criterion. All these ambiguities are solved by the SNR criterion,

Criterion	Success [%]	$\eta_{\Delta\gamma_1}$ [deg]	$\eta_{\Delta\gamma_2}$ [deg]	$\overline{\zeta}$
Max Occ.	98.1	7.0e-03	1.0e-02	-
Delta-k	100	6.9e-03	1.0e-02	-
OD (SR)	98.4	6.9e-03	1.0e-02	8.2e-02
OD (DS)	98.1	6.9e-03	1.0e-02	5.5e-01
SNR (SR)	100	6.9e-03	1.0e-02	8.2e-02
SNR (DS)	100	6.9e-03	1.0e-02	2.8e-01
SR	98.0	7.5e-03	1.0e-02	1.4e-01

Table 4.2: Uncatalogued case: statistical analysis on synthetic data. Each row is related to one of the different solving criteria introduced in Sec. 3.6: Max Occ. stands for the maximum occurrence criterion, Delta-k for the *delta-k* method criterion, OD (SR) and OD (DS) for the OD-based criterion when SR is available and when DS is available respectively, SNR (SR) and SNR (DS) for the SNR criterion when SR is available, and SR stands for SR criterion.

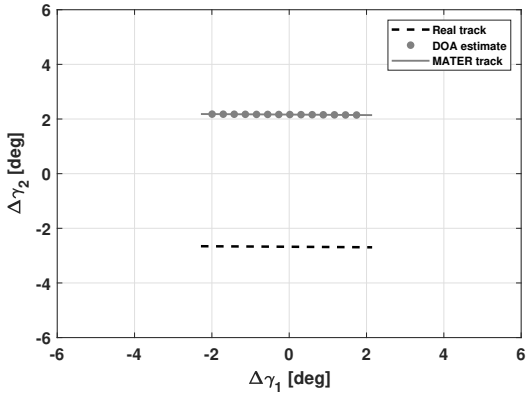

Figure 4-3: Uncatalogued case: erroneous track result in the maximum occurrence criterion, due to DOAs erroneously estimation. The algorithm converges to a more central ambiguous solution.

which better exploits the pass geometry and turns out to be very robust.

Concerning the maximum occurrence criterion, its failure cases regard passes spending significant time in FoV side regions. A failure case of the maximum occurrence cluster criterion is represented in Fig. 4-3.

Overall, the median angular RMSE is comparable to the catalogued case one, and is a bit lower in the E-W direction ($\eta_{\Delta\gamma_1}$) than in the N-S one ($\eta_{\Delta\gamma_2}$). Another general consideration is that the mean correlation index $\overline{\zeta}$, when available, is comparable to the one of the catalogued case, and it increases for those orbit determinations performed by reconstructing the SR from DS. Concerning the computational demand, MATER takes between 2 min and 3 min (depending on the track length), but when the maximum occurrence or the *delta-k*

technique based criteria are used. In these cases, no OD is performed, and this makes the former criterion faster. However the *delta-k* technique needs a double DOAs sequence estimation, and this increases the computational time remarkably. All these evaluations were performed with the same processor as above, by using a single core.

Figure 4-4 represents the empirical cumulative distribution function of the angular RMSE on the entire data set, both in terms of $\Delta\gamma_1$ and $\Delta\gamma_2$, for the catalogued and the uncatalogued cases, the latter with all the ambiguity solving criteria analysed. All of them share a similar remarkably non-Gaussian trend, and it may be noticed that Fig. 4-4d presents much larger RMSE maxima. Indeed, for that case ambiguous and correct tracks are very close each other, and the SR criterion converges to a wrong candidate, but the angular RMSE is so small that the reconstructed angular track is still compliant. It can be also observed that the $\Delta\gamma_2$ CDF is always below the $\Delta\gamma_1$ one, but for the extremely small RMSE values: it means that, although $\Delta\gamma_1$ errors are generally smaller than the $\Delta\gamma_2$ ones (as commented above about Tab. 4.1 and Tab. 4.2), the angular estimation along $\Delta\gamma_2$ can reach a finer accuracy than the one along $\Delta\gamma_1$, and this is due to the resolution, which is higher along the former direction.

To sum up, based on the statistical analysis performed with the numerical tests, the track reconstruction problem can be solved for both catalogued and uncatalogued objects. In the latter case, the SNR criterion turns out to be the most reliable one, together with the *delta-k* method (which does not need additional measurements). The OD-based and the SR criteria provide good success rates, although they featured some failures, as like as the maximum occurrence criterion. However, this last method tends to fail for passes close to the FoV border.

4.3 Numerical Sensitivity Analysis

A sensitivity analysis of MATER performance is carried out in this section. In particular, the analysis aims at testing algorithm robustness, both in terms of track estimate and track refinement phases, especially in the solution of the track ambiguity problem. The uncatalogued case is investigated, as it allows to carry out a more complete analysis than the catalogued one. To solve the ambiguity, both the *delta-k* criterion and the SNR one with measured SR are exploited, as they represent the optimal ways to select the proper track

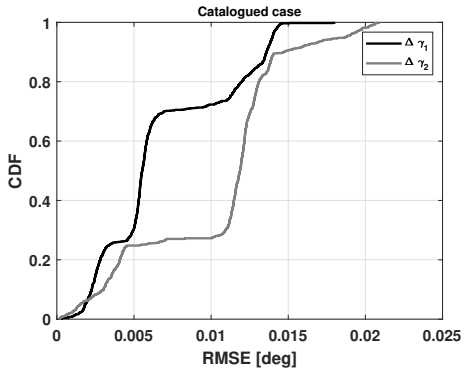

(a) Catalogued case.

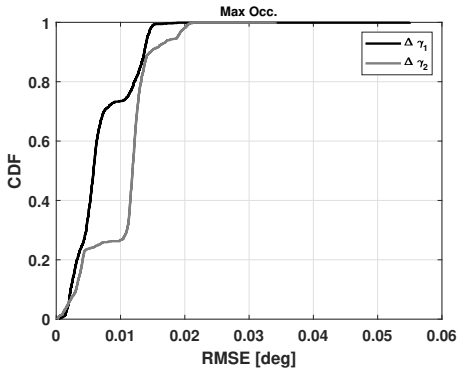

(b) Uncatalogued case: maximum occurrence criterion.

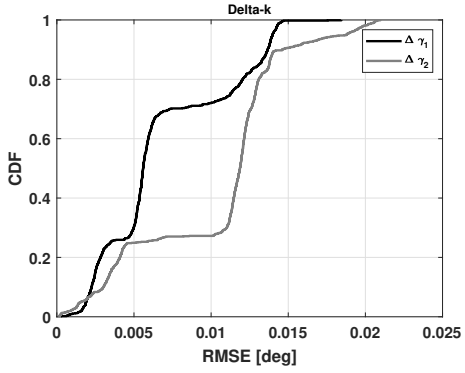

(c) Uncatalogued case: *delta-k* criterion.

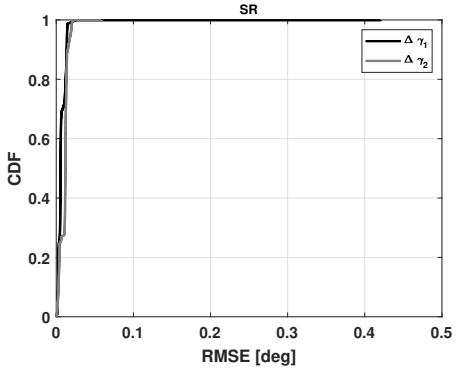

(d) Uncatalogued case: SR criterion.

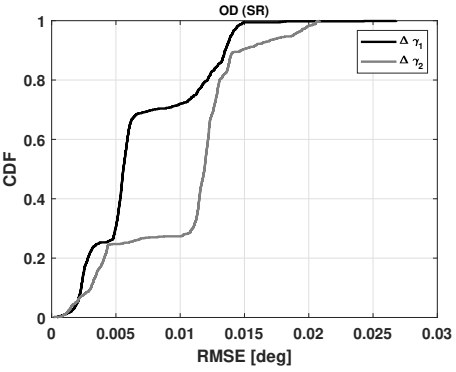

(e) Uncatalogued case: OD criterion (with SR).

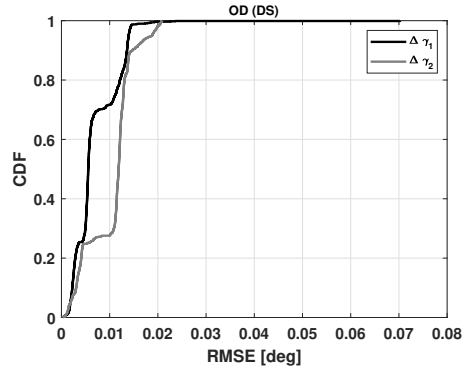

(f) Uncatalogued case: OD criterion (with DS).

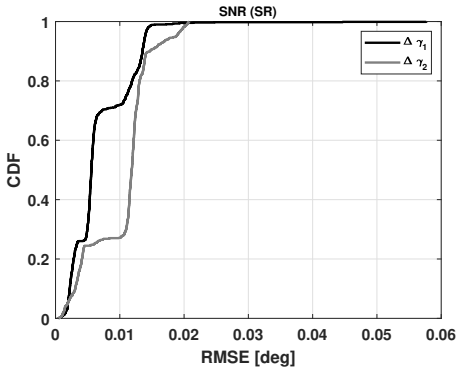

(g) Uncatalogued case: SNR criterion (with SR).

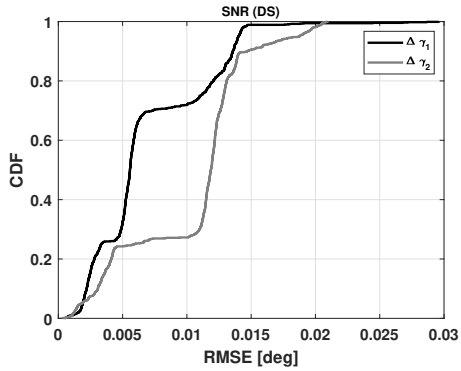

(h) Uncatalogued case: SNR criterion (with DS).

Figure 4-4: Empirical cumulative distribution functions of the angular RMSE on the entire data set, both for $\Delta\gamma_1$ and $\Delta\gamma_2$.

(according to the numerical analysis shown in Sec. 4.2).

The same data set of 899 simulated passes is generally used hereafter and the off-nominal scenarios in which the sensitivity analysis is performed are listed as follows:

- *Different TX and RX pointing directions*: this is modelled by simulating observations in which BIRALES receiver points towards 45N (azimuth 0 deg and elevation 45 deg) and 90 (elevation 90 deg). Indeed, it is fundamental to investigate if performances vary for different pointing elevation. For this analysis, data sets for 45N and 90 pointing, of 493 and 361 passes respectively, corresponding to an observation window of 1 day (May 20^{th}, 2021), are used. This is the only case in which the data sets differ from the one of 899 passes.

- *Interruption of the detected signal, both for SNR, SR and DS*: this is simulated by randomly subtracting a certain percentage (10%, 20% and 50%) of measurements, such that, for those instants, the CM is built based on noise only. Signal interruption may occur for different reasons, such as the target tumbling motion or a possible interference.

- *Lower transmitted power*: this is simulated by modifying the transmitted power from 1e+05 W to 1e+04 W, 5e+03 W and 1e+03 W. According to Eq. 2.14, this makes the signal less distinguishable from the noise and, so, decreases the percentage of detected passes (a further quantity evaluated in the analysis). A decrease in transmitted power can be either planned (decided by the operator), or unexpected (for instance, a sudden

decrease in the electric feed).

- *RCS fluctuations* (due to target tumbling, for instance): this is simulated by modifying the standard deviation of the measured SNR additional Gaussian noise from 0.5 dB to 1 dB, 2 dB and 5 dB, following an analogous analysis presented in [41].

- *Different sampling frequency*: as commented above, the MATER performance depends on the integration time and, so, on the sampling frequency acquisition. So, the sampling frequency is modified from 1 kHz to 500 Hz, 2 kHz and 10 kHz, and the integration time is modified accordingly, as detailed later.

- *Mismatching between the actual RCS and the one used to predict the SNR (in the SNR criterion only)*: this is modelled by modifying the RCS adopted for the prediction from 1 m^2 to 0.1 m^2, 5 m^2 and 10 m^2. The RCS used to solve the ambiguity through SNR criterion is instead kept fixed to the nominal value of 1 m^2. The *delta-k* method criterion is not applied to this case.

Referring to Tab. 4.3, it is possible to notice that MATER performances are not altered by the pointing direction. On the contrary, Tab. 4.4 and Tab. 4.5 show that the algorithm accuracy (in terms of $\eta_{\Delta\gamma_1}$ and $\eta_{\Delta\gamma_2}$) deteriorates for increasing signal interruption rate (with the appearance of 3 failure cases in the 50% interruption, for the SNR criterion) and, moreover, for decreasing transmitted power. In this latter scenario, also the percentage of detected passes (with respect to the original 899 transits data set) is reported, and the smaller the transmitted power, the weaker the signal impinging the receiver array, the lower the number of detected objects. On the one hand, the detection percentage decrease is more remarkable in applying the *delta-k* technique (as two different signals are involved and only the instants when both of them are detectable can be retained), on the other hand such an ambiguity solving method always guarantees the convergence to the correct solution. Comparing Tab. 4.5 with Tab. 4.2, it can be further observed that the deterioration in $\Delta\gamma_1$ is much larger than in $\Delta\gamma_2$ one. Indeed, the effect of the SNR decrease on the accuracy of the angular estimate is strongly linked to the resolution, which is higher along $\Delta\gamma_2$ direction, as it owns more receivers. Consequently, $\Delta\gamma_1$ tends to be more affected than $\Delta\gamma_2$. Figure 4-5 shows that the lower the SNR level, the broader the error distribution, coherently with the resolution relationship.

Pointing [deg]	Success [%]	$\eta_{\Delta\gamma_1}$ [deg]	$\eta_{\Delta\gamma_2}$ [deg]	$\overline{\zeta}$
SNR criterion (SR)				
45 N	100	7.5e-03	1.2e-02	7.5e-02
90 N	100	7.0e-03	1.9e-02	8.1e-02
***delta-k* method criterion**				
45 N	100	9.3e-03	1.3e-02	-
90 N	100	7.3e-03	1.9e-02	-

Table 4.3: Uncatalogued case: statistical analysis on synthetic data by considering different pointing directions.

Interruption [%]	Success [%]	$\eta_{\Delta\gamma_1}$ [deg]	$\eta_{\Delta\gamma_2}$ [deg]	$\overline{\zeta}$
SNR criterion (SR)				
10	100	8.7e-03	1.2e-02	1.2e-01
20	100	1.2e-02	1.5e-02	1.8e-01
50	99.7	1.9e-02	2.3e-02	4.4e-01
***delta-k* method criterion**				
10	100	7.4e-03	1.2e-02	-
20	100	8.6e-03	1.3e-02	-
50	100	1.6e-02	2.0e-02	-

Table 4.4: Uncatalogued case: statistical analysis on synthetic data by varying the percentage of the pass in which no signal is detected.

TX Power [W]	Success [%]	Detection [%]	$\eta_{\Delta\gamma_1}$ [deg]	$\eta_{\Delta\gamma_2}$ [deg]	$\overline{\zeta}$
SNR criterion (SR)					
1e+04	64.2	99.8	5.2e-03	1.3e-02	7.8e-02
5e+03	55.6	97.7	6.0e-03	1.3e-02	9.7e-02
1e+03	90.0	10.5	3.1e-02	3.0e-02	1.1e-01
***delta-k* method criterion**					
1e+04	100	99.4	1.1e-02	1.1e-02	-
5e+03	100	93.9	1.3e-02	1.2e-02	-
1e+03	100	5.6	1.1e-02	1.8e-02	-

Table 4.5: Uncatalogued case: statistical analysis on synthetic data by varying the transmitted power.

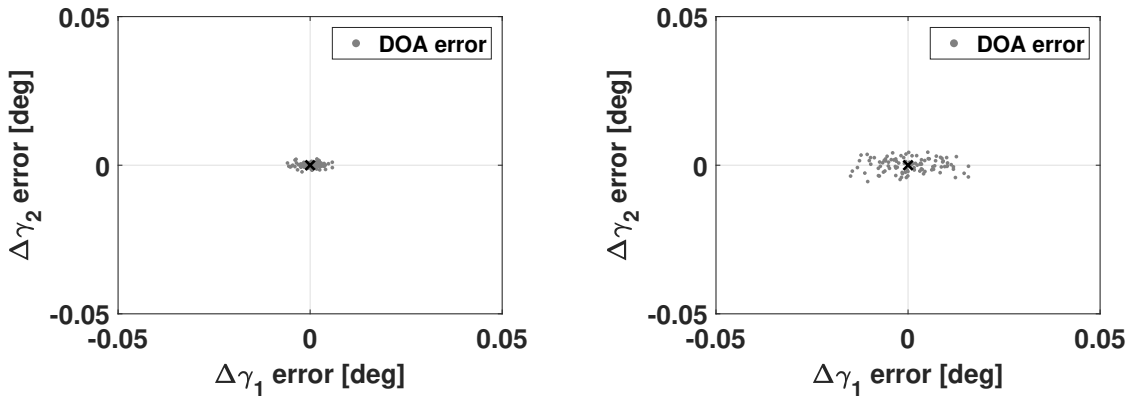

(a) SNR = 15 dB

(b) SNR = 5 dB

Figure 4-5: Signal DOA error distribution for two SNR levels. Each sample is related to a CM computed with differently distributed noise, whose mean and standard deviation do not change. It can be noticed that the smaller the SNR level, the broader the error distribution, with a larger elongation along $\Delta\gamma_1$ than along $\Delta\gamma_2$, coherently with the resolution relationship.

On average, this effect induces an angular error comparable to the one linked to the integration time, and this smooths out the accuracy difference between the two coordinates shown in Tab. 4.2.

Table 4.6 reports the sensitivity analysis results by varying the sampling frequency: 500 Hz, 2000 Hz and 10000 Hz. To keep the same number of samples per integration as adopted in the nominal analysis ($N_k = 100$), the integration time is modified accordingly: 0.2 s for 500 Hz, 0.05 s for 2000 Hz and 0.01 s for 10000 Hz. From Tab. 4.6 it can be observed that, generally, the larger the sampling frequency, the finer the angular estimation, and this can be linked to the smaller integration time used. However, the smaller the integration time, the larger the computational demand, as more and more DOAs shall be estimated. Furthermore, an increase in the sampling frequency leads to an increase in the receiver bandwidth (that is to the noise term in Eq. 2.16), which attenuates the percentage of the detected signal and makes the SNR profile more noisy. The former effect is visible for the *delta-k* method criterion, as some targets are not observed in the 10000 Hz case, while the latter affects the SNR criterion, which presents oscillating performance by increasing the sampling frequency.

The RCS fluctuations slightly deteriorate the results, but both of the criteria result to be robust, as reported in Tab. 4.7. Finally, the RCS mismatching case, regarding the SNR

Sampling frequency [Hz]	Success [%]	Detection [%]	$\eta_{\Delta\gamma_1}$ [deg]	$\eta_{\Delta\gamma_2}$ [deg]	$\overline{\zeta}$
SNR criterion (SR)					
5e+02	100	100	1.5e-02	2.1e-02	1.5e+00
2e+03	100	100	7.4e-03	9.0e-03	1.2e-01
1e+04	100	100	1.3e-02	1.4e-02	1.7e-01
***delta-k* method criterion**					
5e+02	100	100	1.5e-02	2.1e-02	-
2e+03	100	100	5.8e-03	8.1e-03	-
1e+04	100	99.7	4.6e-03	5.2e-03	-

Table 4.6: Uncatalogued case: statistical analysis on synthetic data by varying the sampling frequency.

Fluctuations [dB]	Success [%]	$\eta_{\Delta\gamma_1}$ [deg]	$\eta_{\Delta\gamma_2}$ [deg]	$\overline{\zeta}$
SNR criterion (SR)				
1	100	6.8e-03	1.0e-02	8.2e-02
2	100	6.9e-03	1.0e-02	8.2e-02
5	100	7.5e-03	1.1e-02	8.6e-02
***delta-k* method criterion**				
1	100	6.9e-03	1.0e-02	-
2	100	7.1e-03	1.0e-02	-
5	100	1.1e-02	1.1e-02	-

Table 4.7: Uncatalogued case: statistical analysis on synthetic data by varying the considered RCS fluctuations.

criterion only (as commented above), is reported in Tab. 4.8. It is possible to appreciate that the SNR criterion turns out to be fully robust to RCS mismatching.

To recap, the sensitivity analysis shows that MATER is quite robust to off-nominal conditions, and both the SNR and the *delta-k* method criteria confirm to be a reliable approach to solve the ambiguity problem. Major limitations may arise for transmitted power decrease, as the signal impinging the array is less intensive. A larger sampling frequency enhances the DOA estimation precision, as, keeping fixed the number of samples used to generate the CM, the integration time (and so the related time uncertainty) can be reduced. However, besides the larger computational demand, it leads to an increase of the receiver noise, which can possibly deteriorate both the detection capability and the estimation quality.

Actual RCS [m^2]	Success [%]	$\eta_{\Delta\gamma_1}$ [deg]	$\eta_{\Delta\gamma_2}$ [deg]	$\overline{\zeta}$
SNR criterion (SR)				
0.1	100	7.9e-03	1.0e-02	9.3e-02
5	100	6.8e-03	1.0e-02	8.1e-02
10	100	6.8e-03	1.0e-02	8.2e-02

Table 4.8: Uncatalogued case: statistical analysis on synthetic data by varying the actual RCS of the observed object. The RCS used in SNR criterion is kept fixed to the nominal value of 1 m^2.

Real signal

For the sake of completeness, the following analysis focuses on a test case in which the CMs are computed synthetically, while the SNR used to simulate the signal in Eq. 3.9 is derived from a real satellite pass. This analysis is conducted as an intermediate step between synthetic simulations and real observation. Similarly to the sensitivity analysis, this section deals with the uncatalogued case by applying the *delta-k* method and the SNR criteria, the latter with measured SR.

The selected scenario is the re-entry of the Chinese launcher CZ-5B R/B core stage occurred in May 2021. This re-entry event was monitored by EUSST and BIRALES contributed to this observation campaign. In particular, the pass of May 5^{th}, 2021 at 02:18:53 a.m. (UTC), is here analysed. The object was transiting southwards from the receiver, at an elevation of 37.1 deg. This was below the receiver minimum mechanical elevation of 42 deg (see Sec. 1.5) and so an electronic steering was exploited. The transmitter pointing was 40.8 deg in azimuth and 42.1 deg in elevation. This pass is selected because it is a real worst case scenario. Indeed, the object flies at low elevation with respect to the receiver and the signal exhibits strong variations and regularly repeating peaks due to the uncontrolled tumbling motion of the target. The recorded signal is reported in Fig. 4-6. Overall, about 58.2 % of the pass produce no SNR, which is more than the worst case scenario analysed in the previous section.

This varying signal produces frequent failures in the DOA estimation, as illustrated in Fig. 4-7a, which shows the output of the track estimation phase. It is possible to notice that the estimates are spread over the entire FoV, except for those instants corresponding to a high intensity signal. Then, the track refinement phase is performed: the DOAs are clustered, their regression is performed and the ambiguity solving criterion is applied. In this way,

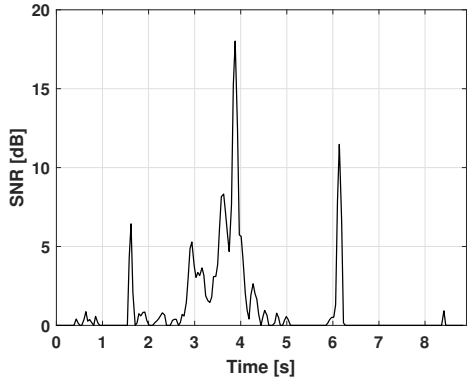

Figure 4-6: Real SNR profile of the CZ-5B R/B pass observed by BIRALES on the 5$^{\text{th}}$ of May 2021. The strongly varying signal and the regularly repeating peaks are due to the uncontrolled tumbling motion of the target.

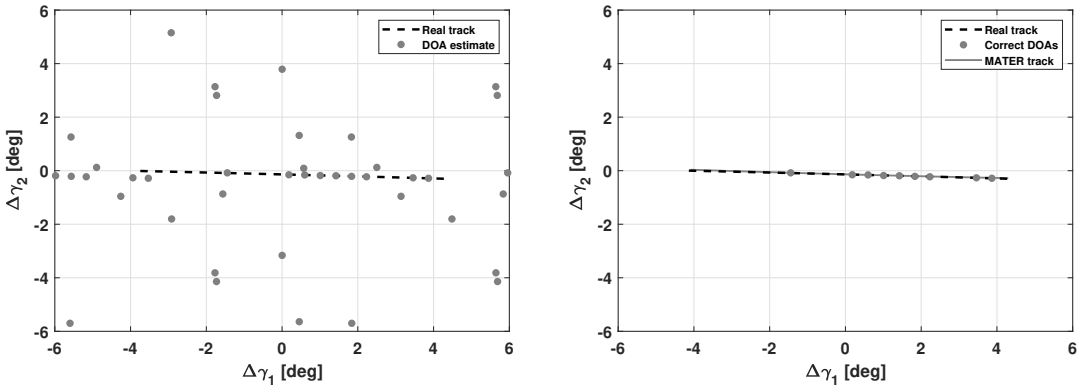

(a) Track estimate phase result.

(b) Track refinement phase result.

Figure 4-7: MATER applied to the real SNR profile of the CZ-5B R/B pass observed by BIRALES on the 5$^{\text{th}}$ of May 2021. Figure 4-7b also represents the correct DOAs used for the final regression.

$\eta_{\Delta\gamma_1}$ [deg]	$\eta_{\Delta\gamma_2}$ [deg]	$\overline{\zeta}$
SNR criterion (SR)		
1.6e-02	4.0e-02	1.6e-01
***delta-k* method criterion**		
6.0e-02	5.8e-02	-

Table 4.9: MATER results related to the real SNR profile of the CZ-5B R/B pass observed by BIRALES on the 5$^{\text{th}}$ of May 2021.

MATER provides the track reported in Fig. 4-7b, together with the correct DOAs identified by solving the ambiguity and then used for the final regression.
The analysis results are reported in Tab. 4.9. It is possible to notice that, for both of the solving criteria, $\eta_{\Delta\gamma_1}$ and $\eta_{\Delta\gamma_2}$ are comparable: indeed, the path along E-W direction is larger than the one along the N-S one, but the DOA estimations used to derive the angular track are too few to appreciate a larger error along the former direction. Overall, there is a deterioration in the track reconstruction accuracy with respect to Tab. 4.2, and this is due to the noisy DOA estimates. Yet, especially considering the relevant noise of the SNR measurements, MATER provides a reasonably accurate track estimate.

4.4 SST services numerical simulations

Given the nominal and the sensitivity analyses provided in Sec. 4.2 and Sec. 4.3, MATER algorithm is tested on numerical simulations regarding SST services. In particular, the Re-entry Analysis and Collision Avoidance services are investigated, as they are related to the single source observation.

4.4.1 Re-entry

During the re-entry, the object experiences a very highly perturbed environment, as it flies at low altitudes, where both the air drag and the gravitational harmonics are extremely effective. This makes the pass prediction unreliable and, especially for the last phases, may force the observation to be lead in an uncatalogued mode, that is without exploiting the pass prediction. For this reason, it is fundamental to assess what is the difference between

A_{aer}/m [m^2/kg]	A_{rad}/m [m^2/kg]	Cd [-]	Cr [-]
5.9e-03	5.9e-03	2.2	2.2

Table 4.10: Physical parameters of the reentering object.

carrying out the re-entry monitoring in the catalogued and in the uncatalogued way, in terms of both orbit determination and angular accuracy (that is just for what concerns MATER algorithm).

The selected synthetic scenario reproduces the observation campaign of the Chinese launcher CZ-5B R/B occurred in May 2021 and already introduced in Sec. 4.3. The analysis simulates the observations carried out by BIRALES in the ten days before the re-entry epoch, and all the physical parameters of the reentering object (reported in Tab. 4.10) are assumed to be known.

To reproduce the re-entry, the object last available TLE from [13] is taken and numerically propagated up to the re-entry epoch (according to the high-fidelity propagator described in Sec. 2.2). Then, the state at the re-entry epoch is back-propagated (in the same manner as before) for the previous ten days, such that the target states from April 29^{th}, 2021 up to May 09^{th}, 2021 are computed. BIRALES observations are simulated on this time window.

First, the process is run considering the MATER catalogued case: the signal DOA estimation is performed by giving the pass prediction as first guess in the optimisation of Eq. 3.14, and the angular track is derived as described in Sec. 3.5. The computed angular measurements are joint to the SR and DS ones, to which a Gaussian noise is associated with a standard deviation retrieved from BIRALES accuracy (30 m and 10 Hz, for SR and DS respectively). Then, a ROD process based on a Non-linear Least Squares with a-priori estimation (as presented in Sec. 2.5.2) is performed, embedding the high-fidelity propagation.

Observation epoch [UTC]	$RMSE_{\Delta\gamma_1}$ [deg]	$RMSE_{\Delta\gamma_2}$ [deg]	ζ -	Pos. Err. [km]	Vel. Err. [km/s]
29-Apr-2021 03:32:47	2.7e-02	3.7e-03	1.2e-01	3.3e-03	3.5e-03
29-Apr-2021 05:07:09	5.8e-02	2.4e-03	1.1e-01	7.2e-03	2.6e-03
29-Apr-2021 06:41:13	4.7e-02	4.9e-03	1.3e-01	9.1e-03	2.5e-03

30-Apr-2021 03:27:05	3.4e-02	3.9e-03	1.2e-01	4.1e-04	4.4e-03
30-Apr-2021 05:01:11	6.1e-02	1.5e-04	1.3e-01	3.6e-03	3.9e-03
30-Apr-2021 06:35:11	3.8e-02	4.6e-03	1.2e-01	9.5e-03	1.1e-02
01-May-2021 01:44:40	1.6e-02	2.8e-03	1.2e-01	5.9e-04	3.1e-03
01-May-2021 03:19:14	4.1e-02	4.2e-03	1.2e-01	6.2e-04	1.2e-03
01-May-2021 04:53:08	6.0e-02	2.3e-03	1.4e-01	6.9e-03	2.4e-03
01-May-2021 06:27:05	3.1e-02	4.1e-03	1.3e-01	1.3e-03	1.3e-03
02-May-2021 01:34:56	2.0e-02	2.8e-03	1.2e-01	1.4e-03	9.1e-03
02-May-2021 03:09:10	4.8e-02	4.1e-03	1.2e-01	2.6e-03	3.9e-03
02-May-2021 04:42:53	5.6e-02	4.0e-03	9.7e-02	5.8e-03	4.1e-03
02-May-2021 06:16:50	2.5e-02	3.5e-03	1.2e-01	2.5e-03	1.7e-03
03-May-2021 01:22:52	2.4e-02	3.1e-03	1.2e-01	2.9e-03	8.5e-04
03-May-2021 02:56:48	5.3e-02	3.5e-03	1.2e-01	3.0e-03	1.4e-03
03-May-2021 04:30:21	5.1e-02	4.8e-03	1.5e-01	1.1e-03	8.6e-04
03-May-2021 06:04:16	2.0e-02	3.1e-03	1.2e-01	3.5e-04	3.1e-03
04-May-2021 01:08:17	2.7e-02	3.5e-03	1.3e-01	2.6e-03	2.3e-03
04-May-2021 02:41:57	5.7e-02	2.4e-03	1.1e-01	1.1e-02	5.1e-03
04-May-2021 04:15:22	4.5e-02	5.0e-03	1.2e-01	2.1e-04	1.9e-03
05-May-2021 00:51:00	3.1e-02	4.1e-03	1.2e-01	3.0e-03	6.0e-03
05-May-2021 02:24:25	5.9e-02	1.3e-03	1.2e-01	1.0e-03	6.9e-03
05-May-2021 03:57:41	4.1e-02	4.9e-03	1.0e-01	5.4e-04	2.0e-03
06-May-2021 00:30:43	3.4e-02	4.1e-03	1.1e-01	1.2e-03	2.8e-03
06-May-2021 02:03:53	6.0e-02	3.3e-04	1.1e-01	5.8e-04	8.0e-04
06-May-2021 03:36:57	3.8e-02	4.6e-03	1.3e-01	1.8e-03	2.7e-03
07-May-2021 00:06:54	3.7e-02	4.1e-03	1.3e-01	2.0e-03	2.6e-03
07-May-2021 01:39:47	6.1e-02	3.3e-04	1.1e-01	7.7e-03	3.1e-03
07-May-2021 03:12:37	3.6e-02	4.4e-03	1.4e-01	2.3e-03	2.9e-03
07-May-2021 23:38:31	3.8e-02	3.9e-03	1.3e-01	9.8e-04	1.5e-03
08-May-2021 01:11:01	6.3e-02	4.0e-04	1.1e-01	4.8e-03	3.9e-03
08-May-2021 02:43:29	3.6e-02	4.1e-03	1.2e-01	5.4e-03	3.8e-03
08-May-2021 23:02:16	3.7e-02	3.2e-03	1.3e-01	3.7e-04	1.3e-03
09-May-2021 00:33:49	6.8e-02	3.3e-04	1.0e-01	7.9e-03	1.5e-03

09-May-2021 02:04:58	4.1e-02	3.0e-03	1.2e-01	3.2e-03	2.1e-03
Median values					
-	3.9e-02	3.6e-03	1.2e-01	2.5e-03	2.7e-03

Table 4.11: Re-entry simulation: results of the catalogued case observation.

The results are reported in Tab. 4.11, divided for each observation and with the median values at the end. It is possible to observe that, contrary to the analyses in Sec. 4.2 and (generally) in Sec. 4.3, the $\Delta\gamma_2$ estimation is finer than the $\Delta\gamma_1$ one, as the transit is along the E-W direction and, during the integration time, the path covered along $\Delta\gamma_1$ is longer than the one along $\Delta\gamma_2$, which makes the former estimation less accurate. About this, it is important to remark that the flying velocity is high (oscillating between 7.7 km/s and 7.8 km/s), and this increases the path covered during the integration time. The orbit determination errors are in the order of e-03 both in position and in velocity, even if the latter is expected to present a smaller order of magnitude, and this suggests that the measurements noise and the integration time uncertainty affect that quantity more. Nevertheless, the correlation index ζ is similar to the results of the analyses in Sec. 4.2 and Sec. 4.3, and this confirms the compliance of the result. Finally, it is worth to notice that both the MATER result accuracy and the orbit determination errors are stable along all the observations, although the later the observation, the more perturbing the environment crossed by the target, and this confirms that the algorithm represents a reliable solution in re-entry campaigns.

Next, the same scenario is studied in the uncatalogued case. First MATER is run without the a-priori prediction and following the logical scheme presented in Sec. 3.6 and by solving the ambiguity through the SNR criterion. Then, the radar IOD procedure described in Sec. 2.5.3 is run based on the computed track and on the SR measurement (to which a noise with 30 m standard deviation is applied, as above). Finally, the computed state is refined in a Non-linear Least Squares, which embeds the high-fidelity propagator, with an a-priori estimation represented by the IOD result.

Observation epoch [UTC]	$\text{RMSE}_{\Delta\gamma_1}$ [deg]	$\text{RMSE}_{\Delta\gamma_2}$ [deg]	ζ -	Pos. Err. [km]	Vel. Err. [km/s]
29-Apr-2021 03:32:47	2.7e-02	3.4e-03	2.7e-01	3.9e-02	2.9e-02
29-Apr-2021 05:07:09	5.8e-02	2.4e-03	2.1e-01	3.6e-02	8.0e-02
29-Apr-2021 06:41:13	4.7e-02	4.9e-03	1.9e-01	5.1e-02	6.5e-02
30-Apr-2021 03:27:05	3.4e-02	3.9e-03	2.8e-01	4.1e-02	4.0e-02
30-Apr-2021 05:01:11	6.1e-02	1.4e-04	2.4e-01	2.8e-02	8.4e-02
30-Apr-2021 06:35:11	3.8e-02	4.6e-03	2.0e-01	3.9e-02	4.6e-02
01-May-2021 01:44:40	1.6e-02	2.9e-03	1.9e-01	4.6e-02	1.4e-02
01-May-2021 03:19:14	4.1e-02	4.2e-03	2.5e-01	4.2e-02	5.2e-02
01-May-2021 04:53:08	6.0e-02	2.4e-03	2.3e-01	4.1e-02	7.7e-02
01-May-2021 06:27:05	3.1e-02	4.1e-03	1.9e-01	3.4e-02	3.5e-02
02-May-2021 01:34:56	1.9e-02	3.2e-03	2.1e-01	3.8e-02	2.0e-02
02-May-2021 03:09:10	4.8e-02	4.1e-03	2.4e-01	4.1e-02	6.1e-02
02-May-2021 04:42:53	5.6e-02	4.0e-03	2.7e-01	4.1e-02	7.6e-02
02-May-2021 06:16:50	2.5e-02	3.5e-03	1.9e-01	3.6e-02	2.7e-02
03-May-2021 01:22:52	2.3e-02	3.4e-03	2.3e-01	3.9e-02	2.4e-02
03-May-2021 02:56:48	5.3e-02	3.5e-03	2.3e-01	3.3e-02	7.1e-02
03-May-2021 04:30:21	5.1e-02	4.8e-03	2.4e-01	4.5e-02	6.4e-02
03-May-2021 06:04:16	2.0e-02	3.3e-03	1.7e-01	3.2e-02	2.2e-02
04-May-2021 01:08:17	2.7e-02	3.7e-03	2.5e-01	4.6e-02	3.0e-02
04-May-2021 02:41:57	5.7e-02	2.5e-03	2.3e-01	4.9e-02	7.2e-02
04-May-2021 04:15:22	4.5e-02	5.0e-03	2.1e-01	4.6e-02	5.8e-02
05-May-2021 00:51:00	3.1e-02	3.8e-03	2.6e-01	4.3e-02	3.5e-02
05-May-2021 02:24:25	5.9e-02	1.2e-03	2.3e-01	3.5e-02	7.7e-02
05-May-2021 03:57:41	4.1e-02	4.9e-03	2.0e-01	4.3e-02	4.9e-02
06-May-2021 00:30:43	3.4e-02	4.1e-03	2.9e-01	4.2e-02	4.0e-02
06-May-2021 02:03:53	6.0e-02	4.0e-04	2.1e-01	3.7e-02	8.6e-02
06-May-2021 03:36:57	3.8e-02	4.6e-03	1.9e-01	3.4e-02	4.5e-02
07-May-2021 00:06:54	3.7e-02	4.1e-03	2.6e-01	4.3e-02	4.3e-02
07-May-2021 01:39:47	6.1e-02	2.6e-04	2.5e-01	3.3e-02	8.6e-02

07-May-2021 03:12:37	3.6e-02	4.4e-03	2.4e-01	3.4e-02	4.2e-02
07-May-2021 23:38:31	3.8e-02	4.0e-03	2.7e-01	4.3e-02	4.7e-02
08-May-2021 01:11:01	6.3e-02	6.1e-04	2.7e-01	4.7e-02	9.0e-02
08-May-2021 02:43:29	3.6e-02	4.0e-03	1.9e-01	3.7e-02	4.3e-02
08-May-2021 23:02:16	3.7e-02	3.3e-03	2.5e-01	3.8e-02	4.6e-02
09-May-2021 00:33:49	6.8e-02	3.1e-04	2.2e-01	2.8e-02	1.1e-01
09-May-2021 02:04:58	4.0e-02	2.1e-03	1.5e-01	3.0e-02	5.2e-02
Median values					
-	3.9e-02	3.6e-03	2.3e-01	3.9e-02	4.8e-02

Table 4.12: Re-entry simulation: results of the uncatalogued case observation.

Tab 4.12 reports the results of the simulation. It can be noticed that, although the angular accuracy is comparable to the catalogued case one (always with $\Delta\gamma_2$ more accurate than $\Delta\gamma_1$), the orbit determination error increases of one order of magnitude both for position and velocity. This is due to the orbit determination algorithm implemented, as the IOD procedure exploited to retrieve the Non-linear Least Squares first guess is analytical, and so it does not provide an accurate result for the highly perturbed scenario here analysed. The Non-linear Least Squares does not improve the estimation in a remarkable way, mainly for its dependence on the first guess. Nevertheless, the result is compliant, as confirmed by the correlation index median ζ. Finally, similarly to the catalogued case, the results do not deteriorate moving from the first to the last transits, and this once again confirms the applicability of MATER to reconstruct track in all the phases of the re-entry.
To recap, the Re-entry service can profit from MATER algorithm across all the phases, both in the catalogued and in the uncatalogued case. However, the latter situation may lead to a deterioration in orbital state estimation because of the IOD algorithm used.

4.4.2 Collision Avoidance

The Collision Avoidance service is devoted to the conjunction analyses: it is in charge of assessing possible conjunctions among catalogued objects and, for those which overcome

	a [km]	e	i [deg]	Ω [deg]	ω [deg]
IRIDIUM 33	7145.1	7.0e-04	86.4	121.2	190.0
COSMOS 2251	7155.5	1.2e-03	74.0	17.2	84.1

Table 4.13: Orbital parameters of IRIDIUM 33 and COSMOS 2251.

threshold quantities, a Conjunction Data Message (CDM) [10] is created, which groups the information of the satellites involved. Usually, the objects are distinguished in primary (the one which is manoeuvrable, for instance) and secondary (as space debris, for example) [88]. For them, the CDM reports the satellites state, both in terms of mean and covariance, the Time of Closest Approach (TCA), the related Miss Distance (MD) and the Probability of Collision (PoC). Several methods exist to compute the PoC, depending on the type of conjunction. Under particular assumptions, such as high relative velocity during the conjunction, the short-term encounter model can be used, which allows to reduce the computational demand. According to this model, multiple PoC computation methods have been developed, which are either numerical, like [89] and [90], or analytical, like [91], [92] and [93].

OD applications for CA service related tasks consist in determining the orbital state of the observed target (either IOD or ROD, depending on the application) to maintain the objects catalogue and, so, to allow CA operations.

To assess the performance of MATER algorithm in contributing to the CA service, a simulation is carried out referred to the collision between COSMOS 2251 and IRIDIUM 33, occurred on February 10^{th}, 2009, at 16:56 UTC [94]. A CDM is simulated starting from the temporally closest TLEs [14], resulting in a TCA dated at 16:55:59.809 (UTC) and in 827.5242 km of MD. The PoC is computed through the Chan's method [91] and results equal to 9.851e-08. It may be argued that the MD is too large and the PoC is too small for a conjunction in which the satellites eventually collided. However, this is a quantity coherent with the fact that no manoeuvre was applied by operators, as the threshold quantities (on either MD or PoC) were not overcome. Both IRIDIUM 33 and COSMOS 2251 orbital parameters (with the exception of the true anomaly) are reported in Tab. 4.13.

The orbital mean state of COSMOS 2251 is backward propagated in time via SGP4 [52] up to February 09^{th}, 2009, at 17:39:44.809 UTC. At this epoch, the pass prediction is simulated by associating a covariance to the orbital mean state, according to the method described in

	Reference	1 kHz	5 kHz	10 kHz
TCA (2009-02-10)	16:55:59.809	16:56:01.048	16:55:59.588	16:55:58.500
MD [km]	827.5242	10982.7491	3440.7894	13572.9589
PoC (Chan)	9.851e-08	6.9209e-09	2.4199e-08	7.0188e-11

Table 4.14: Conjunction analysis simulation by varying the sampling frequency.

[95], and the mean is perturbed accordingly, resulting in an error of 9.53e-02 km in position and 4.6e-04 km/s in velocity. By this way, a difference is set between the ground truth (represented by the backward propagation) and the pass prediction.

The obtained orbital state (in terms of both mean and covariance) is forward propagated via UT [58], for 8.33 h, when the COSMOS 2251 enters in BIRALES FoV and is detected. At this point, measurements are synthetically generated, both in terms of SR, DS and CMs. To both SR and DS a Gaussian noise is associated (with 30 m and 10 Hz standard deviation), while the signal is sampled with a varying frequency (1 kHz, 5 kHz, 10 kHz) and keeping fixed to 100 the number of samples used to compute the CM. This makes the integration time varying according to the sampling frequency: 0.1 s, 0.02 s and 0.01 s for the 1 kHz, 5 kHz and 10 kHz cases respectively. The angular measurements are computed by MATER algorithm, and ROD via UKF is run [66], embedding SGP4. The determined orbital state is forward propagated, and both TCA, MD and PoC (still according to Chan's method [91]) are computed. The results are reported in Tab. 4.14.

It can be observed that the TCA varies within about 1 s due to the OD error, and this provokes a change in both the MD and the PoC. In addition, it is to point out that, increasing f_s up to 10 kHz does not imply an improvement in the results, as the case in which the best matching is reached is the 5 kHz case. This is coherent with what obtained in the sensitivity analysis in Sec. 4.3: the larger the sampling frequency, the smaller the integration time uncertainty, but the larger the noise contribution, and this may deteriorate the track estimation and, so, the OD accuracy.

Figure 4-8 reports, for the 5 kHz case, the time trends of the error (with respect to the ground truth) and the standard deviation, both for the tracked position and velocity of the satellite state. The orbital state knowledge is represented by the prediction propagated up to the OD epoch, and then by the OD result up to the TCA. In correspondence of the OD, a fall both in error and standard deviation occurs, due to the refinement resulting from the

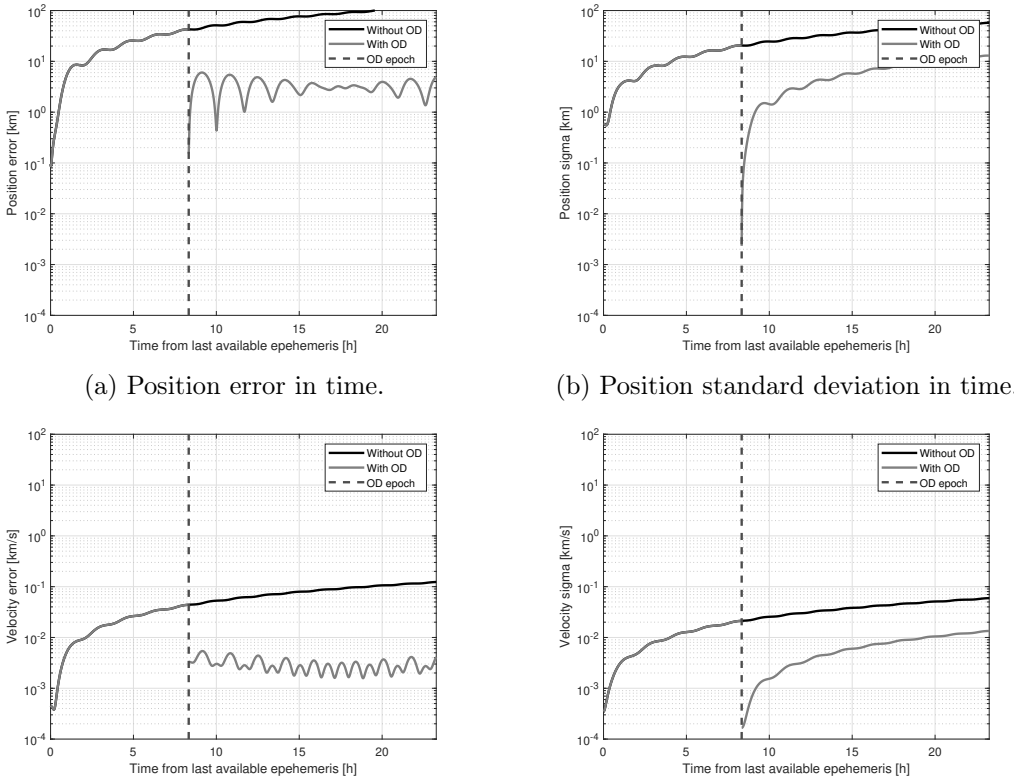

(a) Position error in time.

(b) Position standard deviation in time.

(c) Velocity error in time.

(d) Velocity standard deviation in time.

Figure 4-8: Time trend of error and standard deviation both for position and velocity of the tracked satellite state, for the 5 kHz case. The error is computed with respect to the ground truth. It is possible to appreciate the fall, both in error and in standard deviation, due to the ROD process, which allows to reach smaller error and uncertainty at the TCA.

ROD, and this allows to reach errors and uncertainties at the TCA much smaller than what would have been obtained by directly propagating the predicted orbital state (also visible in the plots). It must be remarked that the errors remain bounded and are generally smaller than the associated uncertainties, but right after the OD.

It is interesting to asses the results for the IOD case. In this situation, the angular track is computed by MATER algorithm by solving the ambiguity through the *delta-k* method, and a first guess for the orbital state (both in terms of mean state and covariance) is retrieved based on [69], and then refined according to UKF [66]. As Fig. 4-9 shows, the result from IOD induces very large errors both in position and in velocity at the correct TCA, and this prevents the conjunction data computation to provide reliable results. In particular, using the orbital state determined by the IOD, no conjunction is alerted by the tool which computes TCA, MD and PoC. Such a decrease in performance is due to the IOD algorithm

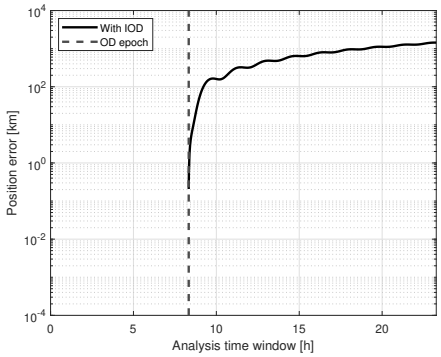

(a) Position error in time.

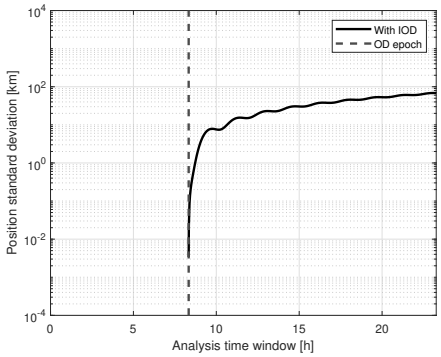

(b) Position standard deviation in time.

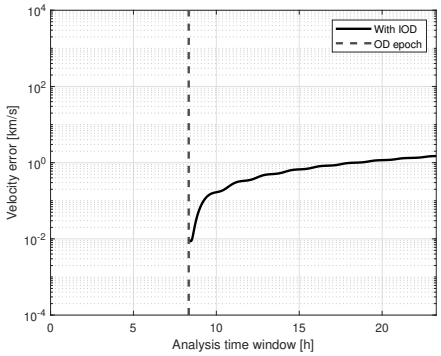

(c) Velocity error in time.

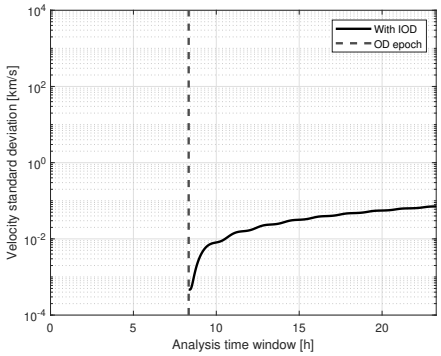

(d) Velocity standard deviation in time.

Figure 4-9: Time trend of error and standard deviation both for position and velocity after the IOD, for the 5 kHz case. The error is computed with respect to the ground truth. Given that no conjunction is identified by the screening process, the plots show the propagation on the same time window as in the ROD case to better compare the results.

used rather than to MATER performance, which provides an angular track with the same accuracy as in the ROD case, as visible in Tab. 4.15. Indeed the orbital state first guess is computed through [69], which is an analytical method, and this introduces an error the UKF [66] is not able to fully compensate. Therefore, larger errors with respect to the ROD at the OD epoch are obtained, as reported in Tab. 4.15. Finally, it is to point out that the position and velocity errors are always larger than the respective uncertainties.

To recap, this section provided an example of MATER algorithm used in OD applications for CA service tasks. Appreciable results are reached by a ROD based on UKF [66] and embedding SGP4 [52], while, similarly to the Re-entry service analysis in Sec. 4.4.1, performance deteriorates with IOD applications because of the IOD algorithm used.

	$\text{RMSE}_{\Delta\gamma_1}$ [deg]	$\text{RMSE}_{\Delta\gamma_2}$ [deg]	Pos. Err. [km]	Vel. Err. [km/s]
ROD	2.1e-03	6.6e-03	1.5e-01	3.3e-03
IOD	2.1e-03	6.6e-03	2.1e-01	9.2e-03

Table 4.15: Angular RMSE and OD results, both for ROD and IOD processes.

a [km]	e	i [deg]	Ω [deg]	ω [deg]
6794.9	6.1e-04	51.5	228.8	45.6

Table 4.16: Real observation: International Space Station orbital parameters.

4.5 Real Observation

In this section, MATER performance is assessed on real data from one BIRALES observation. The algorithm could only be run using the current receiver back-end of BIRALES, which allows to post-process recorded raw data (operationally a key aspect, as mentioned in Sec. 1.6), but it does not match exactly the typical requirements for optimal MATER performance. BIRALES is currently configured to use the static multibeam strategy described in Sec. 1.5, and the corresponding settings prevented an optimal generation of the real CMs. On the one hand, the CM integration time was 0.42 s, which introduces a significant uncertainty on the estimated DOA. On the other hand, the CM can only be built on a signal acquired with a channel with 78 kHz bandwidth. This limitation poses a severe constraint, as the current BIRALES back-end allows MATER to be realistically applied only on the observation of resident space objects providing a relatively intense received signal (i.e., large RCS and/or short slant range). For this reason, the results obtained on an observation of the International Space Station (ISS) is reported hereafter.

The observed pass of the ISS occurred on April 28^{th}, 2021 at 08:44:32 (UTC), southwards from the receiver, at an elevation of 83.9 deg. The predicted orbital parameters, according to the TLE [14], are reported in Tab. 4.16 (with the exception of the true anomaly). The transmitter pointing angles were 19.3 deg in azimuth and 35.1 deg in elevation.

The resulting MUSIC pattern, for a generic instant, is illustrated in Fig. 4-10, where it is possible to appreciate the presence of multiple peaks, similarly to Fig. 4-1. The DOAs resulting from the track estimate phase are reported in Fig. 4-11a, while the reconstructed angular profile after the track refinement phase (exploiting the OD-based criterion with

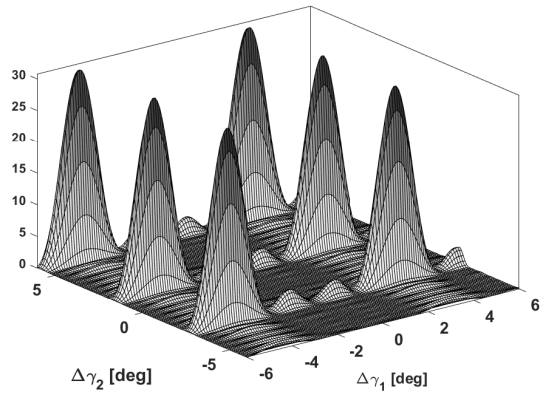

Figure 4-10: Three-dimensional array response for the real pass of the International Space Station (ISS) on April 28$^{\text{th}}$, 2021 at 08:44:32 (UTC).

$\text{RMSE}_{\Delta\gamma_1}$ [deg]	$\text{RMSE}_{\Delta\gamma_2}$ [deg]	$\overline{\zeta}$
1.5e-01	9.2e-02	2.0e-01

Table 4.17: MATER results related to the real pass of the International Space Station (ISS) on April 28$^{\text{th}}$, 2021 at 08:44:32 (UTC).

measured SR) is reported in Fig. 4-11b, together with the correct DOAs (identified by solving the ambiguity) used to obtain the final regression. The estimated DOAs are along the real track for a large portion of the pass. Yet, a slight time shift between the real track and the one estimated by MATER can be observed (e.g., close to the end points of the track). This shift can be mainly attributed to four possible factors: the relatively long CM integration time and the associated time uncertainty introduced in the estimated DOA, the signal quality (attenuated by the 78 kHz channel bandwidth), the inaccuracy of the reference ISS track (which has been retrieved from TLE) the result is compared to and, possibly, sensor calibration inaccuracies. All of these factors have an impact on the performance reported in Tab. 4.17 (for the uncatalogued case): the angular RMSEs are about 1 order of magnitude larger than those obtained with the statistical analysis presented in Sec. 4.2, but the correlation index is of coherent magnitude with the nominal analyses. Nevertheless, the results are encouraging as they show that MATER algorithm can reconstruct the track for orbit determination purposes, even when a not optimal back-end is used, as in the current settings.

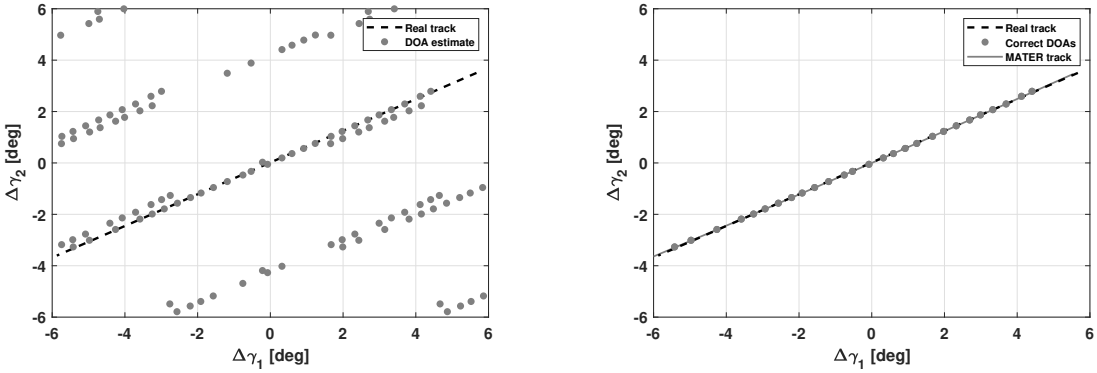

(a) Track estimate phase result.

(b) Track refinement phase result.

Figure 4-11: MATER applied to the real pass of the International Space Station (ISS) on April 28$^{\text{th}}$, 2021 at 08:44:32 (UTC). In Fig. 4-11b also the DOAs used for the final regression are represented.

Chapter 5

MATER applied to multiple sources observations

This chapter discusses MATER application to the multiple sources scenario, that is when, for certain observation epochs, more than one source is present in the receiver FoV. Section 5.1 describes the procedure, both for the catalogued and the uncatalogued case. The process in evaluated through both nominal and sensitivity analyses, in Sec. 5.2.1 and in Sec. 5.2.2 respectively. Finally, Sec. 5.3 presents SST applications of MATER for multiple sources scenario: a proximity operation monitoring and a fragments cloud observation. The latter analysis is fundamental for the Fragmentation Analysis service introduced in Sec. 1.4, the thesis further contributes to in Ch. 6 and in Ch. 7.
All the simulations were implemented and run in MATLAB [87].

5.1 Multiple sources scenario

During survey observations, it may occur that multiple sources simultaneously cross the receiver FoV. This can occur during a survey observation, but also when either a formation flying, or a fragments cloud is observed, or even a proximity operation is monitored. In these scenarios, the detection epochs of the target signals overlap, as represented in Fig. 5-1, which reports the SNR trend during a generic survey observation, and where it is possible to appreciate the simultaneous presence of multiple sources signal at the same epochs. In these scenarios, the MATER algorithm described in Ch. 3 can be adapted to

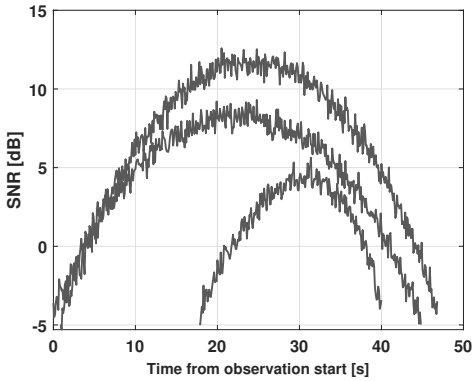

Figure 5-1: Generic SNR profile acquired during a survey observation. It is possible to appreciate the presence of multiple detected signals, that is multiple observed sources, at the same epochs.

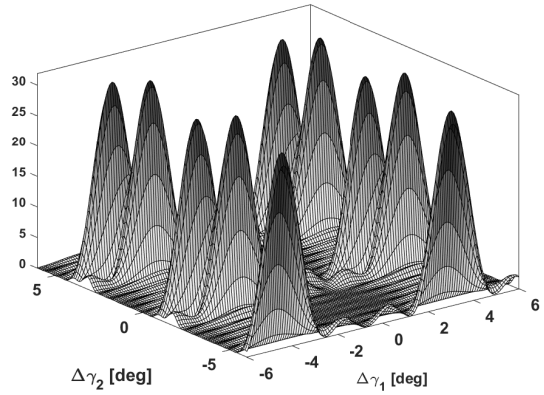

Figure 5-2: BIRALES array response based on MUSIC for two sources observation.

derive the tracks of targets whose detection epochs overlap, that is when, for some epochs, the number of observed sources N_s is larger than 1. In this case, at a generic observation epoch, both correct and ambiguous DOAs are estimated, for all the observed targets. Figure 5-2 represents the array response of BIRALES (always used as baseline, like in Ch. 4) when two targets are detected.

To adapt MATER to the multiple sources scenario, the key point is to isolate the detection instants related to a same target. This is accomplished through the SNR profile, from which it is possible to derive the information about the number of detected targets N_s at a given epoch, that is the number of impinging signals that, at that epoch, overcome a SNR threshold. Based on this information, the MATER track estimate phase, at that epoch, searches for N_s DOAs and, like in Ch. 3, the process is divided in catalogued and uncatalogued case.

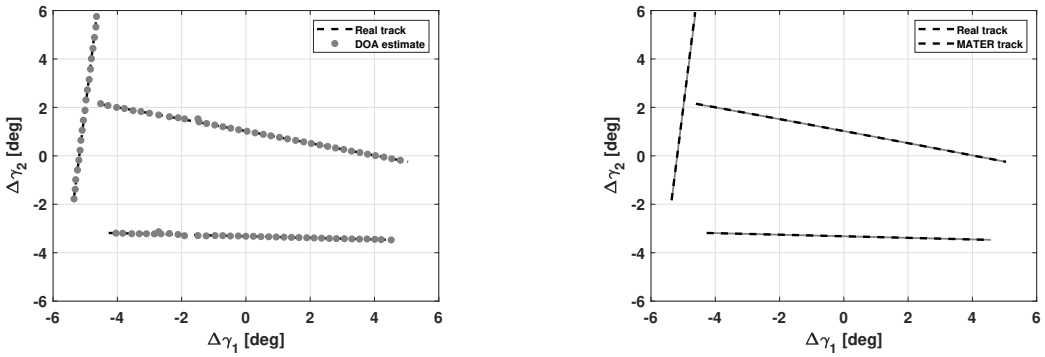

(a) Track estimate phase result.

(b) Track refinement phase result.

Figure 5-3: Catalogued case in multiple sources scenario.

5.1.1 Catalogued case

The flow of the catalogued case for the multiple sources scenario is the same as the one reported in Fig. 3-1, by considering possible multiple DOA estimations for each epoch. Like in Sec. 3.5, the DOAs estimation ambiguity can be solved based on the pass prediction and, so, through the reference track. This, for a time window in which multiple sources pass (like in Fig. 5-1), results in a number of estimated DOAs trends equal to the number of the observed targets, as represented in Fig. 5-3a. Then, after the clustering and regression, the output tracks are returned, as represented in Fig. 5-3b.

5.1.2 Uncatalogued case

In the uncatalogued case for the multiple sources scenario, one of the processes described in Sec. 3.6 can be exploited. Based on the nominal numerical analysis carried out in Sec. 4.2, the ambiguity solving approach based on the *delta-k* method is the most robust and, so, it is selected. Thus, the same process described in Sec. 3.6.2 and schematised in Fig. 3-6 is here exploited.

First of all, for each observation epoch, MATER searches for N_s sources retaining also the related ambiguous solutions. This, at the end of the estimate track phase, results in a FoV very populated of DOA estimations, as represented in Fig. 5-4a. The estimation is then refined according to the *delta-k* technique, and this results in a much less populated FoV, as represented in Fig. 5-4b. Then, the algorithm proceeds by isolating the epochs related to a same target detection (like described in the catalogued case above), and the

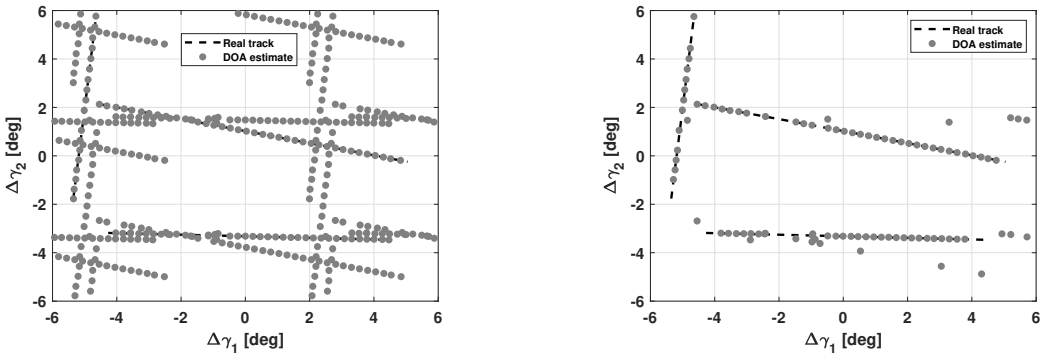

(a) Track estimate phase result.

(b) DOA ambiguity solved.

Figure 5-4: Uncatalogued case (*delta-k* technique) in multiple sources scenario.

N. of passes per slot	2	3	4	5	6	7	8	TOT
Obj. per slot	129	50	17	4	2	2	1	530

Table 5.1: Slots composed of passes temporally overlapping each other.

quadratic regression is performed for the two angular coordinates separately. The final result is analogous the one reported in fig. 5-3b.

5.2 Numerical Analysis

MATER algorithm performance in the multiple sources scenario is assessed through a numerical simulation. Besides the nominal conditions, also a sensitivity analysis on the transmitted power is conducted, retracing what presented in Sec. 4.3 for the single source scenario.

5.2.1 Nominal Analysis

A synthetic data set composed of 530 passes related to 253 LEO objects from the NORAD catalogue [52] is analysed. The analysis considers an observation window of one day, on June 16^{th}, 2021. These passes temporally superimpose each other and they can be subdivided in slots, each slot being composed of a sequence of temporally overlapping transits (with overlapping SNR trends, like in Fig. 5-1). The correspondence between the number of overlapping transits and the slots is reported in Tab. 5.1: 129 slots composed of 2 temporally overlapping passes, 50 slots with 3 temporally overlapping passes, and so on.

The passes projections in the measurements space provide their nominal angular track. The

	Success [%]	$\eta_{\Delta\gamma_1}$ [deg]	$\eta_{\Delta\gamma_2}$ [deg]
Catalogued	100	7.0e-03	1.1e-02
Uncatalogued	100	6.0e-03	1.1e-02

Table 5.2: Statistical analysis on synthetic data, for catalogued and uncatalogued case.

transmitter and receiver pointing angles, in terms of azimuth and elevation, are set equal to [7, 40.5] deg and [0, 60] deg respectively. For the remaining quantities, the same values as in Sec. 4.2 are used (like RCS, transmitted power, and so on). Then, the data for the testing procedure are generated similarly to Sec. 4.2, but no SR, nor DS are simulated, as the ambiguity solving based on the *delta-k* technique does not need additional measurements.
Starting from these data, MATER is run and the performance is assessed in terms of convergence rate and of median values η of the root mean square error (RMSE), computed through Eq. 4.1, for the two angular coordinates separately.
First of all, MATER is run by assuming that all the objects are catalogued, i.e. an a-priori estimate of their orbit is available. The results are summarised in Tab. 5.2, which reports the success rate (in percentage), and $\eta_{\Delta\gamma_1}$ and $\eta_{\Delta\gamma_2}$ (in degree). The algorithm is able to converge in all the cases. In addition, the very low values of angular error confirm the accurate performances of MATER in reconstructing the angular track for a set of catalogued objects simultaneously detected. Then, it is worth observing that the angular RMSE is lower in the E-W direction ($\eta_{\Delta\gamma_2}$) than in the N-S direction ($\eta_{\Delta\gamma_1}$). As discussed in Sec. 4.2, this is due to the length of the angular path travelled during the integration time, as the estimated DOA may correspond to any actual value assumed in the meanwhile. Since most of the data set passes correspond to high-inclination orbits, the angular path travelled in the N-S direction is usually larger than the one travelled in the E-W one, and this makes the angular RMSE larger along $\Delta\gamma_2$ than along $\Delta\gamma_1$.
Then, MATER is applied on the same passes in the uncatalogued case, that is by considering no a-priori orbital estimate for the observed objects. As mentioned above, in this case the ambiguity is solved according to the *delta-k* method, as presented in Sec. 3.6.2, by considering two frequencies equal to 411.5 MHz and 413.5 MHz, which induce an angular shift of 0.017 deg (see Sec. 4.1). The results are reported in Tab. 5.2 and show that the correct solution is always matched, with an accuracy similar to the catalogued case one.
Both for the catalogued and the uncatalogued case, the computational demand increases

N. of passes per slot	TX Power [W]	2	3	4	5	6	7	8	TOT
Obj. per slot	1e+04	90	14	4	2	1	0	0	254
	5e+03	57	8	3	1	0	0	0	155
	1e+03	0	0	0	0	0	0	0	0

Table 5.3: Slots composed of passes temporally overlapping each other, by varying the transmitted power.

with respect to Sec. 4.2 (with the same processor and using a single core) as multiple DOAs are estimated at each overlapping epoch and the clustering is performed for each detected source.

5.2.2 Sensitivity Analysis

A sensitivity analysis is carried out on the multiple sources observations scenario, considering the same different transmitted power levels as the one of the single source sensitivity analysis in Sec. 4.3.

Since a decrease of the transmitted power shortens the length of the detected signal, the number of temporally overlapping passes decrease, as represented in Tab. 5.3: the slots for each intersecting passes number become smaller and smaller and, in particular, no temporally overlapping sources are present for the 1e+03 W transmitted power case. Therefore, a decrease of the transmitted power makes the detected tracks less overlapping, such that they are analysed separately. This may imply an advantage in terms of algorithm complexity, but the portion of the detected tracks becomes shorter and shorter, and this is eventually a drawback in terms of orbit determination routines and of contribution to catalogue maintenance.

The analysis results are reported in Tab. 5.4. Similarly to Tab. 4.5 (for the *delta-k* technique), the correct solution is always matched, with a slight angular accuracy deterioration with respect to the nominal analysis.

5.3 SST services numerical simulations

Given the nominal and the sensitivity analyses provided in Sec. 5.2.1 and Sec. 5.2.2, and analogously to what done in Sec. 4.4, MATER algorithm is tested on numerical simulations

TX Power [W]	Success [%]	$\eta_{\Delta\gamma_1}$ [deg]	$\eta_{\Delta\gamma_2}$ [deg]
1e+04	100	7.8e-03	1.1e-02
5e+03	100	9.2e-03	1.2e-02
1e+03	-	-	-

Table 5.4: Statistical analysis on synthetic data, for the uncatalogued case, by varying the transmitted power.

regarding those SST applications for which the multiple sources angular track reconstruction is fundamental. In particular, the observation of a proximity operation and of a fragments cloud are investigated, the latter being strictly related to the Fragmentation Analysis service.

5.3.1 Close proximity operation

The first simulation is represented by the proximity operation. These scenarios are of increasing concern, given the importance attributed to the satellite inspections activities, both for military and civilian applications. An example of the latter application are the operations studied for the active debris removal programs.

In this simulation, the proximity operation is represented by a chaser moving around the target according to the football orbit model [96], for which the period of the relative orbit is equivalent to the target orbit one. In such a model, the football orbit semi-major axis is aligned towards the transversal direction of the target RTN reference frame (defined in Sec. 2.1), and it is doubled with respect to the semi-minor axis. In the analysed scenario, the football orbit semi-major and semi-minor axes are set equal to 10 km and 5 km respectively, the latter being aligned towards the radial direction (no cross-track component is considered). Figure 5-5a shows the selected football orbit in the target RTN reference frame.

The observation geometry used in the simulation is retrieved from the ISS transit conducted on the April 28$^{\text{th}}$, 2021, already discussed in Sec. 4.5 about the real application of MATER algorithm. In particular, the ISS ephemeris are used to retrieve target orbital state (its RCS is set equal to 1 m^2), and the chaser relative orbit is generated around it. Four cases are assessed, in terms of angular distance of the target in the transversal-radial reference frame, moving in clockwise direction from the point [10 0] km: 0 deg (positive transversal distance), 90 deg (negative radial distance), 180 deg (negative transversal distance), 270 deg (positive radial distance). These four cases are represented in Fig. 5-5b. It is important to

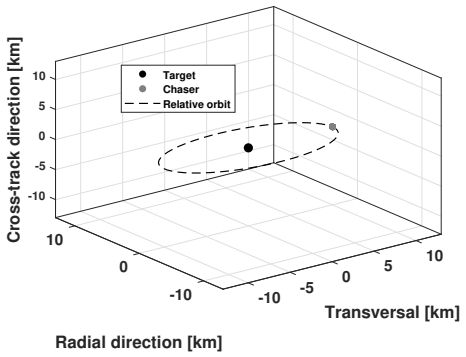

(a) RTN reference frame.

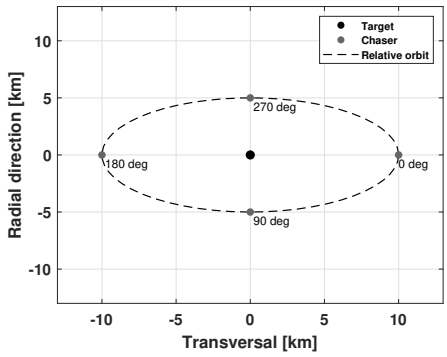

(b) TR reference frame.

Figure 5-5: Proximity operation simulation: football orbit. In Fig. 5-5b the four analysed chaser angular positions with respect to the target are represented as well.

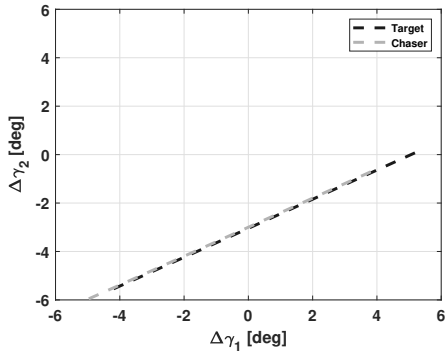

(a) 0 deg situation.

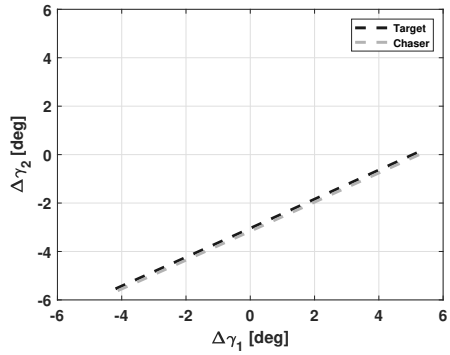

(b) 90 deg situation.

Figure 5-6: Proximity operation simulation: predicted track in the receiver FoV.

point out that, being the observation time window about 3 order of magnitude smaller than the target orbital period (and, so, of the football orbit period as well), the angular position of the chaser with respect to the target does not change significantly during the observation. The chaser position in the football orbit has an impact on the mutual positions between target and chaser angular tracks in the receiver FoV, as clearly visible in Fig. 5-6a and Fig. 5-6b. In particular, those situations for which the distance chaser-target is along the target transversal direction (0 deg and 180 deg) feature aligned tracks in the FoV, but with a time gap, as the chaser is either in advance (0 deg situation) or in late (180 deg). This motivates, in the track refinement phase, a cluster performed on time coordinates. On the contrary, the situations for which the distance chaser-target is along the radial direction (90 deg and 270 deg) feature parallel tracks in the FoV. Therefore, this motivates the choice of clustering in the FoV, as usually done in the rest of Ch. 5.

The angular difference between the sources in the receiver FoV are reported in Tab. 5.5 in terms of root mean square between the predicted tracks. It is possible to notice that the transversal separation causes a remarkable angular difference along $\Delta\gamma_1$ (cases 0 deg and 180 deg), while the radial one does not (cases 90 deg and 270 deg). Besides their magnitude (10 km and 5 km respectively), this is mainly due to the fact that the line receiver-target is almost aligned towards the target radial direction, considering that the sensor pointing is close to the zenith (83.9 deg). So, a radial separation of the chaser makes it either almost hiding or almost being hidden by the target, and, so, the two sources result extremely close in the receiver FoV.

	$\text{RMS}_{\Delta\gamma_1}$ [deg]	$\text{RMS}_{\Delta\gamma_2}$ [deg]
0 deg	1.4e+00	7.70e-01
90 deg	3.5e-02	1.1e-01
180 deg	1.4e+00	7.8e-01
270 deg	3.4e-02	1.01e-01

Table 5.5: Proximity operation simulation: root mean square angular difference in the receiver FoV.

For each case, MATER is run on simulated data through the *delta-k* method, considering three different scenarios: the catalogued, the uncatalogued and the semi-uncatalogued one. In this last situation, one of the two observed objects (in this case the target) is considered as catalogued, while the latter is not, and this allows to have, at the end of the track estimate phase, a FoV less populated of DOAs estimations, as the target ambiguities have been already solved. Figure 5-7a and Fig. 5-7b show the result difference, at the end of the track estimate phase, between the uncatalogued and the semi-uncatalogued scenarios (for the 0 deg case): in the former all the DOAs are kept, both for the target and the chaser, while in the latter just the chaser ambiguities remain, as the target ones have been removed. Table 5.6 shows the results of the analysis, in terms of success rate in solving the angular track ("Convergence" column) and angular RMSE, for the target and the chaser. It can be seen that the angular accuracy deteriorates with respect to the nominal analysis in Sec. 5.2.1, and this is basically due to the mutual interference produced by the two sources, which are close each other for the entire observation. Both for the catalogued, uncatalogued

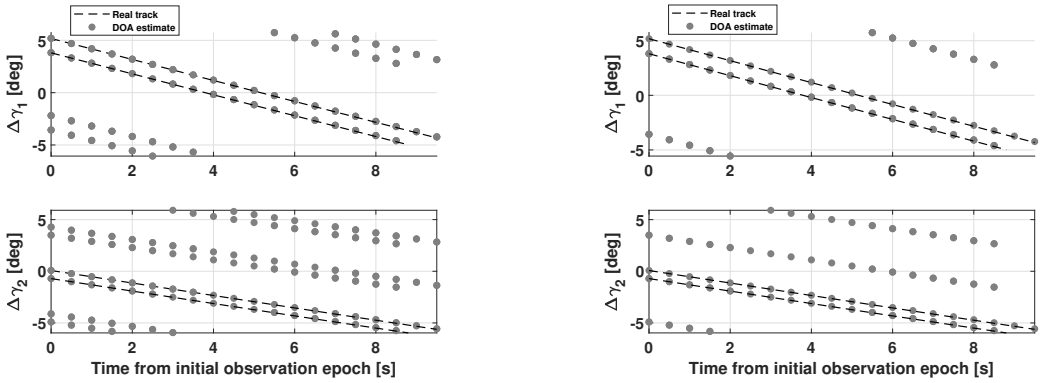

(a) Uncatalogued scenario. (b) Semi-uncatalogued scenario.

Figure 5-7: Proximity operation simulation: track estimate phase result, represented through the two angular coordinates trends in time.

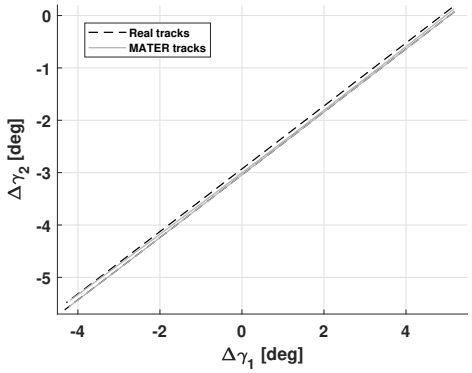

Figure 5-8: Proximity operation simulation: MATER failure for the scenario semi-uncatalogued 270 deg. It can be seen that the tracks are erroneously estimated, even if the angular accuracy, in terms of RMSE, is low.

and semi-uncatalogued scenario, the 0 deg and the 180 deg cases converge to the correct solution, while the others do not, even if they always exhibit a similar angular accuracy. Indeed, comparing the results in Tab. 5.6 with the angular distances in Tab. 5.5, it can be observed that the angular accuracy is much smaller than the predicted angular distance in the 0 deg and 180 deg cases, while it is of comparable magnitude in the 90 deg and 270 deg ones. In this two latter situations, the sources are so close each other that, also because of the noise, the clustering phase possibly erroneously group the signal DOAs, grouping in a same cluster estimations related to different sources. This results in erroneous tracks, as represented in Fig. 5-8, which shows a zoomed FoV to better appreciate the failure.
Regardless the track reconstruction accuracy, the presence of two targets can be assessed by looking at the CM eigenvalues trends, as shown in Fig. 5-9. It is always possible to identify

	Convergence	$RMSE^{t}_{\Delta\gamma_1}$ [deg]	$RMSE^{t}_{\Delta\gamma_2}$ [deg]	$RMSE^{ch}_{\Delta\gamma_1}$ [deg]	$RMSE^{ch}_{\Delta\gamma_2}$ [deg]
		0 deg			
Catalogued	yes	5.6e-02	3.4e-02	5.2e-02	2.9e-02
Uncatalogued	yes	5.6e-02	3.4e-02	5.2e-02	3.1e-02
Semi-uncatalogued	yes	5.8e-02	3.4e-02	5.3e-02	3.1e-02
		90 deg			
Catalogued	no	6.3e-02	3.5e-02	7.1e-02	1.3e-01
Uncatalogued	no	5.2e-02	4.4e-02	5.6e-02	5.6e-02
Semi-uncatalogued	no	5.8e-02	3.4e-02	6.6e-02	1.1e-01
		180 deg			
Catalogued	yes	5.6e-02	3.5e-02	5.8e-02	3.4e-02
Uncatalogued	yes	5.6e-02	3.4e-02	5.8e-02	3.5e-02
Semi-uncatalogued	yes	5.8e-02	3.4e-02	5.8e-02	3.5e-02
		270 deg			
Catalogued	no	7.1e-02	1.3e-01	6.2e-02	3.5e-02
Uncatalogued	no	5.2e-02	4.8e-02	5.0e-02	5.9e-02
Semi-uncatalogued	no	5.8e-02	3.4e-02	6.0e-02	4.0e-02

Table 5.6: Proximity operation simulation: results.

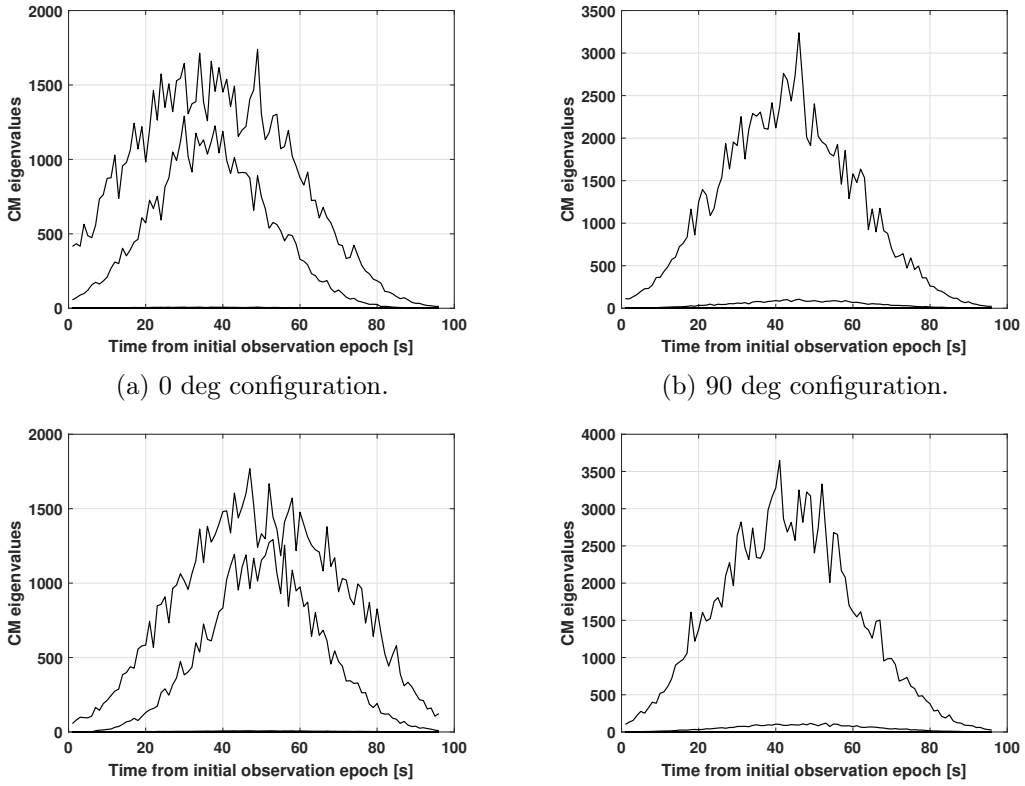

(a) 0 deg configuration.

(b) 90 deg configuration.

(c) 180 deg configuration.

(d) 270 deg configuration.

Figure 5-9: Proximity operation simulation: CM eigenvalues trend for the four configurations. It is possible to notice that two trends are always present, but they are better visible in the 0 deg and in the 180 deg configurations.

2 sources, that is 2 eigenvalues trends which are remarkably different from the noise ones (slightly visible in the bottom of the graph). However this is better visible in the 0 deg and 180 deg configurations (Fig. 5-9a and Fig. 5-9c), whereas in the 90 deg and 270 deg configurations (Fig. 5-9b and Fig. 5-9d) the first eigenvalue increases in magnitude and the second one decreases with respect to the other two cases. Another aspect to point out is that, in the 0 deg graph (Fig. 5-9a), 2 sources are visible from the beginning, and in the very final instants of the observation time just one remains, while the situation is opposite in the 180 deg graph (Fig. 5-9c). This is due to the fact that the observation, and so the time window of the measurements acquisition, is planned based on the target visibility. Indeed, in the 0 deg configuration (Fig. 5-9a), the chaser object is already present in the receiver FoV when the target object is first detected, and 2 sources are present. Then, in the final instants of the target object visibility, the chaser is not in the FoV anymore, and so only 1 source is present. The situation is opposite in the 180 deg configuration (Fig. 5-9c).

To conclude, a proximity operation scenario, simulated according to a football orbit model, has been analysed. MATER correctly estimates the angular tracks when the chaser relative position in the target RTN reference frame is towards the transversal direction, while the angular distance between the two sources in the receiver FoV falls at the resolution level when the chaser relative position is towards the radial direction, because of the observation geometry. In both cases it is possible to recognise the presence of 2 sources, but it turns out much better visible when the chaser relative position is towards the transversal direction.

5.3.2 Fragments cloud observation

Generally speaking, a fragmentation event can be originated either by a single spacecraft explosion or a collision between two satellites. The widely used NASA Standard Break-up model [97] [98] provides a distribution of fragmentation impulses and physical characteristics of the cloud which depends on the involved satellite characteristics. A more detailed dissertation about the fragmentation modelling techniques is presented in Ch. 6 and is beyond the objective of this section.

The NASA Standard Break-up Model is here applied to create a fragments cloud which is then observed by BIRALES. The simulation considers the observation of the ISS occurred on April 28$^{\text{th}}$, 2021 at 08:44:32 (UTC), already discussed in Sec. 4.5. The current simulation considers the ISS pass prediction as the parent object ephemeris. BIRALES receiver pointing is kept southwards at an elevation of 83.9 deg, whereas the transmitter pointing angles are 19.3 deg in azimuth and 35.1 deg in elevation, that is the same configuration as the one in Sec. 4.5.

The fragmentation event is set at 08:00:00 (UTC). The generated fragments are propagated and MATER is applied to those detected by BIRALES sensor. To assess the algorithm sensitivity on fragment size, an analysis is carried out considering different RCS: 1 m^2, 0.1 m^2, 0.01 m^2.

For them, Tab. 5.7 reports the correspondence between the number of intersecting passes and slots, and the total number of observed fragments. It is possible to notice that the smaller the RCS, the less the observed objects and the less overlapping the passes are, as a smaller portion of each pass is detected, similarly to what obtained in Sec. 5.2.2 by decreasing the transmitted power.

N. of passes per slot	RCS [m^2]	2	3	4	5	6	7	8	9	TOT
Obj. per slot	1	21	11	4	0	1	0	0	1	102
	0.1	21	9	3	1	1	0	0	1	100
	0.01	23	8	1	0	1	0	0	0	80

Table 5.7: Fragments cloud simulation: slots composed of fragments temporally superimposing each other, by varying the fragment RCS.

RCS [m^2]	Success [%]	$\eta_{\Delta\gamma_1}$ [deg]	$\eta_{\Delta\gamma_2}$ [deg]
1	99	4.5e-02	2.7e-02
0.1	98	4.6e-02	2.8e-02
0.01	100	4.7e-02	2.9e-02

Table 5.8: Fragments cloud simulation: statistical analysis on fragmentation scenario, by varying the detected fragment RCS.

Table 5.8 shows the MATER results for the analysis: the accuracy slightly deteriorates with RCS decreases and, overall, some failures occur. In particular, in the 1 m^2 case MATER does not reconstruct the track of one object: it is a fragment marginally illuminated by the TRF (its projected track crosses a side region of the transmitter FoV) and its SNR is so small that, even if it passes the detection block, it is completely hidden by the other sources, as represented in Fig. 5-10a. This, in the track estimate phase, makes the pattern associated to the weakest source very noisy along all its detection, and the associated maximisation of Eq. 3.14 provide estimations of the other sources angular positions, either correct or ambiguous. For this reason, no DOA estimation of that source is present at the end of the track estimate phase, as can be seen in Fig. 5-10b, and this provokes the failure of MATER for this source observation.

In the 0.1 m^2 case, this fragment is not detected anymore, but another failure occurs involving two fragments whose actual tracks are so close in the receiver FoV that they cannot be separately estimated. Figure 5-11 reports the DOA estimation in time for the two angular coordinates separately. The two failures regard the last two fragments detected, whose estimated DOAs cannot be distinguished during the clustering phase. This issue does not occur in the 1 m^2 scenario, because of the larger SNR, which makes the DOA estimations less noisy for both of the sources and allows the clustering to distinguish them. In the 0.01 m^2 case these fragments are not detected anymore, and no failure occurs.

To conclude, the same analysis is carried out by using the fragment cross section derived

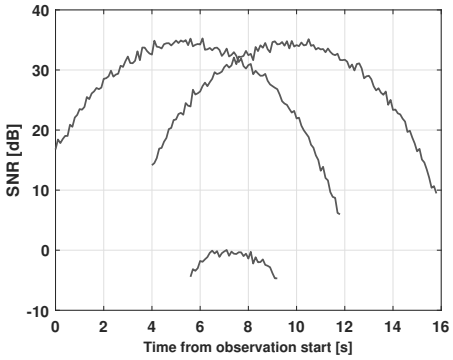

(a) SNR trends.

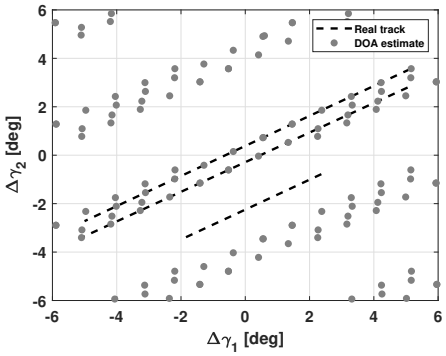

(b) DOA estimations.

Figure 5-10: Fragments cloud simulation: MATER failure case in the analysis which considers 1 m^2 RCS for all the fragments. It is possible to notice that the smallest SNR is completely hidden by the other two (in Fig. 5-10a) and that no DOA estimation related to the shortest track is present, as it is related to the weakest source detected (in Fig. 5-10b)

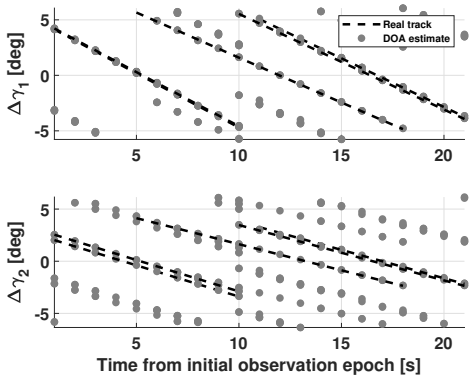

Figure 5-11: Fragments cloud simulation: DOA estimation of the failure case in the analysis which considers 0.1 m^2 RCS for all the fragments. It is possible to notice that the last two detected sources are so close in time that cannot be distinguished in the clustering phase.

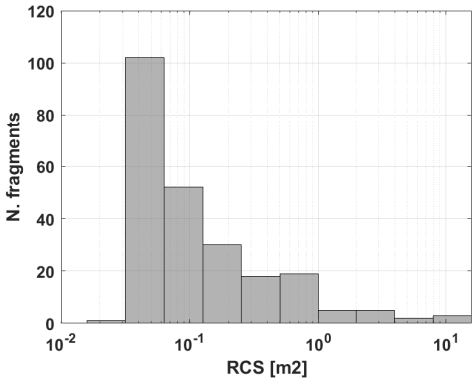

Figure 5-12: Operational fragments cloud simulation: logarithmic distribution of the detected target RCS, which are assumed equal to the fragments cross section modeled according to the NASA Standard Break-up model.

N. of passes per slot	1	2	3	4	5	6	7	8	9	TOT
Obj. per slot	88	20	9	3	0	1	0	0	1	182

Table 5.9: Operational fragments cloud simulation: slots composed of fragments temporally overlapping each other, considering the NASA Standard Break-up Model fragment cross section as RCS. Also the single source cases are considered.

from the NASA Standard Break-up Model as the RCS, and considering also the single source transit, that is like in a realistic fragments cloud observation. The RCS logarithmic distribution is reported in Fig. 5-12, where it can be appreciated that the vast majority of the targets have a RCS much smaller than 1 m^2. The correspondence between the number of intersecting passes and slots is reported in Tab. 5.9 and the results are shown in Tab. 5.10, where no failure occurs and the track accuracy is even better than the previous analysis case. This improvement in accuracy is basically due to the inclusion of the single source scenario, which does not suffer any mutual sources interference (as each target is detected alone), and this improves the angular accuracy.

To recap, MATER algorithm for multiple sources observation can be applied to the SST

Success [%]	$\eta_{\Delta\gamma_1}$ [deg]	$\eta_{\Delta\gamma_2}$ [deg]
100	4.7e-03	2.9e-02

Table 5.10: Operational fragments cloud simulation: fragmentation scenario, considering the NASA Standard Break-up Model fragment cross section as RCS. Also single transits are considered.

service of Fragmentation Analysis. Both the accuracy and the resolution depend on the size of the observed fragment, as this is strictly linked to the SNR detected by the receiver array. The analysis also highlights that a source with a very low SNR and which flies simultaneously to other sources with much larger SNR cannot be properly detected, as its signal is hidden by theirs.

This section has shown the capability of MATER algorithm to provide the angular track for a detected fragment, and this may allow to couple such a measurement with SR (and eventually with DS) to run an IOD. Besides accomplishing the catalogue maintenance purpose, the reconstructed orbital state of the detected fragment can be further exploited within the Fragmentation Analysis service tasks to detect the fragmentation epoch. This possible application is deepened in Ch. 6 with the FRED algorithm presentation and in Ch. 7 with numerical simulations, also involving MATER algorithm.

Chapter 6

Fragmentation Epoch Detector Algorithm

Given the benefit of MATER algorithm for the Fragmentation Analysis service, described in Sec. 5.3.2, possible additional contributions of on-ground multi-receiver radars to the fragmentation events monitoring are here assessed. In particular, the present chapter deals with the fragmentation epoch identification problem focusing on the case in which, besides the last available ephemeris of the parent object, just one single fragment orbital state, obtained by one single surveillance radar observation, is available and already linked to the event. In such a scenario, a single measurements track of slant range and of angles, retrieved through MATER algorithm, is sufficient to initially determine the orbit, but the uncertainty associated to the computed orbital state cannot be neglected by the process, as discussed in Sec. 6.1. For this reason, FRED algorithm is described in Sec. 6.2, involving a stochastic approach which first obtains fragmentation epoch candidates and then rank them according to the statistical matching between the relative distance and the minimum orbital intersection distance distributions. Finally, analogies and difference with conjunction analysis methodologies are discussed.

6.1 Fragmentation epoch identification problem

In the last years, fragmentation events have become of utmost concern. As mentioned in Ch. 1, from the start of the space era, more than 630 break-ups, explosions, collisions,

or anomalous events resulting in fragmentation have been recorded [1], which have further contributed to increase the number of space debris. Therefore, it is fundamental to predict the fragments cloud evolution, in order to assess possible collisions, as done in [99] and [100], where the information on fragment position is translated into a continuous function, using an analytical expression for the fragment density probability along the orbit. By this way, the evolution of the cloud density with time, under the effect of atmospheric drag, is obtained through the continuity equation.

To apply the models predicting the fragments cloud evolution, the epoch when the break-up occurred shall be identified. In [101] the event epoch is evaluated as the point of minimum distance of all the fragments with respect to the cloud centre of mass. Besides the accurate orbital ephemeris, this approach also assumes to own the physical information of each fragment, such as the mass and the cross sectional area. In [102] the break-up epoch is determined by detecting a convergence of fragments in the space of inclination and right ascension of the ascending node. In [103] a critical study is conducted to identify the best criterion to assess the event epoch from the fragments ephemerides and a sensitivity analysis on the cloud orbital position is also conducted. In [104] a process is proposed, which screens a catalogue of ephemerides and identifies those related to fragments, through the filters presented in [105]. After the filtering phase, the same criteria are applied combined with SGP4 propagation [52] and, by comparing the algorithm outputs among all the fragments, the fragmentation epoch is identified. All these approaches need many fragments ephemerides, and use them as a deterministic information.

The numerous accurate ephemerides availability of the space debris originated by the fragmentation event is a quite optimistic assumption, as, from an operational point of view, it could be necessary to estimate the fragmentation epoch just few hours after the event and very few ephemerides (even only one) could be available. In addition, when a fragments cloud is observed, the correlation of measurements to a single fragment is a very challenging task, and this further decreases the number of ephemerides which can be used in a reliable way. Next, such ephemerides could be inaccurate, because of the noise of the observation measurements and the error introduced by the IOD algorithm exploited, and their uncertainty cannot be neglected during the event characterisation. Nevertheless, a prompt knowledge of the fragmentation epoch would be fundamental to plan additional observations of the fragments cloud, e.g. by tasking the sensors to point at the right ascension and dec-

lination where the parent was when broke up. In addition, this would also be important to refine the processing of the observation measurements, aiming at obtaining more and more accurate orbit determination results. This would lead to also refine the estimation of the fragmentation epoch and, so, a virtuous cycle would be generated.

The aim of this chapter is to provide an operational procedure to estimate the fragmentation epoch starting from the last available ephemeris of the parent object (assumed as a deterministic quantity) and a single fragment orbital state provided with uncertainty. The latter is considered as determined by a multi-receiver array surveillance radar, as, besides being the topic of this thesis, it allows to run IOD from a single observation with no transit prediction. To accomplish this purpose, the FRagmentation Epoch Detector (FRED) algorithm, implementing a stochastic approach, has been developed and is described as follows. To support the reader, the nomenclature lists the description of the involved quantities.

6.2 Fragmentation epoch detector algorithm

Let's consider the fragmentation of a space object whose last available ephemeris $\boldsymbol{x}^p$ is dated to t_{eph}, and is considered as a deterministic information. The event has occurred at $t_0 > t_{eph}$ and the related alert has been notified at $t_a > t_0$. Some hours later, one fragment is detected by a surveillance radar at t_{obs} (with $t_{obs} > t_a$) and its orbital state $\left\{\boldsymbol{x}^{fg}, \boldsymbol{P}^{fg}\right\}$ is first determined, where the mean $\boldsymbol{x}^{fg}$ and covariance $\boldsymbol{P}^{fg}$ are directly derived from the IOD process.

If the orbit determination were very accurate and the physical parameters were well known, it would be theoretically possible to propagate both the fragment and the parent object in the time window $[t_{eph}, t_a]$ and search for the epoch of the minimum relative distance, which would correspond to the fragmentation epoch t_0. However, in real applications, both the measurements accuracy and the IOD process introduce an error in the reconstruction of the observed fragment state vector, and the above-mentioned method turns out to be unreliable. Figure 6-1 represents the relative distance trend on an analysis time window between the parent object last available ephemeris and an observed fragment mean state to which an IOD error of 1.85e-02 km in position and 4.99e-04 km/s in velocity is attributed (continuous line). It can be observed that the epoch of the minimum relative distance between the fragment mean state and the parent (dashed dense line) is completely different from the

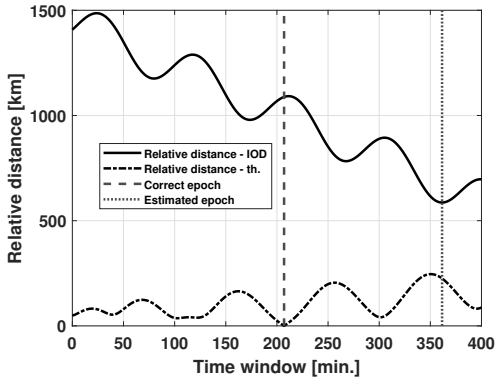

Figure 6-1: Relative distance between the parent object and the mean state of one observed fragment. Their state vectors are propagated on a time window ranging from the last available ephemeris of the parent object to the event alert. The dashed curve line shows the theoretical trend and the dashed straight line corresponds to the epoch of minimum value, that is the fragmentation epoch. On the contrary, the continuous black line shows the relative distance trend when an IOD error is attributed to the fragment mean state, and the dashed dense line corresponds to the minimum value, that is the estimated fragmentation epoch. It is possible to see that the estimated fragmentation epoch is completely different from the correct value.

correct fragmentation epoch (dashed line), that is the epoch corresponding to the theoretical minimum relative distance (dashed black line). A further source of error is represented by the mismatching between the actual fragment trajectory and the propagation model used, due, for instance, to the fact that the actual physical parameters of the observed fragment are not known. For all these reasons, assessing the fragmentation epoch by just searching for the minimum relative distance between $\boldsymbol{x}^p$ and $\boldsymbol{x}^{fg}$ in the time window $[t_{eph}, t_a]$ is an unreliable methodology.

The considerations above imply that the orbit determination uncertainty cannot be a-priori neglected. For this reason FRED algorithm deals with the fragmentation epoch identification problem through a stochastic approach, starting from a Monte Carlo distribution of the orbit determination result. Ideally, at the fragmentation epoch, both the Minimum Orbital Intersection Distance (MOID) [106] and the relative distance between the parent and the fragment are expected to be zero. Due to the considerations above, in practical cases neither MOID nor relative distance turn out to be null, but they should statistically match each other. Therefore, the correct fragmentation epoch is expected to feature a matching between the MOID and the relative distance distributions.

FRED algorithm flowchart is reported in Fig. 6-2, and is structured as follows.

1. In order to include the fragment state uncertainty in the event epoch identification, N_s samples $\boldsymbol{x}^s$ are generated from the orbital state $\left\{\boldsymbol{x}^{fg}, \boldsymbol{P}^{fg}\right\}$ according to a multinormal distribution [59].

2. The time window $[t_{eph}, t_a]$ is sampled with frequency $1/T^p$ (where T^p is the parent orbital period). This results in the epochs t_i, whose number is n_{orb}.

3. Both parent and fragment samples orbital states are propagated to each t_i.

4. For each t_i and for each j-th fragment sample, the epochs of transit through the MOID of both the parent and the fragment j-th sample are computed analytically, according to [106], and indicated as t_j^p and t_j^s. The parent and the j-th sample state vectors are propagated up to t_j^p and t_j^s respectively, resulting in the orbital states $\boldsymbol{x}^p(t_j^p)$ and $\boldsymbol{x}^s(t_j^s)$, and the analytical computations of t_j^p and t_j^s are updated. The epochs t_j^p and t_j^s are iteratively modified in this manner until, between two consecutive steps, they do not change anymore (according to a tolerance set equal to 1e-03 s).
   This iterative process results in $N_s \times n_{orb}$ couples of $\left(t_j^p,\ t_j^s\right)$ and $\left(\boldsymbol{x}^p(t_j^p),\ \boldsymbol{x}^s(t_j^s)\right)$. It is important to observe that the difference between $\boldsymbol{p}^s(t_j^s)$ and $\boldsymbol{p}^p(t_j^p)$ (the $\boldsymbol{x}^s(t_j^s)$ and $\boldsymbol{x}^p(t_j^p)$ positions) allows to compute the MOID (usually described in a scalar way [106]) in 3 dimensions: $\boldsymbol{m}_j = \boldsymbol{p}^s(t_j^s) - \boldsymbol{p}^p(t_j^p)$.

5. The fragment j-th sample state vector $\boldsymbol{x}^s(t_j^s)$ is propagated up to the epoch of parent transit through the MOID, resulting in $\boldsymbol{x}^s(t_j^p)$. It is worth to observe that the difference between the $\boldsymbol{p}^s(t_j^p)$ (the $\boldsymbol{x}^s(t_j^p)$ position) and $\boldsymbol{p}^p(t_j^p)$ provides the three-dimensional relative distance between the j-th sample and the parent, at the epoch of parent transit through the MOID: $\boldsymbol{\rho}_j = \boldsymbol{p}^s(t_j^p) - \boldsymbol{p}^p(t_j^p)$. Figure 6-3 provides a two-dimensional sketch of the parent and fragment sample orbits, with the involved quantities.

6. To exclude unfeasible solutions, the $N_s \times n_{orb}$ couples enter a filtering phase, which is based on the epoch of parent transit through the MOID t_j^p. Being related to the parent ephemeris, that is the information considered more reliable (and so assumed as deterministic), it is selected instead of the time of the fragment j-th sample transit through the MOID t_j^s:

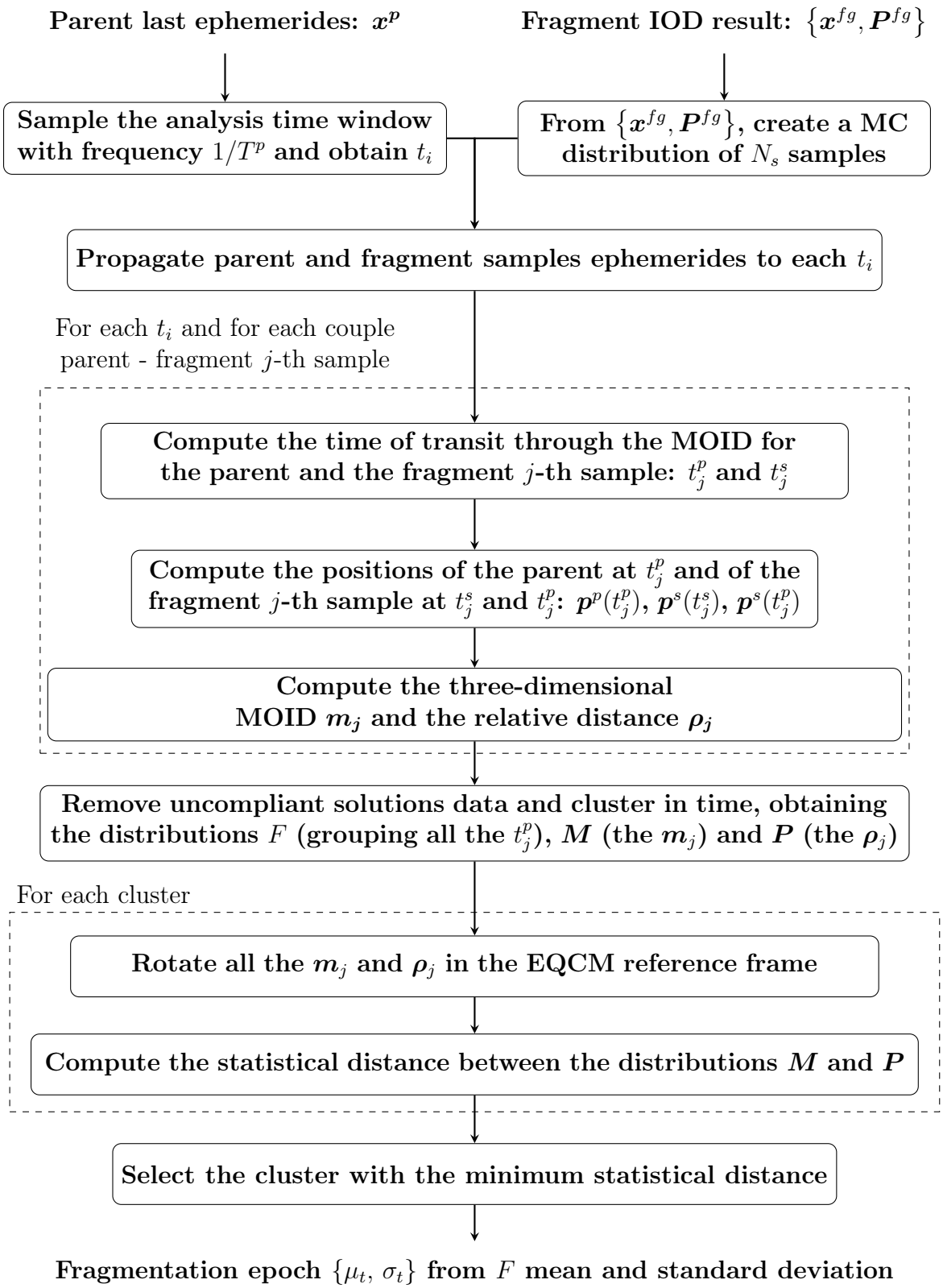

Figure 6-2: FRED algorithm flowchart.

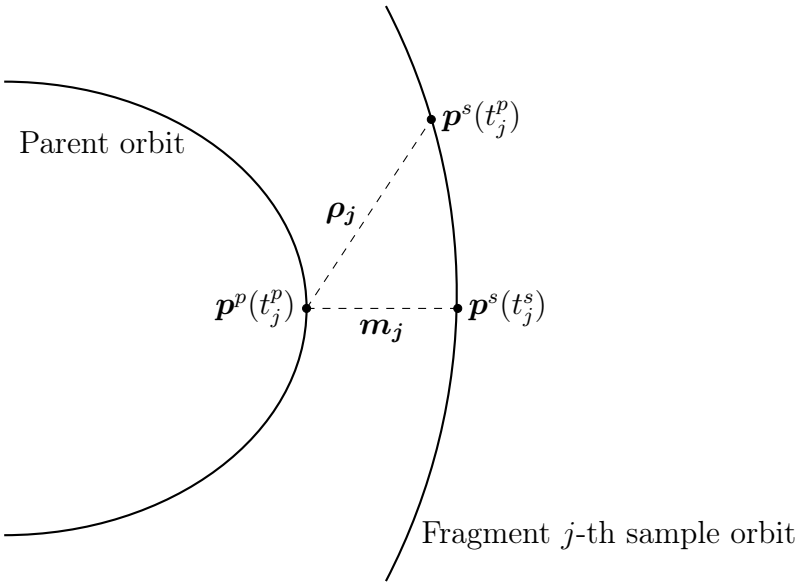

Figure 6-3: Sketch of the parent and fragment sample orbits, with the quantities involved in FRED algorithm process.

(a) First, the couples for which t_j^p is not included in the boundaries $[t_{eph}, t_a]$ are filtered out.

(b) Then, the couples computed from the state vectors propagated at epoch t_i and for which $t_j^p < (t_i - T^p/2)$ or $t_j^p > (t_i + T^p/2)$ are removed from the data set. This operation is done because the MOID data are computed for each periodicity. Thus, if t_j^p is computed from orbital states at t_i, it must belong to the i-th periodicity, that is the time difference $|t_i - t_j^p|$ shall be smaller than half of the orbital period T^p.

7. All the remaining n_{filter} epochs t_j^p are clustered according to a Density-Based Spatial Clustering of Applications with Noise (DBSCAN) [107]. From this operation, n_{orb} are expected to be identified. However, for those situations in which parent and fragment orbits are similar (especially in inclination and ascending node right ascension), multiple clusters are possibly identified for each i-th periodicity, as the epochs t_j^p change significantly from a j-th sample to another one. So, more generally, n_{cl} clusters are considered to be identified. Figure 6-4a presents the obtained clusters, in the plane t_j^p (in Coordinated Universal Time, UTC) versus scalar MOID. It is worth to remark that the MOID values are equal from a periodicity to the other, as the graph is related

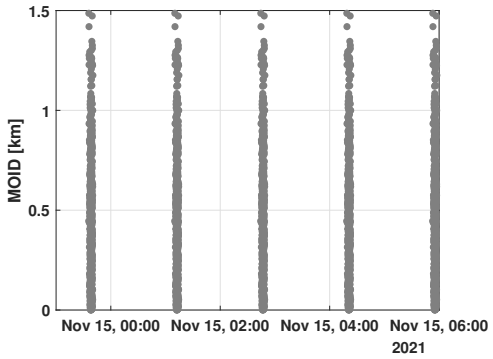

(a) Distribution of the t_j^p epochs in the time window of the analysis.

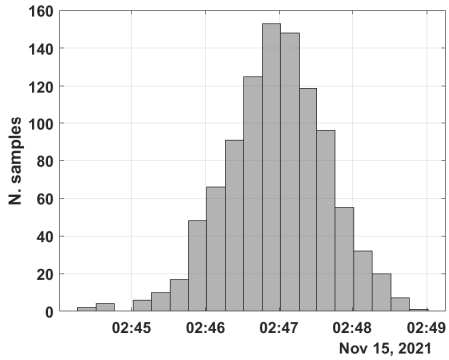

(b) Distribution of the t_j^p epochs for the cluster related to the correct solution.

Figure 6-4: Results of the clustering phase. The epochs are reported in UTC.

to a Keplerian scenario, in which, for a single parent j-th sample couple, the MOID does not change.

8. For each n-th cluster, the candidate fragmentation epoch t_n^{fg} can be computed (in terms of mean and standard deviation) from the distribution of the epoch of parent transit through the MOID, which is indicated as F, and which is represented in Fig. 6-4b (for the correct cluster). In addition, $\boldsymbol{M}$ and $\boldsymbol{P}$ distributions (grouping the $\boldsymbol{m_j}$ and $\boldsymbol{\rho_j}$ respectively) are associated to each cluster. Figure 6-5 shows the two distributions in Earth-Central-Inertial (ECI) reference frame, both for the correct candidate and for a non-correct one. It is possible to observe that the three-dimensional MOID distribution $\boldsymbol{M}$ is much more concentrated than the relative distance one $\boldsymbol{P}$. This is due to the fact that, from sample to sample, the change in t_j^p causes a remarkable modification in the relative distance $\boldsymbol{\rho_j}$ (as it is time-dependent), but not in the MOID $\boldsymbol{m_j}$, which is the geometrical difference between the parent and the j-th sample orbits and, so, does not vary remarkably from a sample to another.

9. Afterwards, for each cluster:

   (a) All the $\boldsymbol{m_j}$ and $\boldsymbol{\rho_j}$ are rotated in the Modified Equidistant Cylindrical (EQCM) reference frame [108]. This operation results in MOID and relative distance distributions like in Fig. 6-6. The MOID distribution $\boldsymbol{M}$ is almost two-dimensional, as, in all the $\boldsymbol{m_j}$, the y-component, expressing the along orbit curvature relative distance, is negligible.

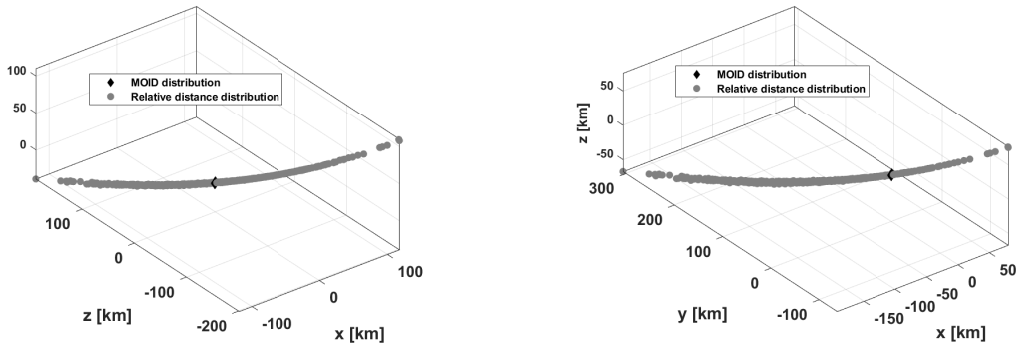

(a) Cluster related to the correct epoch. (b) Cluster related to a wrong epoch.

Figure 6-5: $\boldsymbol{M}$ and $\boldsymbol{P}$ distributions in ECI reference frame, for the correct cluster and a non-correct one.

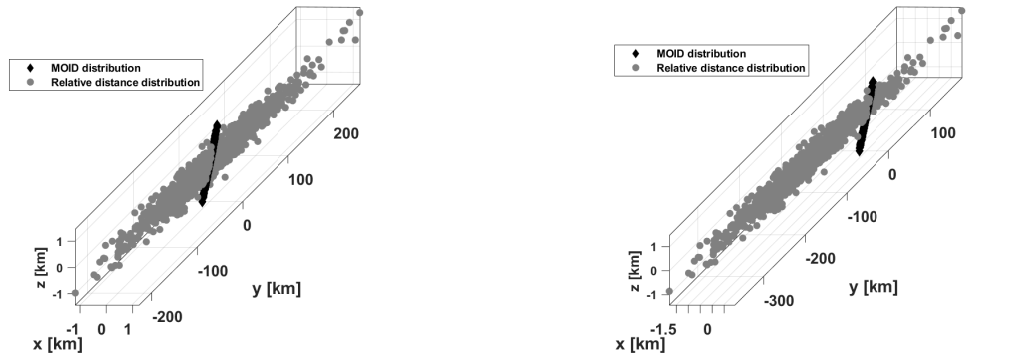

(a) Cluster related to the correct epoch. (b) Cluster related to a wrong epoch.

Figure 6-6: $\boldsymbol{M}$ and $\boldsymbol{P}$ distributions in EQCM reference frame, for the correct cluster and a non-correct one.

(b) The statistical distance between $\boldsymbol{M}$ and $\boldsymbol{P}$ distributions is computed according to one of the metrics discussed below.

10. Repeating the operations above for each cluster results in Fig. 6-7, which shows the statistical distance computed through the Earth Mover's Distance (EMD) [109] (discussed below) in function of the F distribution mean. Finally, the cluster featuring the minimum statistical distance between the $\boldsymbol{M}$ and $\boldsymbol{P}$ distributions is selected, and the fragmentation epoch is returned from the related distribution F, in terms of mean μ_t and standard deviation σ_t.

As mentioned above, this process provides a pattern to derive the fragmentation epoch (in

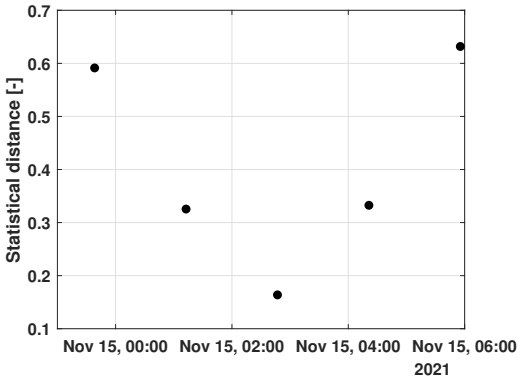

Figure 6-7: EMD statistical distance computed for each cluster.

terms of mean and standard deviation) through a stochastic approach, starting from the last available parent ephemeris and the fragment IOD result. However, there are two theoretical sources of failure:

- The MOID computation turns out to be unstable when the orbital planes of the fragment and parent orbits are very close each other (that is, they have similar inclination and right ascension of the ascending node). In this case, the change in the fragment orbit, occurring from sample to sample, may provoke a remarkable variation in the MOID data computation. As result, for the correct candidate, F distribution does not cluster around the actual fragmentation epoch, but around an epoch distant up to tens of minutes.

- The relative distance distribution $\boldsymbol{P}$ does not change from a cluster to another when the fragment and parent orbital periods are very close each other (that is, they have similar semi-major axis). In this case, for a j-th sample, from a i-th periodicity to the following one, the relative distance $\boldsymbol{\rho_j}$ does not change significantly. As result, it is not straightforward to recognise the correct cluster from the statistical distance metrics, and the wrong fragmentation epoch is possibly returned by the process.

As introduced above, FRED needs a statistical distance metrics to assess the best epoch candidate. A possible choice would be represented by the Mahalanobis Distance, which has been already introduced in Eq. 2.19, but it applies to Gaussian distributions only. Even if supported by the rotation to EQCM reference frame, assuming Gaussian distributions would be a particularly strong assumption for $\boldsymbol{M}$ and $\boldsymbol{P}$ distributions. To be as generic and agnostic as possible regarding the distributions characteristics, metrics suitable both for

Gaussian and no Gaussian distributions are investigated.
A first choice is represented by the Earth Mover's Distance (EMD) [109], which measures the flow to pass from a distribution to the other one. Such a flow can be evaluated based on different distance metrics, and the Euclidean distance weighted on the distribution variance is chosen to better account for $\boldsymbol{M}$ and $\boldsymbol{P}$ distributions shape and elongation. The implementation provided in [110] is used.
A third metrics is investigated, which has been developed specifically for FRED algorithm. It is addressed as the *quantile* metrics given its workflow, which is described as follows.

1. For both $\boldsymbol{M}$ and $\boldsymbol{P}$ distributions a Principal Component Analysis (PCA) is performed to rotate them in their respective principal coordinate reference frame [111]. Then, for each distribution, the quantiles 10%, 25%, 50%, 75% and 90% are computed for the three coordinates separately. This operation does not account for the correlations among coordinates, but these have been minimised thanks to the rotation to the principal coordinate reference frame. This results in two sequences (for $\boldsymbol{M}$ and $\boldsymbol{P}$) of three-dimensional points, expressed in two different principal coordinate reference frames.

2. The two sequences of three-dimensional points (expressing the quantiles) are rotated back to the original EQCM reference frame, in order to have them in a common coordinate system. Figure 6-8 shows the two sequences of three-dimensional points, for the correct and for a wrong epoch. Then, the five quantile-to-quantile Euclidean distances are computed and summed together in a weighted manner according to the quantile percentage (that is, by advantaging more the central quantiles with respect to the side ones). This weighted sum provides the statistical distance which accounts for the similarity between the two non-Gaussian distributions $\boldsymbol{M}$ and $\boldsymbol{P}$.

A critical comparison among the metrics presented above is proposed during the numerical analysis in Sec. 7.2.

Analogies and differences with conjunction analysis

From the FRED description, the reader may easily notice that dealing with the fragmentation detection problem in such a stochastic way presents analogies with the conjunction

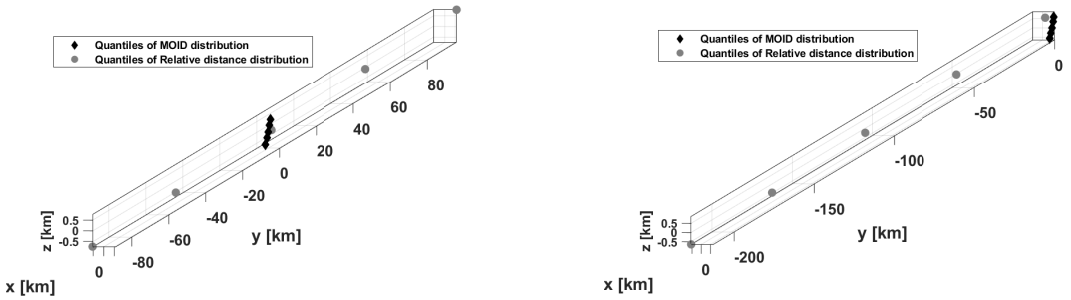

(a) Cluster related to the correct epoch.

(b) Cluster related to a wrong epoch.

Figure 6-8: Quantile sequences for $\boldsymbol{M}$ and $\boldsymbol{P}$ distributions in EQCM reference frame.

analysis. In particular, the process involves the MOID and the relative distance, which are quantities usually exploited also in the screening part of the conjunction assessment [105], as well as in other fragmentation epoch identification algorithms (like [103] and [104]) which use the availability of many fragments orbital states (then processed in a deterministic way). However, at this level a first difference arises. Indeed, in FRED, the screening is fully stochastic and is only based on the time of parent transit through the MOID. In addition, the FRED screening phase does not aim at identifying possible conjunctions, as the fragmentation is already known to have occurred, but to rank conjunction (that is fragmentation epoch) candidates. Thus, the MOID and the relative distance are not quantities used to search for a possible conjunction in a deterministic way, but they are stochastically represented at the fragmentation epoch candidates, and then their statistical distance is computed.

At this point, a second analogy may be noticed, as in both cases a stochastic quantity is expressed at the time of closest approach: the PoC in the conjunction analysis and the statistical distance between MOID and relative distance distributions in FRED. However, besides the two metrics differently defined, a remarkable difference arises: while in conjunction analysis the PoC is a quantity assessing the danger associated to a single conjunction and, so, expresses an absolute meaning, in FRED the statistical distance is used to rank the fragmentation epoch candidates previously identified, and so it has a relative meaning.

Certainly, further studies may be conducted in the future to assess alternative procedures to the statistical distance metrics. A possible choice would be to rank the fragmentation epoch candidates according to a long-term PoC computation associated to them, that is analo-

gous to the short-term PoC based method presented in [112] for the manoeuvre detection in geostationary orbits. Vice versa, the statistical distance metrics used in FRED may be investigated as a possible application for long-term encounter models.

Chapter 7

FRED Simulations and Results

This chapter assesses FRED performance through numerical simulations, run in MATLAB [87], by eventually including MATER algorithm in the analysis. Section 7.1 describes the investigated fragmentation scenario, related to the Russian satellite COSMOS 1408, which broke up on November 15^{th}, 2021, and the related data set generation.

Concerning the simulations, Sec. 7.2 evaluates a fully Keplerian scenario with no orbit determination error associated to the fragment orbital state. The Earth Mover's Distance is identified as the most performing metrics and is selected for all the following analyses. Generally, the algorithm converges to the correct solution, but it gets less robust when fragment and parent orbits are similarly oriented, or have a similar shape. Also, these cases correspond to a larger standard deviation associated to the solution. A sensitivity analysis shows that there is no dependence on the number of samples used in representing the fragment orbital state.

Then, Sec. 7.3 assesses a perturbed scenario with no orbit determination error, which is instead introduced in Sec. 7.4 using simulated measurements provided with Gaussian noise. This provokes a remarkable deterioration in converging to the correct fragmentation epoch, which is however always present among candidates. Furthermore, alternative deterministic metrics are performing worse, especially when the fragmentation epoch is identified as the time of minimum relative distance between parent ephemeris and fragment mean state propagated on the analysis time window (that is analogously to the approach described at the beginning of Sec. 6.2). Next, a sensitivity analysis in Sec. 7.5 shows a FRED performance deterioration by increasing the angular noise associated to the solution, or enlarging the

time elapsed between the event and the observation. However, FRED is always much more performing than the deterministic metrics. Furthermore, no remarkable change is present for a fragment physical parameter mismatching between the actual value and the one used in the algorithm.

Afterwards, Sec. 7.6 presents an operational scenario which involves BIRALES, whose observations are scheduled according to the prediction of parent transit, and simulating the measurements as soon as the fragment enters in the receiver FoV. Results are consistent with the previous analyses.

Finally, Sec. 7.7 assesses an operational scenario in which the angular track is obtained with MATER. Since for BIRALES there is no visibility of COSMOS 1408 fragments cloud on the first hours after the event (that is when FRED algorithm aims at providing a contribution to the Fragmentation Analysis service), an ISS fragmentation is simulated. Results get deteriorated because the angular track has non-Gaussian and non-zero mean error. Nevertheless, performance are much more appreciable with respect to the deterministic metrics ones.

7.1 Data set generation

A numerical simulation is here conducted to test FRED algorithm described in Ch. 6. The fragmentation scenario is the one which involved the Russian satellite COSMOS 1408 during the kinetic anti-satellite (ASAT) test which occurred around 02:47 UTC of November 15$^{\text{th}}$, 2021 [113]. The ASAT test took place when the satellite was flying over the north-west Russia and the sensors of the EUSST consortium [22] (introduced in Sec. 1.4.1) observed the fragments generated by such an event.

The data set to test FRED algorithm is generated as follows:

1. The last available COSMOS 1408 ephemeris before the event are retrieved from the last TLE (Two-Line Elements) available on Spacetrack, which are dated to 00:55 UTC of November 15$^{\text{th}}$ [13]. To make the analysis time window more symmetrical with respect to the break-up epoch, they are propagated one orbital period back to the 23:20 UTC of November 14$^{\text{th}}$, and the orbital state at this epoch is considered as $\boldsymbol{x^p}$.

2. The state vector $\boldsymbol{x^p}$ is propagated up to 02:47:00 UTC of November 15$^{\text{th}}$. Table 7.1

a [km]	e	i [deg]	Ω [deg]	ω [deg]
6844.7	1.8e-03	82.7	123.3	134.5

Table 7.1: COSMOS 1408 orbital parameters.

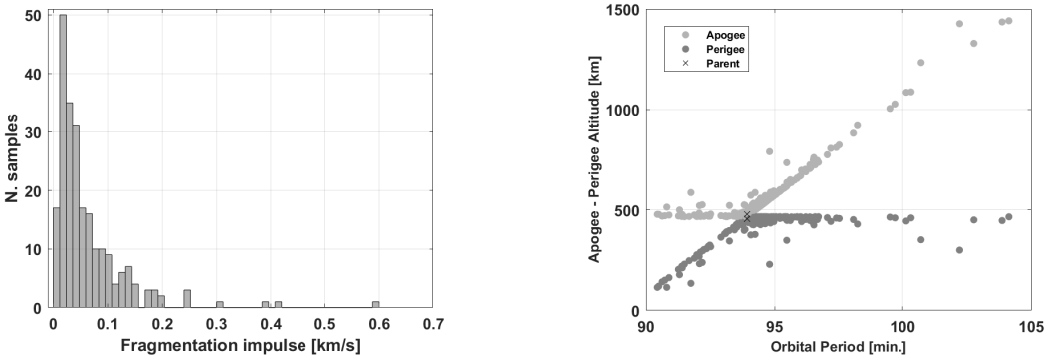

(a) Impulses magnitude distribution.

(b) Gabbard diagram.

Figure 7-1: Fragmentation event.

reports COSMOS 1408 orbital parameters (with the exception of the true anomaly), at the simulated fragmentation epoch.

3. The fragmentation event is modelled as a set of impulses applied to the satellite orbital state at 02:47:00 UTC. These impulses are retrieved from the NASA standard break-up model [97] [98]. A data set of 231 fragments is generated by this way, and its characteristics are described in Fig. 7-1, both in terms of impulse magnitude distribution of the fragmentation event and Gabbard diagram.

The obtained ephemerides, representing the fragments, are propagated until the epoch t_{obs}, when they are detected by a surveillance radar, and the orbital states $\left\{\boldsymbol{x}^{fg}, \boldsymbol{P}^{fg}\right\}$ are determined.

In this way all the inputs for the process described in Sec. 6.2 are obtained and FRED algorithm can be tested, considering an analysis time window ranging from 23:20 UTC of November 14^{th} (epoch of the simulated last available ephemeris of the parent object) to 06:00 UTC of November 15^{th}, retracing the fact that the COSMOS 1408 fragmentation alert was provided in the early morning (considering UTC time coordinates). These two epochs correspond to t_{eph} and t_a introduced in Sec. 6.2. Instead, the t_{obs} changes from an analysis to the other, as discussed below.

Based on this data set, FRED is run on each fragment IOD result $\left\{\boldsymbol{x}^{fg}, \boldsymbol{P}^{fg}\right\}$ separately,

considering N_s=1e+03 samples for the multinormal distribution.

7.2 Unperturbed scenario with no IOD error

First, the unperturbed scenario with no IOD orbital state error is tested to assess the theoretical characteristics of FRED algorithm in ideal conditions. This simulation just associates a covariance $\boldsymbol{P}^{fg}$ (with standard deviations 2.6e-02 km and 7.0e-04 km/s, for position and velocity respectively, computed simulating an IOD with the method presented in [69]) to the nominal value $\boldsymbol{x}^{fg}$, that is the fragments propagated state vectors. Thus, the fragment mean state $\boldsymbol{\mu}^{fg}$ is the actual fragment position and velocity at t_{obs}. The parent last available ephemeris $\boldsymbol{x}^{p}$ is the same used above to generate the fragmentation, and the observation epoch t_{obs} is set 13 h after the fragmentation, as the method aims at reconstructing the fragmentation epoch from a single fragment observation conducted in the hours right after the event.

For a single fragment analysis, the result is considered successful if the difference between the epoch estimation and the correct value (t_{err}) is below a threshold quantity, which is set equal to 1 min in the analysis, coherently with the time uncertainty associated to the estimated fragmentation epoch in [114]. As introduced in Sec. 6.2, possible FRED failures can be linked to either the MOID computation or to the distributions comparison performed through the statistical metrics, and for this reason they are classified as follows:

- MOID failures - compliant: 1 min $< t_{err}$ and $t_{err} < 3\sigma_t$. These are cases for which the fragment orbit orientation is so similar to the parent one that a slight change in the fragment orbit, occurring from fragment mean state to its samples, causes a remarkable variation in the MOID data computation. This leads to an erroneous estimation of the mean epoch of parent transit through the MOID, but the distribution is wide enough to include such an error. Therefore, the resulting epoch estimation is wrong, but statistically compliant.

- MOID failures - uncompliant: 1 min $< t_{err}$ and $3\sigma_t < t_{err} < T^p/2$. In these cases, the erroneous estimation of the epoch is not mitigated by its uncertainty. The epoch estimation is wrong, but the error is smaller than the half of the parent orbital period.

Metrics	Correct solutions	MOID failures compliant	MOID failures uncompliant	Periodicity failures
Mahalanobis Distance	91.1%	4.2 %	1.3 %	3.4 %
EMD	92.8 %	4.7 %	0.4 %	2.1 %
Quantiles	89.5 %	4.2 %	0.8 %	5.5 %

Table 7.2: Unperturbed scenario results for the different statistical distance metrics.

- Periodicity failures: $t_{err} > T^p/2$. In these cases, the statistical comparison among clusters identifies a wrong candidate and, so, a wrong result is returned. It is worth to remark that MOID failures may occur also when a wrong candidate is identified. Nevertheless, also this situation is addressed as a periodicity failure, as the time error is anyways larger than half of the parent orbital period.

The results are reported on Tab. 7.2, for each statistical distance metrics introduced in Sec. 6.2. It can be observed that all the metrics feature comparable results, but the EMD ones are the most appreciable.

An analysis is also conducted to assess the Gaussianity of the problem, in order to evaluate whether the Mahalanobis Distance metrics, which needs the Gaussian assumption of the involved distributions, is a suitable choice. For each fragment, the Mahalanobis Distances between each $\boldsymbol{\rho_j}$ and each $\boldsymbol{m_j}$ and the distributions $\boldsymbol{P}$ and $\boldsymbol{M}$ respectively is computed, and a χ^2 test is conducted to check how many Mahalanobis Distances are smaller than the 3σ level, for all the n_{cl} clusters. To fulfil the Gaussian assumption, this condition shall be matched in the 99% of cases. Figure 7-2 shows the number of fragments (in logarithmic scale) in function of the mean percentage of samples (across the clusters) satisfying the 3σ level, both for the MOID distribution $\boldsymbol{M}$ and for the relative distance distribution $\boldsymbol{P}$, by also focusing on the portion of the diagram closest to the expected value of 99%. It can be observed that no fragment satisfies the 99% requirement in the MOID distribution $\boldsymbol{M}$, with lot of cases showing a low percentage of samples within the 3σ level. For some fragments the relative distance distribution $\boldsymbol{P}$ features Gaussianity, but the 99% requirement is not fulfilled in most cases.

This analysis proves that a non-Gaussian metrics shall be considered and, so, the Mahalanobis Distance is rejected. Furthermore, given the results in Tab. 7.2, the Earth Mover Distance metrics is selected, as it features the best performances. Therefore, next analyses

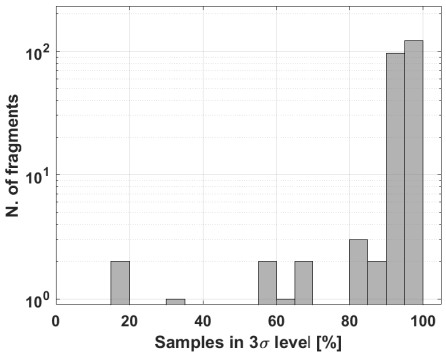

(a) MOID distribution.

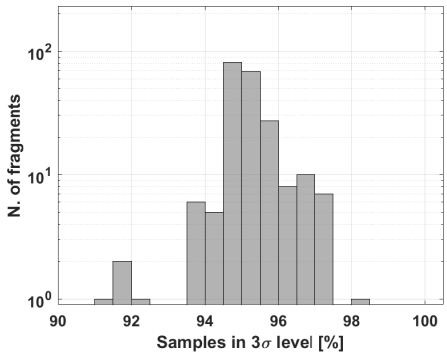

(b) Focus on the MOID distribution.

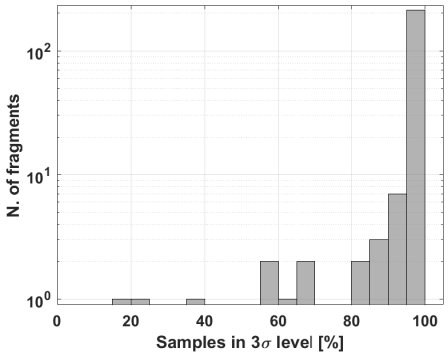

(c) Relative distance distribution.

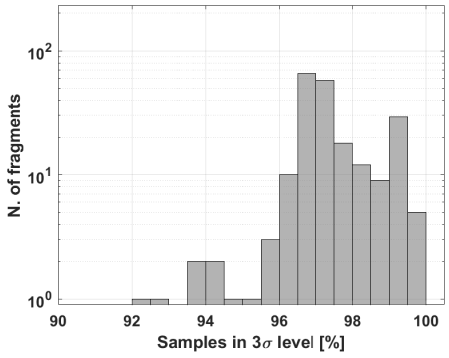

(d) Focus on the relative distance distribution.

Figure 7-2: Number of fragments (in logarithmic scale) in function of the mean percentage of samples (across the clusters) satisfying the 3σ level, both for the MOID distribution $\boldsymbol{M}$ and for the relative distance distribution $\boldsymbol{P}$, by also focusing on the portion of the diagram closest to the expected value of 99%.

always apply EMD to identify the best epoch candidates.

EMD results and failures assessment

Figure 7-3a shows, for each fragment analysed, the time error between the estimated and the correct fragmentation epochs. It is possible to notice that, over the 231 fragments analysed, 12 MOID failures occur, out of which 11 are compliant and 1 is not. Then, 5 periodicity failures are present, and they are cases for which the EMD metrics returns similar values across the candidates, among which the correct solution is always present. Figure 7-3b shows the relationship between the time standard deviation associated to the estimated epoch and the magnitude of the impulse which generated the fragment. It is possible to notice that the compliant MOID failures are more likely to occur in those regions with small impulse magnitude and large time standard deviation associated to the solution. On the contrary, both uncompliant MOID and periodicity failures generally present a much smaller time uncertainty (with one exception), but still with a not high fragmentation impulse.
As for Ch. 4 and Ch. 5 analyses, a detailed computational demand study is not carried out, given the current prototype implementation in MATLAB [87], but it can be quantified in about 30 s per fragment by using a single core with the same Intel(R) Core(TM) i7-8700 CPU @ 3.20 GHz - 3.19 GHz processor as the one used for Ch. 4 and Ch. 5 analyses. This low computational demand is linked to the analytical propagation exploited in the unperturbed scenario (see Sec. 2.2).
To better assess the failures characteristics, the difference between parent and fragments orbital parameters is studied. From Fig. 7-4a and Fig. 7-4b it is possible to observe that the periodicity failures regard cases in which the fragment orbit semi-major axis and eccentricity are very close to the parent values. Indeed, in this situation, the two orbits have a similar period and shape, and, from a i-th periodicity to the following one, there is not a remarkable difference in the relative distance distribution $\boldsymbol{P}$ (the MOID distribution $\boldsymbol{M}$ is always the same, being the scenario Keplerian). This weakens the statistical comparison result, as the EMD is similar across multiple clusters, and the algorithm possibly converges to an erroneous solution. Instead, from Fig. 7-4c and Fig. 7-4d it is worth to notice that both compliant and uncompliant MOID failures regard cases in which fragment and parent inclination and right ascension of the ascending node are very close each other, as the similar

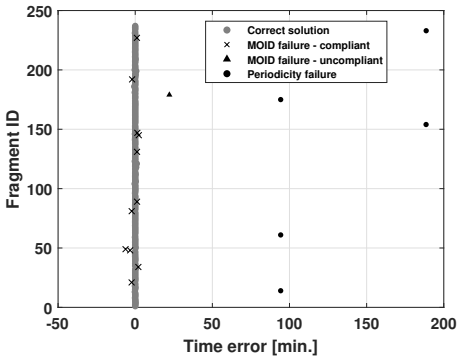

(a) Time error for each fragment of the data set.

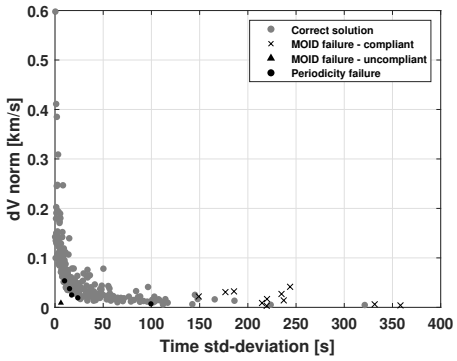

(b) Impulse magnitude vs the output time standard deviation.

Figure 7-3: Results of the numerical analysis on the unperturbed scenario with no orbital state error, by using the EMD metrics. The fragments for which a failure occurs are highlighted according to the legend.

orientation provokes a remarkable excursion of MOID data from a sample to another, and the samples cluster around a quantity corresponding to an epoch which is not the correct value.

Another useful representation is to relate the time standard deviation of the computed fragmentation epoch to the orbital parameters, as reported in Fig. 7-5. The closer the fragment orbit to the parent one, the larger the time standard deviation associated to the FRED solution, especially for what concerns the inclination and the right ascension of the ascending node (Fig. 7-5c and Fig. 7-5d respectively). This behaviour is linked to the fact that the closer the fragment orbit orientation to the parent one, the larger the excursion of the MOID data from a sample to another and, so, the larger the uncertainty of the time of parent transit through the MOID, that is of the fragmentation epoch candidates. On the contrary, the smallest time uncertainty is related to those fragments with an orbit significantly different from the parent one, as the MOID data do not vary much from a sample to another.

Sensitivity analysis on the number of samples used

As described in Sec. 6.2, FRED algorithm starts from the IOD result (expressed in terms of mean state and covariance), and populate it by samples according to a multi-normal distribution. Thus, the larger the number of samples used, the more accurate the IOD uncertainty

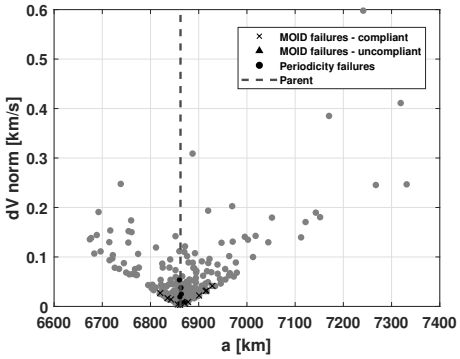

(a) Semi-major axis.

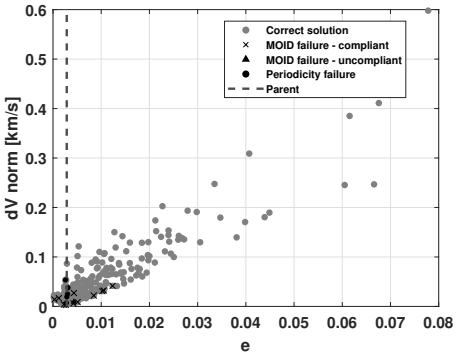

(b) Eccentricity.

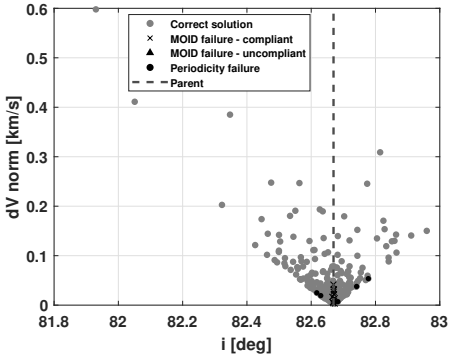

(c) Inclination.

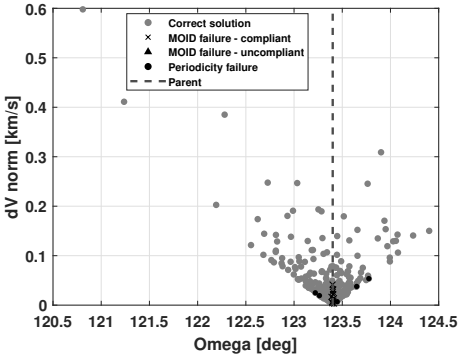

(d) Right ascension of the ascending node.

Figure 7-4: Unperturbed scenario: relationship between the impulse magnitude originating each fragment and the fragment semi-major axis, eccentricity, inclination and right ascension of the ascending node. The fragments for which a failure occurs are highlighted according to the legend, and the dashed line shows the parent orbital parameters.

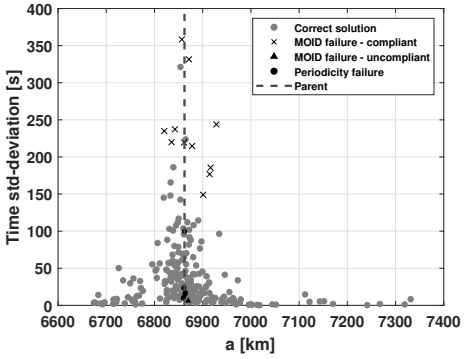

(a) Semi-major axis.

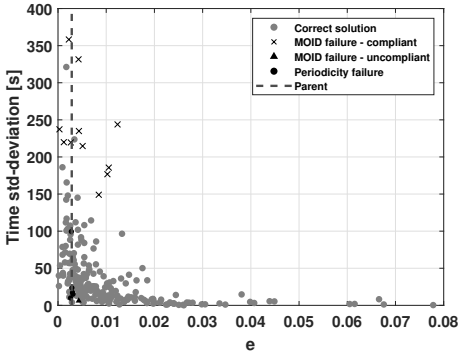

(b) Eccentricity.

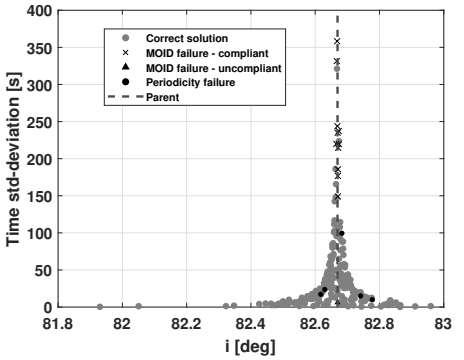

(c) Inclination.

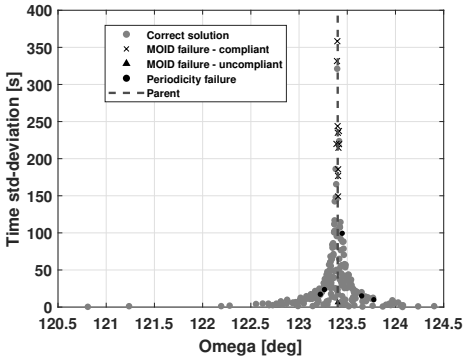

(d) Right ascension of the ascending node.

Figure 7-5: Unperturbed scenario: relationship between the standard deviation associated to the computed fragmentation epoch and the fragment semi-major axis, eccentricity, inclination and the right ascension of the ascending node. The fragments for which a failure occurs are highlighted according to the legend, and the dashed line shows the parent orbital parameters.

	Correct solutions	MOID failures compliant	MOID failures uncompliant	Periodicity failures
100	92.4 %	3.9 %	0.4 %	3.4 %
500	92.0 %	4.2 %	0.4 %	3.4 %
2000	92.4 %	4.2 %	0.4 %	3.0 %
10000	92.8 %	4.2 %	0.4 %	2.6 %

Table 7.3: Unperturbed scenario: sensitivity analysis on the number of samples used.

representation. The number of samples used is a key point in assessing FRED performance and, for this reason, a sensitivity analysis is here conducted by modifying the nominal value of $N_s = 1000$ to 100, 500, 2000 and 10000. It must be pointed out that the larger the number of samples used, the larger the computational cost, as more conjunctions for each fragment are to be computed (both in terms of MOID and relative distance evaluation). In addition, also the computational demand of the Earth Mover Distance metrics is proportional to the number of samples.

The results are reported in Tab. 7.3. It is possible to notice that the performance are stable across the different values of N_s, and remain similar to the EMD metrics results reported in Tab. 7.2. In particular, it is to point out that the convergence rate to the correct solution does not improve for a larger number of samples used in a monotonic way, and this confirms that the failure cases are not related to a not correct uncertainty representation, but to the mutual geometry between parent and fragment, as discussed above regarding Fig. 7-4 and Fig. 7-5. On the one hand, this is an important result, as the method computational demand can be reduced by using a lower number of samples, without a performance degradation. On the other hand, the larger the number of samples, the better the representation of the IOD uncertainty. Therefore, a trade off choice must be conducted. For these reasons, the nominal value of $N_s = 1000$ samples is kept in the following analyses.

7.3 Perturbed scenario with no IOD error

The same analysis as above is conducted on a perturbed scenario in which SGP4 [52] is used both to derive the fragments actual trajectory, and in FRED algorithm. The data set is created as follows:

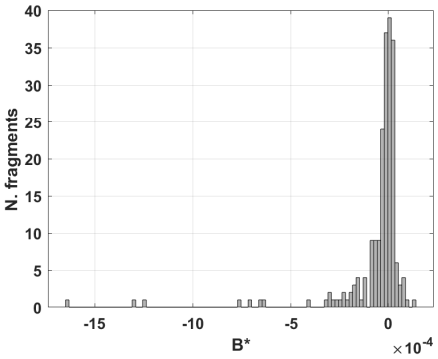

(a) B* distribution from the matching between SGP4 and the high-fidelity propagation.

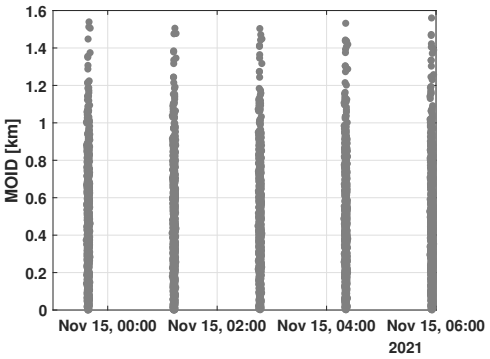

(b) Distribution of the t_j^p epochs in the time window of the analysis.

Figure 7-6: B* distribution and FRED clusters in the perturbed scenario.

1. The last available TLE of the parent object is propagated up to the fragmentation epoch, which is always set at 02:47:00 UTC of November 15$^{\text{th}}$, 2021, and converted in Cartesian coordinates.

2. The fragmentation impulses are applied (still according to the NASA standard breakup model [97] [98])

3. Each fragment state is converted in SGP4 elements. The B*, which accounts for the physical characteristics of the object, is defined by:

   (a) Propagating the fragment orbital state through the high-fidelity model presented in Sec. 2.2.

   (b) Searching for the B* which allows the SGP4 propagation to best match the high-fidelity propagation, through a Non-linear Least Squares filter. Out of the 237 fragments of the original data set, for 28 the process does not converge to a solution. Thus, a data set of 209 fragments is considered from now on.

   The computed B* distribution is reported in Fig. 7-6a.

4. Similarly to the analysis in Sec. 7.2, each fragment elements are propagated through SGP4 for 13 h, when the observation is simulated by computing the fragment orbital state in Cartesian coordinates and associating a covariance to it.

Then, in FRED algorithm, each fragment sample is propagated through SGP4. This operation implies a first conversion from Cartesian coordinates to SGP4 elements (at the OD

Correct solutions	MOID failures compliant	MOID failures uncompliant	Periodicity failures
90.0 %	5.3 %	0.9 %	3.8 %

Table 7.4: Perturbed scenario results for EMD metrics.

epoch), and then from SGP4 elements to Cartesian coordinates at the end of the propagation (that is at the epochs t_i defined in Sec. 6.2) to compute the MOID quantities.

Both in data set generation and inside FRED algorithm, the conversion from Cartesian coordinates to SGP4 elements is performed through a fixed-point iteration loop, and this introduces an error which, although negligible at the considered epoch, increases with the propagation and may affect results at the epochs t_i. On the contrary, the presence of perturbations in the propagation introduces an additional difference among clusters, besides the one related to the phasing effect between parent and fragment samples orbital states. This can be observed in Fig. 7-6b., which reports the clusters in the plane time of transit of parent through the MOID versus MOID magnitude, for the same case as the one reported in Fig. 6-4a for the Keplerian scenario. Comparing the two figures, it can be appreciated how the perturbations introduce a difference among the clusters.

The results of the perturbation analysis are reported in Tab. 7.4 considering the Earth Mover Distance metrics, and represented in Fig. 7-7. For the failure cases, the relationship between the time standard deviation associated to the solution and the impulse magnitude is analogous to the one in Fig. 7-3b, as the compliant MOID failures are still more likely to occur in those regions with small impulse magnitude and large time standard deviation, while both uncompliant MOID and periodicity failures present a much smaller time uncertainty, but still with a not high fragmentation impulse. On the contrary, there is a deterioration in performance due to the fact that the number of fragments in data set decreases, as mentioned above, and both the uncompliant MOID and the periodicity failures increase, passing from 1 and 5 to 2 and 8 respectively.

The computational demand increases with respect to the unperturbed scenario (under the same conditions), resulting in about 5 min per fragment analysed. This is due both to SGP4, which requires more computational time than the analytical propagation, and to the fact that, for each j-th fragment sample, the MOID data are recursively refined until the flying time to the MOID falls below 1e-03 s (as described in Sec. 6.2).

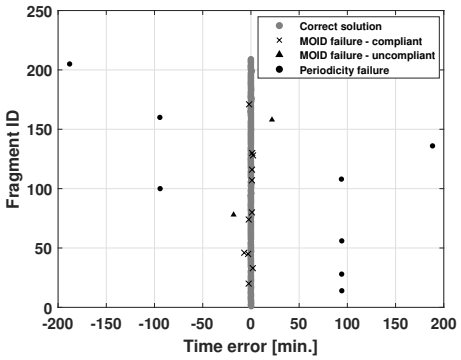

(a) Time error for each fragment of the data set.

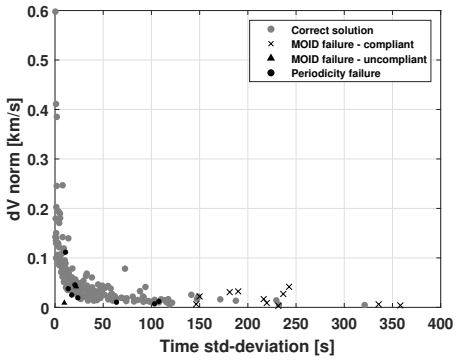

(b) Impulse magnitude vs the output time standard deviation.

Figure 7-7: Results of the numerical analysis on the perturbed scenario with no orbital state error. The fragments for which a failure occurs are highlighted according to the legend.

Similarly to Sec. 7.2, the difference between parent and fragments orbital parameters is studied to better assess the failures characteristics. From Fig. 7-8a it is possible to observe that the periodicity failures regard cases in which the fragment orbit semi-major axis is very close to the parent values. Then, Fig. 7-8c and Fig. 7-8d show that both compliant and uncompliant MOID failures regard cases in which fragment and parent inclination and right ascension of the ascending node are very close each other. Unlike Fig. 7-4b, in Fig. 7-8b there is no relationship between the periodicity failure and the eccentricity, and this confirms that this type of failure is due to the similar orbital period, which depends on the semi-major axis only. All these considerations are analogous to those stated about the Keplerian scenario, to testify that the most failure prone situations (similar orbital period and orientation) do not change when perturbations are considered in the dynamics.

As above, it is interesting to study also the relationship between the time standard deviation associated to the solution and the orbital parameters, as represented in Fig. 7-9. It can be noticed that the more similar the fragment and the parent object are, the larger the time uncertainty associated to the FRED solution, especially for what concerns the orientation, that is the inclination (Fig. 7-9c) and the right ascension of the ascending node (Fig. 7-9d). Therefore, the same considerations as those in Sec. 7.2 about Fig. 7-5 hold.

To recap, the inclusion of perturbations modifies both the relative distance and the MOID and the fragmentation epoch candidates distributions at t_i. The EMD capability to identify the correct candidate is affected by this, as well as by the effect of the error introduced by the conversion from Cartesian coordinates to SGP4 elements. Nevertheless, the distributions

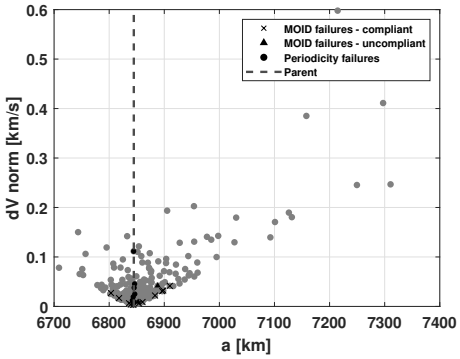

(a) Semi-major axis.

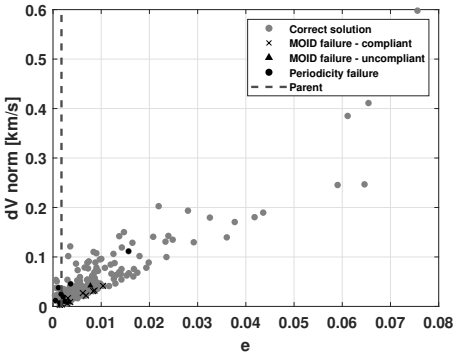

(b) Eccentricity.

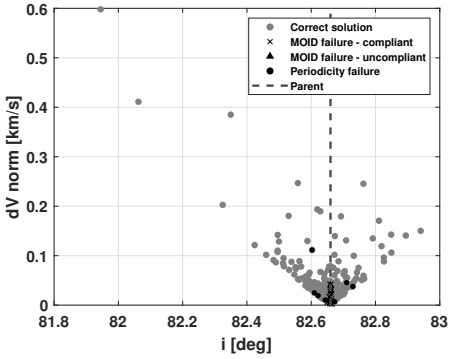

(c) Inclination.

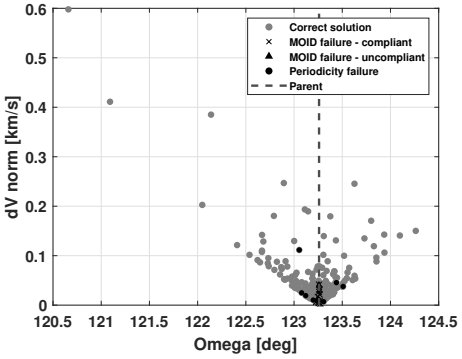

(d) Right ascension of the ascending node.

Figure 7-8: Perturbed scenario: relationship between the impulse magnitude originating each fragment and the fragment semi-major axis, eccentricity, inclination and right ascension of the ascending node. The fragments for which a failure occurs are highlighted according to the legend, and the dashed line shows the parent orbital parameters.

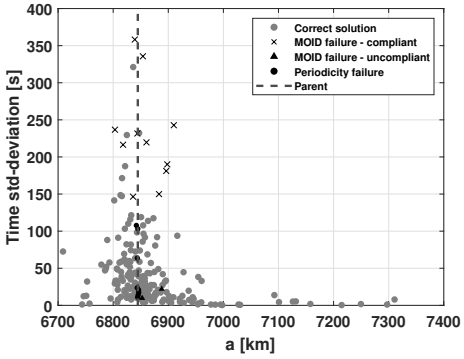

(a) Semi-major axis.

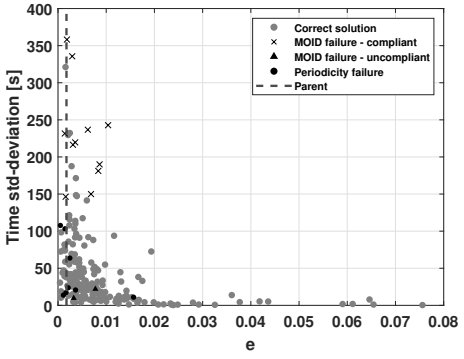

(b) Eccentricity.

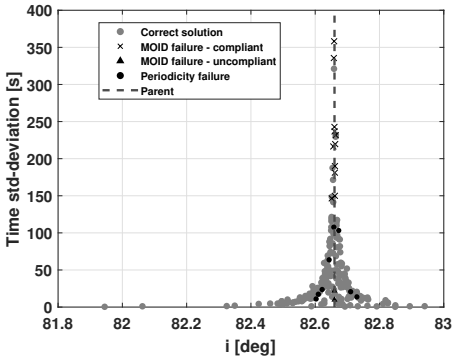

(c) Inclination.

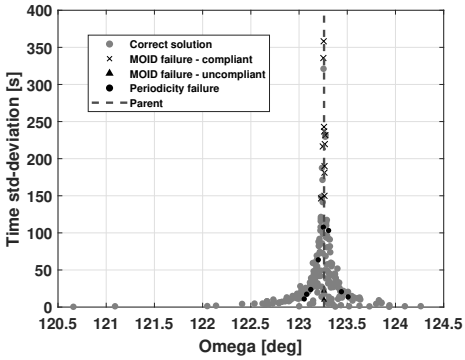

(d) Right ascension of the ascending node.

Figure 7-9: Perturbed scenario: relationship between the standard deviation associated to the computed fragmentation epoch and the fragment semi-major axis, eccentricity, inclination and right ascension of the ascending node. The fragments for which a failure occurs are highlighted according to the legend, and the dashed line shows the parent orbital parameters.

of the errors and of the uncertainty associated to the FRED solution are equivalent to the Keplerian scenario in Sec. 7.2.

7.4 Perturbed scenario with IOD error

The analyses in Sec. 7.2 and Sec. 7.3 are conducted with no error associated to IOD, that is starting from an orbital state obtained by simply propagating the fragment nominal ephemeris up to a certain epoch, considering it as the mean state and associating a covariance to it. However, in real applications, at the orbit determination epoch a mismatching between the orbital state mean and the ground truth is introduced by the IOD process, and its effects on FRED algorithm must be assessed.
For this purpose, an analysis is carried out by starting from an orbital state generated as follows:

- The ground truth of the fragment orbital state is generated in the same manner as in Sec. 7.3, that is propagating the fragment ephemeris for 13 h from the event through SGP4 [52] and with the estimated B*.
- Geodetic latitude and longitude are computed from the fragment position, and a monostatic radar station is simulated, at the same coordinates (with a small variation of +1 deg) and at 0 km altitude.
- Azimuth, elevation and slant range are simulated for the following 30 s. A Gaussian noise is added of 0.01 deg (on angular coordinates) and 30 m (on slant range).
- The orbital state is computed at the initial observation epoch, through the IOD procedure presented in [69], which analytically computes the orbital state at the first observation epoch. The estimate might be later refined through an additional filter (like what done in Sec. 4.4), but this refinement is voluntarily not done in the simulations, to test the procedure for a coarse IOD result.

In this way, the fragment orbital state $\left\{\boldsymbol{x}^{fg}, \boldsymbol{P}^{fg}\right\}$ is obtained, and FRED algorithm is run. It is worth to stress that an error between $\boldsymbol{x}^{fg}$ and the fragment actual position and velocity is now present, and the covariance $\boldsymbol{P}^{fg}$ is computed from the measurements through the IOD procedure, that is differently from what done in Sec. 7.2 and in Sec. 7.3.

Correct solutions	MOID failures compliant	MOID failures uncompliant	Periodicity failures
68.9 %	9.6 %	0.5 %	21.0 %

Table 7.5: Results for the perturbed scenario and accounting for the orbital state error introduced by the IOD process. The EMD metrics is used.

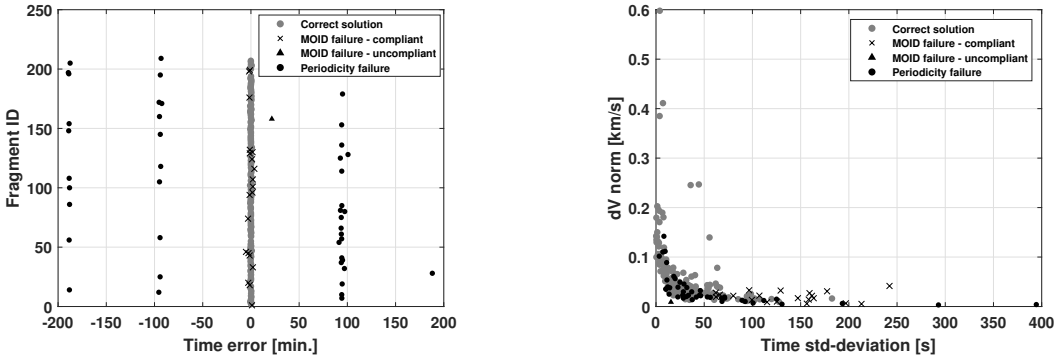

(a) Time error for each fragment of the data set.

(b) Impulse magnitude vs the output time standard deviation.

Figure 7-10: Results for the perturbed scenario and accounting for the orbital state error introduced by the IOD process. The fragments for which a failure occurs are highlighted according to the legend.

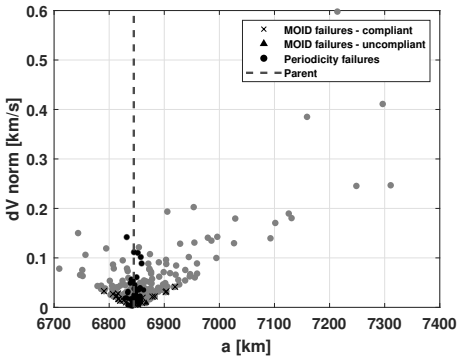

(a) Semi-major axis.

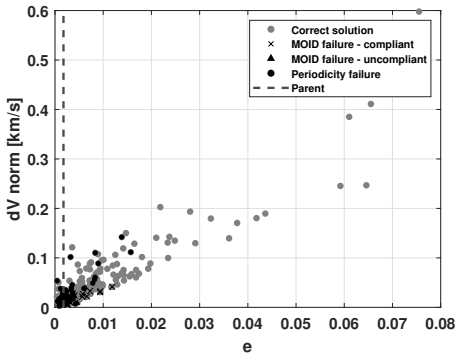

(b) Eccentricity.

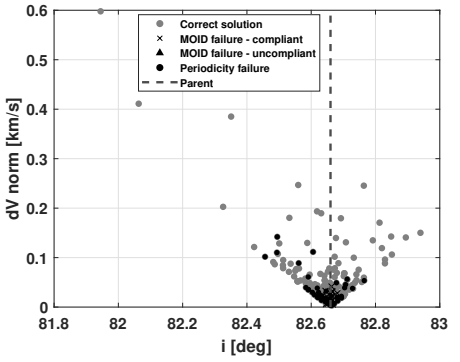

(c) Inclination.

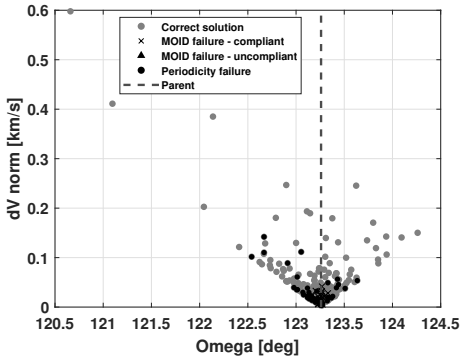

(d) Right ascension of the ascending node.

Figure 7-11: Perturbed scenario and accounting for the orbital state error introduced by the IOD process: relationship between the impulse magnitude originating each fragment and the fragment semi-major axis, eccentricity, inclination and right ascension of the ascending node. The fragments for which a failure occurs are highlighted according to the legend, and the dashed line shows the parent orbital parameters.

Results are reported in Tab. 7.5 and represented in Fig. 7-10 . It is worth to observe that in most cases the algorithm converges to the correct solution. However, comparing Tab. 7.5 to Tab. 7.2 and Tab. 7.4, it can be noticed that the IOD mismatching remarkably affects the algorithm performance, especially for what concerns the metrics to select the correct candidate. This can be visualised also by comparing Fig. 7-10a with Fig. 7-3a and Fig. 7-7a. Overall, the computational time is similar to the one in Sec. 7.3.

Analogously to Sec. 7.2 and Sec. 7.3, the difference between parent and fragments orbital parameters and its relationship with the time standard deviation associated to the solution are deepened. Comparing Fig. 7-11 with Fig. 7-8, it can be observed that the periodicity failures occur more often, and also in situations in which fragment and parent semi-major axes are not extremely close. On the contrary, MOID failures tend to regard still cases with

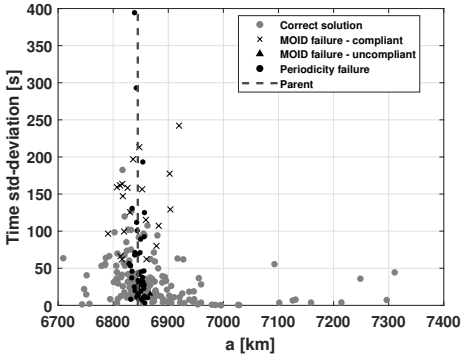

(a) Semi-major axis.

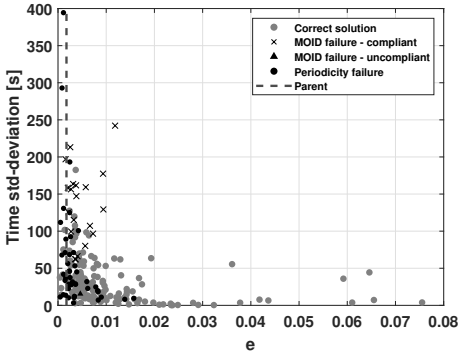

(b) Eccentricity.

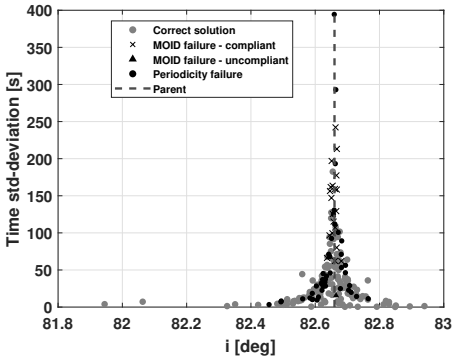

(c) Inclination.

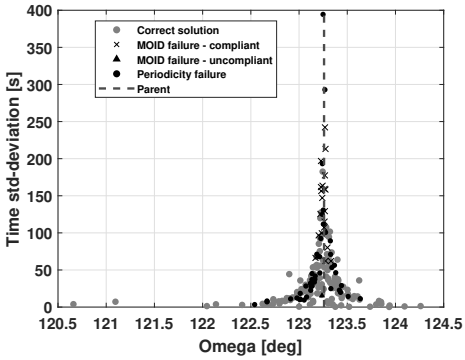

(d) Right ascension of the ascending node.

Figure 7-12: Perturbed scenario and accounting for the orbital state error introduced by the IOD process: relationship between the standard deviation associated to the computed fragmentation epoch and the fragment semi-major axis, eccentricity, inclination and right ascension of the ascending node. The fragments for which a failure occurs are highlighted according to the legend, and the dashed line shows the parent orbital parameters.

	Correct solutions	1 min $< t_{err} < T^p/2$	$t_{err} > T^p/2$
Deterministic FRED	67.0 %	11.5 %	21.5 %
Relative distance	12.4 %	67.0 %	20.6 %

Table 7.6: Results for the perturbed scenario and accounting for the orbital state error introduced by the IOD process. Both a deterministic FRED and a relative distance metrics are used. In the former, the metrics to assess the best candidate is represented by the euclidean distance between the relative distance and the MOID.

the same orbital plane orientation. In addition, the relationship between the time standard deviation associated to the solution and the orbital parameters, represented in Fig. 7-12, shows that the more similar the fragment and the parent object are, the larger the time uncertainty associated to the FRED solution, as already discussed about Fig. 7-5 and Fig. 7-9. This relationship is more evident for the inclination (Fig. 7-12c) and the right ascension of the ascending node (Fig. 7-12d).

It may be investigated which result would have been returned by a deterministic FRED procedure, that is by starting from the fragment mean state without performing the multivariate normal distribution based on the covariance. In this case, the metrics to assess the best candidate is just the euclidean distance between the relative distance and the MOID. Results are reported in Tab. 7.6, where no considerations about failure compliance can be stated, as no uncertainty is associated to the solution. Although less computational demanding, this deterministic approach presents results a bit deteriorated with respect to the FRED ones in Tab. 7.5, confirming the benefit of a stochastic approach to the problem.

To further appreciate FRED results, an alternative analysis, analogous to the method described at the beginning of Sec. 6.2, is carried out. Such an approach assesses the fragmentation epoch as the time of the minimum relative distance between the parent and the fragment mean state (both assumed as deterministic), propagated on the analysis time window. This would allow a lower computational demand. The results are still reported in Tab. 7.6, where a much smaller convergence to the correct solution can be observed. Therefore, besides providing statistical information and the correct solution among fragmentation epoch candidates, FRED convergence to the correct solution turns out to be more robust.

To recap, the IOD accuracy affects FRED algorithm results, by increasing both the compliant MOID and the periodicity failures. Nevertheless, the algorithm mostly converge to the

correct solution and, besides being more performing than a deterministic relative distance metrics, the correct solution is always present among epoch candidates even when a periodicity failure occurs. Then, applying FRED algorithm in a deterministic way is possible, but it decreases the performance, because of the statistical comparison removal.

7.5 Sensitivity Analysis

A sensitivity analysis is conducted to test FRED robustness. Operationally, three aspects may negatively affect the results:

- A larger time elapsed between the event and the IOD: given the IOD error, the larger the propagation time, the larger the mismatching at the fragmentation epoch.
- A wrong evaluation of the physical parameter of the fragment: the physical characteristics of the fragment can be either assumed or reconstructed during the IOD process, and this likely create an additional source of mismatching.
- A larger measurements noise: this generally induces a more noisy IOD result, with larger mismatching between IOD mean state and larger covariance.

For all these aspects a sensitivity analysis is carried out as follows, by also comparing the FRED results with the ones obtained through the relative distance metrics introduced in Sec. 7.4.

7.5.1 Sensitivity Analysis on the IOD epoch

In Sec. 7.2, Sec. 7.3 and Sec. 7.4, the IOD epoch is always set 13 h after the event, as FRED algorithm aims at providing a method to identify the fragmentation epoch from a single observation conducted by a surveillance radar in the first hours right after the event. However, in real case scenarios, the algorithm may be applied starting from an orbital state resulting from an IOD conducted later. For this reason, it is fundamental to assess the FRED performance by considering larger time elapsed between the fragmentation and the IOD epochs. Three cases are investigated: 24 h, 48 h and 72 h from the event to the first observation epoch. As above, the IOD method presented in [69] is applied. Results are reported in Tab. 7.7 and show a deterioration in performance, and this confirms that the

Time from the event	Correct solutions	MOID failures compliant	MOID failures uncompliant	Periodicity failures
24 h	60.8 %	5.7 %	0.0 %	33.5 %
48 h	43.1 %	3.8 %	1.0 %	52.1 %
72 h	31.6 %	2.4 %	0.5 %	65.5 %

Table 7.7: Perturbed scenario with orbital state error introduced by the IOD process: FRED results for the sensitivity analysis on the time elapsed between the fragmentation and the IOD epoch.

Time from the event	Correct solutions	1 min $< t_{err} < T^p/2$	$t_{err} > T^p/2$
24 h	8.1 %	57.9 %	34.0 %
48 h	3.4 %	42.1 %	54.5 %
72 h	4.3 %	31.6 %	64.1 %

Table 7.8: Perturbed scenario with orbital state error introduced by the IOD process: deterministic relative distance metrics results for the sensitivity analysis on the time elapsed between the fragmentation and the IOD epoch.

longer the time elapsed, the less robust the algorithm is. Furthermore, a longer time elapsed implies a longer fragment samples propagation, which increases the computational cost.
The FRED results are compared to those which could be obtained with the deterministic relative distance metrics, which are reported in Tab. 7.8. There is an oscillating behaviour of the correct solution, but the general trend confirms that the longer the time elapsed, the less performing the deterministic metrics. Moreover, the results are always much worse than the FRED ones.

7.5.2 Sensitivity Analysis on the B* mismatching

In the above analyses, the same B* (expressing the physical parameter in the SGP4 propagator [52]) is used to generate the ground truth and inside FRED algorithm. This is a simplification, as operationally no physical information about the observed fragment is known. Generally, during an OD process, the physical parameters can be estimated as well, but accurate measurements are needed, as well as a long observation arc (possibly obtained by linking more measurements tracks). This is not the case for a single observation right after a fragmentation event, and the physical parameters are either roughly estimated or

Factor multiplying B*	Correct solutions	MOID failures compliant	MOID failures uncompliant	Periodicity failures
1e-01	68.9 %	9.6 %	0.5 %	21.0 %
1e-02	69.4 %	9.1 %	0.5 %	21.0 %
1e-03	68.9 %	9.6 %	0.5 %	21.0 %

Table 7.9: Perturbed scenario with orbital state error introduced by the IOD process: FRED results for the sensitivity analysis on the B*.

Factor multiplying B*	Correct solutions	1 min $< t_{err} < T^p/2$	$t_{err} > T^p/2$
1e-01	12.4 %	67.0 %	20.6 %
1e-02	12.4 %	67.0 %	20.6 %
1e-03	12.4 %	67.0 %	20.6 %

Table 7.10: Perturbed scenario with orbital state error introduced by the IOD process: deterministic relative distance metrics results for the sensitivity analysis on the B*.

not estimated at all and, so, assumed. In addition, the IOD procedure used [69] estimates the orbital state only, which is voluntarily not refined through additional filters, as stated in Sec. 7.4.

To test FRED algorithm robustness to the physical parameter mismatching, a sensitivity analysis is carried out considering, inside the FRED algorithm, B* values different from the one used to generate the ground truth. This modification is obtained by multiplying the correct B* times: 1e-01, 1e-02, 1e-03.

The results are reported in Tab. 7.9. FRED performance results robust to erroneous physical parameter estimation, and, for the 1e-01 and 1e-03 cases, the percentages are exactly the same as the ones in Tab. 7.5. In the 1e-02 case the result for one fragment passes from being a compliant MOID failure to a correct solution. Overall, these results cannot be considered as a general algorithm behaviour, as the algorithm sensitivity on the physical parameters always depends on the perturbations experienced by the fragment and, so, on its orbital regimen. For the scenario analysed, also the distribution of the relative distance metrics result does not change, as visible in Tab. 7.10.

Angular noise [deg]	Correct solutions	MOID failures compliant	MOID failures uncompliant	Periodicity failures
2e-02	66.5 %	11.5 %	0.5 %	21.5 %
5e-02	53.1 %	20.6 %	0.0 %	26.3 %
1e-01	33.5 %	29.7 %	0.0 %	36.8 %

Table 7.11: Perturbed scenario with orbital state error introduced by the IOD process: FRED results for the sensitivity analysis on the angular track noise.

7.5.3 Sensitivity Analysis on the measurements noise

As mentioned above, the performance of FRED algorithm in operational scenarios strongly depends on the IOD accuracy, which in turn depends on the algorithm used, the observation geometry and length, and on the measurements quality. Indeed, the deterioration of measurements can lead to two effects on the IOD result and, so, on FRED performance: an erroneous orbital mean state and a larger uncertainty. For this reason, it is fundamental to assess FRED algorithm sensitivity to the measurements noise. In particular, since in surveillance radars the angular track is the less accurate measurement (as also stated in Sec. 1.4.3), the noise associated to the range is kept fixed to the nominal value of 30 m, while the angular noise is made varying from the nominal value of 1e-02 deg to: 2e-02 deg, 5e-02 deg and 1e-01 deg.

The results are reported in Tab. 7.11. It is possible to notice that the larger the noise associated to the angular track, the lower the convergence to the correct solution and the larger the periodicity failures percentage. There is a slight increase also in the MOID compliant failures, while the uncompliant ones tend to zero. These results depend on the IOD result deterioration, which introduces a mismatching affecting the estimation of MOID data. On the one hand this may lead to a wrong evaluation by EMD metrics, with still the correct epoch among candidates. On the other hand the IOD result may induce a wrong computation of time of parent transit through the MOID and, so, the epoch candidates may be wrongly estimated, and this may result in the absence of the correct solution among candidates. In any case, FRED is always better performing than the relative distance metrics, whose results are reported in Tab. 7.12. Also in this case there is a performance deterioration with the angular noise increase.

Angular noise [deg]	Correct solutions	1 min $< t_{err} < T^p/2$	$t_{err} > T^p/2$
2e-02	13.4 %	57.4 %	29.2 %
5e-02	12.0 %	59.8 %	28.2 %
1e-01	11.5 %	57.9 %	30.6 %

Table 7.12: Perturbed scenario with orbital state error introduced by the IOD process: deterministic relative distance metrics results for the sensitivity analysis on the angular track noise.

To recap, the sensitivity analysis highlights an algorithm deterioration with a longer time elapsed between the event and the fragmentation epoch and with a larger angular track noise. On the contrary, the physical parameter mismatching is less effective, because of the poor sensitivity of the MOID quantities to it on short propagation time window. Overall, FRED is more performing than the deterministic metrics.

7.6 Operational scenario

The same analysis as the one in Sec. 7.4, that is the perturbed one with IOD error simulation, is now conducted on an operational scenario involving BIRALES, which was one of the EUSST sensors most contributing to monitor the fragments generated by COSMOS 1408 fragmentation. Four observations are scheduled based on the transit predictions of the parent object last available ephemeris, which are foreseen to occur 36.4 h, 59.9 h, 97.3 h and 120.75 h after the event. In these time ranges, only the first detected measurements track for each fragment is considered.

On the one hand, this observation schedule implies quite long propagation times, and this would deteriorate FRED performance, as highlighted in Sec. 7.5.1. On the other hand, this choice possibly mitigates the drawback for which, in proximity to the epoch of the parent transit prediction, only fragments with an orbit pretty similar to the parent object one might be observed, that is those which would induce periodicity failures in FRED algorithm. The observations characteristics are reported in Tab. 7.13, where no elevation pointing limit is considered for BIRALES, together with the foreseen epoch of parent transit. It can be noticed that in each observation only a portion of the fragments data set used in previous sections is observed, which is remarkably small for the cases 3.2 - 51.2 h and 99.2 - 123.2 h.

Time range from the event	Estimated parent pass from the event	RX point. Az [deg]	RX point. El [deg]	N. of fragments observed
3.2 - 51.2 h	36.4 h	180.0	65.9	35
51.2 - 75.2 h	59.9 h	0.0	7.8	144
75.2 - 99.2 h	97.3 h	0.0	11.7	116
99.2 - 123.2 h	120.75 h	180.0	22.5	52

Table 7.13: Operational scenario: observation characteristics.

Time range from the event	Correct solutions	MOID failures compliant	MOID failures uncompliant	Periodicity failures
3.2 - 51.2 h	22.9 %	2.9 %	5.7 %	68.5 %
51.2 - 75.2 h	24.3 %	0.7 %	0.0 %	75.0 %
75.2 - 99.2 h	19.8 %	0.9 %	0.0 %	79.3 %
99.2 - 123.2 h	17.3 %	0.0 %	1.9 %	80.8 %

Table 7.14: Operational scenario: FRED results.

The fragments IOD epoch distribution (in terms of hours from the event) for the four observations is represented in Fig. 7-13, as well as the failures case, and FRED algorithm results are reported in Tab. 7.14. Both the IOD accuracy and the long propagation time deteriorate the EMD performance. In particular, a trend similar to the IOD epoch sensitivity analysis (reported in Tab. 7.7) is obtained, that is the longer the time elapsed between the event and the observation, the smaller the convergence to the correct solution. However, the convergence rate is even smaller than the one in Tab. 7.7, and this change is due both to the more realistic observation geometry (the measurements are simulated when the fragment crosses the receiver FoV) and, moreover, to the fact that generally the fragments with an orbit pretty similar are observed, as the observation has been scheduled from the parent transit prediction. This represents an operational drawback of the method, as the fragments with an orbit similar to the parent one are the most likely to be observed. Nevertheless, it is worth to remark that multiple candidates are provided by the algorithm.

Similarly to what done in Sec. 7.2 and Sec. 7.3, for the 51.2 - 75.2 h case the relationship between orbital parameters and time standard deviation associated to the solution is reported. From Fig. 7-14 it is possible to notice that the relationship observed in Fig. 7-5, Fig. 7-9 and Fig. 7-12 holds, that is the closer the fragment and the parent orbits, the larger the time standard deviation (especially for what regards inclination and right ascension of

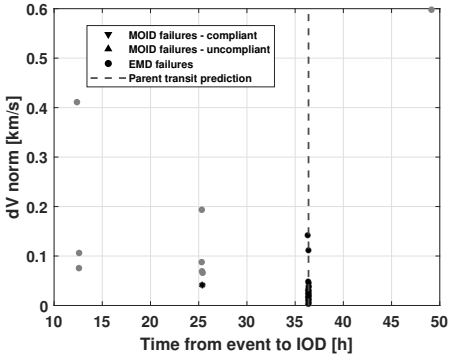

(a) 3.2 - 51.2 h observation.

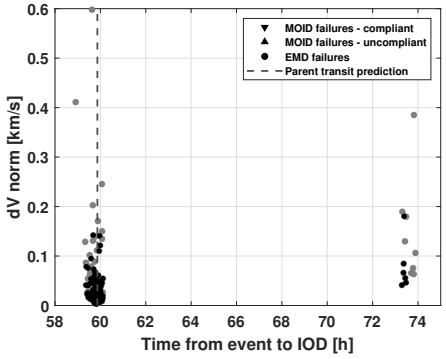

(b) 51.2 - 75.2 h observation.

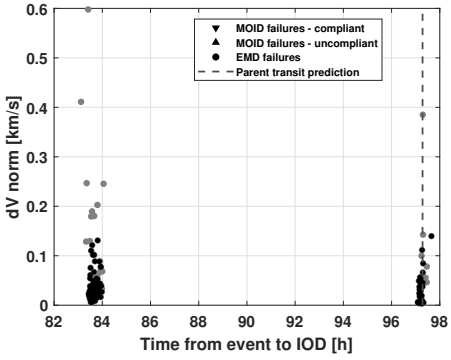

(c) 75.2 - 99.2 h observation.

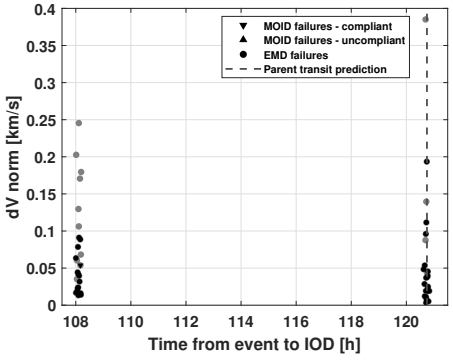

(d) 99.2 - 123.2 h observation.

Figure 7-13: Operational scenario: relationship between the impulse magnitude originating each fragment and the IOD epoch, for the four observations. The dashed line indicates the predicted transit epoch of the parent object.

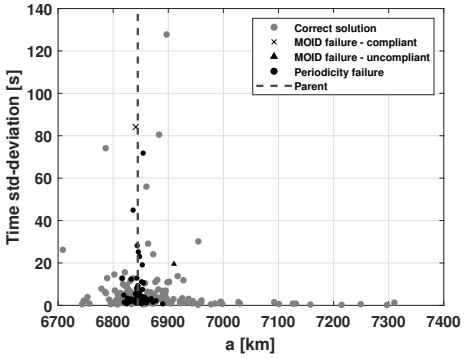

(a) Semi-major axis.

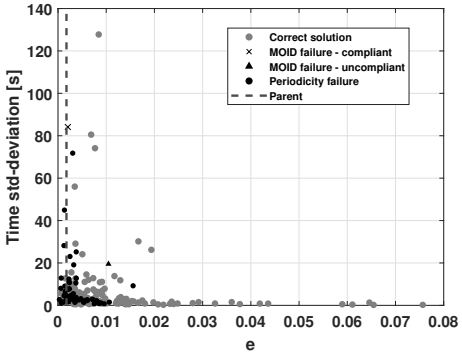

(b) Eccentricity.

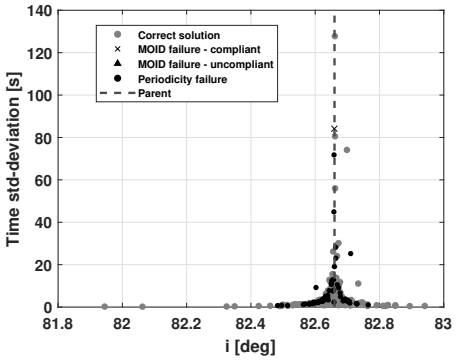

(c) Inclination.

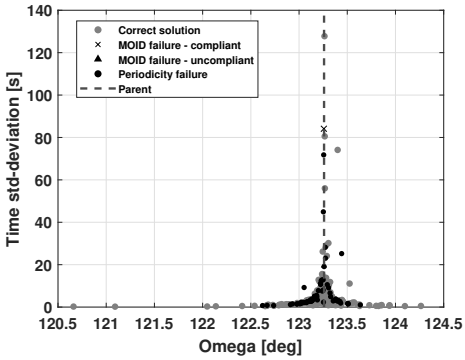

(d) Right ascension of the ascending node.

Figure 7-14: Operational scenario: relationship between the standard deviation associated to the computed fragmentation epoch and the fragment semi-major axis, eccentricity, inclination and right ascension of the ascending node. The fragments for which a failure occurs are highlighted according to the legend, and the dashed line shows the parent orbital parameters. The results are reported for the 51.2 - 75.2 h case.

the ascending node, in Fig. 7-14c and Fig. 7-14d respectively). Figure 7-14 also provides an explanation for the remarkable decrease of MOID failures percentages (both compliant and uncompliant) in Tab. 7.14 with respect to Tab. 7.5: differently from Fig. 7-9, the periodicity failures regard cases in which the fragment orbit is similar to the parent one also in inclination and right ascension of the ascending node, which are also the situations where MOID failures occur. Thus, this type of failure merges in the periodicity one.

As in Sec. 7.4 and in Sec. 7.5, the deterministic relative distance is assessed to better appreciate FRED algorithm . The results are reported in Tab. 7.15, where the convergence to the correct solution is much smaller than the FRED one. For the 51.2 - 75.2 h case, the results are graphically compared in Fig. 7-15, which reports the time error associated to FRED and to the relative distance metrics result.

Time range from the event	Correct solutions	1 min $< t_{err} < T^p/2$	$t_{err} > T^p/2$
3.2 - 51.2 h	5.7 %	20.0 %	74.3 %
51.2 - 75.2 h	0.7 %	27.1 %	72.2 %
75.2 - 99.2 h	0.8 %	20.7 %	78.5 %
99.2 - 123.2 h	1.9 %	15.4 %	82.7 %

Table 7.15: Operational scenario: deterministic relative distance metrics results.

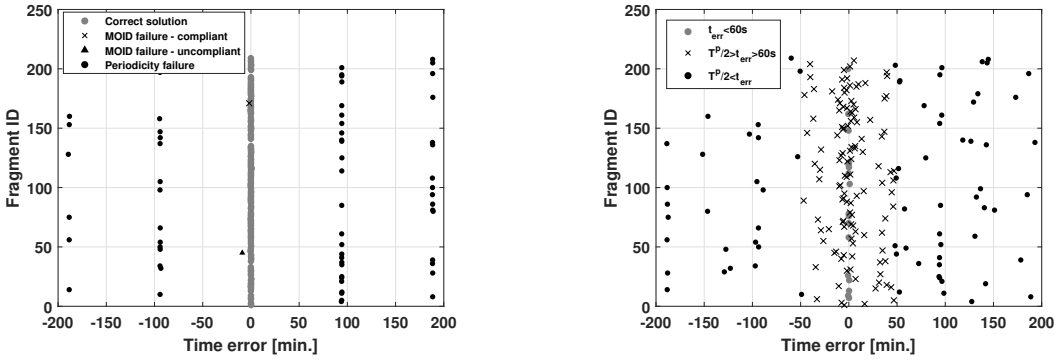

(a) FRED result.

(b) Relative distance metrics result.

Figure 7-15: Operational scenario: time error for each fragment of the data set by using FRED and the minimum relative distance between parent and fragment mean state to assess the fragmentation epoch. The results are reported for the 51.2 - 75.2 h case.

To conclude, although the performance deterioration, the analysis proves that, also in operational scenarios, the fragmentation epoch identification problem would benefit from FRED algorithm.

7.7 Operational scenario with MATER

As stated in Sec. 1.6, the aim of this thesis is to show the benefit for SST activities of using an adaptive beamforming technique to derive the angular track in array radars. In Ch. 4 the applications to Re-entry Analysis and Collision Avoidance services are presented, as well as what done in Ch. 5 for the proximity operations and the fragments cloud monitoring, the latter being related to the Fragmentation Analysis service. Since this last application motivates the interest on fragmentation events, FRED algorithm is presented in Ch. 6 and its performance is assessed in this chapter. For the sake of a comprehensive analysis,, an application of FRED algorithm starting from measurements computed through MATER algorithm is here proposed.

As shown in Sec. 7.6, there was no possibility for BIRALES to observe COSMOS 1408 fragments cloud on the first day after the event. The long time elapsed between the fragmentation and the observations induces a remarkable deterioration in performance. Since FRED algorithm aims at providing an operational procedure to identify the fragmentation epoch in a stochastic way in the first hours after the event, another scenario is considered.

An International Space Station fragmentation is simulated, through the NASA standard break-up model [97] [98], on the April 27$^{\text{th}}$, 2021, at 19:30:00 UTC, and the ISS orbital parameters at the fragmentation epoch are reported in Tab. 7.16 (with the exception of the true anomaly). The last available ephemeris and the alert are considered at 16:00:00 UTC and at 22:45:00 UTC, respectively. BIRALES receiver pointing is kept southwards at an elevation of 83.9 deg, whereas the transmitter pointing angles are 19.3 deg in azimuth and 35.1 deg in elevation, that is the same pointing as in Sec. 4.5 and in Sec. 5.3. The RCSs are derived from the break-up model and, for those fragments which intersect the receiver FoV, the SNR is simulated, which enters the detection block. In this way, 99 fragments are observed between 08:39:35 UTC and 08:50:12 UTC of April 28$^{\text{th}}$, 2021. For each fragment observed, both the signal CM, with a 5 kHz sampling frequency and 0.02 s integration time, and the slant range are generated, and MATER algorithm is run considering the multiple

a [km]	e	i [deg]	Ω [deg]	ω [deg]
6792.7	1.2e-03	51.5	231.5	95.2

Table 7.16: Operational scenario with MATER ISS orbital parameters.

Time range from the event	N. with 1 sources	N. with 2 sources	N. with 3 sources	$\eta_{\Delta\gamma_1}$ [deg]	$\eta_{\Delta\gamma_2}$ [deg]
13.2 - 13.3 h	88	4	1	1.2e-02	6.7e-03

Table 7.17: Operational scenario with MATER: number of passes temporally overlapping each other and angular track median RMSE.

sources scenario, that is similarly to the simulations reported in Ch. 5. The correspondence between the number of overlapping transits and the slots is reported in Tab. 7.17, together with the median value η on the data set of the angular RMSE of the MATER result, as defined in Sec. 4.2, for the two angular coordinates separately. All the tracks converged to the correct solution.

It can be noticed that the angular RMSE along $\Delta\gamma_2$ is better than along $\Delta\gamma_1$. This can be explained both considering that the parent object inclination is around 51.6 deg and the fragments ones do not deviate remarkably from this value. Thus, in the same time window, the path along $\Delta\gamma_1$ and along $\Delta\gamma_2$ is of comparable length and the short integration time allows the $\Delta\gamma_2$ direction to be finer because of the sensor resolution.

From the simulated slant range and the angular track computed with MATER algorithm, IOD is run based on [69] and the fragment orbital state $\left\{\boldsymbol{x}^{fg}, \boldsymbol{P}^{fg}\right\}$ is computed for each fragment.

Given these data, FRED algorithm is run and the results are reported in Tab. 7.18, which presents also the number of fragments for which FRED returns a solution. For the sake of comparison, also the results are reported for the *no MATER case*, in which the angular track is simulated in the same manner as in Sec. 7.4, by associating a Gaussian noise equal to the angular error standard deviation obtained through MATER, for each observed fragment. It is worth to remark that this associated noise has zero mean, while the MATER angular track one has not.

It is possible to notice that, while the *no MATER case* presents a convergence rate comparable to the ones in Tab. 7.14, the *MATER case* shows a remarkable deterioration with

	Correct solutions	MOID failures compliant	MOID failures uncompliant	Periodicity failures	N. of FRED results
MATER	4.8 %	7.9 %	1.6 %	85.7 %	63
No MATER	32.3 %	1.0 %	0.0 %	66.7 %	99

Table 7.18: Operational scenario with MATER: FRED results.

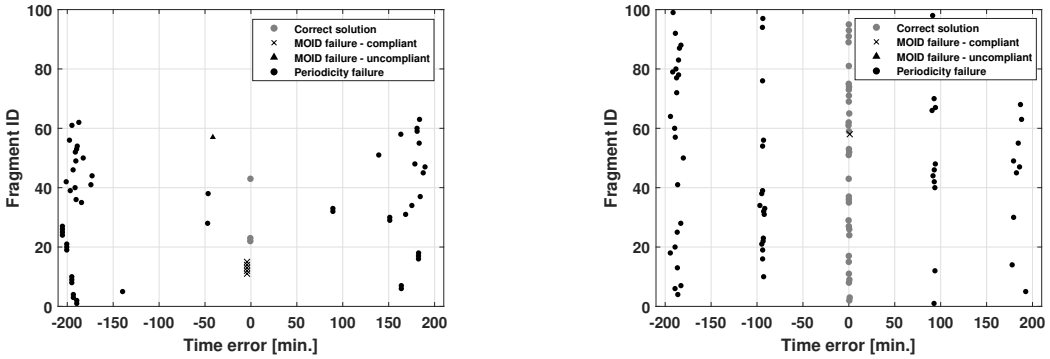

(a) MATER case.

(b) No MATER case.

Figure 7-16: Operational scenario with MATER: FRED solution by starting from an angular track simulated through MATER algorithm and from the correct profile in which a Gaussian noise with the same standard deviation as the MATER track one is associated.

respect to the previous analyses, with few correct results. This may also be assessed by looking at Fig. 7-16, which reports the time error for the two cases: it can be noticed that the failures in the *no MATER case* align towards sound candidates (they are separated from the correct solution according to the parent orbital period), while the *MATER case* results are less ordered. The performance deterioration in *MATER case* can also be assessed considering that the number of solutions returned by FRED is larger in the *no MATER case* than in the *MATER case* (Tab. 7.18): indeed, when no solution is returned, the IOD orbital state obtained from MATER angular track (coupled with the slant range) is so inaccurate that no result is provided by FRED.

Therefore, this deterioration in FRED results is linked to the IOD error, whose median values (considering only the fragments for which FRED returns a result) in position and velocity are 47.0 m, 23.0 m/s and in 8.5 m, 1.1 m/s, for the *MATER case* and the *no MATER case* respectively. Thus, the *MATER case* features errors one order of magnitude larger than the *no MATER case* one, and this is the main responsible for the significant deterioration. Concerning the angular error trend, a remarkable deviation from a Gaussian

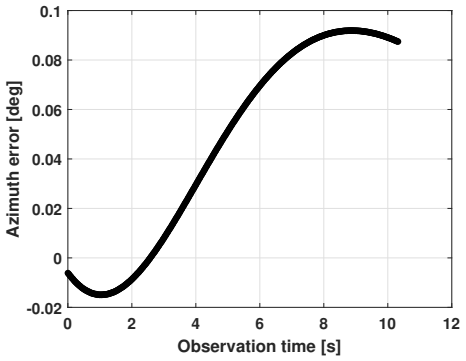

(a) MATER case: azimuth.

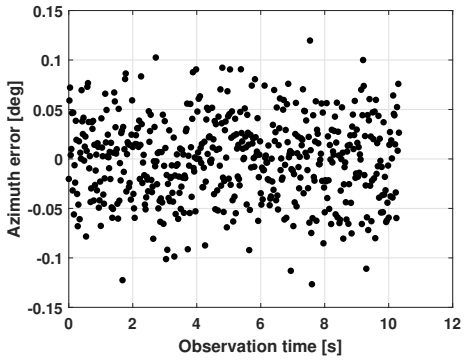

(b) No MATER case: azimuth.

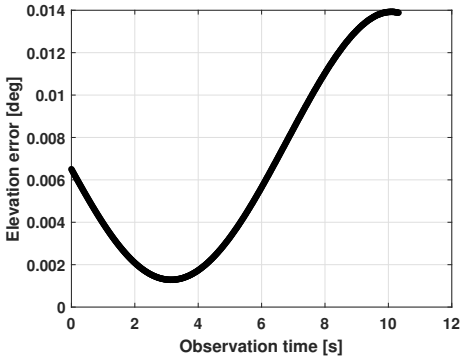

(c) MATER case: elevation.

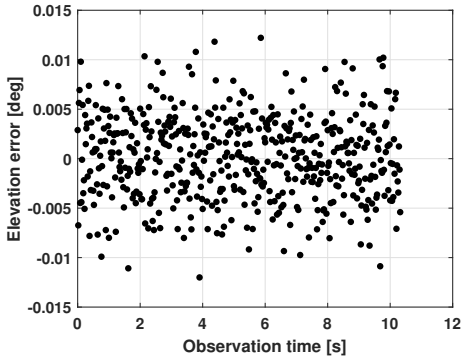

(d) No MATER case: elevation.

Figure 7-17: Operational scenario with MATER: MATER algorithm angular error distribution (in azimuth and elevation) compared to Gaussian distribution case, with the same standard deviation.

distribution occurs, as represented in Fig. 7-17 for a single fragment. For this case, the Cumulative Distribution Function is also reported in Fig. 7-18, by representing both the *MATER case*, the *no MATER case* and the theoretical trends. From both of figures, it is possible to notice a bias effect in the MATER angular track error.

Finally, also the results for the relative distance metrics are reported, both for the *MATER case* and the *no MATER case*. The results are shown in Tab. 7.19 and represented in Fig. 7-19. Comparing them both with Tab. 7.18 and Fig. 7-16 respectively, it is possible to notice the better results provided by FRED.

To recap, the operational application of FRED from an angular track determined by MATER highlights some critical issues. First of all, the angular track computed with MATER is often not fine enough to determine an accurate orbital state, because both of the non-zero mean and the non-Gaussian distribution of the angular error. In many cases, this also prevents FRED from returning results, and this forces to track the detected fragment with additional

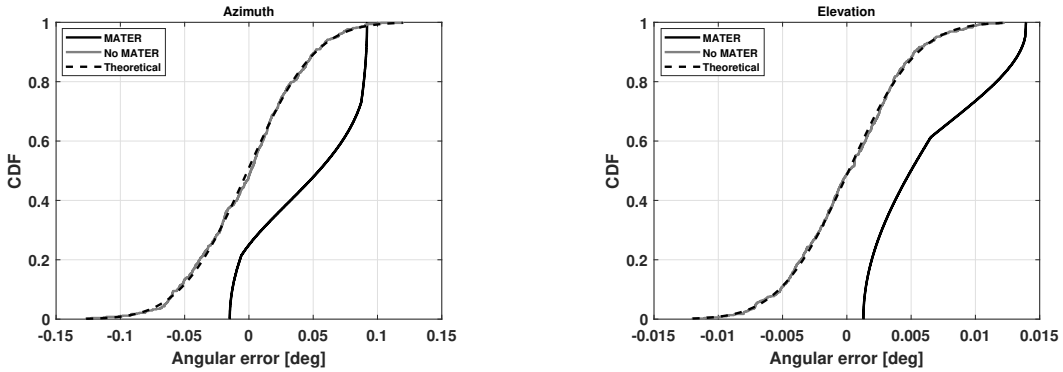

(a) Azimuth CDF. (b) Elevation CDF.

Figure 7-18: Operational scenario with MATER: angular error distribution Cumulative Distribution Function (CDF) in azimuth and elevation. Both the MATER, no MATER and theoretical cases are represented.

	Correct solutions	1 min $< t_{err} < T^p/2$	$t_{err} > T^p/2$	N. of FRED results
MATER	0.0 %	0.0 %	100 %	99
No MATER	8.1 %	23.2 %	68.7%	99

Table 7.19: Operational scenario with MATER: deterministic relative distance metrics results starting from the IOD conducted either with MATER or without MATER.

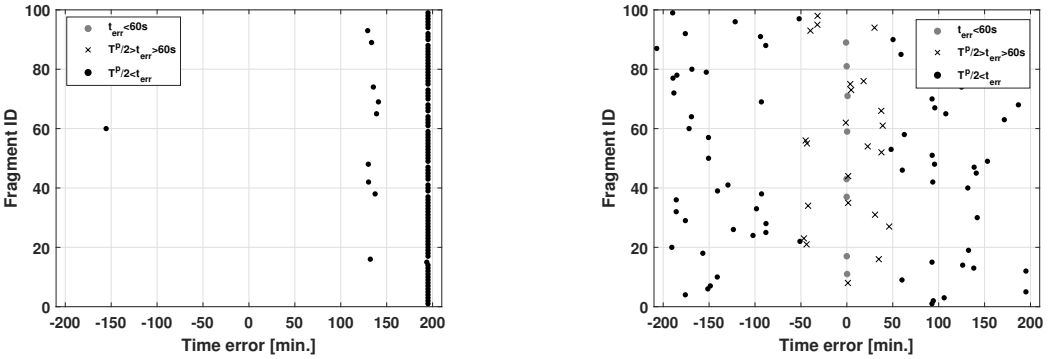

(a) MATER case. (b) No MATER case.

Figure 7-19: Operational scenario with MATER: time error of the deterministic relative distance metrics starting from the IOD conducted either with MATER or without MATER.

sensors to derive a more accurate orbital state to be used in the algorithm. Nevertheless, determining the fragmentation epoch starting from a fragment IOD conducted from MATER result performs better with FRED algorithm than with the deterministic relative distance metrics.

Chapter 8

Conclusions

This thesis illustrates the potential of the adaptive beamforming technique to derive the angular track in array radars devoted to space surveillance, and assesses the consequent benefits for the SST activities. This objective is accomplished with the development of MATER, presented in Ch. 3, an algorithm embedding MUSIC to estimate the signal directions of arrival, which are then clustered to provide the angular track measurement in the receiver FoV. Ambiguous solutions may be possibly generated because of the mutual distance among array receivers and, to solve this problem, MATER exploits the transit prediction in the catalogued case, or tailored criteria otherwise. These criteria are based either on statistical considerations, or on the signal processing, or even on the merging with additional measurements.

Chapter 4 assessed MATER performance for the single target case, by considering BIRALES as baseline. The nominal analysis, conducted both on the catalogued and the uncatalogued case, provided a 50-th percentile of the angular track root mean square error between 6.9e-03 deg and 1.0e-02 deg. All of the ambiguity solving criteria for the uncatalogued case provided a high-rate convergence to the correct solution. A sensitivity analysis highlighted that the angular track accuracy depends on four main factors. First, the higher the detected signal, the higher the signal direction of arrival precision and, so, the more accurate the reconstructed angular track. Thus, the accuracy strongly depends on the transmitted power and, if it is not sufficient, the target would not even be detected. Second, with the same number of samples integrated to generate a single estimation, the smaller the integration time, the shorter the time uncertainty associated to the estimation and the smaller the related angu-

lar error. However, to keep the number of samples constant, the sampling frequency would increase accordingly, and this would enlarge the receiver bandwidth noise and, so, attenuate the detected signal. Hence, a trade-off choice is necessary. Third, with the same integration time, the longer the angular path along a direction, the larger the angular error associated to that coordinate because of the estimation time uncertainty. Fourth, the larger the number of receivers along a direction, the higher the theoretical accuracy along that coordinate, but this effect may be hidden by the previous one. Practical applications in Re-entry Analysis and Collision Avoidance services are simulated and discussed, and a real observation of the International Space Station is presented.

Chapter 5 was then dedicated to the multiple sources scenario, that is when more than one target is simultaneously present in the receiver FoV, like what may occur during a survey observation. MATER is also adapted to manage such situations, by associating the computed signal direction of arrival to the correct target. A numerical nominal analysis obtains an angular track accuracy similar to the single target one in Ch. 4. Based on a sensitivity analysis on the transmitted power, the smaller it is, the less multiple sources are observed simultaneously, as the detection arc is shortened and the epochs of overlapping between sources reduces as well. Simulations involving proximity operations monitoring and fragments cloud observation are carried out and discussed. In particular, the latter analysis motivates the interest in on-ground multi-receiver radars applications to the Fragmentation Analysis service, MATER algorithm might further contribute to.

Therefore, Ch. 6 deals with the fragmentation epoch identification problem focusing on the case in which, besides the last available ephemeris of the parent object, just one single fragment orbital state obtained by one single surveillance radar observation is available and already linked to the event. Thus, the problem is approached in a stochastic way through FRED algorithm, which assumes the last available ephemeris of the parent object as a deterministic quantity, while the fragment orbital state is represented according to a multinormal distribution from its mean and covariance, resulting in samples. All of them, together with the parent ephemeris, are propagated on the analysis time window, sampled according to the parent orbital period. For each periodicity and for each couple parent-sample, the Minimum Orbital Intersection Distance (MOID) is determined, as well as the epochs of parent transit through it and the relative distance at those epochs. Computing these quantities for all the parent-sample couples provides the distribution of the fragmentation epoch candidate (from

the epoch of parent transit through the MOID), of the relative distance and of the MOID. This process is repeated for all the periodicities, resulting in fragmentation epoch candidates, which are ranked according to the matching between MOID and relative distance distributions, given that, at the actual fragmentation epoch, the MOID and the relative distance were equal. To compute the statistical matching, three metrics are discussed: the Mahalanobis distance, the Earth Mover's Distance (EMD) and a tailored procedure based on the quantiles coupled with a Principal Component Analysis (PCA).

FRED performance are then assessed in Ch. 7. First a Keplerian scenario with no orbit determination errors highlights that the distributions involved in the process are not Gaussian and, for this reason, the Mahalanobis distance is rejected as metrics. Then, the EMD results better performing and is selected for all the following analyses. Generally, the algorithm converges to the correct solution, but it gets less robust when fragment and parent orbits are similarly oriented, or have a similar shape. Furthermore, these cases correspond to a larger standard deviation associated to the solution. A sensitivity analysis shows that there is no dependence on the number of samples used in representing the fragment orbital state. The inclusion of the perturbations and, moreover, of the orbit determination error provokes a remarkable deterioration in performance, but the correct fragmentation epoch is always present among candidates. In addition, alternative deterministic metrics are performing worse, especially when the fragmentation epoch is identified as the time of the minimum relative distance between the parent ephemeris and the fragment mean state propagated on the analysis time window. A further sensitivity analysis shows a deterioration proportional to the angular noise associated to the solution and to the time elapsed between the event and the observation, but FRED is always much more performing than the relative distance metrics. Instead, no remarkable change is present for a fragment physical parameter mismatching between the actual value and the one used in the algorithm, but this depends on the fragment orbital regimen and on the elapsed time from the event to the observation, and so it is not possible to consider it as a general result.

An operational application involving BIRALES highlights the operational critical aspects of this method: since, in practical cases, the observation can be scheduled only according to the parent object transit prediction, it is easy to run in cases in which the fragment and parent orbits are similarly oriented or have a similar shape, that is the most critical ones. Finally, to include MATER algorithm and to evaluate its contribution to this Fragmentation

Analysis service problem, an operational scenario in which the angular track is obtained with MATER is assessed. Results get deteriorated because the angular track has non-Gaussian and non-zero mean error. Nevertheless, FRED performance is much more appreciable than the deterministic metrics ones.

The thesis objective can be considered accomplished, as the adaptive beamforming technique widely showed its potential, with some particular aspects it is fundamental to take care of. First of all, the angular track accuracy strongly depends on the detected signal intensity and the integration time, which are also related each other. Indeed, a high-intensity signal would allow to have enough signal to noise ratio even for high frequency sampling, and this would allow to shorten the integration time, with benefit in the angular track accuracy. Therefore, to obtain the best performance it is necessary to maximise the detected signal intensity, by increasing the transmitted power or the stations gain, like enlarging the number of receivers. This latter action would also improve the angular resolution, as long as the integration time is short enough. Based on the SST services simulations discussed in Ch. 4, Ch. 5 and Ch. 7, it is worth to point out that the angular track obtained with MATER is not sufficient to initially determine the target orbital state with a high-level accuracy, but this is compliant with the purpose of surveillance radars, which usually first determine the target orbit, later refined and monitored by tracking radars and telescopes. Furthermore, the capability of determining the angular track of multiple sources simultaneously is of utmost importance, and constitutes a significant advantage with respect the static beamforming techniques. The next step is to carry out an extensive validation campaign on real data, both to validate the approach and to find out possible aspects which may improve the procedure. Finally, for the operational use of the approach, a rigorous analysis of the MATER computational demand shall be carried out and the algorithm properly implemented to minimise it.

A separate discussion must be dedicated to FRED algorithm. Ch. 7 shows the advantage of this stochastic approach in the fragmentation epoch identification problem, but the more realistic the simulation is, the more deteriorated the performance turns out to be. First, this is due to the fragment orbital state accuracy, which is voluntarily kept consistent with the surveillance radar ones. In operational scenario, besides the positive contribution of a more accurate angular track (as discussed above), the fragment orbital state could be either refined from the same measurements with a smarter orbit determination process, or improved through other sensor contributions. Furthermore, the plausibility of the frag-

mentation epoch candidates can be examined by tasking the sensors to point at the right ascensions and declinations where the parent was at those epochs and retain only candidates featuring a sufficient number of fragments detected. This action cannot be decisive, as periodicity failures may share the same right ascension and declination as the correct solution, but it can support to shrink the candidates set. Another point concerns the uncertainty representation: the multivariate normal distribution used represents the most generic approach, but a smarter way of covariance propagation may be integrated in the process, for example combining the UT [58] with the Gaussian mixtures [65]. This choice, if properly implemented, would decrease the computational demand, as less orbital states would be propagated. In addition, the process considers the last available ephemeris as a deterministic information, while an uncertainty is associated also to it. Thus, a possible improvement to be investigated is to apply FRED at a lower algorithm level, by also keeping the samples strategy for the fragment orbital state, and then repeating this process for all the samples representing the parent object uncertainty (defined like through UT). Another aspect which may be further studied is the fragmentation epoch candidates ranking strategy, which is currently performed based on the statistical matching between the relative distance and the MOID distributions, but which may profit from other conjunction analysis tools, like the long term risk assessment. Finally, it would be interesting to deal with the fragmentation epoch identification in the case that it is not possible to determine the fragment orbital state, with a tailored procedure conducted in the measurements space. Overall, all these possible algorithm improvements and developments should be carried out together with test on real data and the final operational implementation shall include a detailed computational demand assessment and minimisation.

Bibliography

[1] Space debris by the numbers. European Space Agency, 2022. Accessed 12.04.2022, https://www.esa.int/Our_Activities/Operations/Space_Safety_Security/Space_Debris/Space_debris_by_the_numbers.

[2] ESA Space Debris Office. *ESA's Annual Space Environment Report*, 2022.

[3] D. J. Kessler and B. G. Cour-Palais. Collision frequency of artificial satellites: The creation of a debris belt. *Journal of Geophysical Research*, page 2637–2646, 1978.

[4] Inter-Agency Space Debris Coordination Committee. *Space Debris Mitigation Guidelines*, 2002.

[5] International Standards Organisation. *Space systems - Space debris mitigation requirements*, 2019.

[6] International Standards Organisation. *Guidelines for the Long-term Sustainability of Outer Space Activities*, 2019.

[7] Chairman of the Joint Chiefs of Staff (CJCS). *Space Operations*, 2020.

[8] Space Situational Awareness Programme overview. European Space Agency, 2022. Accessed 12.04.2022, https://www.esa.int/Safety_Security/SSA_Programme_overview.

[9] Consultative Committee for Space Data Systems. *Tracking Data Message*, 2007.

[10] Consultative Committee for Space Data Systems. *Conjunction Data Message*, 2013.

[11] Maj. E. P. Chatters and Maj. Brian J. Crothers. Chapter 19 - Space Surveillance Network. In *AU-18 Space Primer*, pages 249–258. Air University Press, Maxwell Air Force Base, 131 West Shumacher Avenue, Maxwell AFB, AL 36112-5962, September 2009. ISBN 978-1-58566-194-7.

[12] 614th Air Operations Center. *U.S. Strategic Command Fact Sheet Combined Space Operations Center*, 2018.

[13] Space-track. Space-track website, 2022. Accessed 18.08.2022, https://www.space-track.org/auth/login.

[14] F. R. Hoots and R. L. Roehrich. *Models for Propagation of NORAD Element Sets*, 1980.

[15] J. A. Haimerl and G. P. Fonder. Space fence system overview. In *Proceedings of the Advanced Maui Optical and Space Surveillance Technology Conference*. Curran Associates, Inc, 2015.

[16] Space Fence surveillance radar site declared operational. Space News, 2020. Accessed 12.04.2022, `https://spacenews.com/space-fence-surveillance-radar-site-declared-operational/`.

[17] G. Fonder, M. Hughes, M. Dickson, M. Schoenfeld, and J. Gardner. Space fence radar overview. In *2019 International Applied Computational Electromagnetics Society Symposium (ACES)*, pages 1–2. IEEE, 2019.

[18] D. L. Pechkis, N. S. Pacheco, and T. W. Botting. Statistical approach to the operational testing of space fence. *IEEE Aerospace and Electronic Systems Magazine*, 31 (11):30–39, 2016.

[19] Haney: U.S. Partners To Have Indirect Access to Space Fence Data. Space News, 2014. Accessed 12.04.2022, `https://archive.ph/20141201175242/http://www.spacenews.com/article/military-space/42619haney-us-partners-to-have-indirect-access-to-space-fence-data`.

[20] Parliament and the Council of the European Union. Decision No 541/2014/EU of the European Parliament and of the Council of 16 April 2014 establishing a Framework for Space Surveillance and Tracking Support. *Official Journal of the European Union*, 2014.

[21] European Space Surveillance and Tracking website. EUSST, 2022. Accessed 12.04.2022, `https://www.eusst.eu/`.

[22] European Space Surveillance and Tracking. *EUSST Service Portfolio*, 2021.

[23] European Space Surveillance and Tracking. *EUSST Leaflet*, 2022.

[24] T. Flohrer and H. Krag. Space surveillance and tracking in ESA's SSA programme. In *7th European Conference on Space Debris*, volume 7, 2017.

[25] European Space Agency SSA program - SST Segment. ESA, 2022. Accessed 12.04.2022, `https://www.esa.int/Safety_Security/Space_Surveillance_and_Tracking_-_SST_Segment`.

[26] Consultative Committee for Space Data Systems website. CCSDS, 2022. Accessed 12.04.2022, `https://public.ccsds.org/default.aspx`.

[27] European Committee for Standardization website. CENELEC, 2022. Accessed 12.04.2022, `https://www.cencenelec.eu/about-cen/`.

[28] European Electrotechnical Committee for Standardization website. CENELEC, 2022. Accessed 12.04.2022, `https://www.cencenelec.eu/about-cenelec/`.

[29] B. Reihs, A. Vananti, T. Schildknecht, J. Siminski, and T. Flohrer. Application of attributables to the correlation of surveillance radar measurements. *Acta Astronautica*, 182:399–415, 2021. ISSN 0094-5765. doi: https://doi.org/10.1016/j.actaastro.2021.01.059. URL `https://www.sciencedirect.com/science/article/pii/S0094576521000709`.

[30] D. Cerutti-Maori, J. Rosebrock, C. Carloni, M. Budoni, and J. Klare. A Novel High-Precision Observation Mode for the Tracking and Imaging Radar TIRA – Principle and Performance Evaluation. In *8th European Conference on Space Debris*, volume 8, 2021.

[31] A. Jouadé and A. Barka. Massively Parallel Implementation of FETI-2LM Methods for the Simulation of the Sparse Receiving Array Evolution of the GRAVES Radar System for Space Surveillance and Tracking. *IEEE Access*, 7:128968–128979, 2019. doi: 10.1109/ACCESS.2019.2938011.

[32] F. Muller. GRAVES Space Surveillance System: Life Extension and Upgrade Program. In *7th European Conference on Space Debris*, volume 7, 2017.

[33] R. C. Gómez, P. Besso, G. M. Pinna, M. Alessandrini, J. M. Salmerón, and M. A. R. Prada. Initial operations of the breakthrough Spanish Space Surveillance and Tracking Radar (S3TSR) in the European Context. In *1st NEO and Debris Detection Conference*, volume 1, 2019.

[34] H. Wilden, B. N. Bekhti, R. Hoffmann, C. Kirchner, R. Kohlleppel, C. Reising, A. Brenner, and T. Eversberg. GESTRA - Recent Progress, Mode Design and Signal Processing. In *2019 IEEE International Symposium on Phased Array System Technology (PAST)*, pages 1–8, 2019. doi: 10.1109/PAST43306.2019.9020744.

[35] DLR. GESTRA - German Experimental Space Surveillance and Tracking Radar. Technical report, 58 th session of the Scientific and Technical Subcommittee of UNCOPUOS, 2021.

[36] H. Wilden, C. Kirchner, O. Peters, N. B. Bekhti, R. Kohlleppel, A. Brenner, and T. Eversberg. GESTRA - Technology Aspects and Mode Design for Space Surveillance and Tracking. In *7th European Conference on Space Debris*, volume 7, 2017.

[37] EISCAT Scientific Association website. EISCAT, 2016. Accessed 14.04.2022, `https://eiscat.se/eiscat3d-information/`.

[38] J. Vierinen. Use of EISCAT 3D for Observations of space debris. In *7th European Conference on Space Debris*, volume 7, 2017.

[39] T. Pisanu, L. Schirru, E. Urru, F. Gaudiomonte, P. Ortu, G. Bianchi, C. Bortolotti, M. Roma, G. Muntoni, G. Montisci, F. Protopapa, A. Podda, A. Sulis, and G. Valente. Upgrading the Italian BIRALES system to a pulse compression radar for space debris range measurements. In *2018 22nd International Microwave and Radar Conference (MIKON)*, pages 317–320, 2018. doi: 10.23919/MIKON.2018.8405212.

[40] M. Losacco. *Orbit determination of resident space objects using radar sensors in multibeam configuration*. PhD thesis, Politecnico di Milano, 2020.

[41] M. Losacco, P. Di Lizia, M. Massari, G. Naldi, G. Pupillo, G. Bianchi, and J. Siminski. Initial orbit determination with the multibeam radar sensor BIRALES. *Acta Astronautica*, 167:374–390, 2020. ISSN 0094-5765. doi: https://doi.org/10.1016/j.actaastro.2019.10.043. URL https://www.sciencedirect.com/science/article/pii/S0094576519313712.

[42] G. Bianchi, C. Bortolotti, M. Roma, G. Pupillo, G. Naldi, L. Lama, F. Perini, M. Schiaffino, A. Maccaferri, A. Mattana, A. Podda, S. Casu, F. Protopapa, A. Coppola, P. Di Lizia, G. Purpura, M. Massari, M. F. Montaruli, T. Pisanu, L. Schirru, and E. Urru. Exploration of an innovative ranging method for bi-static radar, applied in LEO Space Debris surveying and tracking. In *Proceedings of the International Astronautical Congress, IAC*, October 2020.

[43] G. Bianchi, G. Naldi, F. Fiocchi, P. Di Lizia, C. Bortolotti, A. Mattana, A. Maccaferri, A. Magro, M. Roma, M. Schiaffino, A. Cattani, D. Cutajar, G. Pupillo, F. Perini, L. Facchini, L. Lama, M. Morsiani, and M. F. Montaruli. A new concept of bi-static radar for space debris detection and monitoring. In *International Conference on Electrical, Computer, Communications and Mechatronics Engineering, ICECCME 2021*, 2021. doi: 10.1109/ICECCME52200.2021.9590991. URL https://www.scopus.com/inward/record.uri?eid=2-s2.0-85119418072&doi=10.1109%2fICECCME52200.2021.9590991&partnerID=40&md5=00f78c2fc869199eb6cedf93529a1496.

[44] T. Pisanu, L. Schirru, E. Urru, G. Bianchi, A. Podda, and P. Di Lizia. The Italian BIRALET Radar System to Perform Range and Range Rate Measurements in the EUSST European Space Surveillance and Tracking Program. In *Proceedings of the International Astronautical Congress, IAC*, October 2020.

[45] B. D. Tapley, B. E. Schutz, and G. H. Born. Chapter 2 - The Orbit Problem. In B. D. Tapley, B. E. Schutz, and G. H. Born, editors, *Statistical Orbit Determination*, pages 17–91. Academic Press, Burlington, 2004. ISBN 978-0-12-683630-1. doi: https://doi.org/10.1016/B978-012683630-1/50021-7. URL https://www.sciencedirect.com/science/article/pii/B9780126836301500217.

[46] C. H. Acton. Ancillary data services of NASA's Navigation and Ancillary Information Facility. *Planetary and Space Science*, 44(1):65–70, 1996. ISSN 0032-0633. doi: https://doi.org/10.1016/0032-0633(95)00107-7. URL https://www.sciencedirect.com/science/article/pii/0032063395001077. Planetary data system.

[47] T. C. Cheston and J. Frank. Chapter 7 - Phased Array Radar Antennas. In M. I. Skolnik, editor, *Radar Handbook*, pages 7.17–7.22. McGraw Hill, 1990. ISBN 0-07-057913-X.

[48] H. D. Curtis. Chapter 3 - Orbital Position as a Function of Time. In H. D. Curtis, editor, *Orbital Mechanics for Engineering Students (Third Edition)*, pages 145–186. Butterworth-Heinemann, Boston, third edition edition, 2014. ISBN 978-0-08-097747-8. doi: https://doi.org/10.1016/B978-0-08-097747-8.00003-7. URL https://www.sciencedirect.com/science/article/pii/B9780080977478000037.

[49] H. D. Curtis. Chapter 12 - Introduction to Orbital Perturbations. In H. D. Curtis, editor, *Orbital Mechanics for Engineering Students (Third Edition)*, pages 651–720.

Butterworth-Heinemann, Boston, third edition edition, 2014. ISBN 978-0-08-097747-8. doi: https://doi.org/10.1016/B978-0-08-097747-8.00012-8. URL https://www.sciencedirect.com/science/article/pii/B9780080977478000128.

[50] P. C. Knocke, J. C. Ries, and B. D. Tapley. Earth radiation pressure effects on satellites. In *Astrodynamics Conference*, 1988.

[51] P.J. Prince and J.R. Dormand. High order embedded Runge-Kutta formulae. *Journal of Computational and Applied Mathematics*, 7(1):67–75, 1981. ISSN 0377-0427. doi: https://doi.org/10.1016/0771-050X(81)90010-3. URL https://www.sciencedirect.com/science/article/pii/0771050X81900103.

[52] D. A. Vallado, P. Crawford, R. Hujsak, and T. S. Kelso. Revisiting Spacetrack Report \#3 In *AIAA Astrodynamics Specialists Conference and Exhibit*, August 2006.

[53] P. Cefola, Z. Folcik, R. Di-Costanzo, N. Bernard, S. Setty, and J. San Juan. Revisiting the DSST Standalone Orbit Propagator. *Advances in the Astronautical Sciences*, 152: 2891–2914, January 2014.

[54] S. W. Shepperd. Universal Keplerian state transition matrix. *Celestial mechanics*, 35: 129–144, 1985.

[55] J. T. Horwood and A. B. Poore. Adaptive Gaussian Sum Filters for Space Surveillance. *IEEE Transactions on Automatic Control*, 56(8):1777–1790, 2011. doi: 10.1109/TAC.2011.2142610.

[56] J. M. Aristoff, J. T. Horwood, and K. T. Alfriend. On a set of J_2 equinoctial orbital elements and their use for uncertainty propagation. *Celestial Mechanics and Dynamical Astronomy*, 133(3):9, March 2021. doi: 10.1007/s10569-021-10004-0.

[57] R. Broucke and P. J. Cefola. On the equinoctial orbit elements. *Celestial mechanics*, 5:303–310, 1972.

[58] S. Julier, J. Uhlmann, and H.F. Durrant-Whyte. A new method for the nonlinear transformation of means and covariances in filters and estimators. *IEEE Transactions on Automatic Control*, 45(3):477–482, 2000. doi: 10.1109/9.847726.

[59] S. Kotz, N. Balakrishnan, and N. L. Johnson. *Continuous Multivariate Distributions. Models and Applications*, volume 1: Models and Applications. New York: John Wiley, 2nd edition edition, 2000.

[60] B. D. Tapley, B. E. Schutz, and G. H. Born. Chapter 4 - Fundamentals of Orbit Determination. In B. D. Tapley, B. E. Schutz, and G. H. Born, editors, *Statistical Orbit Determination*, pages 159–284. Academic Press, Burlington, 2004. ISBN 978-0-12-683630-1. doi: https://doi.org/10.1016/B978-012683630-1/50023-0. URL https://www.sciencedirect.com/science/article/pii/B9780126836301500230.

[61] M. I. Skolnik. Chapter 1 - An Introduction to Radar. In M. I. Skolnik, editor, *Radar Handbook*, pages 1.6–1.10. McGraw Hill, 1990. ISBN 0-07-057913-X.

[62] M. I. Skolnik. Chapter 25 - Bistatic Radar. In M. I. Skolnik, editor, *Radar Handbook*, pages 25.5–25.35. McGraw Hill, 1990. ISBN 0-07-057913-X.

[63] P. C. Mahalanobis. On the generalized distance in statistics. *Proceedings of the National Institute of Sciences (Calcutta)*, 2:49–55, 1936.

[64] S. M. Lenz, H. G. Bock, J. P. Schlöder, E. A. Kostina, G. Gienger, and G. Ziegler. Multiple Shooting Method for Initial Satellite Orbit Determination. *Journal of Guidance, Control, and Dynamics*, 33(5):1334–1346, 2010. doi: 10.2514/1.48929. URL `https://doi.org/10.2514/1.48929`.

[65] M. L. Psiaki. Gaussian Mixture Filter for Angles-Only Orbit Determination in Modified Equinoctial Elements. *Journal of Guidance, Control, and Dynamics*, 45(1):73–83, 2022. doi: 10.2514/1.G005891. URL `https://doi.org/10.2514/1.G005891`.

[66] S. J. Julier and J. K. Uhlmann. Unscented filtering and nonlinear estimation. *Proceedings of the IEEE*, 92(3):401–422, 2004. doi: 10.1109/JPROC.2003.823141.

[67] D. A. Vallado. Chapter 6 - Initial Orbit Determination. In Wiley J. Larson, editor, *Fundamentals of Astrodynamics and Applications*, pages 371–464. McGraw Hill, New York, 1997. ISBN 0-07-066829-9.

[68] A. C. Long, J. O. Cappellari, C. E. Velez, and A. J. Fuchs. Chapter 9 - Launch and Early Orbit Methods. In *Goddard Trajectory Determination System (GDTS) Mathematical Theory (revision 1)*, pages 9.44–9.52. Computer Sciences Corporation, 1989.

[69] J. Siminski. Techniques for assessing space object cataloguing performance during design of surveillance systems. In *6th International Conference on Astrodynamics Tools and Techniques (ICATT)*, pages 14–17, 2016.

[70] D. A. Vallado. Chapter 4 - Initial Orbit Determination. In Wiley J. Larson, editor, *Fundamentals of Astrodynamics and Applications*, pages 249–261. McGraw Hill, New York, 1997. ISBN 0-07-066829-9.

[71] C. Yanez, F. Mercier, and J. C. Dolado. A Novel Initial Orbit Determination Algorithm from Doppler and Angular Observations. In *7th European Conference on Space Debris*, volume 7, 2017.

[72] H. L. Van Trees. Optimum Waveform Estimation. In *Optimum Array Processing*, chapter 6, pages 428–709. John Wiley & Sons, Ltd, 2002. ISBN 9780471221104. doi: https://doi.org/10.1002/0471221104.ch6. URL `https://onlinelibrary.wiley.com/doi/abs/10.1002/0471221104.ch6`.

[73] H. L. Van Trees. Adaptive Beamformers. In *Optimum Array Processing*, chapter 7, pages 710–916. John Wiley & Sons, Ltd, 2002. ISBN 9780471221104. doi: https://doi.org/10.1002/0471221104.ch7. URL `https://onlinelibrary.wiley.com/doi/abs/10.1002/0471221104.ch7`.

[74] H. L. Van Trees. Parameter Estimation I: Maximum Likelihood. In *Optimum Array Processing*, chapter 8, pages 917–1138. John Wiley & Sons, Ltd, 2002. ISBN 9780471221104. doi: https://doi.org/10.1002/0471221104.ch8. URL `https://onlinelibrary.wiley.com/doi/abs/10.1002/0471221104.ch8`.

[75] H. L. Van Trees. Parameter Estimation II. In *Optimum Array Processing*, chapter 9, pages 1139–1317. John Wiley & Sons, Ltd, 2002. ISBN 9780471221104. doi: https://doi.org/10.1002/0471221104.ch9. URL https://onlinelibrary.wiley.com/doi/abs/10.1002/0471221104.ch9.

[76] R. O. Schmidt. *A signal subspace approach to multiple emitter location and spectral estimation*. Stanford University, 1981.

[77] R. Schmidt. Multiple emitter location and signal parameter estimation. *IEEE Transactions on Antennas and Propagation*, 34(3):276–280, 1986. doi: 10.1109/TAP.1986.1143830.

[78] A. J. Barabell, J. Capon, D. F. Delong, J. R. Johnson, and K. D. Senne. *Performance Comparison of Superresolution Array Processing Algorithms. Revised*, 1998.

[79] G. F. Masters and S. F. Gregson. Coordinate System Plotting for Antenna Measurements. In *Antenna Measurement Techniques Association*, 2007.

[80] H. L. Van Trees. Arrays and Spatial Filters. In *Optimum Array Processing*, chapter 2, pages 17–89. John Wiley & Sons, Ltd, 2002. ISBN 9780471221104. doi: https://doi.org/10.1002/0471221104.ch2. URL https://onlinelibrary.wiley.com/doi/abs/10.1002/0471221104.ch2.

[81] S. N. Madsen and H. A. Zebker. Automated Absolute Phase Retrieval in Across-Track Interferometry. In *IGARSS '92 International Geoscience and Remote Sensing Symposium*, volume 2, pages 1582–1584, 1992. doi: 10.1109/IGARSS.1992.578639.

[82] S. N. Madsen, H. A. Zebker, and J. Martin. Topographic mapping using radar interferometry: processing techniques. *IEEE Transactions on Geoscience and Remote Sensing*, 31(1):246–256, 1993. doi: 10.1109/36.210464.

[83] R. Bamler and M. Eineder. Accuracy of differential shift estimation by correlation and split-bandwidth interferometry for wideband and delta-k SAR systems. *IEEE Geoscience and Remote Sensing Letters*, 2(2):151–155, 2005. doi: 10.1109/LGRS.2004.843203.

[84] R. Brcic, M. Eineder, and R. Bamler. Absolute Phase Estimation from TerraSAR-X Acquisitions using Wideband Interferometry. In *CEOS SAR Calibration and Validation Workshop*, November 2008.

[85] G. Gomba, A. Parizzi, F. De Zan, M. Eineder, and R. Bamler. Toward Operational Compensation of Ionospheric Effects in SAR Interferograms: The Split-Spectrum Method. *IEEE Transactions on Geoscience and Remote Sensing*, 54(3):1446–1461, 2016. doi: 10.1109/TGRS.2015.2481079.

[86] R. Brcic, A. Parizzi, M. Eineder, R. Bamler, and F. Meyer. Estimation and compensation of ionospheric delay for SAR interferometry. In *2010 IEEE International Geoscience and Remote Sensing Symposium*, pages 2908–2911, 2010. doi: 10.1109/IGARSS.2010.5652231.

[87] MATLAB. *9.9.0.1538559 (R2020b)*. The MathWorks Inc., Natick, Massachusetts, 2020.

[88] M. F. Montaruli. Collision risk assessment and collision avoidance maneuver planning. Master's thesis, Politecnico di Milano, 2019.

[89] S. Alfano. Satellite conjunction Monte Carlo analysis. *Advances in the Astronautical Sciences*, 134:2007–2024, January 2009.

[90] R. P. Patera. General Method for Calculating Satellite Collision Probability. *Journal of Guidance, Control, and Dynamics*, 24(4):716–722, 2001. doi: 10.2514/2.4771. URL `https://doi.org/10.2514/2.4771`.

[91] F. K. Chan. *Spacecraft collision probability*. Aerospace Press El Segundo, CA, 2008.

[92] R. Serra, D. Arzelier, M. Joldes, J.-B. Lasserre, A. Rondepierre, and B. Salvy. A Power Series Expansion based Method to compute the Probability of Collision for Short-term Space Encounters. *Archive ouverte*, March 2015.

[93] R. García-Pelayo and J. Hernando-Ayuso. Series for Collision Probability in Short-Encounter Model. *Journal of Guidance, Control, and Dynamics*, 39(8):1904–1912, 2016. doi: 10.2514/1.G001754. URL `https://doi.org/10.2514/1.G001754`.

[94] NASA. Satellite Collision Leaves Significant Debris Clouds. *Orbital Debris Quarterly News*, 13(2):1–2, 2011.

[95] T. Flohrer, H. Krag, and H. Klinkrad. Assessment and Categorization of TLE Orbit Errors for the US SSN Catalogue. In *Advanced Maui Optical and Space Surveillance Technologies Conference*, pages 53–, January 2008.

[96] M. Maestrini and P. Di Lizia. Guidance Strategy for Autonomous Inspection of Unknown Non-Cooperative Resident Space Objects. *Journal of Guidance, Control, and Dynamics*, 45(6):1126–1136, 2022. doi: 10.2514/1.G006126. URL `https://doi.org/10.2514/1.G006126`.

[97] N. L. Johnson, P. H. Krisko, J.-C. Lieu, and P. D. Anz-Meador. NASA's new breakup model of evolve 4.0. *Advances in Space Research*, 28(9):1377–1384, 2001. ISSN 0273-1177. doi: https://doi.org/10.1016/S0273-1177(01)00423-9. URL `https://www.sciencedirect.com/science/article/pii/S0273117701004239`.

[98] NASA. Proper implementation of the 1998 NASA breakup model. *Orbital Debris Quarterly News*, 15(4):4–5, 2011.

[99] F. Letizia, C. Colombo, and H. G. Lewis. Analytical Model for the Propagation of Small-Debris-Object Clouds After Fragmentations. *Journal of Guidance, Control, and Dynamics*, 7ı38(8):1478–1491, 2015.

[100] F. Letizia, C. Colombo, and H. G. Lewis. Multidimensional extension of the continuity equation method for debris clouds evolution. *Advances in Space Research*, 57(8):1624–1640, 2016.

[101] R. L. Andrisan, A. Ioniţă, R. Domínguez González, N. Sánchez Ortiz, F. Pina Caballero, and H. Krag. Fragmentation Event Model and Assessment Tool (FREMAT) Supporting On-Orbit Fragmentation Analysis. In *7th European Conference on Space Debris*, 2016.

[102] S. Frey, C. Colombo, and S. Lemmens. Density based modelling and indication of break-up location and epoch from fragments using backwards propagation. In *5thEuropean Workshop on Space Debris Modelling and Remediation*, June 2018.

[103] L. Di Mare, S. Cicalò, A. Rossi, E. M. Alessi, and G. B. Valsecchi. In-Orbit Fragmentation Characterization and Parent Bodies Identification by Means of Orbital Distances. In *First International Orbital Debris Conference*, volume 2109 of *LPI Contributions*, page 6007, December 2019.

[104] M. Romano, A. Muciaccia, M. Trisolini, P. Di Lizia, C. Colombo, A. Di Cecco, and L. Salotti. Characterising in-orbit fragmentations with the PUZZLE software. In *8th International Conference on Astrodynamics Tools and Techniques (ICATT)*, 2021.

[105] F. R. Hoots, L. L. Crawford, and R. L. Roehrich. An analytic method to determine future close approaches between satellites. *Journal of Celestial Mechanics and Dynamical Astronomy*, 33(2):143–158, June 1984.

[106] G. F. Gronchi. An Algebraic Method to Compute the Critical Points of the Distance Function Between Two Keplerian Orbits. *Journal of Celestial Mechanics and Dynamical Astronomy*, 93(1):295–329, September 2005.

[107] M. Ester, H.-P. Kriegel, J. Sander, and X. Xu. A Density-Based Algorithm for Discovering Clusters in Large Spatial Databases with Noise. In *Proceedings of the Second International Conference on Knowledge Discovery and Data Mining*, KDD'96, page 226–231. AAAI Press, 1996.

[108] D. Vallado and S. Alfano. Curvilinear coordinate transformations for relative motion. *Celestial Mechanics and Dynamical Astronomy*, 118, February 2014. doi: 10.1007/s10569-014-9531-1.

[109] E. Levina and P. Bickel. The Earth Mover's distance is the Mallows distance: some insights from statistics. In *Proceedings Eighth IEEE International Conference on Computer Vision. ICCV 2001*, volume 2, pages 251–256 vol.2, 2001. doi: 10.1109/ICCV.2001.937632.

[110] SciPy. SciPy documentation, 2022. URL `https://docs.scipy.org/doc/scipy/`. Last accessed August 18$^{\text{th}}$, 2022.

[111] Ian Jolliffe. *Principal Component Analysis*, pages 1094–1096. Springer Berlin Heidelberg, Berlin, Heidelberg, 2011. ISBN 978-3-642-04898-2. doi: 10.1007/978-3-642-04898-2_455. URL `https://doi.org/10.1007/978-3-642-04898-2_455`.

[112] J. Herzog, H. Fiedler, and T. Schildknecht. Using Conjunctuion Analysis Methods for Manoeuvre Detection. In *7th European Conference on Space Debris*, January 2017.

[113] EUSST. COSMOS 1408 fragmentation, 2021. Accessed 18.08.2022, https://www.eusst.eu/newsroom/eu-sst-confirms-fragmentation-cosmos-1408/.

[114] A Muciaccia, L Facchini, MF Montaruli, G Purpura, R Detomaso, C Colombo, M Massari, P Di Lizia, A Di Cecco, L Salotti, et al. Observation and analysis of cosmos 1408 fragmentation. In *INTERNATIONAL ASTRONAUTICAL CONGRESS: IAC PROCEEDINGS*, pages 1–7, 2022.